UNIVERSITY OF HUDDERSFIELD

DOCTORAL THESIS

Mechanical Design of Permanent Magnet Rotors for High-Speed Electric Machines

Author:

Levi MALLIN

Supervisor:

Prof. Simon BARRANS

A thesis submitted in fulfillment of the requirements

for the degree of Doctor of Philosophy

Turbo Research Group

Department of Engineering and Technology

May 6, 2022

UNIVERSITY OF HUDDERSFIELD

Abstract

School of Computing & Engineering

Department of Engineering and Technology

Doctor of Philosophy

Mechanical Design of Permanent Magnet Rotors for High-Speed Electric Machines

by Levi MALLIN

With an ever-increasing drive towards greener energy and a reduction in emissions, high-speed electric machines (HSEMs) have an important role to play. Heavy-duty vehicle usage is growing, and electrification remains difficult, therefore there is a potentially large market for HSEMs in the form of electric assisted turbochargers (EATs).

The surface-mounted permanent magnet (SPM) rotor configuration is most suited to high-speed applications. However, as the magnets are sintered, they have low tensile strength and become a critical factor for rotor durability. Therefore, the stress analysis for SPM rotors must be accurate, however the existing literature is limited. Theoretical analysis on three-cylinder SPM rotors is unexplored for the plane strain and generalise plane strain (GPS) approaches, while it is vastly under-explored for the plane stress approach.

The aim of this project was to develop an efficient methodology of accurately predicting high-speed SPM rotor stresses to enable the selection of an optimal rotor design based on a variety of design parameters. To achieve this, an accurate closed form analysis for SPM rotor stresses was developed. The accuracy of the theoretical analysis was then verified via finite element analysis (FEA) and experimental testing. Once verified, the theoretical equations were used to develop an optimisation tool for the design of SPM rotors.

For three-cylinder rotors, the novel development of the GPS theory was shown to be the most accurate approach when compared to the FEA simulations. Utilising digital image correlation (DIC), test results were extracted from the rotor surface aligning with the FEA predictions and adding validity to the accuracy of the GPS theory. The results culminated in the development of an efficient multi-criteria optimisation tool based on the GPS theory that met the project aim.

Significant contributions to knowledge were made through the derivation of novel theoretical stress theory and the application of axisymmetric FEA rotor modelling, enabling important axial changes to be analysed. The verification testing methodologies provide a novel technique of extracting results directly from an SPM rotor, typically not attempted in the literature. The optimisation tool is a substantial contribution to existing knowledge through its implementation of novel theory and the ability to provide users with an efficient method of obtaining accurate, optimal SPM rotor designs.

Acknowledgements

First and foremost, I would like to thank my supervisor, Prof. Simon Barrans, for his continued support throughout this project. The expert guidance and support provided by him has been invaluable over the past four years and I will be forever grateful for his efforts.

I would also like to thank the director of the Turbo Research Group (TRG), Prof. John Allport, for his advice and allowing me to be a part of the fantastic team at the TRG. Many thanks must also go to the technical support team within the School of Computing & Engineering. I would like to specifically thank Ben Lear and Luke Barron for their input and support during this project.

Finally, I would like to thank my partner, Rebecca Stead, for her continual support and encouragement throughout this journey. Without her, the past four years would have been even more difficult.

Statement of Publications Arising from this Thesis

- S. Barrans and L. Mallin, *Mechanical Design of Rotors with Surface Mounted Permanent Magnets* .IntechOpen, 2018.

  Contribution of the author: While my co-author was the main author of this research, I devleoped the MatLab code to produce the results for this publication. Sections of this book chapter are repeated in Chapter 3.

- L. Mallin and S. Barrans, "A review of the high-speed permanent magnet rotor stress analysis used for automotive air-handling machines," *European Journal of Engineering Research and Science*, vol. 5, no. 4, pp. 448–456, 2020.

  Contribution of the author: I conducted the research and wrote the entire manuscript for this paper, while my co-author had an editorial role. Sections of this paper are repeated in Chapters 1 and 2.

- L. Mallin and S. Barrans, "Comparison of theoretical approaches to determine the stresses in surface mounted permanent magnet rotors for high speed electric machines," *The Journal of Strain Analysis for Engineering Design*, 2021.

  Contribution of the author: I conducted the research and wrote the entire manuscript for this paper, while my co-author had an editorial role. Sections of this paper are repeated in Chapters 4 and 5.

- L. Mallin, "Design of a rig to assess the structural performance of rotors for high speed electric machines," in *Advances in Manufacturing Engineering and Materials II: Proceedings of the International Conference on Manufacturing Engineering and Materials (ICMEM 2020), 21–25 June, 2021, Novy Smokovec, Slovakia.* Springer, 2021, pp. 301–323.

  Contribution of the author: I conducted the research and wrote the entire manuscript for this paper, while my supervisor had an editorial role. Sections of this paper are repeated in Chapter 6.

- L. Mallin and S. Barrans, "Development of an optimisation tool for the mechanical design of permanent magnet rotors in high-speed electric machines," in *2021 12th International Conference on Mechanical and Aerospace Engineering (ICMAE)*, 2021, pp. 208–214.

  Contribution of the author: I conducted the research and wrote the entire manuscript for this paper, while my co-author had an editorial role. Sections of this paper are repeated in Chapter 8.

Contents

List of Figures

List of Tables

List of Abbreviations

CMM	Coordinate-Measuring Machine
CO_2	Carbon Dioxide
DIC	Digital Image Correlation
EAT	Electric Assisted Turbocharger
EMF	Electromotive Force
EU	European Union
FEA	Finite Element Analysis
GPS	Generalised Plane Strain
HSEM	High-Speed Electric Machine
IPM	Interior Permanent Magnet
MCEA	Multi-Criteria Evolutionary Algorithm
MCO	Multi-Criteria Optimisation
NSGA-II	Non-dominated Superiority Genetic Algorithm-II
NRMM	Non-Road Mobile Machinery
PM	Permanent Magnet
SPM	Surface-Mounted Permanent Magnet
TOPSIS	Technique for Order of Preference by Similarity to Ideal Solution
VIKOR	Multi-Criteria Optimisation and Compromise Solution
WPM	Weighted Product Method
WSM	Weighted Sum Method
2D	2 Dimensional
3D	3 Dimensional

List of Symbols

c	Inner common radius notation	m
d	Outer common radius notation	m
dr	Thickness of a cylinder element	m
ds	Change in thickness of a cylinder element	m
$d\theta$	Segment angle of a cylinder element	rad
$\dot{m}_C$	Compressor mass flow rate	$\mathrm{kg\,s^{-1}}$
$\dot{m}_T$	Turbine mass flow rate	$\mathrm{kg\,s^{-1}}$
r	Variable radial dimension	m
s	Change in radius of a cylinder element	m
t	Cylinder thickness	m
x	Initial FEA mesh density	
y	Criteria notation for optimisation tool	
A	Constant of integration	
B	Constant of integration	
C	Constant of integration	
E	Young's Modulus	Pa
E_i	Young's Modulus for inner cylinder	Pa
E_m	Young's Modulus for middle cylinder	Pa
E_o	Young's Modulus for outer cylinder	Pa
F_z	Axial force	N
F_{zi}	Axial force on inner cylinder	N
F_{zm}	Axial force on middle cylinder	N
F_{zo}	Axial force on outer cylinder	N
P_{atm}	Atmospheric pressure	Pa
P_{Cin}	Compressor inlet pressure	Pa
P_{Cout}	Compressor outlet pressure	Pa
P_{Tin}	Turbine inlet pressure	Pa
P_{Tout}	Turbine outlet pressure	Pa
R	Cylinder radius	m
R_c	Common radius in two-cylinder analysis	m
R_{ci}	Original outer radius for inner cylinder in two-cylinder analysis	m
R_{co}	Original inner radius for outer cylinder in two-cylinder analysis	m
R_i	Inner radius of rotor in two-cylinder analysis	m
R_{ic}	Outer radius of inner cylinder	m
R_{ii}	Inner radius of inner cylinder	m
R_{mc}	Inner radius of middle cylinder	m
R_{md}	Outer radius of middle cylinder	m
R_o	Outer radius of rotor in two-cylinder analysis	m
R_{od}	Inner radius of outer cylinder	m
R_{oo}	Outer radius of outer cylinder	m
S	Interference shrinkage pressure	Pa
S_1	Interference shrinkage pressure at c	Pa
S_2	Interference shrinkage pressure at d	Pa
α	Coefficient of thermal expansion	
α_i	Coefficient of thermal expansion for inner cylinder	

α_m	Coefficient of thermal expansion for middle cylinder	
α_o	Coefficient of thermal expansion for outer cylinder	
δ	Radial interference between cylinders	m
δ_c	Radial interference at c	m
δ_d	Radial interference at d	m
ε_θ	Circumferential strain	
$\varepsilon_{\theta ic}$	Circumferential strain at outer surface of inner cylinder	
$\varepsilon_{\theta mc}$	Circumferential strain at inner surface of middle cylinder	
$\varepsilon_{\theta md}$	Circumferential strain at outer surface of middle cylinder	
$\varepsilon_{\theta oc}$	Circumferential strain at inner surface of outer cylinder in two-cylinder analysis	
$\varepsilon_{\theta od}$	Circumferential strain at inner surface of outer cylinder	
ε_r	Radial strain	
ε_z	Axial strain	
ε_{zi}	Axial strain of inner cylinder	
ε_{zm}	Axial strain of middle cylinder	
ε_{zo}	Axial strain of outer cylinder	
ν	Poisson's ratio	
ν_i	Poisson's ratio for inner cylinder	
ν_m	Poisson's ratio for middle cylinder	
ν_o	Poisson's ratio for outer cylinder	
$\nu\varepsilon$	Microstrain	
π	Pi	
ρ	Density	$\mathrm{kgm^{-3}}$
ρ_i	Density of inner cylinder	$\mathrm{kgm^{-3}}$
ρ_m	Density of middle cylinder	$\mathrm{kgm^{-3}}$
ρ_o	Density of outer cylinder	$\mathrm{kgm^{-3}}$
σ_θ	Circumferential stress	Pa
$\sigma_{\theta i}$	Circumferential stress in the inner cylinder	Pa
$\sigma_{\theta ic}$	Circumferential stress at outer surface of inner cylinder	Pa
$\sigma_{\theta ii}$	Circumferential stress at inner surface of inner cylinder	Pa
$\sigma_{\theta m}$	Circumferential stress in middle cylinder	Pa
$\sigma_{\theta mc}$	Circumferential stress at inner surface of middle cylinder	Pa
$\sigma_{\theta md}$	Circumferential stress at outer surface of middle cylinder	Pa
$\sigma_{\theta od}$	Circumferential stress at inner surface of outer cylinder	Pa
$\sigma_{\theta oo}$	Circumferential stress at outer surface of outer cylinder	Pa
σ_r	Radial stress	Pa
σ_{ri}	Radial stress at inner radius of rotor in two-cylinder analysis	Pa
σ_{ric}	Radial stress at outer surface of inner cylinder	Pa
σ_{rii}	Radial stress at inner surface of inner cylinder	Pa
σ_{rm}	Radial stress in middle cylinder	Pa
σ_{rmc}	Radial stress at inner surface of middle cylinder	Pa
σ_{rmd}	Radial stress at outer surface of middle cylinder	Pa
σ_{ro}	Radial stress at outer surface of rotor in two-cylinder analysis	Pa
σ_{roc}	Radial stress at inner surface of outer cylinder in two-cylinder analysis	Pa
σ_{rod}	Radial stress at inner surface of outer cylinder	Pa
σ_{roo}	Radial stress at outer surface of outer cylinder	Pa
σ_{VM}	Von Mises stress	Pa
σ_{VMi}	Von Mises stress in the inner cylinder	Pa
σ_{VMic}	Von Mises stress at outer surface of inner cylinder	Pa

σ_{VMii}	Von Mises stress at inner surface of inner cylinder	Pa
σ_{VMm}	Von Mises stress in middle cylinder	Pa
σ_{VMmc}	Von Mises stress at inner surface of middle cylinder	Pa
σ_{VMmd}	Von Mises stress at outer surface of middle cylinder	Pa
σ_{VMo}	Von Mises stressin in outer cylinder	Pa
σ_{VMoc}	Von Mises stress at inner surface of outer cylinder n two-cylinder analysis	Pa
σ_z	Axial stress	Pa
σ_{zi}	Axial stress in the inner cylinder	Pa
σ_{zic}	Axial stress at outer surface of inner cylinder	Pa
σ_{zii}	Axial stress at inner surface of inner cylinder	Pa
σ_{zmc}	Axial stress at inner surface of middle cylinder	Pa
σ_{zoc}	Axial stress at inner surface of outer cylinder in two-cylinder analysis	Pa
ω	Rotational velocity	$\mathrm{rad\,s}^{-1}$
Δ_T	Change in temperature	^{o}C

1 Introduction

1.1 High-Speed Electric Machines

1.1.1 Applications of High-Speed Electric Machines

As discussed by Tenconi et al. [1], high-speed electric machine (HSEM) usage has increased over the last decade due to the performance benefits over mechanical transmission. Benefits provided by HSEMs include: efficiency, as stated by Tenconi et al., Rahman et al., and Fang et al. [1–3]; reliability, power density, weight and size, as mentioned by Li and Sarlioglu and Kolondzovski et al. [4, 5]. HSEMs can utilise alternately poled, circumferentially arranged permanent magnets (PMs) attached to or within a rotor. A stator surrounding the rotor is excited via phase current to produce a rotating magnetic field which interacts with the PMs to produce the driving force [6]. The induced rotation matches the speed of the rotating magnetic field, known as synchronous rotors, which Keller et al. [7] identified as the most efficient and power dense type of rotor. Gerada et al. [8, 9] describes that HSEMs rotating via electromagnetic forces, improves reliability over parts in contact, while PMs provide an increase in power density. As Barrans et al. [10] states, sintered PMs such as Samarium Cobalt (SmCo, $SmCo_5$ or Sm_2Co_{17}) or Neodymium ($Nd_2Fe_{14}B$) are used. These high-energy density magnets enable a rotor size reduction for the same output, whilst also increasing operating speed according to Burnand et al. [11].

Burnand et al. [11] lists compressors, vacuum pumps, turbine generators and machining spindles as HSEM applications while Gerada et al. [9] includes fuel pumps and turbochargers, all of which operate above 10,000 rpm. Gerada et al. and Zwyssig et al. [9, 12] states the benefit of HSEM's in spindles is to enable ultra-precision machining through smaller diameter spindles and higher operating speeds. One such tool was developed by Westwind Air Bearings; a printed circuit board spindle capable of achieving speeds of 300 krpm. Tsao et al. [13] discussed how integrating a HSEM and a flywheel brings multiple advantages compared to composite rotors;

especially for applications that require short, high-powered discharges such as hybrid vehicle load-levelling devices. By combining the flywheel and electromagnetic rotor as the same rotor, the HSEM housing can be used as part of the flywheel vacuum and containment, reducing the weight and volume of the of the system. Figure 1.1 shows the integrated designed compared to two other flywheel designs using electromagnetic rotors as well as an energy storage rotor. Tsao et al. [13] states that the integrated design improves energy storage density and reduces mechanical complexity compared to composite rotors.
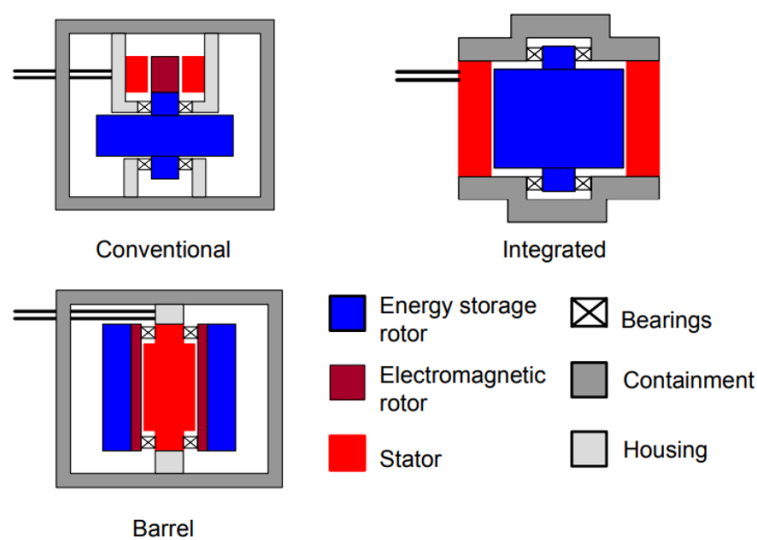
FIGURE 1.1: Integrated flywheel and electromagnetic rotor design versus existing designs [14]

A particularly demanding but potentially large market for HSEM's is within automotive air-handling machines, such as electrically assisted turbochargers (EATs). Turbochargers extract waste energy from exhaust gases via a turbine connected to a compressor wheel. The compressor wheel draws in air and delivers it to the engine above ambient density for complete fuel combustion, maximising power and enabling engines to be *down-sized*, as discussed by Lee et al. [15]. However, Lee et al. [15] stated slow transient response at low engine speeds caused by insufficient exhaust gas is a drawback to the turbocharger system.

EATs, shown in Figure 1.2, utilise a PM motor to achieve optimum operating speed at low engine speeds, improving slow transient response. As stated by Terdich and Martinez-Botas [16], EATs therefore improve engine power density more than

mechanical turbochargers. The speed and size requirements of EATs for light-duty vehicles makes application difficult, as discussed by Barrans et al. [10]; operating speed requirements are 100-300 krpm whilst dimensions must be minimised to fit within the limited engine space.
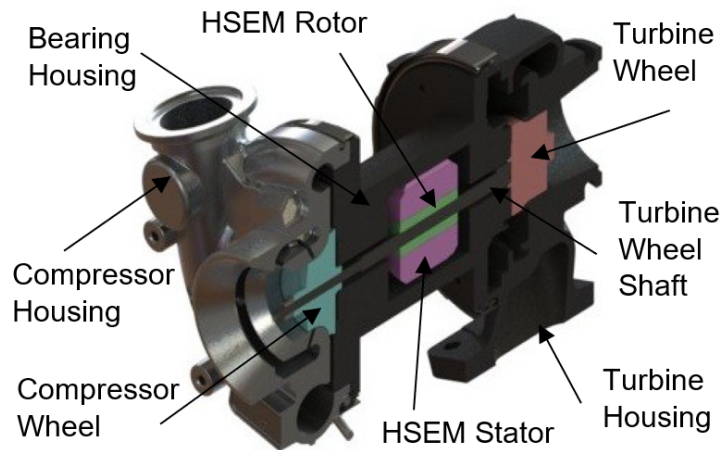
FIGURE 1.2: Section of an electric assisted turbocharger, adapted from
Terdich and Martinez-Botas [16]

Continental [17] showed in Figure 1.3 that road transport was responsible for 82% of all transport energy consumption and 27% of the total energy consumption in 2016. Therefore, reducing the energy consumption in vehicles, through machines such as EATs, could have a significant impact on reducing the total energy used and therefore, the emissions.

Continental [17] states that the European Union (EU) voted to impose a reduction
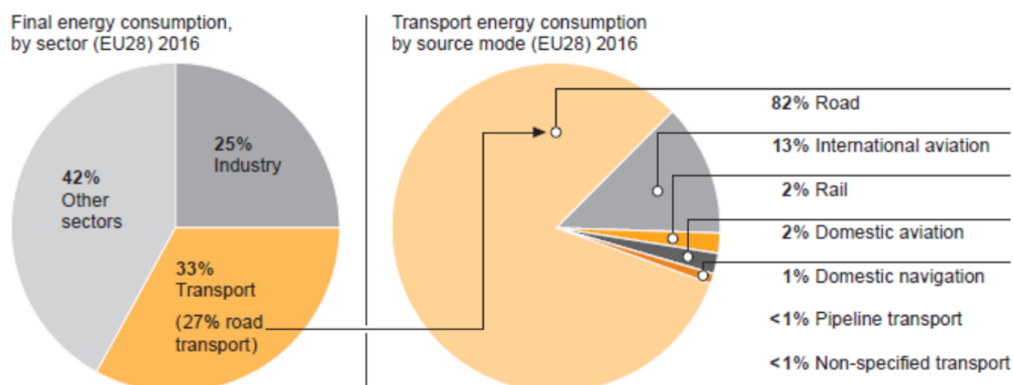
FIGURE 1.3: Road transport sector energy consumption in 2016 [17]

in the CO_2 emission targets of 37.5% for passenger cars and 31% for light commercial vehicles, from 2021 to 2030. Arsie et al. [18] adds that light-duty vehicle emission targets are set at a 70% reduction by 2050. However, as discussed by Gis and Merkisz [19], the number of electric passenger vehicles has grown rapidly over the past decade and is predicted to continue increasing, reducing the requirement for EATs on light-duty vehicles.

For heavy-duty vehicles, the European Union [20] states that heavy-duty vehicles are responsible for around a quarter of all transport emissions in the EU. Targets have been set to reduce emissions 15% from 2025 and 30% from 2030. Çabukoglu et al. [21] acknowledges that electrification is difficult and will remain niche unless the necessary infrastructure is built. Çabukoglu et al. [21] also states that the use of heavy-duty vehicles is expected to grow roughly twice as fast as passenger vehicle usage, until 2040. Therefore, for the foreseeable future, heavy-duty road vehicles will still use diesel engines and will provide an increasingly significant market that can utilise EATs to meet emission targets.

There is also a market for EATs on non-road mobile machinery (NRMM). During a real-world test of a tractor presented by Merkisz et al. [22] and shown in Figure 1.4, constant engine speed changes were identified. The UK government [23] published guidelines requiring NRMM with a net power between 37 kW and 560 kW to meet specific nitrogen oxides (NOx) emission targets within London. These targets are
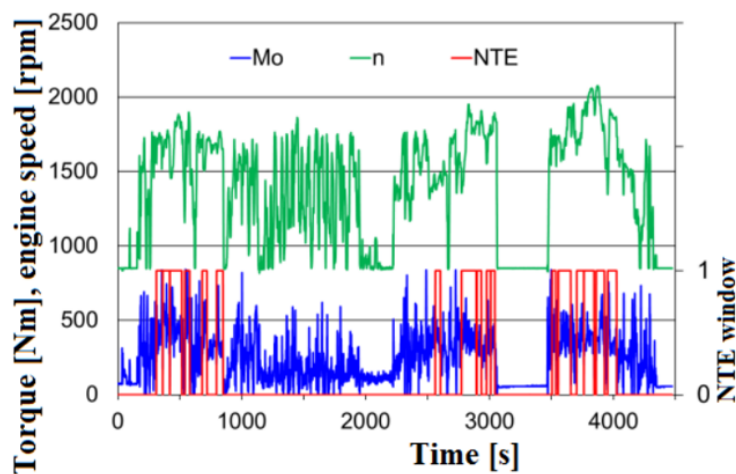
FIGURE 1.4: Tractor engine speed (n) changes frequently in real-world test [22]

set to be reduced further in 2020 for all NRMM within that net power range. EATs would be regularly used to improve the transient response during the change in engine speed, making them a useful machine for this application to utilise to meet restricting emission regulations.

1.1.2 Structure of High-Speed Electric Machines

As stated earlier, EATs utilise a PM rotor to assist rotation and improve engine transient response. Barrans et al. [10] defines *interior* (IPM) and *surface-mounted* (SPM) as the two configurations of PM rotors, shown in Figure 1.5. IPM rotors have PMs buried within the shaft or rotor iron while SPM rotors have PMs attached to the surface, compressed via a retaining sleeve. SPM topologies exist where no distinction between the shaft and rotor iron is made, therefore just a shaft is present as shown by Borisavljevic et al. [24]. Binder et al., Gieras, and Smith et al. [25–27] acknowledge that the stress concentrations generated within IPM rotors due to the magnet slots, limit operating speeds. SPM rotors do not contain these stress concentrating features. Therefore Binder et al. and Smith et al. [25, 27] recommended SPM rotors for high speed applications despite losses in efficiency due to the retaining sleeve acting as an electromagnetic air gap [10].

(A) IPM rotor [25].　　　　　　　　(B) SPM rotor, adapted from [25].
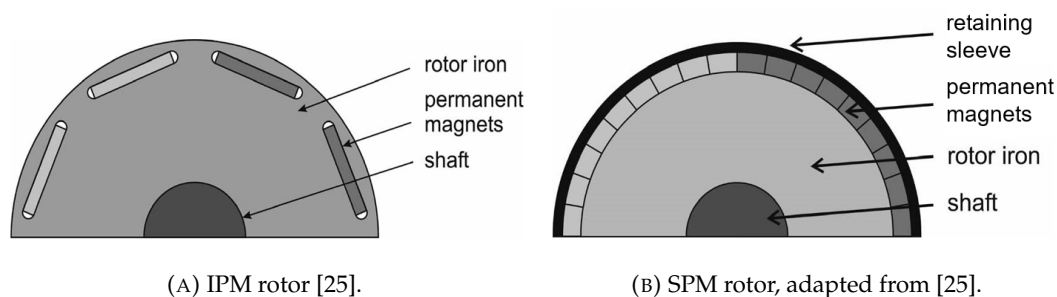
FIGURE 1.5: PM rotor configurations.

Barrans et al. and Smith et al. [10, 27] state that due to the sintering manufacturing process used in the manufacture of Samarium Cobalt and Neodymium magnets, they have low tensile strength. The retaining sleeve keeps the magnets in compression to counter the tensile stresses generated during operation and enable a high-speed to be achieved. This is a critical factor for rotor durability, so the stress analysis must be accurate.

1.2   Project Aims

As discussed in Section 1.1, HSEM popularity is expected to continue increasing due to the performance benefits over mechanical transmission; with the SPM rotor configuration being most suited to high-speed applications. Accurate stress analysis of high-speed rotors was identified as critical due to the fragile nature of the permanent magnets and must be investigated. Therefore, the project aim is:

- Develop an efficient methodology of accurately predicting high-speed rotor stresses to enable the selection of an optimal rotor design based on a variety of design parameters.

To achieve this aim, the following methodology will be required:

- Develop accurate closed form analysis equations for efficient SPM rotor stress calculations.
- Verify the theoretical analysis accuracy via finite element analysis (FEA) simulations.
- Confirm the FEA and theoretical equations accuracy through experimental testing.
- Use the verified theoretical equations to produce an optimisation tool for SPM rotor design.

1.3   Project Objectives

Based on the project methodology from Section 1.2, the project objectives are:

- Develop theoretical stress calculations for three-cylinder rotors for the generalised plane strain (GPS), plane stress and plane strain approaches.
- Investigate the differences between the GPS, plane stress and plane strain results over a range of different rotor topologies.
- Produce axisymmetric FEA studies and use them to verify the accuracy of the theoretical models.

- Design a test rig for a three-cylinder rotor by adapting an existing air handling machine to power the rotor that can utilise digital image correlation (DIC) to obtain the results.

- Design a three-cylinder test rotor that can be assembled via shrink fitting and is compatible with the test rig. Reduce the complexity with alternative materials to weak sintered magnets.

- Conduct a series of experimental tests at stationary and a variety of operating speeds. Obtain the results using the DIC and strobe light system and use them to verify the accuracy of the FEA, and therefore the theoretical calculations.

- Develop a multi-criteria optimisation tool in MatLab, using Non-dominated Superiority Genetic Algorithm-II (NSGA-II), that enables users to identify optimal rotor designs based on their individual criteria and constraints.

- Verify the optimisation tool by comparing an optimal result from the Pareto front against an axisymmetric FEA study.

1.4   Structure of Thesis

As discussed in Section 1.1, this chapter identified the applications of high-speed electric machines (HSEMs) and the future requirements of these machines. The different types of permanent magnet (PM) rotor structures used within HSEMs were explored and the importance of analysing stresses within surface-mounted PM (SPM) rotors was identified. A project aim was then defined, with the methodology and objectives outlined.

Chapter 2 consists of a comprehensive literature review that explores the existing work surrounding the key aspects of the project methodology. For rotor stress analysis, the current theoretical approaches and finite element analysis (FEA) methods were explored along with experimental testing practices and optimisation techniques. After identifying the current state of the literature, a series of key findings were outlined.

In Chapter 3, the fundamentals of rotor stress theory are detailed and used to show how existing equations for plane stress, plane strain and generalised plane

strain (GPS) theory for two-cylinder rotors, were derived. The different methodologies are then compared against each other to explore potential differences, highlighting the need for further development for three-cylinder rotors.

Chapter 4 shows the derivation process of the plane stress, plane strain, and GPS theoretical stress analysis equations for three-cylinder SPM rotors. The developed theory is then compared against the corresponding two-cylinder theory to prove they were successfully derived.

Chapter 5 aims to verify the accuracy of the developed theory equations from Chapter 4. The axisymmetric behaviour of the SPM rotor is explored, while the key assumptions made in the plane stress, plane strain, and GPS theories are analysed. Across a range of operating conditions and varying rotor length the theoretical stress models are compared against FEA models, assessing their accuracy, where GPS is identified as the most accurate approach.

In Chapter 6, the design process of a test rig and rotor is shown based on the experimental instrumentation and components. Design constraints are outlined, and the designs are iterated until they operate within the constraints. The test rig and rotor are designed to validate FEA models and the GPS theoretical stress equations from Chapters 5 and 4, respectively.

Chapter 7 explains the experimental procedure for tests used to either validate the test rig design concept or extract results directly from the test rotor. The test rig was demonstrated to run at speed while digital image correlation (DIC) was used to extract rotor surface strains. The results were analysed to determine the accuracy of the GPS theory and the success of the test rig design.

Chapter 8 details the development of an efficient optimisation tool that enables the selection of an optimal rotor design. The GPS theoretical equations are input into an optimisation framework alongside criteria, design variables, and constraints. The results for a rotor optimisation problem are demonstrated to be successful when optimal rotor GPS results are compared to FEA simulations. The tool enables a range of potential rotor designs to be identified within a variety of design parameters, achieving the project brief from Chapter 1.

2 Literature Review

2.1 Introduction

Based on the project objectives identified in Section 1.3, existing literature relating to closed-form and numerical analysis methods, optimisation, rotor assembly, experimental testing, and digital image correlation (DIC) will be explored. Some of the work from this chapter, presented in Sections 2.2, 2.3, and 2.4, has previously been published by Mallin and Barrans [28]. However, much more detail has been added to these sections while other avenues of of research have been introduced to expand upon this work.

2.2 Closed Form Analysis Methods

2.2.1 Background

As stated by Wolfram [29], "An equation is said to be a closed-form solution if it solves a given problem in terms of functions and mathematical operations from a given generally-accepted set." As shown by existing papers, the goal of rotor stress analysis is to identify a set of equations that can accurately predict rotor stresses. To apply closed-form analysis techniques to surface-mounted permanent magnet (SPM) rotor design, approximations are required regarding rotor behaviour. Existing papers differ amongst three main areas of approximation: state of the stress-strain field; impact of thermal effects; and the use of compound cylinder theory. For the stress-strain field, one of three assumptions will be used: plane stress; plane strain; or generalised plane strain. To apply these analysis methods, certain conditions are required:

- The body must be bound by two parallel planes. For example, these would be the two ends of a cylinder.

- Hoop and radial stresses and strains must be uniform throughout the plane body thickness, or over the length in the case of a rotor.

Hearn [30] states a plane body is when two parallel planes are bounded by a closed surface. This applies to cylindrical rotors where the end faces are the parallel planes. Hearn [30] explains that, in relation to the diameter, a very short cylinder (i.e. a disk) is suitable for plane stress analysis whereas a long cylinder is suitable for plane strain.

It is important to note that although Hearn [30] cites rotating cylinders as an example of plane strain, the equations derived from Hearn [31] assume generalized plane strain. This does not require either axial stress or axial strain to be known to determine the radial and circumferential stresses. So, whilst the theory presented is applicable to a state of plane strain (i.e. where there is no change in axial dimension), it is not restricted to that case.

The relationship between stress and strain in the rotor is given by the general constitutive relationship expressed in cylindrical coordinates as:

$$
\begin{bmatrix} \varepsilon_r \\ \varepsilon_\theta \\ \varepsilon_z \end{bmatrix} = \begin{bmatrix} \frac{1}{E} & -\frac{\nu}{E} & -\frac{\nu}{E} \\ -\frac{\nu}{E} & \frac{1}{E} & -\frac{\nu}{E} \\ -\frac{\nu}{E} & -\frac{\nu}{E} & \frac{1}{E} \end{bmatrix} \begin{bmatrix} \sigma_r \\ \sigma_\theta \\ \sigma_z \end{bmatrix}
\tag{2.1}
$$

Where ε_r, ε_θ and ε_z are the strains in the radial, circumferential and axial directions; σ_r, σ_θ and σ_z are the equivalent stress components. E is the Young's modulus of the material and ν is the Poisson's ratio.

There can be no stress where there is no material, therefore a plane of vanishing thickness can be assumed to have no axial stress and be under plane stress condition, as discussed by Kotousov and Wang [32]. Axial strain is still present under this assumption, i.e.:

$$
\sigma_z = 0 \tag{2.2}
$$

$$
\varepsilon_z \neq 0 \tag{2.3}
$$

As argued by Kotousov and Wang [32], if a long cylinder is assumed to be infinite, then there can be no axial change in length and axial strain can be assumed

zero for plane strain analysis. Axial stress is acknowledged in this assumption, represented by Burnand et al. [11] as:

$$\sigma_z \neq 0 \tag{2.4}$$

$$\varepsilon_z = 0 \tag{2.5}$$

However, rotors are not of infinite length and would require to be held rigidly for the plane strain theory to be accurate. This is unrealistic as no structure has a sufficiently greater stiffness than the rotor to be regarded as rigid.

Barrans [10] states that axial stress is present in the rotor, which does not align with the plane stress theory. Generalised plane strain (GPS) assumes axial stress is present and axial strain is constant in the rotor cylinders, which is true for most of the rotor body apart from at the rotor ends. At the rotor end the strain switches from being in GPS to three-dimensional (3D) strain, while the stress switches from 3D stress to a state of plane stress [10]. This due to axial load transfer between the rotor cylinders as they try to strain at different rates. GPS is therefore a more suitable approach than plane stress or plane strain for most of the rotor and can be presented as:

$$\sigma_z \neq 0 \tag{2.6}$$

$$\varepsilon_z \neq 0 \tag{2.7}$$

$$\frac{d\varepsilon_z}{dr} = 0 \tag{2.8}$$

2.2.2 Plane Stress Based Methods

In previous work, the plane stress assumption was the most common approach, used by many authors [24, 33–49]. However, it was only justified by Fang et al., Zhu and Chen, and Cheng et al. [33, 36, 38], which causes uncertainty in the exploration of the other analysis methods by the other sources. Fang et al. [33] explored both the plane stress and plane strain methods before choosing plane stress due to simplicity; generalised plane strain was not investigated. Cheng et al. [38] justified using plane stress due to a very small axial load, while Zhu and Chen [36] stated no axial load was present. Although overall axial stress will be zero, Barrans [10] observed that due to differential axial deformation during rotation, axial loads will be present on

each cylinder, acting in opposite directions to maintain equilibrium. This presence of axial stress may lead to unreliable results when plane stress is assumed.

Multiple authors [35, 37, 43, 44, 46, 50] all acknowledged the use of plane stress theory, but did not justify why it was used over another analysis method. Papini et al. [50] stated the use of plane stress, but upon investigation used the plane strain equations instead; casting considerable doubt on the application of the chosen method. Gilson et al. [44] referenced Pfister and Perriard [43] for the use of plane stress analysis while Chen and Zhu, and Xu et al. [35, 37, 46] all stated the use of plane stress but gave no justification for its application. However, Pfister and Perriard, and Xu et al. [43, 46] both based their calculations on rotors with longer lengths than diameters and can therefore not be considered short rotors which would be acceptable to plane stress analysis. Chen and Zhu [35, 37] do not mention axial length in their rotor design parameters and therefore use a suitable theory if applied to a short rotor.

The remaining papers [34, 39–43, 45, 47–49] to use plane stress did not specify they had done so, raising questions of awareness of other theoretical approaches. To show how the calculations were conducted, Pfister and Perriard [43] and Gerada et al. [49] referenced themselves [41] and Wang et al. [39] respectively. However, Wang et al, and Pfister and Perriard [39, 41, 43] based their calculations on a rotor with a length multiple times greater than the diameter which is unsuitable for the plane stress assumption, while Gerada et al. [49] specified no axial length. This may be indicative of being unaware of the axial length importance for the analysis method used.

Only Fang et al. [3] referenced a paper [33] which justified the use of plane stress. Fang et al. [3] discussed a segmented magnet rotor design and therefore referenced Binder et al., and Yon et al. [25, 51]. However, Binder et al., and Yon et al. [25, 51] did not specify the assumptions underpinning their theoretical approach and will be discussed later. Overall, there is a clear lack of explicitness in the reasoning behind the use of the plane stress assumption. Many references do not acknowledge the assumption, while others apply it to incompatible rotor designs. This suggests a lack of knowledge or understanding of the various theoretical approaches available. Only a small minority of papers justify the use of plane stress effectively [33, 38].

2.2.3 Plane Strain Based Methods

Burnand et al., Papini et al., and Zhou and Fang [11, 50, 52] were the only papers reviewed to use plane strain methodology to calculate interfering cylinder stresses. This method assumes there is no axial strain acting on the cylinders. The rotor topology used by Zhou and Fang [52] was the shaft, magnets and sleeve arranged as three concentric cylinders. It is stated by Zhou and Fang [52] that the equations are based on the thick-walled cylinder theory, using the plane strain assumption. The analytical equations only related to the interfering magnets and sleeve. As discussed later, analytical calculations of three interfering cylinders was rarely attempted. The rotor used by Zhou and Fang [52] does appear to be a long rotor and therefore the plane strain approach is suited to the rotor, however this justification is not stated. Burnand et al. [11] focussed on a three-cylinder rotor and stated the use of plane strain equations for the stresses of all three cylinders. However, Burnand et al. [11] assumed no interference between the shafts and magnets, leaving an approach that only considers interference between two cylinders. There is also no justification for plane strain by Burnand et al. [11], but the rotor length was ignored so it could be suitable if the rotor was classed as a long rotor. The plane stress assumption was stated by Papini et al. [50], but the stress equations related to the plane strain theory. Papini et al. [50] also failed to acknowledge any interfering surfaces between the cylinders. This potentially highlights a lack of knowledge about the different theoretical approaches, while results may differ from rotors with interference.

The exploration of the plane strain theory has been very limited and has not been applied to a compound cylinder of three-cylinder components. Like the papers using plane stress, there is a lack of justification for using plane strain, however there is awareness of the method being used. Only Papini et al. [50] creates significant uncertainty regarding the knowledge of potential theoretical approaches.

2.2.4 Generalised Plane Strain Method

Barrans et al. [10] was the only paper to explore generalised plane strain explicitly. The method was only applied to a two-cylinder rotor, but limitations of the GPS theory and other methods were all explored. This showed a good knowledge of the

available approaches for rotor stress analysis. GPS theory acknowledges axial stress in the rotor components and assumes axial strain is constant through the body. According to Barrans et al. [10], axial stresses become more concentrated at the rotor ends when friction between the bodies increases. Smith et al. [27] corroborated this by observing that shear stresses induced at the rotor ends caused magnet failure. The only other paper to use GPS was Riemer et al. [53], which sourced equations from Czichos [54] to compare Von Mises stress across rotor configurations. However, they excluded stresses due to interference and therefore did not investigate compound cylinders. The use of generalised plane strain was also not justified or even mentioned by Riemer et al. [53], which may point to a naivety regarding the theoretical approach options.

GPS was explored even less than plane strain and therefore requires much further investigation. Only one paper showed a knowledge of GPS theory, however it was applied to two-cylinder rotors leaving three-cylinder rotors unexplored. There is evidence that this theory is the most realistic of the three different approaches, but further investigation is required to quantify the differences.

2.2.5 Other Analysis Methods

Many sources [12, 25, 51, 55–64] were not categorised, either because the theoretical assumptions were not clear or because they did not use one of the three main methods above. The complex approach using both thin cylinder and thick walled cylinder equations proposed by Binder et al. [25] requires careful study to ensure that all the embedded assumptions remain valid. A thin cylinder approximation assumes the cylinder is thin (relative to its diameter) and has constant axial and circumferential stresses through the wall thickness, while neglecting radial stress. Thick cylinder equations correctly acknowledge stress variation through the wall thickness.

Zwyssig and Kolar [64] stated the thin cylinder equation for their analytical methodology but showed no further equations. Also, the rotor dimensions used by Zwyssig and Kolar [64] do not appear to be suitable to the thin cylinder theory due to the sleeve thickness. Zwyssig et al. and Luomi et al. [12, 62, 63] all referenced Zwyssig and Kolar [64] for analytical calculations and are therefore subject

to the limitations of thin cylinder theory. However, all appear to use a similar rotor geometry as Zwyssig and Kolar [64] and are likely to be unsuitable for the thin cylinder approximation. None of these papers [12, 62–64] acknowledge the use of thin cylinder approximation, making it unclear whether the authors were aware of the limitations behind their approach.

When calculating sleeve circumferential stress due to the shrink fit assembly, Binder et al. [25] assumed the sleeve to be a thin cylinder. The thin cylinder assumption remained when the contact pressure (due to shrink fit) between the magnets and sleeve was calculated. This contact pressure was also assumed to be acting at the back-iron to magnet interface. This approximation is reasonable for situations where the thickness of the magnets is small compared to their radius and many, small, separated magnets are distributed around the back-iron. For thicker sleeves, Binder et al. [25] calculated the contact pressure using a thick cylinder equation, but this equation used the circumferential stress previously calculated with the thin walled cylinder assumption. Binder et al. [25] used thin magnets and a thin sleeve and hence their approximations were reasonable. However, this approach would lead to potentially significant errors for: cylindrical or thick magnets; or thick sleeves.

For circumferential stress due to rotation, Binder et al. [25] used a thick walled cylinder approach with what appears to be the plain strain assumption. Whilst a Poisson's ratio was not specified in the equations, it can be calculated that a value of 0.231 was consistently assumed. Work using this equation for materials with a different Poisson's ratio will therefore be in error. Also, Binder et al. [25] discussed glass fibre and carbon fibre retaining sleeves which would cause errors with this equation as they require different Poisson's ratios.

Binder et al. [25] presented equations calculating centripetal force, each on the magnets and the sleeve, at a given radius. The equations will give reasonable approximations if the magnets are considered thin independent blocks and if the sleeve is considered thin. Calculations using these equations will generate errors if these conditions are not met. Many authors [3, 55–57, 60, 61, 65, 66] all referenced Binder et al. [25] to calculate stress.

Varaticeanu et al. and Thomas et al. [55, 60] referenced stress equations directly from Binder et al. [25], but Varaticeanu et al. [55] used a titanium sleeve with 0.33

Poisson's ratio while Thomas et al. [60] used a material with a Poisson's ratio of 0.3. Tao et al. [56] also used the same analytical model as Binder et al. [25] but used glass-fibre and carbon-fibre as sleeve materials with a Poisson's ratio of 0.22 and 0.199 respectively. These sleeve materials used by Tao et al. [56] are composites but they failed to acknowledge Poisson's ratio being directional in anisotropic materials. Fernando and Gerada [61] used the thick cylinder contact pressure equation (requiring thin magnets) from Binder et al. [25] and also the thick walled cylinder equation to calculate circumferential stress. However, Fernando and Gerada [61] stated Inconel alloy 718SPF as the sleeve material, which has a Poisson's ratio of circa 0.3. Without adjusting the equation from Binder et al. [25], errors will be induced using Inconel. Fernando and Gerada [61] also stated that due to non-uniform stress distribution through the sleeve thickness, a de-rating factor was used to accommodate peak stress locations within the sleeve. This limited the maximum circumferential stress to reduce the risk of failure. Schubert and Sarlioglu [66] referenced centripetal force equations from Binder et al. [25], which are acceptable if the magnet is constructed using individual blocks and if the sleeve is relatively thin. Schubert and Sarlioglu [66] used segmented magnets, but not many small segments and only one of the two finite element analysis (FEA) models had a thin sleeve. Lastly, Zhu et al. [65] took circumferential stress and contact pressure equations (due to shrink fitting) from Binder et al. [25] but overlooked referencing. Therefore, Zhu et al. [65] used thin cylinder equations and assumed rigid magnets which is a significant simplification of rotor stress behaviour. Other papers [5, 58, 67, 68] all used the thin cylinder approximation within their calculations.

Yon et al. [51] dismissed standard equations and justified this with four points:

1. Their model includes a sleeve laminated axially, using glue to bind the layers.

2. Their magnet material is different to the shaft and sleeve.

3. Their magnets are axially segmented.

4. Their magnets are segmented circumferentially.

For point 1, a thin disk approximation could be used on each sleeve layer, with a correction for the interaction between the layers. For points 2 and 3, standard equations can account for different materials and magnets segmented axially can

be analysed using standard equations. Regarding point 4, the standard stress calculations are valid for circumferentially segmented magnets, providing they do not go into circumferential tension. This is the case for Yon et al. [51] as they require a high compressive stress to withstand operating centrifugal forces on the rotor. Ahn et al. [59] used a rotor with a solid shaft as the inner radius value is zero. Implementing this, their interference pressure equation and the radial and circumferential stress equations for the assembly at standstill match the equations used by many others (see for example Barrans et al. [10]), but the interference pressure equation is missing the magnet Young's modulus. An equation to calculate the total radial stress (a compressive stress) in the magnets is then created. However, focussing on circumferential stress would be more relevant due to the magnets being weak in tension. Huang and Fang [57] used a similar approach to Binder et al. [25], but made improvements. The constant Poisson's ratio was removed, but the equation remained unsuitable for orthotropic composite materials.

Most unclassified papers either specified or referenced a paper that specified the use of thin cylinder approximation for the stress equations. As shown, this was only suitable for, or implemented correctly by a minority of papers which indicates a lack of knowledge in the analysis of rotor stresses. Binder et al. [25] was a key paper that mostly used the thin cylinder approximation appropriately, but the equations were not universally applicable. Binder et al. [25] was referenced by many papers that did not identify that the equations were unsuitable for their rotor calculations. Outside of the papers linked to Binder et al. [25], many did not acknowledge reasons for using thin cylinder approximation and also incorrectly used it on a rotor design constructed of thick components. A clear gap in appropriate rotor stress analysis was identified that must be addressed.

2.2.6 Further Analysis Aspects

2.2.6.1 Thermal Effects

Automotive air-handling machines, such as electrically assisted turbochargers (EATs), are exposed to high temperature during operation. The heat is mainly from turbine exhaust gases but also includes heating through compression of the charge air. This

also applies to other compressor applications, e.g. vacuum cleaners. Therefore, thermal effects must be accounted for in stress analyses.

Many authors [3,5,10,11,24,25,33,35,36,39,45,47–49,52,56,57,60,61,64,68–71] all incorporated thermal effects in their analyses, either through analytical calculations or FEA. Of these, most authors [3,10,11,24,25,33,35,36,39,45,47–49,52,56,57,60,61] included thermal analysis in the analytical calculations, where multiple authors [3, 56,57,60,61] and Gerada et al. [49] all took the equations from Binder et al. [25] and Wang et al. [39] respectively.

Most authors [3, 10, 11, 24, 25, 33, 35, 36, 39, 45, 47–49, 52, 56, 57, 60, 61, 64, 68–71] all used uniform rotor temperatures when analysing rotor stresses at elevated temperature, but only Barrans et al., Borisavljevic et al., and Zhou and Fang [10, 24, 52] justified this decision. Borisavljevic et al. and Zhou and Fang [24,52] both stated that the temperature can be assumed to be constant throughout the rotor, while Barrans et al. [10] went further to acknowledge temperature change along the axis. However, this change is small and temperature is constant per axial section. Barrans et al. [10] discussed that rotor temperature is constant in the radial and circumferential directions due to poor heat transfer across the air gap between rotor and stator. The largest heat transfer will be along the rotor shaft, causing the axial temperature variation. Fang et al., Zhu and Chen, and Wang et al. [3,36,69] also stated that there will be poor heat dissipation from the rotor.

It is important to include thermal effects in the analysis of rotors where their structural integrity relies on interference between parts. Where these parts are made from different materials (e.g. the sleeve and the magnets), it is likely that those materials will have different coefficients of thermal expansion. Hence, even uniform changes in temperature within the rotor will alter the degree of interference between parts. Hence, structural integrity may be compromised due to temperature variations.

2.2.6.2 Stacked Cylinder Calculations

When calculating stresses in rotors, the boundary layers between cylindrical bodies normally experience the peak stresses. Therefore, it is important to predict these

values accurately. All papers bar Papini et al. [50] acknowledge this interaction between the layers. Papini et al. [50] focused on electromagnetic performance. Su et al. [72] notes that while these stresses have traditionally been calculated via the use of Lamé's equations for thick walled cylinders subjected to internal and external pressure, there may also be residual stresses generated during the manufacturing process of the rotor elements that are unaccounted for. However, none of the papers explored accounted for this within their calculations, or for resulting effects such as anisotropic surface structures [73].

It is important to note that while most of the papers investigated analyse the magnets as solid cylinders, segmented magnets are commonly used. These components contain manufacturing tolerances, but assembly tolerances are also present on the positioning of the mounted magnets. Kim et al. [74] and Khan et al. [75] both use a positional tolerance of 1°on a circa 30 mm radius. Therefore, segmented magnet arrays will contain gaps between the magnets.

As discussed by Barrans et al. [10], when cylinders are stacked via interference fits an *end-effect* occurs. Barrans et al. [10] states that at the free end of the rotor, the behaviour switches from being in GPS to plane stress. Lewis et al. [76] discusses an end-effect with regard to contact pressure at the interference fit location. Lewis et al. [76] shows that towards the rotor ends, increases in contact pressure are identified across a range of interference levels. This is stated as to be expected because solid mechanics theories associate a stress-raising factor to an edge. However again, none of these effects are incorporated in the stress analysis calculations conducted by any of the papers explored.

As discussed in Section 1.1.2, SPM rotors typically consist of three cylindrical bodies. Binder et al. and Smith et al. [25, 27] recommend SPM rotors for high-speed operation despite often being constructed with three or more interfering cylinders, which can affect electromagnetic performance. Therefore, exploration of theoretical stress calculations for rotors with three interfering cylinders is of great importance.

Multiple papers [11, 33, 36, 38, 50, 52] acknowledged the use of three-cylinder rotors and also conducted theoretical analysis, however their calculations were not conducted for three-cylinder rotors. Papers by Zhang et al., Zhu and Chen, and Cheng et al. [33, 36, 38] discuss three-cylinder rotors, but all simplify the analytical

model to calculate the stresses for two-cylinders and use plane stress analysis, while by Burnand et al., Papini et al., and Zhou and Fang [11, 50, 52] use the plane strain theory approach for their rotors. Burnand et al. [11] provides equations for all three cylinders, however it is assumed that there is no interference present between the shaft and the magnets, leaving a two-cylinder approach with one interference location. Zhou and Fang [52] also focus on three-cylinder rotors, but similarly the analysis equations only relate to two interfering cylinders. Papini et al. [50] makes no discussion of any interfering surfaces within their models. None of these papers discussing three-cylinder rotors ended up conducting calculations that considered more than one interfering location.

Of all the papers conducting stress analysis, few papers [37, 47, 48, 70, 77] incorporated more than two cylindrical bodies in the calculations. Of these, only Chen and Zhu, and Wan et al. [37, 47] completed the analysis with closed form calculations, while the rest used FEA. Being able to complete these calculations analytically is much more efficient than using FEA, particularly where stresses at the interfering surfaces are being found. Chen and Zhu, and Wan et al. [37, 47] incorporated three cylinders in their models but assumed a state of plane stress. As discussed earlier, the plane stress assumption may produce unreliable results due to ignoring the existence of axial stress.

2.3 Numerical Analysis Methods

2.3.1 Background

FEA is a well-established, computer-based stress analysis method. Models are analysed using an assembly of a finite number of elements to approximate the load-displacement (and hence stress) relationship within complex geometries. Boundary conditions applied to the model will typically include constraints as well as loads. Results accuracy cannot be guaranteed as operating conditions may be difficult or impossible to accurately replicate. For a given geometry and boundary conditions, the FEA stress approximation can be improved by increasing the number of elements. However, this increases the computational time significantly, making FEA potentially very time consuming.

FEA models of rotors can be categorised according to the number of dimensions considered and the extent of the geometry included, as follows:

- 2-Dimensional (2D)
    - Full radial cross section
    - Symmetrical radial cross section
- Axisymmetric
    - Full axial section
    - Part axial section
- 3-Dimensional (3D)
    - Full geometry
    - Symmetrical section

For rotors, 2D models use a cross section of the rotor perpendicular to the rotor axis, as shown in Figure 2.1.

Full face or symmetric sections can be used for the analysis using appropriate boundary conditions. 2D models process much quicker than 3D as simpler and fewer elements are used. However, disadvantages of 2D methods are the stress behaviour must be: assumed to be the same along rotor length; and assumed as either
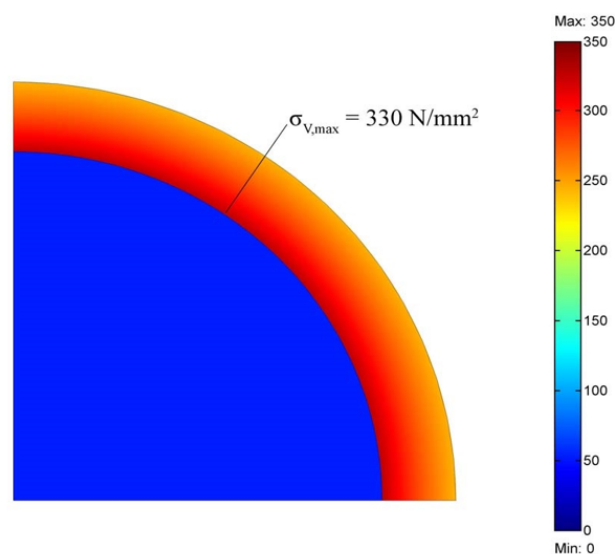
FIGURE 2.1: 2D rotor radial cross section FEA [64]

plane stress or generalised plane strain. This creates a source of results unreliability as it was established that stress changes along the axial direction [10].

2.3.2 2D Finite Element Analysis

Many authors [3, 24, 33, 35–37, 47, 60, 64–66] all used 2D FEA, however the decision to do so was not justified against the use of other FEA analysis techniques. There was also no declaration on whether the FEA analysis was conducted using the same assumptions as in their theoretical calculations i.e. plane stress, plane strain etc. This makes it difficult to understand if the FEA is representative of the theoretical conditions. It is also difficult to validate the FEA results via replication. Of the listed references above, multiple authors [3, 33, 36, 60, 64–66] used a 2D section as their FEA model, reducing unnecessary process time, but some authors [24, 35, 37, 47] just stated a 2D model was used and gave no additional details on the models in their papers. It is therefore difficult to validate the results and difficult to determine whether the model used was efficient. Most authors [24, 33, 35–37, 47, 60, 64, 66] achieved good alignment with their analytical calculations however, good agreement between analytical and FEA results does not guarantee accurate results. For example, if both the theory and the FEA make the plane stress assumption then results will agree but will also contain inaccuracies due to the plane stress theory. There is a lack of detail regarding the set-up of the FEA models and there is also a lack of justification for the models used in these papers.

There was also difficulty in confirming the FEA details reported by many authors [25, 48, 55–57, 60, 61, 65, 66, 68, 70, 71, 78]. Some authors [25, 48, 55–57, 60, 66] obtained good agreement with analytical results but as discussed earlier, this does not necessarily equate to result accuracy; while others [68, 70, 71, 78] relied on FEA alone to collect stress results, without verification. Tao et al. [56] stated that their FEA verified the analytical equations, with an error of 0.21% for the stresses due to interference and temperature. It appears that Huang and Fang [57] conducted separate analyses for the magnets and sleeve, while using a hand calculated contact pressure value as a boundary condition. Other boundary conditions or mesh size were not stated, with the FEA appearing to be processed without boundary constraints. Thomas et al. [60] doesn't indicate the conditions used in the 2D FEA setup,

but they compared the results with the analytical results; obtained via the use of equations by Binder et al. [25]. This comparison showed a potential error of circa 5%. However, Binder et al. [25] contained both thick shell and thin shell equations, but Thomas et al. [60] did not specify which equations were used. Therefore, it is unclear what assumptions were used to generate the results. No boundary conditions, mesh densities or convergence studies are provided by Fernando and Gerada, Zhu et al., and Schubert and Sarlioglu [61, 65, 66]. Also, Fernando and Gerada [61] showed a substantial difference between the analytical and FEA results. Schubert and Sarlioglu [66] highlighted that the thinnest sleeve results agreed most with analytical results due to using the thin cylinder assumption. Using the thick cylinder approach would be required to gain accuracy with thicker sleeves. Both Benlamine et al. [68] and Bianchi et al. [78] omit statements regarding dimensionality or boundary conditions.

No mention or justification of the FEA model being 2D or 3D was given by many authors. Without the FEA details it is extremely difficult to validate any results produced by the papers. The papers above also neglected to state if any assumptions from the analytical calculations had been used, showing that very little information was given regarding the FEA models.

2.3.3 Axisymmetric Finite Element Analysis

A 2D axisymmetric model, as shown in Figure 2.2, uses a cross section of the rotor length wall thickness. When revolved around the central axis, the full cylindrical model is complete. A benefit of this method is that stress changes along the rotor length are simulated. However, a limitation is the assumption that stress does not change in the circumferential direction. As stated by Barrans et al. [10], this condition is true for cylindrical or closely packed magnets whilst the sleeve maintains a compressive stress. Section 5.2.2 also presents a FEA simulation which corroborates Barrans et al. [10] as closely packed segmented magnets act as a solid cylinder which fails instantaneously as the magnets are put into tension. Therefore, the rotor will only operate in the state where the assumption is true. The condition is not appropriate where there are gaps between the magnets as shown by Binder et al. [25].
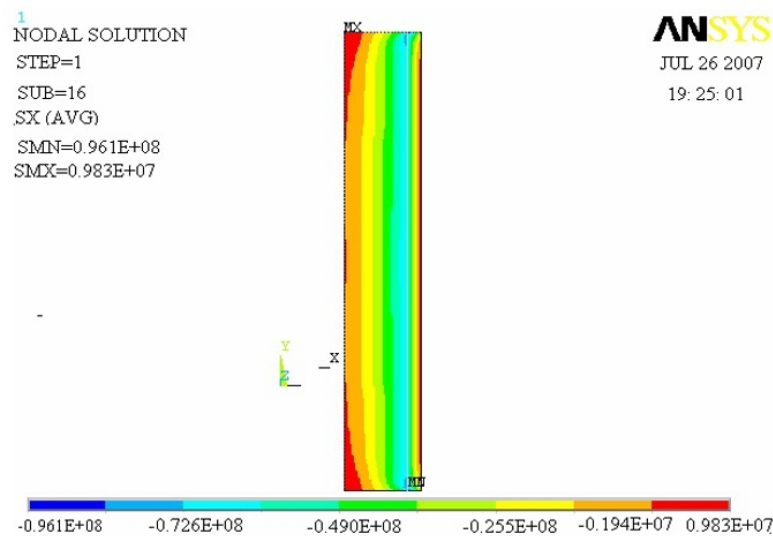
FIGURE 2.2: 2D Axisymmetric FEA [39]

Only Barrans et al. and Zhou and Fang [10, 52] used an axisymmetric model in their FEA. It appears that Wang et al. [39] may have also used an axisymmetric model but did not explicitly confirm it. Neither Wang et al. [39] or Zhou and Fang [52] stated the constraints used on the analysis, but Zhou and Fang [52] obtained FEA results agreeing with analytical results, most within 5%. However, at 150 °C and 600,000 rpm the radial stress error was circa 25%. The agreement adds confidence to the results but without the constraints used on the analysis, the results become difficult to replicate and verify. Despite the axisymmetric model being under explored by the current literature, there is a still a lack of justification in most sources that have used it. Neither Wang et al. [39] or Zhou and Fang [52] explain why they have used axisymmetric model or have justified why it works for their rotor model.

2.3.4 3D Finite Element Analysis

The 3D method usually analyses a 3D rotor section, as shown in Figure 2.3, with symmetry conditions to replicate full rotor behaviour. Symmetry conditions allow rigid body motion to be eliminated without approximating connection to other parts of the electric machine. A 3D model removes the need for stress distribution assumptions, as required in 2D models. However, larger numbers of more complex
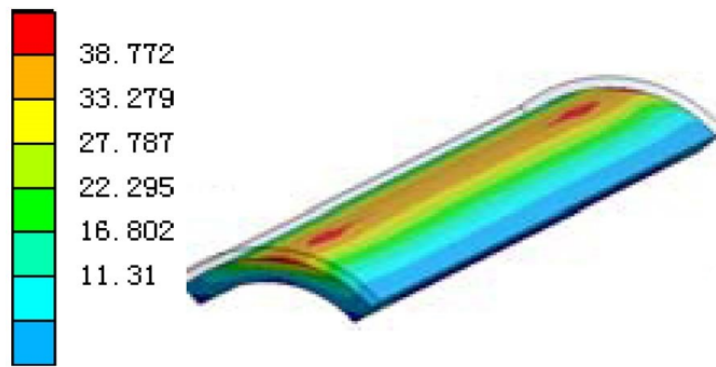
FIGURE 2.3: 3D Section FEA [69]

elements are required to obtain results as accurate as those from 2D analyses. This significantly increases the processing time and should only be used if necessary.

Multiple authors [11, 24, 27, 33, 38, 46, 47, 69, 77] used 3D FEA models. Wan et al. [47] justified using 3D over 2D models due to magnet segments and axial stress distribution not being considered by 2D analysis. However, Barrans et al. [10] states 2D axisymmetric FEA is an acceptable model while a compressive circumferential stress is maintained within the rotor. This model would also show the axial stress distribution. Borisavljevic et al. [24] used 3D FEA as a final verification of the 2D FEA results. Differences in results were found in the magnet inner surface stress due to press-fit; and in the stress at the iron shaft and glass fibre boundary. As noted by Barrans et al. [10], stress predictions at these interfaces are very sensitive to mesh density. With Borisavljevic et al. [24] the mesh density and boundary constraints were not specified. Smith et al. [27] used a 3D model to investigate the cause of a magnet failure. The 3D model showed the high shear stress towards the end of the rotor, causing failure. This high shear stress was also identified by Barrans et al. [10] using an axisymmetric model, showing that the 3D model may have been unnecessary. No other variation was seen that required a 3D model over axisymmetric. Wang et al. [69] stated the temperature and rotor speed used in FEA, but did not explain why a 3D model was used or the constraints applied. Burnand et al. [11] also did not explain boundary conditions or provide mesh details. With Burnand et al. [11] the plain strain analytical results are compared to 3D FEA results and to a plane stress analytical model. The maximum error between the 3D FEA and the

plain strain results was less than 4%. However, when comparing to plane stress results, larger differences were found, in particularly at the shaft. In the shaft, errors of over 1000% were found. Burnand et al. [11] attributed this to the plane stress model ignoring axial stress. This could be significant for mechanically weak magnets.

Beshrati et al. [79] stated that an elastic body subject to loads in three dimensions will result in a 3D system of stresses, but Barrans et al. [10] discussed that 3D FEA models are not a necessity to be able to explore stresses in three directions. Beshrati et al. [79] provided no FEA boundary conditions and did not verify the results against an analytical model or practical test. Zhang et al. [33] used 3D FEA to verify analytical and 2D section FEA results. Of the four locations of stress, the analytical results had an average 21% difference from the 3D FEA and 29% from the 2D FEA model. The plane stress condition was used for the analytical approach after concluding the difference between plane stress and plane strain was negligible, but any constraints on the 2D FEA model were not mentioned. Lastly, Wan et al. [47] used 3D FEA due to magnet configuration. Segmented magnets with fillers were used which would cause a change in circumferential stress and require the use of 3D FEA. However, the boundary conditions and mesh details were not discussed. Axial stress was also not incorporated into the analytical calculations.

Most papers opted for a 3D FEA analysis, but few justified or required it. Mesh details and boundary conditions were also scarcely mentioned in papers making it very difficult to verify the FEA results as reliable or accurate.

2.4 Rotor Optimisation

2.4.1 Mechanical Optimisation

2.4.1.1 Basic Optimisation Parameters

When conducting rotor stress analysis, the reason is to either assess structural integrity or perform rotor optimisation. Few papers [3, 10, 24, 34, 39, 57] focused on or significantly included rotor optimisation with a variety of constraints and criteria

being used to define the optimum solution, with substantial regard to the mechanical performance of the rotor. After reviewing these papers, certain parameters were identified that enable optimisation to be performed. These are:

- Criteria
- Design variables
- Constraints

Criteria must be established as the basis for optimisation and they are the overall goal of the optimisation process. All papers [3, 10, 24, 34, 39, 57] had a specific rotor parameter that was the focus of the optimisation, to maximise its output. Design variables enable experimentation of different design features to determine an optimal design. Barrans et al., Wang et al., and Huang and Fang [10, 39, 57] specifically mention design variables and how they are altered through the optimisation process in search for the optimised result. Constraints set the limits in which the optimisation process can work and help to ensure the optimal result is feasible for the user's application. Constraints applied to the optimisation process can be broken down into three categories:

- Criteria Constraints
- Design Variable Constraints
- Functional Constraints

Criteria and design variable constraints are user defined limits imposed on the range of said aspects. For example, the focus of the criteria by Barrans et al. [10] was also a design variable. Therefore, the range constraint placed on that design variable also constrained the criteria. Functional constraints are specified limits based on other calculated parameters which are not criteria, i.e. not exceeding a material yield stress limit which was used by all papers [3, 10, 24, 34, 39, 57]. To generate a feasible design, the design must fall within all the constraints. The optimal design, or designs, will then fall within this feasible set. Some papers, such as one by Fang et al. [3], may use fixed design parameters which are user defined specifications that must remain a fixed value. However, fixing design parameters will typically restrict

the range of feasible designs and hence could eliminate designs which perform better in terms of the optimisation criteria. Placing minimum and/or maximum limits on design variables will avoid this restriction.

2.4.1.2 Criteria and Design Variables

Of the papers reviewed, most [3, 10, 34, 39, 57] selected a criterion of minimising the sleeve thickness. Fang et al. [3] also included minimising the magnet thickness as part of the criteria. The benefits of a thinner sleeve are: reduced effective air gap; lower circumferential stress due to rotation; smaller volume; and lower mass. These factors contribute to a more efficient rotor, through both mechanical and electromagnetic performance. Only Borisavljevic et al. [24] opted for an alternative criterion which was to maximise rotational speed. Borisavljevic et al. [24] chose their criterion based on a pre-determined electromagnetic design which fixed the effective air gap. Therefore, it appears that rotational speed was focussed on to maximise electromagnetic power output as the sleeve thickness would not affect the effective air gap dimensions.

There was also consensus between papers on the design variables used in the optimisation process. All six papers [3, 10, 24, 34, 39, 57] used interference as a design variable. The level of interference between cylinders has a large impact on rotor stresses and magnet compression. Changing interference enables users to identify a specific value suitable for specific rotor operating conditions. As well as being the criterion for the majority of papers, sleeve thickness was also a common design variable, used by most papers [10, 24, 34, 39, 57]. Sleeve thickness is required to work in conjunction with the interference fit and changes in thickness can alter rotor stresses significantly. Fang et al. [3] did not specify sleeve thickness as a design variable because the outer diameter of the rotor was fixed before optimisation. The magnet thickness was used as the design variable instead, which when changed, determined the sleeve thickness of the rotor. Wang et al. [39] also used magnet thickness as a design variable, which would change the electromagnetic performance of the rotor. Fang et al. [3] used the sleeve material as a design variable, by specifying three potential materials, and was the only paper to introduce fixed design parameters: rotor outer diameter; and air gap flux density.

2.4.1.3 Constraints

As discussed earlier where most papers [3, 10, 34, 39, 57] specified the sleeve thickness as the criteria, Fang et al. and Barrans et al. [3, 10] also placed constraints on this criteria. Barrans et al. [10] constrained the sleeve outer radius to a range of 13 - 14.5 mm, whereas Fang et al. [3] fixed the rotor outer diameter. Where the sleeve thickness was a design variable, Borisavljevic et al. [24] imposed design variable constraints by specifying a maximum sleeve thickness of 2 mm, while Xu et al. [34] did not specify any limitations to the sleeve thickness. Design variable constraints were also applied to the interference fit by Barrans et al.,Wang et al., and Huang and Fang [10, 39, 57]. Borisavljevic et al. [24] discussed an optimal interference value being deduced by other constraints and therefore did not include specific constraints on the interference level. Finally Wang et al. [39] placed limits on the magnet thickness design variable.

All papers [3, 10, 24, 34, 39, 57] defined functional constraints so the sleeve stress remained less than the yield stress. However, it is worth noting that this condition should be applied when the rotor is stationary and in operation. As discussed by Barrans et al. [10], the highest compression on the magnets can occur whilst stationary. At speed, the centrifugal forces can expand the sleeve, lowering the compression on the magnets. There are four conditions, stated by Barrans et al. [10], where the constraint should be satisfied: minimum speed and minimum temperature; minimum speed and maximum temperature; maximum speed and minimum temperature; and maximum speed and maximum temperature. This ensures the constraint is always applied. The sleeve is responsible for keeping the magnets in compression and therefore any failure to the sleeve will result in rotor failure. However, the sleeve stress functional constraint does not ensure the magnets will be held in compression. Therefore, Fang et al., Barrans et al., and Xu et al. [3, 10, 34] applied a constraint stating there must be a compressive contact pressure between the sleeve and the magnets and Huang and Fang [57] specified a range for the contact pressure value. Borisavljevic et al. [24], along with Barrans et al. [10], stated the inner surface of the magnet must also be in compression. Wang et al. [39] did not apply a contact

pressure requirement. Due to the constraints requiring magnets to be in compression, Barrans et al. and Borisavljevic et al. [10, 24] ensured the stress in the magnets could not exceed their ultimate compressive strength during operation. This ensures the magnets do not fail due to excessive compression.

Optimisation aims to identify the optimal feasible design. However, without the correct constraints, infeasible designs can be produced. Xu et al. [34] increased the sleeve thickness of their rotor with every optimisation step until the conditions were satisfied. However, with no constraints on the sleeve thickness, if there was a limit to the rotor outer diameter then an infeasible design could have been produced. Both papers by Fang et al. and Barrans et al. [3, 10] identified infeasible designs through their optimisation process, ensuring the final designs were feasible. Most papers [24, 34, 39, 57] produced a single feasible optimised design from the optimisation process. Fang et al. [3] identified a set of feasible designs which had a single optimal design for each suitable sleeve material. However, Barrans et al. [10] identified a feasible set of designs which satisfied all the constraints. A larger range of designs enables the user to decide which of the feasible designs is most suited to their situation.

There are few papers focusing on optimisation regarding rotor manufacturing and it would therefore benefit from further research. Most papers that included optimisation decided to focus on minimising sleeve thickness as this improves the overall rotor performance. However, without the correct constraints, optimised rotors designs can be produced that cannot be manufactured. For example, excessive interference or very thin sleeve thickness will make rotor assembly difficult. Only Xu et al. [34] mentioned lowering the assembly pressure of the rotor as a target.

2.4.2 Electromagnetic Optimisation

As discussed in Section 2.4.1.2, optimisation of SPM rotors often focusses on reducing the sleeve thickness due to the electromagnetic and mechanical performance benefits. However, research in the current literature has also concentrated on the whole motor and therefore the electromagnetic performance of the stator.

With a focus on electromagnetic performance, maximising efficiency was a common criterion used in the current literature, used by Suthar and Patel, Li et al., and Wang et al. [80–82]. Of those, only Li et al. [81] used a multi-criteria approach which

included minimising rotor weight and minimising torque ripple as other criteria, which were also weighted by the user to add emphasis to the most important criterion. Both Suthar and Patel and Li et al. [80, 81] included flux density and the air gap length in their design variables. Li et al. [81] opted for nine design variables in total including magnet thickness and stator core length. All design variables were constrained by an upper and lower range limit which enabled the optimisation process to explore many designs. The material of the outer sleeve was fixed as carbon fibre as Li et al. [81] discussed conductive materials have higher eddy current losses which could be avoided with carbon fibre. Li et al. [81] noted that the number of stator slots has a large effect on performance and therefore optimised a solution for four different slot number topologies. Optimised designs were produced in a Pareto set of viable options which were selected from by the user. To verify the chosen optimised designs Li et al. [81] compared them against FEA and thermal simulations which showed they were in good agreement. The optimisation process in [80] produced a single optimal design based on the design variables. As shown by Li et al. [81], Suthar and Patel [80] also placed upper and lower range constraints on the design variables and verified the optimised result with good agreement with FEA simulations.

Wang et al. [82] optimised the SPM motor for efficiency and listed design variables of slot pole numbers, axial length, and the number of turns in the stator. It was noted that maximising the performance of one aspect typically reduced the performance of another aspect. For example, to improve machine inductance, reducing the air-gap or magnet thickness can be done, as used in Li et al. [81]. However, Wang et al. [82] states that altering the rotor axial length and the number of turns in the coils can also have the same effect on machine inductance. Wang et al. [82] fixed a variety of rotor structure dimension such as the magnet thickness and air-gap length. This was due to wanting to maintain acceptable flux density and torque density while the air-gap was restricted due to limits of manufacturing tolerances. However, as stated in Section 2.4.1.1, fixing aspects during optimisation often limits the optimal design and can often be avoided by specifying a range for that dimension. One optimised design was produced during the process and was successfully verified via experimental testing.

Other criteria used in electromagnetic optimisation were minimising eddy currents used by Belli and Mekideche [83] and minimising cogging torque used by Abbaszadeh et al. [84]. Both used design variables relating to the permanent magnets in the rotor where Belli and Mekideche [83] had the number of magnets and the magnet gap distance as the two design variables, while Abbaszadeh et al. [84] had the individual magnet gap distance and the combined magnet gaps distance as their two design variables. Both Belli and Mekideche and Abbaszadeh et al. [83, 84] applied range constraints on the design variables. Optimisation by Belli and Mekideche [83] was computed by FEA at each stage of optimisation and a single optimised result was produced for each of two operating frequencies. Abbaszadeh et al. [84] optimisation process successfully identified an alternative magnet gap that minimised the cogging torque.

2.4.3 Constrained, Multi-Criteria Optimisation

Whereas the focus of most of the papers in Sections 2.4.1 and 2.4.2 was a single criterion such as minimising the sleeve thickness of a SPM rotor, multi-criteria optimisation (MCO) focusses on more than one criterion. Das and Dennis [85] provided an example where the construction design of a bridge may simultaneously need to minimise the total mass whilst also maximising the bridge stiffness. Das and Dennis [85] note that naturally there will be a compromise in the final design as criteria can be conflicting. Marler and Arora [86] add that because there is typically no single solution to MCO problems, there is usually a set of points that all fit the parameters of the solution, called a Pareto set.

There are many different MCO methods as discussed by Mela et al. and Odu and Charles-Owaba [87, 88] where potential methods were detailed that can be applied by the user. Weighted sum method (WSM) is one of the most common approaches and involves the user giving the specified criteria a weighting depending on their priority to the final design [88]. However, there are numerous drawbacks with WSM detailed by Odu and Charles-Owaba [88]. The weightings can make it difficult to achieve the task and only one solution is identified each time. Therefore, this requires repeated running to generate a Pareto set, but the set can be poorly distributed. WSM also cannot identify the optimal solution if the Pareto front is not

convex. The weighted product method (WPM) is similar to WSM but the weightings given to each criterion are raised to a power instead. This is mainly used for criteria maximisation problems, but it can also be applied for minimisation problems, however this requires a careful inspection of the numbers due to using negative powers to minimise a criterion. To overcome the problem of unsuitability for non-convex Pareto front solutions, Gunantara [89] stated that the ε-constraint method can be used. This method optimises one objective while the remaining objectives become limits. However, this can result in producing no viable solution. Mela et al. [87] discussed the VIKOR method, which stands for a Serbian term for 'multi-criteria optimisation and compromise solution' [90] and identifies a chosen compromised design from a set of compromised solutions based on how far the design is from the ideal solution. If several designs are equally close to the ideal solution, VIKOR will return a set of preferred compromised designs. Odu and Charles-Owaba [88] discussed this philosophy as 'Compromise Programming' and stated that it is mathematically superior to WSM in identifying the Pareto set. However, it is possible for the user to bias the calculations which would require a normalisation process to remove any unwanted effects from this. Technique for Order of Preference by Similarity to Ideal Solution (TOPSIS) is like VIKOR but it also considers the chosen design being the furthest from the nadir. This point is determined by combining the worst aspects of all the other remaining alternative designs [87]. PEG-procedure works on trading each criterion against each other until an acceptable design for all criterion is found. No weighting is required from the user and the final feasible solutions are not ranked against each other [87]. Odu and Charles-Owaba [88] state that Goal Programming is one of the most powerful and popular MCO methods, where goals are applied to all objective functions. All objectives are also assigned target levels for the goals and a relative importance value for achieving these levels. Despite being popular, Odu and Charles-Owaba [88] state that it is hard for the user to specify sufficiently precise information in complex optimisation problems. The Desirability Function approach allows users to minimise, maximise and apply target values to objectives simultaneously, unlike in Goal Programming [88]. Another method discussed by Odu and Charles-Owaba [88] was Physical Programming which treats objectives, constraints, and goals as equal design metrics. It requires no weighting

input from the user but incorporates preference via numerical preference limits for each design metric. However, Odu and Charles-Owaba [88] state that this method requires programming complexity.

To apply MCO methods, Deb [91] discussed the use of multi-criteria evolutionary algorithms (MCEA). MCEAs are popular and are a population-based approach where more than one solution participates in each iteration, increasing efficiency. Each iteration evolves a new population of solutions which are then compared against existing solutions using dominance to identify the Pareto front. MCEAs identify Pareto sets that are diverse and represent an entire range of solutions. Vrugt and Robinson [92] states that Non-dominated Superiority Genetic Algorithm-II (NSGA-II), proposed by Deb et al. [93], has received the most attention due to its simplicity and superiority over other methods. However, as shown by Vrugt and Robinson [92], MCEAs can require many iterations until a Pareto front is converged to. To run the optimisation simulation, Asadi et al. and Tian et al. [94, 95] used Mat-Lab. Asadi et al. [94] also used GenOpt 3.0.3, which is an optimisation program but stated that it was not capable of MCO. Tian et al. [95] developed an MCO platform in MatLab that incorporated fifty different MCO methodologies, showing that MatLab is a very capable software for a wide range of MCO problems. Lin [96] produced a MatLab code for the implementation of NSGA-II proposed by Deb et al. [93], to enable users to conduct personal multi-criteria optimisation problems.

The applications of multi-criteria optimisation are vast and span different industries. For example, multi-criteria optimisation has been utilised in humanitarian aid, medical planning, sustainability problems and engineering design. Kierkels et al. [97] describes how multi-criteria optimisation was used to enable novice treatment planners to produce high quality treatment plans for patients. Yu et al. [98] used it to plan the implantations in a brachytherapy technique for treating cancer. For humanitarian aid, Vitoriano et al. [99] optimised the delivery logistics of the aid. Criteria such as cost, time, security, or reliability were used simultaneously to provide a range of distribution options. Criteria constraints were used based on targets set by the user to ensure solutions were deliverable. Both Ferrer et al. and Gutjahr and Nolz [100,101] used multi-criteria optimisation with similar criteria to Vitoriano et al. [99], to identify the optimal response plan to deliver disaster relief. In the

energy sector, Wang et al. [102] evaluated trigeneration systems using multi-criteria optimisation. Wang et al. [102] evaluated five trigeneration systems across 17 different criteria which were weighted based on a multi-layer hierarchy system. Criteria were based on technological, economic, environmental, and societal aspects with the final trigeneration system being chosen based on how close it was to the ideal solution. Pilavachi et al. [103] used multi-criteria optimisation to evaluate nine different energy generation systems across seven criteria which included efficiency, emissions, costs, and lifespan. Similarly to Wang et al. [102], the criteria were weighted by the user but Pilavachi et al. [103] created multiple multi-criteria scenarios to compare the energy systems performance when the criteria weights were altered. The most suitable option was determined based on a ranking of how well it performed across all criteria. In engineering design, Jureczko et al. [104] optimised the design of a wind turbine blade against multiple criteria. The criteria aimed to extract the maximum performance of the blade across multiple aspects by minimising blade vibrations, maximising blade output, and minimising blade material cost.

Hopfe et al. [105] explored optimisation in building design but introduced the concept of robust optimisation. Hopfe et al. [105] states that in the real world, designs are subject to uncertainties caused by a variety of factors including manufacturing error, measurement errors and other external factors. Minor deviations from the optimised design may induce large difference on its performance, therefore the optimised design should remain optimal even when these uncertainties are considered. Chen et al. [106] highlights the importance of robust optimisation for proton therapy where processes can be sensitive to errors. Chen et al. [106] states this is achieved by incorporating uncertainty data into the optimisation process so that the results are considered robust and are successful even if small errors are later induced.

Goh et al. [107] also discussed the concept of uncertainty and how it can be applied to computation or analytical models. In these models, Goh et al. [107] mentions potential uncertainties in loads, material properties, geometry, etc. Variations in these factors will affect optimisation results and consideration of potential uncertainties is critical to ensuring a reliable design is produced [108]. Goh et al. [107] states that probabilistic design methods better account for variability in analysis variables, as opposed to deterministic approaches. However the same models are

used between each method, with the probabilistic approach introducing randomness into the variability. Goh et al. [108] lists Monte Carlo simulation and Latin Hypercube sampling as exact simulation techniques. Introducing these types of uncertainty modelling into optimisation would help produce complete robust designs.

2.5 Rotor Manufacturing & Assembly Techniques

2.5.1 Shrink Fitting

Hong et al. [109] states that shrink fitting is a process where cylindrical rotor bodies are manufactured with an interference fit and subjected to a change in temperature to expand or reduce the outer diameter, enabling rotor assembly via sliding the parts together. As the parts cool, the interference fit is restored, and an interference pressure is created at the boundary layer of the parts. It is important to ensure the component diameter change, due to temperature, is sufficient to assemble the parts. To achieve this, Hong et al. [109] discusses cooling the rotor shaft while heating the sleeve, but they did not present the success of this method. A prototype rotor was manufactured but very few details were discussed regarding the assembly and manufacturing process. Fang et al. and Yon et al. [3, 51] note that shrink fitting can be achieved by only subjecting one part to a change in temperature. With Fang et al. [3] a carbon fibre sleeve was proposed, therefore only cooling the inner body would be feasible due to carbon fibre having a low coefficient of thermal expansion. However, the analysis was completed via FEA and did not examine the assembly process, only the stresses due to the interference fit were examined. Multiple authors [3,25,51,109] all acknowledge that the cooling of rotor parts is typically conducted with liquid nitrogen. Yon et al. [51] discusses the typical manufacturing route of heating the sleeve to fit around the PMs which would be bonded to the back iron. However, during their experiment, the back iron was freeze shrunk and inserted inside a sleeve and magnet assembly. They stated that this was conducted in a low humidity environment to avoid ice crystals forming on the back-iron surface.

Shrink fitting can provide important benefits specific to SPM rotors. Fang et al. [3] states that the PMs must be treated carefully due to their low tensile strength, as also stated in Section 1.1.2. Wang et al. [110] agrees, stating that the tensile load

during assembly can be reduced via shrink fitting. Also, whilst discussing axial pressing or shrink fitting, Binder et al. [25] observes a rotor failure, in Figure 2.4, and lists the axial pressing assembly process as harmful to the rotor sleeve strength.
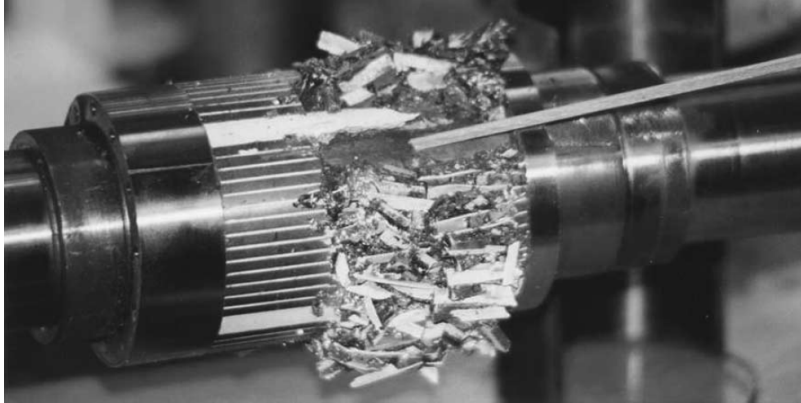
FIGURE 2.4: Destruction of brittle magnets post sleeve failure. [25]

However, it is noted that it is difficult to measure the effect of axial pressing but the location of the failure suggested the weakening of the sleeve due to axial pressing could be partly responsible. In the following experiment, a rotor was created using shrink fitting with liquid nitrogen to remove this potential source of sleeve weakening. Ahn et al. [59, 111] focus on the effect of the shrink fit on the rotor, post assembly. Both produce graphs via analysis showing the change in Von Mises stress in the sleeve and radial stress in the PMs. As the interference between the sleeve and magnets is increased the tensile Von Mises stress in the sleeve appears to increase linearly across all rotor speeds. Within the magnets, the Von Mises stresses switches from tensile to compressive as the interference is increased from a low amount. This is due to the stresses generated via interference counteracting the tensile stresses generated by rotation. As the interference is increased, the magnets can remain in a compressive state at higher speeds, which is important to ensure, as discussed earlier. Jang et al. [112] also notes an increase in sleeve Von Mises stress with increasing interference.

Some papers in existing literature explore potential failures of shrink-fit assemblies. Smith et al. [27] identifies magnet cracking at the axial ends after the rotor is constructed and before experimental loads are place upon the assembly, as shown in Figure 2.5.
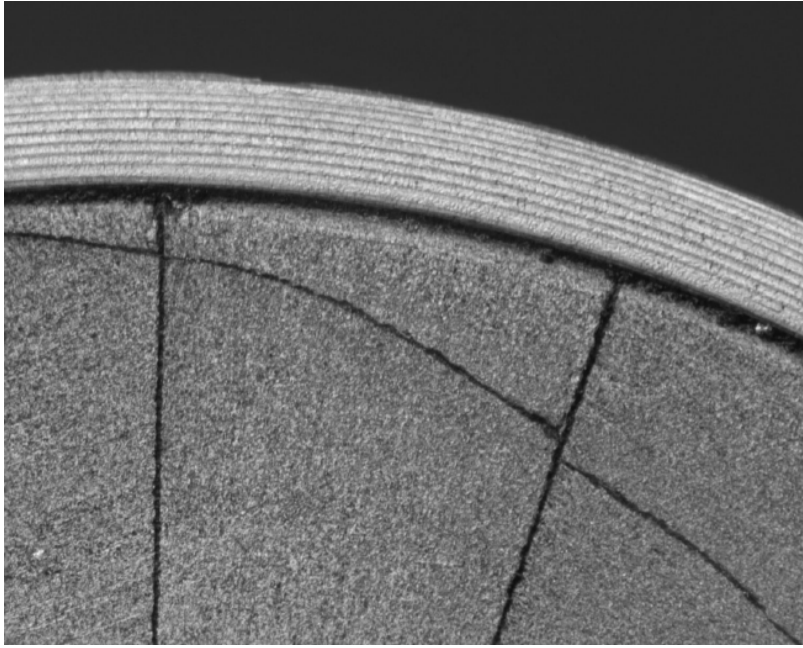
FIGURE 2.5: Magnet cracking at axial ends within shrink-fit assembly.
[27]

Smith et al. [27] states that shear stresses generated via the Poisson effect cause the cracking in sleeved permanent magnet rotors. Juuma [113] discusses two different failure methods of shrink-fit rotors, shown in Figure 2.6. Juuma [113] states
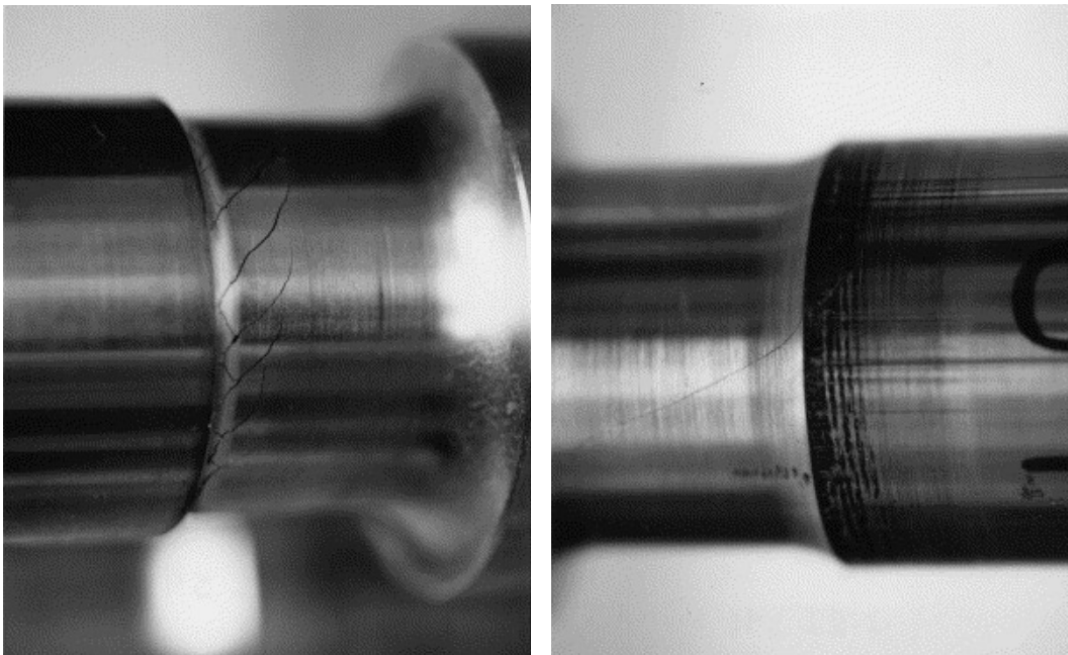
(A) Failure due to stress concentrations at the shaft fillet radius. [113].

(B) Failure due to fretting between the interfering surfaces. [113].

FIGURE 2.6: Two methods of fatigue failures for shrink-fit assemblies.

that one failure method was due to fatigue from increasing stress concentrations at a fillet radius of the shaft. The other shrink-fit failure method was due to fretting fatigue, a phenomenon caused by slip between the contacting surfaces [113].

2.5.2 Press Fitting

Like shrink fitting, press fitting requires the manufacture of cylindrical rotor bodies with an interference fit. However, they are assembled via axial pressing using a hydraulic press. Binder et al. and Smith et al. [25, 27] both discuss how the press fit method has serious problems when applied to the SPM rotor assembly. Binder et al. [25] states that the axial press generates shear stresses at the interference location which can weaken and damage a carbon fibre sleeve, a commonly used sleeve material. As stated in Section 2.5.1, an experiment was conducted with a sleeve failure where a potential cause of failure was identified as the press fitting procedure. Smith et al. [27] adds that the shear stresses can also weaken the low tensile strength magnets and therefore, the axial press method is uncommon for SPM rotor applications.

Few other papers mention axial press fitting, potentially due to the lack of use for the process. Borisavljevic et al. [24] acknowledges press fitting alongside shrink fitting as a possible assembly method, however the negative aspects of the process were not evaluated. A prototype rotor was created using the press fit method, but it was not tested to validate the 2D and 3D FEA results. Wang et al. [39, 110] states how the tensile stress on the PMs can be reduced by opting to assemble via shrink fitting.

2.5.3 Wire Wrapping

While shrink fitting and press fitting use interference fits to hold the magnet in compression, wire wrapping requires wrapping material to be under tension to generate the compressive stress. Multiple strands of the wrapping material are placed under a specified high tension and are wrapped around the PMs until the desired thickness is achieved. The thickness and tension of the strands are determined by the rotor design requirements. Yang et al. [114] shows analytically that as the tension in the strands is increased, the compressive stress at the PM inner surface increases

linearly. Therefore, this can be used to control the compressive stress generated in the rotor. However, Yang et al. [114] states that it is difficult to predict analytically due to the wire wrapping process. A prototype rotor was created and tested, however there were no results presented from the test to validate the analysis on the wire wrapping process. Only a visual check of the rotor was conducted to confirm it was tested successfully.

Smith et al., Zhang et al., and Varaticeanu et al. [27,33,55] agree that wire wrapped SPM rotor sleeves generally use a composite material as their low coefficient of thermal expansion makes shrink fitting inappropriate. The typical composite material used is carbon fibre. Wire wrapping a carbon fibre sleeve provides multiple benefits over shrink fitting a metallic sleeve, particularly on the electromagnetic performance of the rotor. Yang et al. [114] discusses that due to carbon fibre being stronger than the typical metallic sleeve materials, the sleeve can be made thinner. Zhang et al. [33] adds that a thinner sleeve reduces the effective air gap between the rotor and stator, improving performance. Both papers [33, 114] also state that the losses due to eddy currents are low with a non-conductive composite sleeve.

2.6 Rotor Testing

2.6.1 Test Rigs

Theoretical stress calculations and FEA simulations on rotors are efficient stress prediction models compared to testing many rotors. However, the results of the stress prediction models must be validated by correlating with testing results. Compound cylinder rotors only have the outer rotor surface to generate results as all other useful locations are not exposed. Existing literature rarely uses testing to validate the theoretical or FEA stress results. Using a pass or fail criteria on rotor test success, appears to be the extent of validating stress predictions in the current literature as shown in multiple papers [33, 34, 115–117]. This does not confirm whether the theoretical or FEA analyses were accurate. Most experimental studies into high-speed electric machines (HSEMs) do not tend to focus on the mechanical aspect of the rotor.

Of the reviewed literature, over 75% of conducted tests were completed with HSEMs, where many authors [6, 12, 13, 33, 41, 43, 45, 57, 59, 60, 64, 67, 69, 78, 115–124]

utilised the electromagnetic forces to induce rotation. HSEMs are complex machines that require a wide range of mechanical and electrical components, therefore most papers above had a complex design procedure to produce a HSEM to test their specific rotor. However, HSEMs are useful when the focus is on electromagnetic performance. They provide realistic operating conditions and performance whilst utilising power density gains to produce smaller rigs with a higher speed range. Aspects such as windage losses [116], back electromotive force (EMF) [64] and magnet losses [45] can be explored when testing HSEMs.

The second most common approach was an air turbine, as shown in numerous papers [9, 16, 57, 116]. Air turbines can be utilised to rotate rotors by attaching the rotor to the air turbine shaft. Gerada et al. and Terdich and Martinez-Botas [9,16] discussed testing an EAT which included some of the complexities discussed above for HSEMs. However, Gerada et al. and Terdich and Martinez-Botas [9,16] were not testing their own rotor design and therefore could use the set up already in place with the existing electrically assisted turbocharger, reducing the test complexity greatly. The focus of their tests was on performance parameters of the existing EAT. A cold gas stand was used to drive the turbine by Terdich and Martinez-Botas [16] combined with a heater to provide control and a range of operating conditions. Gerada et al. [9] showed engine exhaust gases being used from a Cummins engine test bed which would provide realistic operating conditions. The turbine was only used by Huang and Fang [57] to identify air friction losses, while the rotation was generated via a HSEM setup, requiring the complexities mentioned above. Only Sanchez et al. [116] focussed on the mechanical aspects of the rotor design, using the turbine to rotate the rotor and reducing the complexity of the rig. The expansion of the rotor was measured using an eddy current probe so a stator was not required, and the magnets could be swapped for stainless steel. Another method of powering a rotor is to use a standard air motor. Bonello and Bin Hassan [125] shows an air motor shaft coupled to the rotor. However, to overcome the inertia of the rotor, an electric motor with a pulley system across the rotor was also employed. However, this method still reduces complexity against HSEMs and enables the rotor to be seen while testing. Air turbines and motors greatly reduce the complexity requirement of a test rig when compared to HSEMs and open the possibility of accessing the rotor to

obtain mechanical analysis measurements. However, there is a lack of exploration in testing the mechanical aspect of the rotor.

When testing high speed rotors, suitable bearings will be required to perform a successful and reliable test. Only a relatively small percentage of the reviewed literature discussed the bearings used in the test rig [16,57,64,67,115,116,121,122,124, 125]. They use a wide range of bearings including: standard ball bearings; magnetic bearings, angular contact ball bearings; foil air bearings; and static air bearings.

As discussed by Zwyssig and Kolar and Argrawal [64,126], foil air bearings levitate using air pressure generated by spinning the rotor. This considerably reduces friction on the rotor and requires no lubrication, making them suitable for high speed applications. As discussed by Argrawal [126] this improves reliability through having no parts in contact and removes the requirement for maintenance of the lubrication system. Argrawal [126] also adds that due to the bearing foils, any failure is restrained from excessive movement, confining most of the damage to the bearing and shaft surface only. According to Zwyssig and Kolar [64] foil air bearings are suitable for high speed and high temperature, but are not commercially available and require a complex design.

Static air bearings used by Gong et al. [122,124] levitate with air pressure similar to foil air bearings, however they require an external air supply integrated into the test rig design [64] unlike foil air bearings. Gong et al. [122] states that due to the high-speed application, static air bearings are preferred over ball bearings due to their higher lifespan and efficiency. Zwyssig and Kolar [64] argues for ball bearings due to their simplicity and because they do not require supplementary equipment.

Active magnetic bearings used by multiple papers [57,67,115,121] utilise a magnetic force to stabilise the rotor and give similar advantages to air bearings. However, according to Zwyssig and Kolar [64] active magnetic bearings require a complex design procedure as they use sensors and actuators. Chen et al. [115] was required to use a controller and power amplifier to control the bearings during their test.

Angular contact bearings are ball bearings designed to withstand high axial loads, used by Terdich and Martinez-Botas [16]. This was suitable for Terdich and Martinez-Botas [16] as they utilised an existing EAT in their test procedure, as discussed

earlier. Flowing air through a turbocharger generates an axial thrust as the turbine wheel discards waste gases axially. Therefore, an axial load is placed on the bearings. Angular contact ball bearings are designed with a retaining lip on one side of the ball bearings to withstand an axial load. According to Zwyssig and Kolar [64], ball bearings provide simplicity and are still capable of achieving high-speed, but this is limited by heat generation due to friction and the need to maintain lubrication.

Most current rotor testing has been focused on electromagnetic performance and required complex design procedures for HSEMs. For the few papers which focused on rotor stresses, far less complex power supplies were used. Air power supplies are capable of testing at sufficient speeds and existing products can be used such as turbochargers or air motors. Focusing on rotor stresses also enables the substitution of fragile materials such as sintered permanent magnets, which reduces test complexity further. Whilst ball bearings have limitations that other bearings do not, they have successfully been used in the current literature and would be inexpensive, readily available, and easily integrated into any further rotor testing.

2.6.2 Measurement Methods

As discussed in Section 2.6.1, few papers investigated rotor stresses during testing, instead opting for a pass or fail criteria based on a rotor examination post-test [33, 34, 115, 116]. However, it is important to identify potential methods of obtaining rotor strain measurements during testing as they can be used to validate theoretical or FEA stress prediction models which are much more efficient than testing. This would then enable quick, reliable exploration of rotor design concepts and enable rotor optimisation.

Methods of measuring strains on rotating components are available despite the lack of exploration in the HSEM literature. Strain gauges require being attached to the rotor surface and only measure strain at their placed location. Ha et al. [127] placed a series of these gauges on the rotor, to measure circumferential and radial strains, that were wired to a wireless telemetry transmitter, enabling the extraction of the results. The tests were conducted at speeds up to 30 krpm, with the transmitter placed inside the shaft, requiring the whole rotor system to be balanced up to 10

gmm. Alternatively, slip rings can be used to extract the readings. However, Warren et al. [128] states that slip rings suffer from measurement noise and attached sensors can affect the dynamic response due to mass loading and aerodynamic effects.

Non-intrusive methods of analysing stresses are available, as described by Baqersad et al. [129]. Using dynamic photogrammetry, optical target points on components can be tracked via software. This enables the displacement of those targets to be analysed when compared to a reference stage. However, this method is typically used for a small number of targets on a component, which was used by Baqersad et al. [130] on a rotating helicopter blade. As shown by Baqersad et al. [130] it is far more feasible to analyse more points using dynamic photogrammetry than using strain gauges. Requiring no wires also reduces the complexity of testing procedure compared to using strain gauges.

Digital image correlation (DIC) is a similar technique to dynamic photogrammetry, but provides analysis across whole surfaces to show continuous strain patterns. Baqersad et al. [129] states that the component surface is prepared with a high contrast random speckle pattern, where each speckle is identified and tracked by the software and cameras. However, this is only successful when the object is stationary. Further equipment is required to enable the analysis of moving objects, as shown by Sirohi and Lawson [131]. Sirohi and Lawson [131] used DIC to analyse a rotating rotor blade by incorporating a strobe light to ensure the same blade was captured with every image. The strobe light requires specific timing to illuminate the object as soon as it is correctly placed in the cameras field of view. Despite the benefits of this approach, Baqersad et al. [130] states that due to the surface preparation requirements and the need for high resolution cameras, DIC is not commonly used for rotating components. Baqersad et al. [129] highlights the availability of photogrammetry options that do not use optical targets like DIC or dynamic photogrammetry. Instead, component defects or features are tracked by the software, removing the need to prepare difficult surfaces. However, they are not as accurate as DIC and dynamic photogrammetry.

Alternatively, Marshall et al. [132] describes a non-invasive method of determining the contact pressure between interference fit components. Marshall et al. [132]

states that by generating an ultrasonic pulse towards the components, it will be reflected at the interference interface. This can be conducted across the whole interface and a map of the reflected ultrasound can be recorded. The ultrasound map is used to determine the interface stiffness which can then be used to determine the contact pressure via a calibration procedure. However, according to Brunskill et al. [133], this method is limited to static loading.

To determine the contact pressure via non-invasive methods for dynamic loading, Brunskill et al. [133] uses the same concept as Marshall et al. [132] but utilises an ultrasonic array of 64 linear elements. Brunskill et al. [133] used this method on the contact interface between a moving train wheel and the rail track. Brunskill et al. [133] states that the elements within the array are excited individually in turn as the wheel rolls over the measurement area enabling a contact patch to be determined and used to calculated the contact pressure. However the tests were only conducted at a speed of 10 mm/s.

2.7 Digital Image Correlation

2.7.1 Static and Pseudo-static Applications

As discussed in Section 2.6.2, DIC provides analysis across whole surfaces to show continuous strain patterns on a test specimen. Baqersad et al. and Yoneyama and Murasawa [129, 134] discuss that DIC is an optical measurement technique that works by detecting displacements in a continuous pattern on a specimen surface. Baqersad et al. [129] adds that the specimen surface is prepared with a high contract random speckle pattern which is required for the post processing software. A typical set up is shown in Figure 2.7. The basic process is described by Yoneyama and Murasawa [134] stating that imaging cameras are used to take images of the specimen, one before deformation and one after. The images are then digitised and stored on a computer connected to the cameras. However, to compare the before and after deformation images, the post processing software must be able to identify matching locations on each image.

According to Yoneyama and Murasawa [134] it is not possible to match a single pixel on each image, therefore the software relies on the high-contrast random
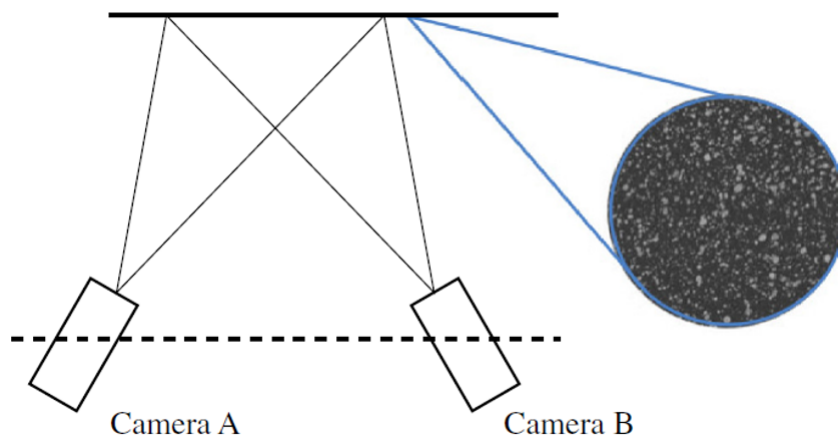
FIGURE 2.7: DIC setup with speckle pattern on test specimen [131]

speckle pattern. As shown in Figure 2.8, an area of the speckle pattern on the initial image is identified, called a subset, made up of multiple pixels. Baqersad et al. and Yoneyama and Murasawa [129, 134] state that each subset has a unique light intensity value based on the speckle pattern within it. Therefore, the speckle pattern must be random to ensure each subset has a unique light intensity. It is assumed that this light intensity does not change after deformation, enabling the same subset to be identified on the image taken after deformation. The software uses this to identify the matched subsets on each image and can then detect the displacement between them. Applying this to many subsets enables the post-processing software to produce continuous strain patterns of the whole surface in the camera's view.
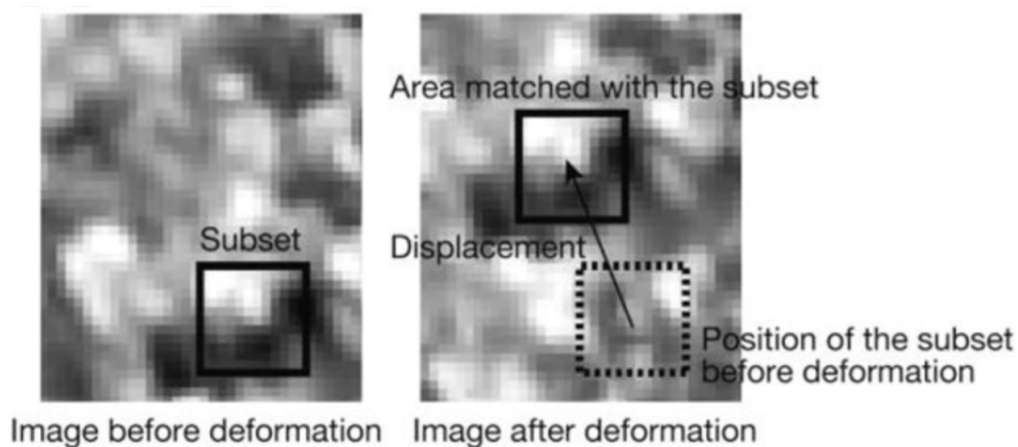
FIGURE 2.8: Matching the subset before and after deformation [134]

Tekieli et al. [135] tensile tested a wide range of materials including textiles and composites, while Bahrami et al. [136] focussed on sharp notch corners cut into their specimens. Tekieli et al. [135] stated that with the cameras 1.2 m away from the textile test specimen and images of 6015 x 4016 pixels (0.11 mm pixel size), a strain resolution of 2-3 $\mu\varepsilon$ was achieved. The average strain over the free length of the specimen was measured using DIC. For the composite specimens, the whole piece was prepared with a speckled pattern while the textile specimens had magnetic markers attached at either end already prepared with a speckled pattern. This enabled the software to use those speckle patterns to determine the strain over the whole length. Tekieli et al. [135] successfully obtained strain results from the DIC system for the textile and composite specimens and discussed a range of benefits DIC provided. Tekieli et al. [135] stated the system helped identify any slippage in the jaws of the tensile machine because the software allows the user to choose the observing area during post-processing and therefore the clamped regions can be eliminated. This aspect can also be utilised to avoid cracks to extract results that are unaffected by them. Tekieli et al. [135] also discussed how the system logged emerging cracks in the specimens by timestamping, shape, size, and location before they were visible to the naked eye. Bahrami et al. [136] investigated sharp corners cut out of their specimen and found good agreement with the FEA results. However, if the manual objective area selected was too close to the sharp corner tip, Bahrami et al. [136] stated large errors could be induced. This was believed to be due to incorrectly estimating the corner tip location. Bahrami et al. [136] discussed that when a gap of 8-12 mm was left between the corner and the objective area, the errors significantly reduced.

Medical science research has investigated uses for DIC on biological material such as human tissue. Shao et al. [137] used DIC to monitor the pulse of a human being. A speckle pattern was placed over the visible blood vessels in the wrist and the DIC successfully detected the out of plane movement caused by each pulse. Hokka et al. [138] used DIC during a heart bypass surgery to calculate the strain on the surface of the heart of the patient. However, no speckle pattern could be used as a biological compatible speckle pattern would require developing. The natural features of the heart provided enough of a contrast for Hokka et al. [138] to obtain

some strain results from the heart surface, but the whole surface could not be picked up by the DIC.

Other uses for DIC include tube bending, fatigue testing and detecting human movement. Both Shadmehri and Hoa and Corigliano et al. [139, 140] investigated tube bending with speckle patterns covering half of the tubes surface. Corigliano et al. [140] used this process to investigate fatigue testing on welded joints. Mazzoleni and Zappa [141] used DIC to estimate the acceleration of people jumping in a stadium, which could then be used to evaluate the load induced by groups of people jumping.

2.7.2 Dynamic Applications

Since DIC was first introduced in the 1970s, the range of applications throughout scientific fields has rapidly grown [139]. As discussed by Baqersad et al. [129], early DIC systems required a larger displacement on the specimen to be able to identify the change, therefore substantial research was conducted in single mode excitations. This is where the shape of an object is identified while it is being excited, replicating operational use.

Helfrick et al. [142] focussed on a dryer-cabinet panel which was hung up in front of the DIC cameras with a mechanical shaker fitted to the corner of the panel. The DIC system was used to identify the shape of the panel whilst it was being excited by the shaker. Helfrick et al. [142] verified the accuracy of the DIC by also simulating the excitation in FEA, where strong correlation between the DIC and FEA was found. However, potential limitations with the equipment were identified. During a noise-floor test, noise was identified on some of the node points and Helfrick et al. [142] pointed out this could be caused by specimen locations not being visible to both cameras, or a substandard speckle pattern in those areas. With the speckle pattern being applied manually, the speckle pattern could be difficult to keep consistent. Helfrick et al. [142] also noted that the maximum vibration speed was limited by the camera frequency, meaning expensive high frequency cameras would be required for high frequency vibration applications. This issue was also corroborated by Tekieli et al. [135]. Various other papers utilised DIC with a focus on vibrations.

Wang et al. [143] and Warren et al. [144] identified operating mode shapes of a composite panel and a base upright respectively, while Genç [145] extracted the operating shape of a wing in a wind tunnel subjected to flow induced vibrations.

In rotating applications, strobe lighting systems can be utilised to enable DIC measurements during high-speed testing. Strobe lighting illuminates the speckled pattern to make the high contrast pattern more visible to the cameras. They are typically triggered by the rotational speed of the test specimen to ensure the correct section of the specimen is illuminated.

Schmidt et al. [146] conducted two high-speed tests for a rotating automobile wheel and a flywheel with both using pulsed lighting to enable DIC measurements of the surface strain. The automobile tyres were successfully tested between 20-30 krpm while the flywheel was operated at 35 krpm. Schmidt et al. [146] stated that an 18-inch diameter flywheel at 35 krpm was well within the capability of the measuring system. The pulsed lighting was also accredited with enabling successful results at those high speeds. Schmidt et al. [146] used a trigger in both tests to activate the strobe light once per revolution, thereby syncing the strobe to the test speed to ensure the same part of the test specimen was illuminated each rotation.

Similar to the application used by Schmidt et al. [146], rotor blades were a focus of DIC dynamic tests, seen in multiple papers [147–149]. Sousa et al. and Sicard and Sirohi [147, 148] applied a speckle pattern on the blades, however they opted for constant lighting of the test specimen. It should be noted that the test speeds used by Sousa et al. and Sicard and Sirohi [147, 148] were 600-1200 rpm, which were relatively slow compared to the tests used by Schmidt et al. [146]. Rizo-Patron and Sirohi [149] also used constant lighting with a relatively low rotational speed of up to 900 rpm. Both Sousa et al. and Rizo-Patron and Sirohi [147, 149] discuss that while they manage to achieve some accurate results, their images were not completely successful. Rizo-Patron and Sirohi [149] had images suffering from blur while Sousa et al. [147] had low contrast images. Both suggest increasing lighting and the camera shutter speed to alleviate the problems identified, while Rizo-Patron and Sirohi [149] also suggest a higher contrast speckled pattern. However, Reu and Sousa et al. [150, 151] discuss the importance of strobe lighting at higher test speeds. To reduce motion blur, the exposure time on the camera needs to be reduced, but

this restricts incoming light. To overcome this problem, strobe lighting with pulses shorter than the camera exposure can be effectively used to reduce exposure time and enable the camera to gather the necessary light to produce unblurred images. Sicard and Sirohi [148] triggered the strobe light every rotation but kept the camera aperture open long enough to gather five light pulses. These pulses were then effectively combined to create a much higher contrast image.

DIC was used to visualise impact testing by Bigger et al. [152], who acknowledged the suitability of strobe lighting in their test but decide against it due to the timing complexities. The specimen was fired into a rigid anvil while the DIC was used to detect the strains during impact. High speed cameras operating at 320 kHz were required due to the launch speeds of up to 393 ms^{-1}. A speckle pattern was dotted with a marker pen onto the specimens. Bigger et al. [152] found successful results up to speeds of 250 ms^{-1} but suggested higher resolution cameras would improve the results as DIC data was lost when the specimen underwent high deformation.

2.8 Summary

After reviewing the literature detailed in this chapter, the key findings were extracted and are listed below. These findings will be used to drive the focus and decisions required for project progression.

- Permanent magnets used in HSEMs have low tensile strength and accurately predicting these stresses is critical to rotor success.
- Theoretical analysis calculations are far more efficient at calculating rotor stresses than FEA studies or experimental testing.
- GPS is the most realistic theoretical model regarding rotor behaviour, but it has rarely been explored, along with plane strain.
- Plane stress and thin cylinder theory have been substantially investigated; however, many papers do not apply the principals of either method correctly to their application.

- Theoretical analysis on three-layer compound cylinders is completely unexplored for the plane strain and GPS approaches, while it is vastly under-explored for plane stress.

- FEA must be conducted to validate theoretical hand calculations.

- 2D FEA was the most common method of analysing rotor stresses, however the use of it was never justified and the lack of details regarding the set up made results difficult to interpret and replicate.

- Axisymmetric FEA is suitable for analysing compound cylinder rotors as the cylindrical or closely packed magnets do not experience circumferential stress changes when held in compression. It also enables the exploration of axial stress changes and is far more efficient than 3D FEA.

- Experimental testing must be conducted to validate the accuracy of FEA and theoretical models.

- Experimental testing of rotor stresses was under explored and any papers that did explore them opted for a pass or fail criteria, based on a post-test inspection.

- HSEMs were the most common method of powering an experimental rotor, however they are extremely complicated and are only necessary if the focus of the experiment is the electromagnetic performance.

- Air turbines can be utilised to power an experimental rotor without the complexities of a HSEM. Existing products such as turbochargers or air motors can be adapted by attaching a rotor to the turbine shaft and introducing simple ball bearings, while still achieving high operating speeds.

- Strain gauges and dynamic photogrammetry can be used to extract test results, but they only focus on specific locations on a surface. Strain gauges have added complexities with wiring and balancing requirements at high speed.

- DIC is the ideal method of extracting results from an experimental rotor. It has low complexity with no parts in contact with the rotor and it provides analysis of a whole surface, a clear advantage over other methods. A speckle pattern is required to be applied to specimens by the user.

- DIC can measure strains on a high-speed specimen and achieve a high accuracy, but a strobe light is required. DIC also requires an unobstructed view of

the test specimen.

- To assemble a rotor with interference fits, shrink fitting via heating and or cooling is the most suitable method and avoids potential damage inflicted by the press fitting procedure, which can weaken parts.

- Alternative materials can be used to replicate a HSEM rotor when the focus of the experiment is the mechanical stresses. This avoids the complexities of using fragile sintered magnets.

- Optimisation can be applied to engineering design and allows a user to define design variables, constraints and criteria which are then used to identify a set of optimal designs.

- There are many optimisation approaches available, including the weighting of criteria or assigning goals to criteria depending on the task. They can often be limited by aspects such as the number of solutions produced, the range of solutions or by the user input into weightings.

- Optimisation problems often require multiple criteria. MCEAs provide a method of converging to a pareto front with a large number and range of solutions, with NSGA II being one of the most popular methods. MatLab has successfully been used to run many MCEAs.

3 Closed Form Analysis

Introduction

3.1 Introduction

Based on the key findings from Section 2.8, this chapter will explore the theoretical fundamentals of compound cylinder stress analysis. Comparisons will then be drawn between the generalised plane strain (GPS), plane strain, and plane stress theories for two-cylinder rotors due to the lack of exploration previously identified. Much of the presented work in this chapter has previously been published by the research team: The initial development of the two-cylinder generalised plane strain theory was first presented by Barrans et al. [10] and then further expanded upon by Barrans and Mallin [153]. This chapter continues the expansion of that work through wider comparisons between the developed theories.

3.2 Single Cylinder Analysis

3.2.1 Theoretical Fundamentals

As discussed in Section 2.2.6.2, using theoretical calculations to predict rotor stresses is far more efficient than using finite element analysis (FEA) simulations. This is especially true for interfering surfaces of surface-mounted permanent magnet (SPM) rotors where a fine mesh and longer computing time would be required by FEA. With theoretical calculations, many rotor topologies can be simulated simultaneously while FEA would require remodelling and remeshing for each topology. Figure 3.1 shows a typical SPM rotor. As stated in Section 1.1.2, the permanent magnets have low tensile strength and are required to remain in compression in a rotor assembly, achieved via an interference fit between the magnets and sleeve. This can create interference pressure at both magnet surfaces. Therefore, a stress prediction
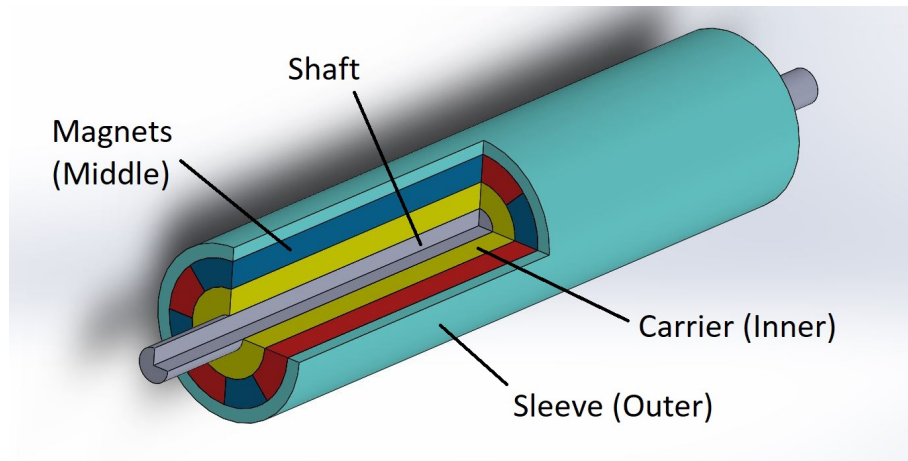
FIGURE 3.1: SPM rotor components [154]

model for three rotor bodies is required. As discussed in Section 2.2.6.2 none of the papers investigated included residual stresses due to manufacturing into their analytical models. Therefore this effect will not be explored, enabling representative comparisons to be made.

Section 2.2 identifies that current literature only explores two-cylinder bodies for plane stress, plane strain and generalised plane strain (GPS) methodologies. As a steppingstone to the development of the three-cylinder stress analysis, the two-cylinder analyses will be compared to explore the differences between them. This will identify differences between the analyses and highlight which ones are most suited to further development to accommodate three-cylinders.

To derive the stress equations, the sleeve can be modelled as a cylinder subject to an internal pressure, caused by the interference fit with the magnets. Modelling the sleeve as a thin-walled cylinder is one of the simplest approaches to SPM rotor mechanical design, as used by papers discussed in Section 2.2.5. The thin-walled cylinder approximation assumes that there is no circumferential stress variation throughout the sleeve thickness therefore, only a single value for it is produced. Figure 3.2 represents a segment of a sleeve under internal pressure where the dotted outline indicates the original sleeve size before any pressure effects.

In Figure 3.2, R is the initial sleeve radius and t is the sleeve thickness. δ, is the radial interference between the magnets and the sleeve, causing the increase in the sleeve radius. The shaft and all rotor bodies apart from the sleeve are assumed to
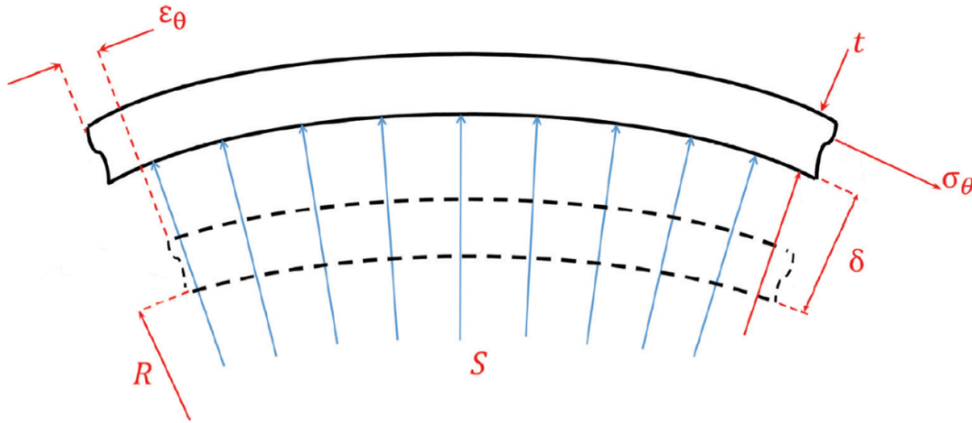
FIGURE 3.2: SPM rotor sleeve with internal pressure, adapted from
Barrans and Mallin [153]

be rigid, so all deformation takes place in the sleeve. The interference generates an interference pressure, S, between the magnets and the sleeve while a circumferential strain and stress are generated in the sleeve.

Due to circumference being directly proportional to the radius, equation 3.1 can be used for the circumferential strain. Using Hooke's law, equation 3.2 is generated considering radial stress is excluded from thin-walled cylinder calculations and axial stress is zero due to rotor cylinders having no end cap. Equation 3.3 shows the relationship between $\varepsilon\theta$, $\sigma\theta$, and S.

$$\varepsilon_\theta = \frac{\delta}{R} \tag{3.1}$$

$$\sigma_\theta = E\varepsilon_\theta = E\frac{\delta}{R} \tag{3.2}$$

$$S = \frac{\sigma_\theta t}{R} = \frac{E\delta t}{R^2} \tag{3.3}$$

These equations are suitable when the rotor is stationary. When the rotor is rotating, the additional loads due to the body forces cause the geometry of the rotor bodies to change, altering the interference level and therefore the interference pressure. This generates errors in the results if the equations are used under rotating operating conditions.

Figure 3.3 shows the approximate error relating to the sleeve thickness and sleeve diameter. As the approach assumes the cylinder is thin enough to have a constant
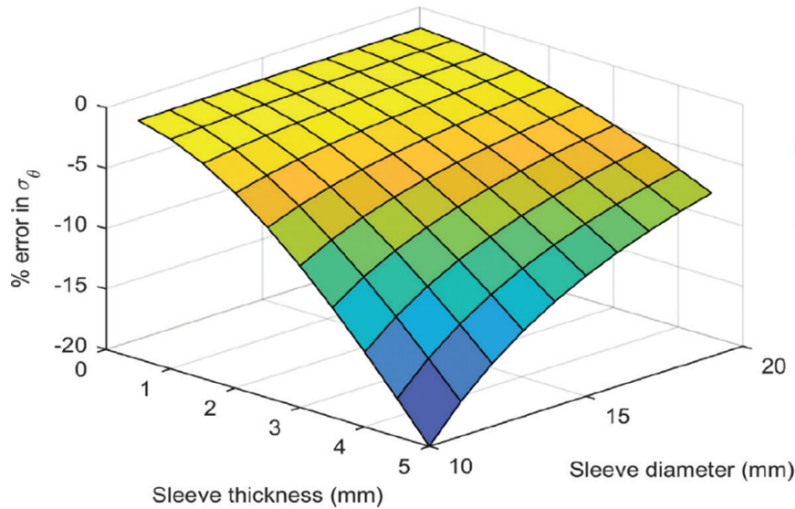
FIGURE 3.3: Approximate error induced via the thin cylinder assumption [153]

circumferential strain and stress through the wall thickness, then increasingly large errors are induced as thicker rotor cylinders are used. The approximate error increases as the sleeve thickness increases and the sleeve diameter reduces, increasing the diameter to thickness ratio.

Thick-walled cylinder approaches correctly assume the stress can vary throughout the wall thickness of the cylinder. They are built on the principles of force equilibrium and the relationship between stress and strain. Figure 3.4 shows an element
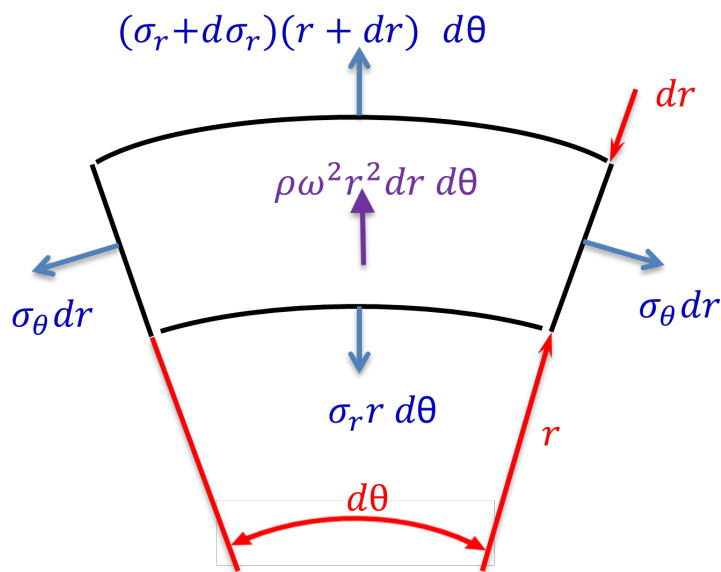
FIGURE 3.4: Stresses in a rotating cylinder or disc element, adapted from Barrans and Mallin [153] and Hearn [155]

in a rotating cylinder or disk, which applies to any SPM rotor body. The element is 2D and perpendicular to the axis. Fenner and Reddy [156] states the equation derivation below is only suitable for axisymmetric problems, which is true for rotors under a compressive stress due to interference.

In Figure 3.4, the element has a radial position r, thickness dr, density ρ, and a segment angle $d\theta$. It is under a rotation speed ω which induces circumferential stresses and radial stresses. In a SPM rotor, circumferential and radial stresses are also generated due to the interference between the rotor bodies. Considering the element must be in equilibrium then the radial equilibrium equation 3.4 is given by Hearn [155], which simplifies to equation 3.5.

$$2\sigma_\theta \, dr \, sin\frac{d\theta}{2} + \sigma_r rd\,\theta - (\sigma_r + d\sigma_r)(r+dr)d\theta = \rho r^2 \omega^2 d\theta \, dr \tag{3.4}$$

$$\sigma_\theta - \sigma_r - r\frac{d\sigma_r}{dr} = \rho\omega^2 r^2 \tag{3.5}$$

Figure 3.5 shows the radial changes of the element geometry due to the internal stresses from equation 3.5.
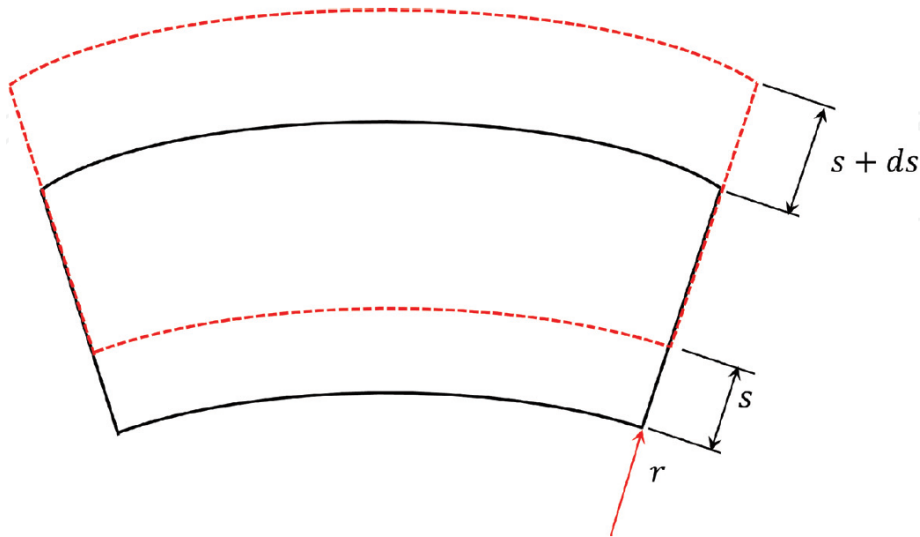
FIGURE 3.5: Change in radial dimensions of the element [153]

In Figure 3.5, s is the change in the radius, and ds is the change in element thickness. As described for equation 3.1 the inner radial strain can be equated to the circumferential strain, while the change in element thickness is the radial strain. Axial strain will also be present in rotors. The radial, circumferential, and axial strain

equations are given in equations 3.6, 3.7, and 3.8 respectively, where α is the coefficient of thermal expansion, and ΔT is the change in temperature of the material.

$$\varepsilon_r = \frac{ds}{dr} = \frac{1}{E}(\sigma_r - \nu\sigma_\theta - \nu\sigma_z) + \Delta T\alpha \tag{3.6}$$

$$\varepsilon_\theta = \frac{s}{r} = \frac{1}{E}(\sigma_\theta - \nu\sigma_r - \nu\sigma_z) + \Delta T\alpha \tag{3.7}$$

$$\varepsilon_z = \frac{1}{E}(\sigma_z - \nu\sigma_r - \nu\sigma_\theta) + \Delta T\alpha \tag{3.8}$$

Equation 3.9 shows the relationship between radial and circumferential strain mentioned above. Inserting equations 3.6 and 3.7 into equation 3.9, produces equation 3.10, assuming that the temperature is constant throughout the wall thickness.

$$\frac{d(r\varepsilon_\theta)}{dr} = \frac{ds}{dr} = \varepsilon_r \tag{3.9}$$

$$(\sigma_r - \sigma_\theta)(1 + \nu) = r\left[\frac{d\sigma_\theta}{dr} - \nu\left(\frac{d\sigma_r}{dr} + \frac{d\sigma_z}{dr}\right)\right] + E\alpha r\frac{d\Delta T}{dr} \tag{3.10}$$

Assuming that $d\Delta T/dr = 0$, equation 3.10 can then be combined with the equilibrium equation 3.5 to provide equation 3.11, which incorporates both the equilibrium and strain relationships of the element. Equation 3.11 is common to all following analytical approaches, but the paths diverge upon further development.

$$\frac{d\sigma_r}{dr} + \frac{d\sigma_\theta}{dr} - \nu\frac{d\sigma_z}{dr} = -(1 + \nu)\rho r\omega^2 \tag{3.11}$$

3.2.2 Plane Stress

Plane stress is the simplest and most common theoretical approach to thick-walled cylinder stress approximation. As discussed in Section 2.2.1, the plane stress approach assumes there is no axial stress present in the rotor and is therefore suitable for short rotors or disks. As stated by Mallin and Barrans [154], in a thin disk the resistance to change in thickness (the axial dimension) is insignificant. Hence, axial stress, σ_z, cannot be generated due to rotation or pressure (e.g. due to interference) and is assumed to be zero. Removing the axial stress from equation 3.11 produces equation 3.12.

$$\frac{d\sigma_r}{dr} + \frac{d\sigma_\theta}{dr} = -(1+v)\rho r\omega^2 \tag{3.12}$$

Hearn [155] shows that equation 3.12 can then be integrated to give:

$$\sigma_\theta + \sigma_r = -\frac{(1+v)\rho\omega^2 r^2}{2} + 2A \tag{3.13}$$

Where $2A$ is a convenient constant of integration [155]. Reintroducing equilibrium equation 3.5 and a further integration allows the separate radial and circumferential equations to be derived.

$$\sigma_r = A - \frac{B}{r^2} - \frac{3+v}{8}\rho\omega^2 r^2 \tag{3.14}$$

$$\sigma_\theta = A + \frac{B}{r^2} - \frac{1+3v}{8}\rho\omega^2 r^2 \tag{3.15}$$

Where $-B$ is another constant of integration [155].

Equations 3.14 and 3.15 provide the starting points to calculating rotor stresses using the plane stress assumption. However, as discussed in Section 2.2.2, axial loads will be present during rotation and therefore, ignoring these stresses may lead to unreliable results when using the plane stress method.

3.2.3 Plane Strain

As discussed in Section 2.2.1, the plane strain approach assumes that there is no axial strain within the rotor, which has led to the method being used for long rotors. This modelling approach is used less frequently, as discussed by Mallin and Barrans [28], and is more complex than plane stress as axial stress will not be zero. However, the assumption that axial strain is zero enables a simplified equation for axial stress. If axial strain is assumed to be zero, then $d\varepsilon_z/dr = 0$. Therefore, differentiating equation 3.8, while still assuming the temperature is constant throughout the wall thickness of the rotor, produces equation 3.16.

$$\frac{d\sigma_z}{dr} = v\left(\frac{d\sigma_r}{dr} + \frac{d\sigma_\theta}{dr}\right) \tag{3.16}$$

Introducing equation 3.16 into equation 3.11 gives:

$$\left(\frac{d\sigma_r}{dr} + \frac{d\sigma_\theta}{dr} \right) = -\frac{\rho r \omega^2}{1 - \nu}$$ (3.17)

Following the procedure shown in Section 3.2.2, the radial and circumferential stress equations for the plane strain method can be derived. Integrating equation 3.17 and introducing the equilibrium equation 3.5, followed by a further integration produces equations 3.18 and 3.19. A and B are the constants of integration.

$$\sigma_r = A - \frac{B}{r^2} - \frac{3 - 2\nu}{8(1 - \nu)} \rho \omega^2 r^2$$ (3.18)

$$\sigma_\theta = A + \frac{B}{r^2} - \frac{1 + 2\nu}{8(1 - \nu)} \rho \omega^2 r^2$$ (3.19)

For the plane strain approach, an axial stress equation is also required and can be derived by equating equation 3.8 to zero, producing:

$$\sigma_z = \nu(\sigma_r + \sigma_\theta) - E\Delta T \alpha$$ (3.20)

Including the axial stress enables the circumferential strain (equation 3.7) and therefore the change in interference during rotation, to be calculated. This is an important inclusion when investigating the accuracy of each method. Barrans and Mallin [153] show how the accuracy of the critical results is severely affected if the interference is not updated with the centrifugal forces produced during rotation, shown in Figure 3.6. As discussed by Barrans and Mallin [153], the critical results in
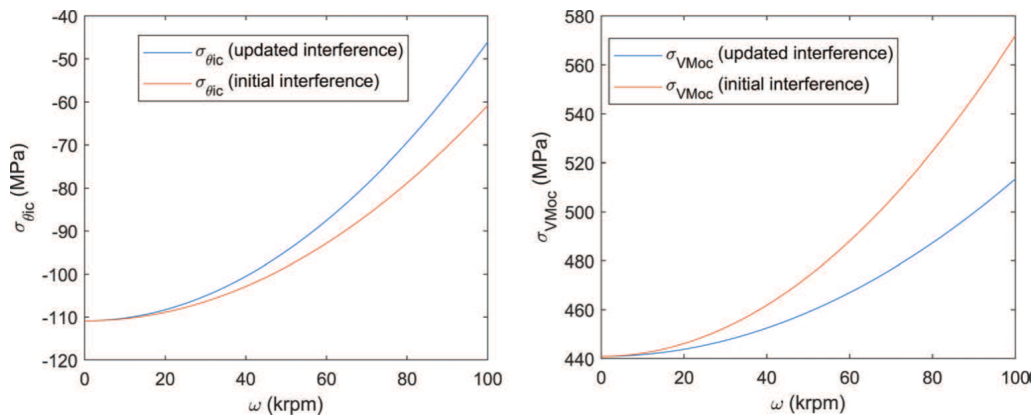
FIGURE 3.6: Effect of critical stresses without updating interference [153]

a two-cylinder rotor are the circumferential stress at the outer surface of the magnets, $\sigma_{\theta ic}$, and the Von Mises stress at the inner surface of the sleeve, σ_{VMoc}. As the rotor speed increases, the induced error in the critical stresses increases. The difference is significant for both the circumferential stress and Von Mises stress; however, it is more severe for the Von Mises stress.

Equations 3.18, 3.19, and 3.20 provide the starting points of calculating rotor stresses using the plane strain assumption. However, as discussed in Section 2.2.1, the plane strain assumption is unrealistic as no structure has a sufficiently great stiffness to be considered rigid to achieve zero axial strain. Therefore, any presence of axial strain may induce errors into the results.

3.2.4 Generalised Plane Strain

As discussed in Section 2.2.1 and by Mallin and Barrans [154], GPS assumes axial stress is present and axial strain does not vary with respect to radial or circumferential position, and is therefore constant through the wall of the cylinder. It is also assumed that there is a high enough level of friction between the cylinders to avoid slip. Due to the assumptions, equation 3.16 is still valid for the GPS approach as differentiating zero and a constant value both result in zero. Therefore, the radial and circumferential stress equations are equations 3.18 and 3.19, respectively. However, as axial strain is not zero, equation 3.20 is not valid to calculate axial stress. To derive the axial stress equation, equation 3.16 can be combined with equation 3.11, to maintain the equilibrium and strain relationships which produces equation 3.21.

$$\frac{d\sigma_z}{dr} = \frac{-rv\rho\omega^2}{1-v} \tag{3.21}$$

Integrating this then produces the following axial stress equation, where C is a constant of integration.

$$\sigma_z = \frac{-r^2 v\rho\omega^2}{2(1-v)} + C \tag{3.22}$$

Equations 3.18, 3.19 and 3.22 provide the radial, circumferential, and axial stress

equations to enables rotor stresses to be calculated using the GPS approach. However, they all contain constants of integration which need to be identified and eliminated to produce complete stress equations.

For single cylinders there are no stresses due to interference, therefore only stresses due to rotation require calculation. The boundary constraints listed below are used to determine constants A and B from equations 3.18 and 3.19, enabling the circumferential and radial stress equations to be identified.

$$\text{When} \quad r = R_o; \quad \sigma_{ro} = 0$$

$$r = R_i; \quad \sigma_{ri} = 0$$

Where σ_{ri} and σ_{ro} represent the radial stress at the inner radius, R_i, and outer radius, R_o, respectively.

By substituting the boundary conditions into equation 3.18, A and B are identified as:

$$A = \frac{3 - 2v_i}{8(1 - v_i)} \rho_i \omega^2 (R_c^2 + R_i^2) \tag{3.23}$$

$$B = \frac{3 - 2v_i}{8(1 - v_i)} \rho_i \omega^2 R_c^2 R_i^2 \tag{3.24}$$

Substituting constants A and B back into equations 3.18 and 3.19 eliminates the constants from the equations and produces the radial and circumferential stress equations shown below.

$$\sigma_{ri} = \frac{3 - 2v_i}{8(1 - v_i)} \rho_i \omega^2 \left(R_c^2 + R_i^2 - \frac{R_c^2 R_i^2}{r^2} - r^2 \right) \tag{3.25}$$

$$\sigma_{\theta i} = \frac{\rho_i \omega^2}{8(1 - v_i)} \left[(3 - 2v_i) \left(R_c^2 + R_i^2 + \frac{R_c^2 R_i^2}{r^2} \right) - (1 + 2v_i) r^2 \right] \tag{3.26}$$

To eliminate the constant in the axial stress equation, axial forces in the cylinder are utilised. Assuming that an external axial force acts on the cylinder, there must be equilibrium with the internal axial force, expressed as equation 3.27. The external axial force, F_z, is calculated by integrating the axial stress through the cylinder cross section.

$$F_z = 2\pi \int_{R_o}^{R_i} r \sigma_z \, dr \tag{3.27}$$

By substituting equation 3.22 into equation 3.27, constant C can be determined when carrying out the integration, shown below.

$$C = \frac{F_z}{\pi(R_o^2 - R_i^2)} + \frac{\nu\rho\omega^2}{4(1-\nu)}(R_o^2 + R_i^2) \tag{3.28}$$

Substituting constant C back into equation 3.22 enables C to be eliminated and the axial stress equation to be determined, given in equation 3.29.

$$\sigma_z = \frac{F_z}{\pi(R_o^2 - R_i^2)} + \frac{\nu\rho\omega^2}{4(1-\nu)}(R_o^2 + R_i^2 - 2r^2) \tag{3.29}$$

As discussed in Section 2.2.1, this approach is the most realistic of the three described approaches as axial strain is constant for most of the rotor length. However, the changes at the rotor ends may cause errors with this method if it is applied to short rotors.

3.3 Two Cylinder Closed Form Analysis

3.3.1 Generalised Plane Strain Theory Development

Figure 3.7 shows a two-cylinder rotor with an interference fit. A common radius, R_c, must be achieved between the inner surface of the outer cylinder, R_{co}, and the outer surface of the inner cylinder, R_{ci}, generating a shrinkage pressure, S.
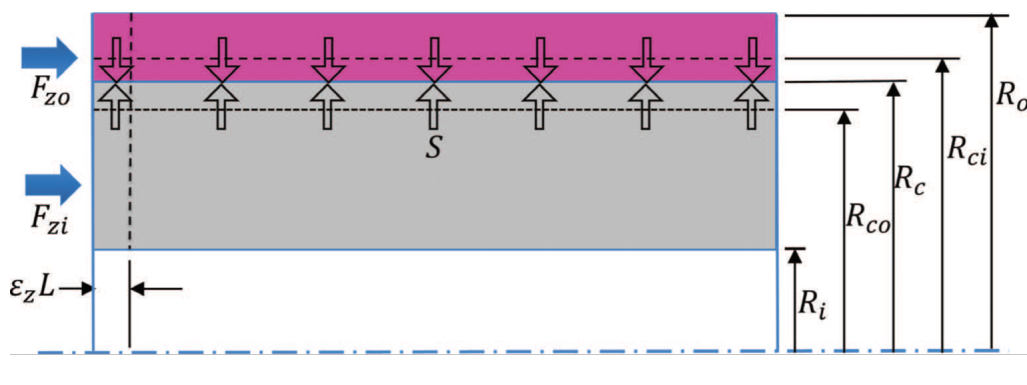
FIGURE 3.7: Boundary notations and interference conditions on a two-cylinder rotor [153]

In Figure 3.7, F_{zo} is the external force acting on the outer cylinder with an outer radius R_o, and F_{zi} is the external force acting on the inner cylinder with an inner

radius R_i. $\varepsilon_z L$ is the change in axial length and is the product of axial strain, ε_z, and the rotor length, L.

To calculate the stresses generated during operation, the following boundary conditions are used.

$$\text{Inner cylinder: When} \quad r = R_i; \quad \sigma_{rii} = 0$$

$$r = R_c; \quad \sigma_{ric} = -S$$

$$\text{Outer cylinder: When} \quad r = R_o; \quad \sigma_{roo} = 0$$

$$r = R_c; \quad \sigma_{roc} = -S$$

Where σ_{rii} is the radial stress at the inner radius of the inner cylinder, σ_{ric} is the radial stress at the common radius of the inner cylinder, σ_{roo} is the radial stress at the outer radius of the outer cylinder, and σ_{roc} is the radial stress at the common radius of the outer cylinder.

For the plane stress and plane strain approaches, the stresses due to interference and rotation can be calculated separately and summed together. Using the boundary conditions above, the stresses due to interference are calculated, while the following boundary conditions are used to calculate the stresses due to rotation.

$$\text{Inner cylinder: When} \quad r = R_i; \quad \sigma_{rii} = 0$$

$$r = R_c; \quad \sigma_{ric} = 0$$

$$\text{Outer cylinder: When} \quad r = R_o; \quad \sigma_{roo} = 0$$

$$r = R_c; \quad \sigma_{roc} = 0$$

For the plane stress approach, each set of boundary conditions can be substituted into equations 3.14 and 3.15, while equations 3.18 and 3.19 are used for the plane strain approach. This allows the constants of integration and thus the shrinkage pressure to be found, enabling the calculation of the radial and circumferential stresses. These can then be used to calculate the axial stress for the plane strain case.

As demonstrated in Section 3.2.4, the axial stress equations for the GPS approach introduce the use of internal and external axial forces, highlighted in Figure 3.7. Barrans [10] states that the GPS approach requires the stresses due to rotation and

interference to be calculated simultaneously. Therefore, the first set of boundary conditions including the shrinkage pressure must be used to derive the stress equations. For demonstration purposes, the inner cylinder will be used to demonstrate the deriving process using the notations used in Figure 3.7. The boundary conditions used are shown below.

$$\text{Inner cylinder: When} \quad r = R_i; \quad \sigma_{rii} = 0$$

$$r = R_c; \quad \sigma_{ric} = -S$$

Substituting the boundary conditions in equation 3.18 enables the constants A and B to be identified.

$$A = \frac{SR_c^2}{R_i^2 - R_c^2} + \frac{3 - 2v_i}{8(1 - v_i)}\rho_i\omega^2(R_c^2 + R_i^2) \tag{3.30}$$

$$B = \frac{SR_c^2 R_i^2}{R_i^2 - R_c^2} + \frac{3 - 2v_i}{8(1 - v_i)}\rho_i\omega^2 R_c^2 R_i^2 \tag{3.31}$$

Where v_i and ρ_i are the Poisson's ratio and density for the inner cylinder material. Substituting the constants, A and B, into equations 3.18 and 3.19 derives the radial and circumferential stress equations for the inner cylinder, taking into account interference and rotation. Equations 3.32 and 3.33 show the radial and circumferential stress equations, respectively.

$$\sigma_{ri} = \frac{SR_c^2}{(R_i^2 - R_c^2)}\left(1 - \frac{R_i^2}{r^2}\right) + \frac{3 - 2v_i}{8(1 - v_i)}\rho_i\omega^2\left(R_c^2 + R_i^2 - \frac{R_c^2 R_i^2}{r^2} - r^2\right) \tag{3.32}$$

$$\sigma_{\theta i} = \frac{SR_c^2}{(R_i^2 - R_c^2)}\left(1 + \frac{R_i^2}{r^2}\right) + \frac{\rho_i\omega^2}{8(1 - v_i)}\left[(3 - 2v_i)\left(R_c^2 + R_i^2 + \frac{R_c^2 R_i^2}{r^2}\right) - (1 + 2v_i)r^2\right] \tag{3.33}$$

The axial stress remains the same as shown in equation 3.29, however the notations are updated to ensure the equations contents are related to the inner cylinder, shown in equation 3.34.

$$\sigma_{zi} = \frac{F_{zi}}{\pi(R_c^2 - R_i^2)} + \frac{v_i\rho_i\omega^2}{4(1 - v_i)}(R_c^2 + R_i^2 - 2r^2) \tag{3.34}$$

According to Barrans and Mallin [153] two equilibrium and two compatibility

conditions, shown below, must be considered for a two-cylinder rotor using the GPS approach.

A. At the interface between the cylinders, there must be force equilibrium in the radial direction.

B. At the interface between the cylinders, there must be circumferential strain compatibility, written as:

$$R_{ci}(1 + \varepsilon_{\theta ic}) = R_{co}(1 + \varepsilon_{\theta oc}) \tag{3.35}$$

Where R_{ci} and R_{co} are the original radii of the interfering surfaces of the inner and outer cylinders, while $\varepsilon_{\theta ic}$ and $\varepsilon_{\theta oc}$ are the circumferential strains of those surfaces, respectively.

C. Assuming sufficient friction, there must be axial strain compatibility between both cylinders. This can be written as:

$$\varepsilon_{zi} = \varepsilon_{zo} \tag{3.36}$$

Where ε_{zi} and ε_{zo} are the axial strains of the inner and outer cylinders, respectively.

D. There must be axial force equilibrium between the two cylinders due to the assumption of there being enough friction to avoid slip. Referencing Figure 3.7, this can be written as:

$$F_{zi} = F_{zo} \tag{3.37}$$

Condition A is satisfied with the use of shrinkage pressure, S, in the boundary constraints used to derive equations 3.32 and 3.33. Conditions B is satisfied by calculating the circumferential strain equations for $\varepsilon_{\theta ic}$ and $\varepsilon_{\theta oc}$ and substituting them into equation 3.35. Substituting the stress equations 3.32, 3.33, and 3.34 into Hooke's law equation 3.7 enables the circumferential strain to be calculated, shown in equation 3.38 for the inner cylinder.

$$\varepsilon_{\theta ic} = \frac{-S\pi \left(R_c^2(1 - \nu_i) + R_i^2(1 + \nu_i) \right) - \nu_i F_{zi}}{E_i \pi (R_c^2 - R_i^2)} \\ + \frac{\rho_i \omega^2}{4E_i(1 - \nu_i)} \left(R_c^2 + 3R_i^2 - 2\nu_i(R_c^2 + R_i^2) - \nu_i^2(R_i^2 - R_c^2) \right) + \Delta_T \alpha_i \tag{3.38}$$

To apply condition C, the axial strain equations for ε_{zi} and ε_{zo} are derived by substituting the stress equations 3.32, 3.33, and 3.34 into Hooke's law equation 3.8. For the inner cylinder, this produces equation 3.39.

$$\varepsilon_{zi} = \frac{1}{E_i}\left(\frac{F_{zi}}{\pi(R_c^2 - R_i^2)} - \frac{2S\nu_i R_c^2}{R_i^2 - R_c^2} - \frac{\nu_i \rho_i \omega^2(R_c^2 + R_i^2)}{2} \right) + \Delta_T \alpha_i \tag{3.39}$$

Condition D is implemented by applying equation 3.37 to equations 3.38 and 3.39, producing equations 3.40 and 3.41 shown below.

$$\varepsilon_{\theta ic} = \frac{-S\pi\left(R_c^2(1 - \nu_i) + R_i^2(1 + \nu_i) \right) + \nu_i F_{zo}}{E_i \pi(R_c^2 - R_i^2)}$$
$$+ \frac{\rho_i \omega^2}{4E_i(1 - \nu_i)}\left(R_c^2 + 3R_i^2 - 2\nu_i(R_c^2 + R_i^2) - \nu_i^2(R_i^2 - R_c^2) \right) + \Delta_T \alpha_i \tag{3.40}$$

$$\varepsilon_{zi} = \frac{1}{E_i}\left(\frac{-F_{zo}}{\pi(R_c^2 - R_i^2)} - \frac{2S\nu_i R_c^2}{R_i^2 - R_c^2} - \frac{\nu_i \rho_i \omega^2(R_c^2 + R_i^2)}{2} \right) + \Delta_T \alpha_i \tag{3.41}$$

By repeating the process for the outer cylinder and substituting the circumferential strain equations into equation 3.35 from condition B, equation 3.42 is produced. Substituting the axial strain equations into equation 3.36 from condition C, produces equation 3.43

$$\frac{F_{zo}}{\pi}\left(R_{ci}E_o\nu_i(R_o^2 - R_c^2) + R_{co}E_i\nu_o(R_c^2 - R_i^2) \right)$$
$$- S\left[R_{ci}E_o(R_o^2 - R_c^2)\left(R_c^2(1 - \nu_i) + R_i^2(1 + \nu_i) \right) \right.$$
$$\left. + R_{co}E_i(R_c^2 - R_i^2)\left(R_o^2(1 + \nu_o) + R_c^2(1 - \nu_o) \right) \right]$$
$$= (R_c^2 - R_i^2)(R_o^2 - R_c^2)\left[E_o E_i\left(R_{co} - R_{ci} + T(\alpha_o R_{co} - \alpha_i R_{ci}) \right) \right.$$
$$+ \frac{R_{co}E_i\rho_o\omega^2}{4(1 - \nu_o)}\left(R_c^2 + 3R_o^2 - 2\nu_o(R_o^2 + R_c^2) - \nu_o^2(R_o^2 - R_c^2) \right)$$
$$\left. - \frac{R_{ci}E_o\rho_i\omega^2}{4(1 - \nu_i)}\left(R_c^2 + 3R_i^2 - 2\nu_i(R_c^2 + R_i^2) - \nu_i^2(R_i^2 - R_c^2) \right) \right] \tag{3.42}$$

$$\frac{F_{zo}}{\pi}\left(E_i(R_i^2 - R_c^2) - E_o(R_o^2 - R_c^2) \right) - 2SR_c^2\left(E_i\nu_o(R_i^2 - R_c^2) - E_o\nu_i(R_o^2 - R_c^2) \right)$$
$$= (R_o^2 - R_c^2)(R_i^2 - R_c^2)\left[\frac{\omega^2}{2}\left(\nu_o E_i\rho_o(R_c^2 + R_o^2) - \nu_i E_o\rho_i(R_c^2 + R_i^2) \right) + T(\alpha_i - \alpha_o)E_i E_o \right] \tag{3.43}$$

By applying the four conditions, equations 3.42 and 3.43 show that the GPS approach leaves two unknowns, F_{zo} and S, to calculate simultaneously. Equations 3.42 and 3.43 can be written as:

$$\begin{bmatrix} U & V \\ X & Y \end{bmatrix} \begin{bmatrix} F_{zo} \\ S \end{bmatrix} = \begin{bmatrix} W \\ Z \end{bmatrix} \tag{3.44}$$

Where:

$$U = \frac{1}{\pi} \left(E_i(R_i^2 - R_c^2) - E_o(R_o^2 - R_c^2) \right) \tag{3.45}$$

$$V = -2R_c^2 \left(E_i \nu_o(R_i^2 - R_c^2) - E_o \nu_i(R_o^2 - R_c^2) \right) \tag{3.46}$$

$$W = (R_o^2 - R_c^2)(R_i^2 - R_c^2)\left[\frac{\omega^2}{2}\left(\nu_o E_i \rho_o(R_c^2 + R_o^2) - \nu_i E_o \rho_i(R_c^2 + R_i^2) \right) + T(\alpha_i - \alpha_o)E_i E_o \right] \tag{3.47}$$

$$X = \frac{1}{\pi}\left(R_{ci}E_o\nu_i(R_o^2 - R_c^2) + R_{co}E_i\nu_o(R_c^2 - R_i^2) \right) \tag{3.48}$$

$$\begin{aligned} Y = -&\left[R_{ci}E_o(R_o^2 - R_c^2)\left(R_c^2(1-\nu_i) + R_i^2(1+\nu_i) \right) \right. \\ &\left. + R_{co}E_i(R_c^2 - R_i^2)\left(R_o^2(1+\nu_o) + R_c^2(1-\nu_o) \right) \right] \end{aligned} \tag{3.49}$$

$$\begin{aligned} Z = &(R_c^2 - R_i^2)(R_o^2 - R_c^2)\left[E_o E_i \left(R_{co} - R_{ci} + T(\alpha_o R_{co} - \alpha_i R_{ci}) \right) \right. \\ &+ \frac{R_{co}E_i\rho_o\omega^2}{4(1-\nu_o)}\left(R_c^2 + 3R_o^2 - 2\nu_o(R_o^2 + R_c^2) - \nu_o^2(R_o^2 - R_c^2) \right) \\ &\left. - \frac{R_{ci}E_o\rho_i\omega^2}{4(1-\nu_i)}\left(R_c^2 + 3R_i^2 - 2\nu_i(R_c^2 + R_i^2) - \nu_i^2(R_i^2 - R_c^2) \right) \right] \end{aligned} \tag{3.50}$$

By using equations 3.44 - 3.50, F_{zo} and S can be calculated and substituted into the radial, circumferential, and axial stress equations to determine the rotor stresses.

3.3.2 Model Parameters and Focus

To compare the plane stress, plane strain and GPS models, the equations for the three different approaches were input into MatLab, shown in Appendix A, to generate a code that enabled efficient simulation of rotor topologies. The parameters shown in Table 3.1 were used to explore a variety of rotor topologies. As stated by Barrans and Mallin [153], the material properties are typical of samarium cobalt magnets and an

Parameter	Value
Magnet inner radius, R_i, (mm)	$4 - 8$
Common radius, R_c, (mm)	$13.95 - 14$
Interference (mm)	$0 - 0.1$
Sleeve thickness (mm)	$0 - 10$
Rotor speed, ω, $(krpm)$	$0 - 100$
Magnet Poisson's ratio, ν_i	0.27
Sleeve Poisson's ratio, ν_o	0.284
Magnet Density, ρ_i, (kg/m^3)	8400
Sleeve Density, ρ_o, (kg/m^3)	8220
Magnet Young's Modulus, E_i, (GPa)	150
Sleeve Young's Modulus, E_o, (GPa)	205

TABLE 3.1: Two-cylinder rotor parameters [153]

Inconel sleeve. The magnet inner radius was set at 6 mm for this example and the effects of temperature were not explored at this stage.

Figure 3.8 shows the behaviour of circumferential stress at the magnet outer surface, $\sigma_{\theta ic}$, with respect to the interference and sleeve thickness. The circumferential stress at the magnet outer surface is compressive at a large interference and large sleeve thickness. This is required as the magnets have low tensile strength and must be held in compression to avoid failure, as discussed in Section 1.1.2. The circumferential stress becomes tensile if the interference or sleeve thickness become too small. As this would cause a rotor failure, this stress is critical to rotor design and must be accurately predicted. For segmented magnets, this stress is still critical as without
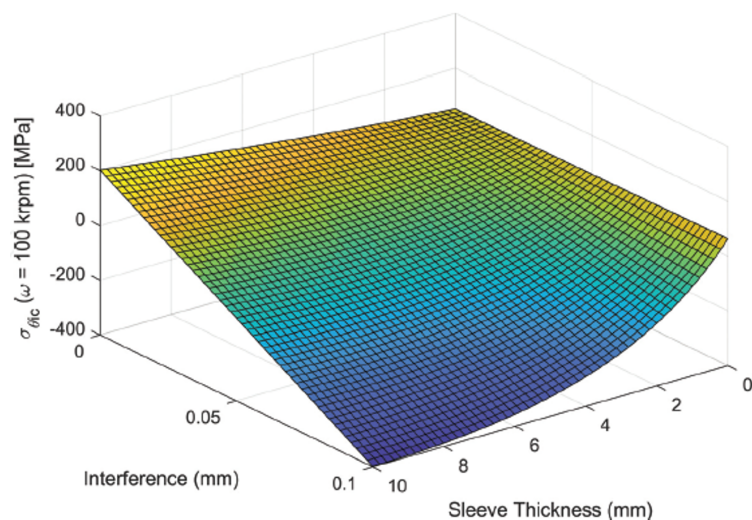
FIGURE 3.8: Circumferential stress at the magnet outer surface at 100 krpm [153].

compression, magnet separation will occur and cause the sleeve to fail.

Figure 3.9 shows the behaviour of the Von Mises stress at the inner surface of the sleeve, σ_{VMoc}, with respect to the interference and sleeve thickness. The stress rises rapidly as the interference is increased, while increasing the sleeve thickness reduces the stress. This stress is critical to rotor design as the sleeve will fail if the material yield stress limit is exceeded, causing a complete rotor failure while the compression on the magnets would also be lost. The critical nature of the stresses explored in Figures 3.8 and 3.9 means they require accurate prediction and will therefore be the focus of the comparison between the three stress prediction models.
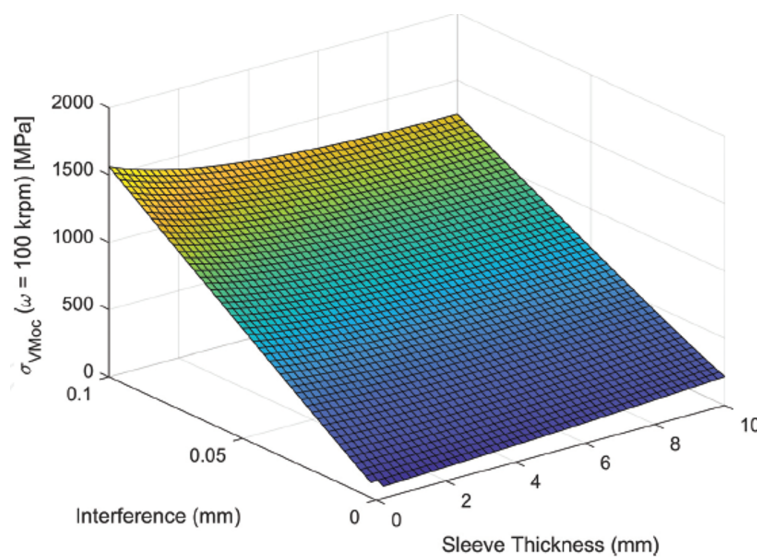
FIGURE 3.9: Von Mises stress at the inner surface of the sleeve at 100 krpm [153].

3.3.3 Comparison of Plane Stress and Plane Strain Models

Figures 3.10 and 3.11 show the percentage difference between the plane stress and plane strain models for the circumferential and Von Mises stresses discussed in Section 3.3.2, when the rotor is stationary and at maximum speed. The magnet inner radius was set to 4 mm.

Figure 3.10 shows the difference between the plane stress and plane strain is not excessive when stationary, increasing marginally as the sleeve thickness increases,

while the interference has minimal impact on the difference between the two models. However, when the rotor is at speed, larger differences occur. Where the circumferential stress values tend to zero, the percentage differences approach infinity and have therefore been removed from the graph to remove the unrealistic distortion
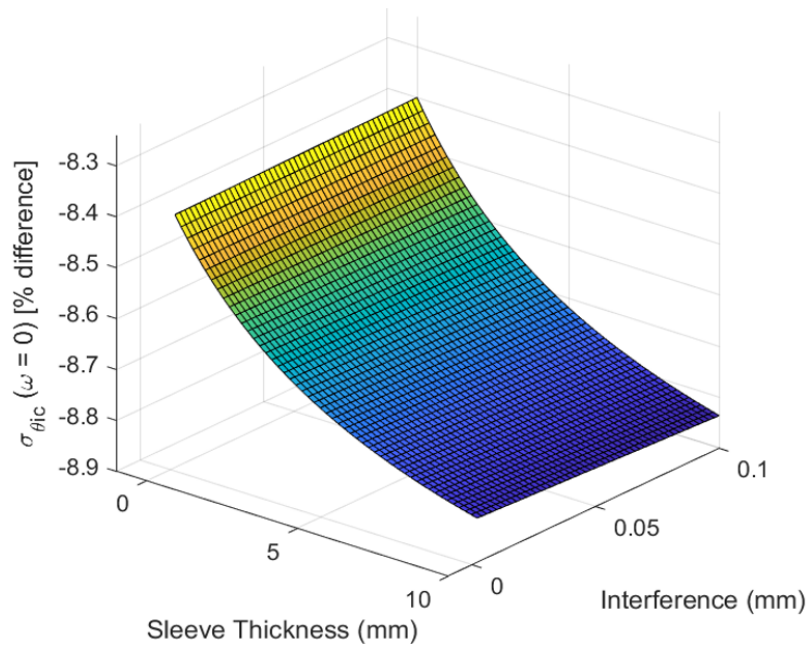
FIGURE 3.10: Percentage difference in circumferential stress at magnet outer surface when stationary.
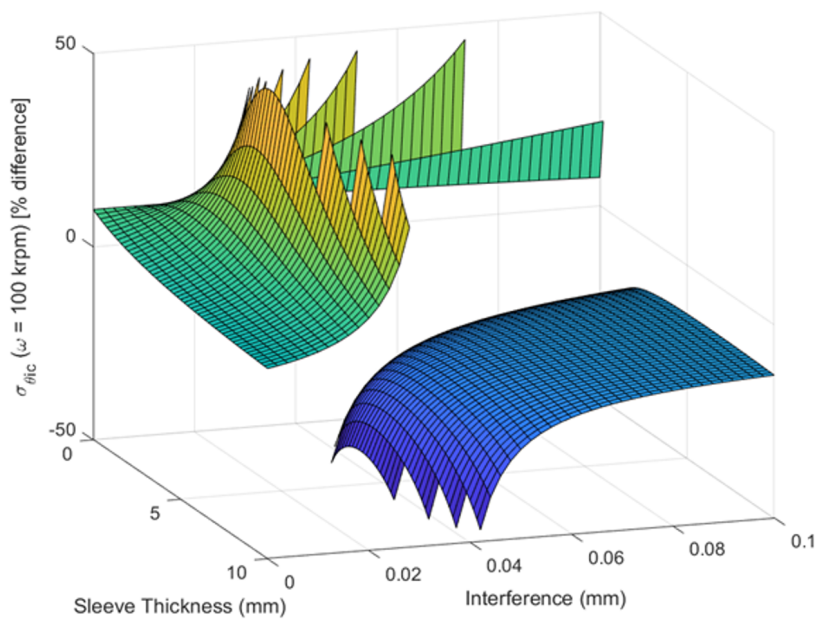
FIGURE 3.11: Percentage difference in circumferential stress at magnet outer surface at maximum speed [153].

they create. While the absolute differences are relatively small, the stresses are still critical and a model which avoids the conflicting assumptions made in plane stress and plane strain is required.

Figures 3.12 - 3.15 show that the difference in circumferential stress for the plane stress and plane strain models remains consistent as the rotor topology is changed. Figures 3.12 and 3.13 were produced with a magnet inner radius of 6 mm while Figures 3.14 and 3.15 used a magnet inner radius of 8 mm.
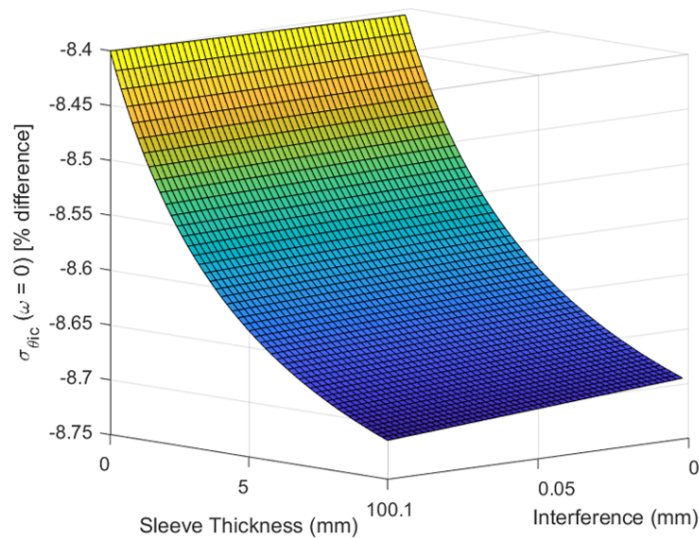
FIGURE 3.12: Percentage difference in circumferential stress at magnet outer surface when stationary with a 6 mm magnet inner radius.
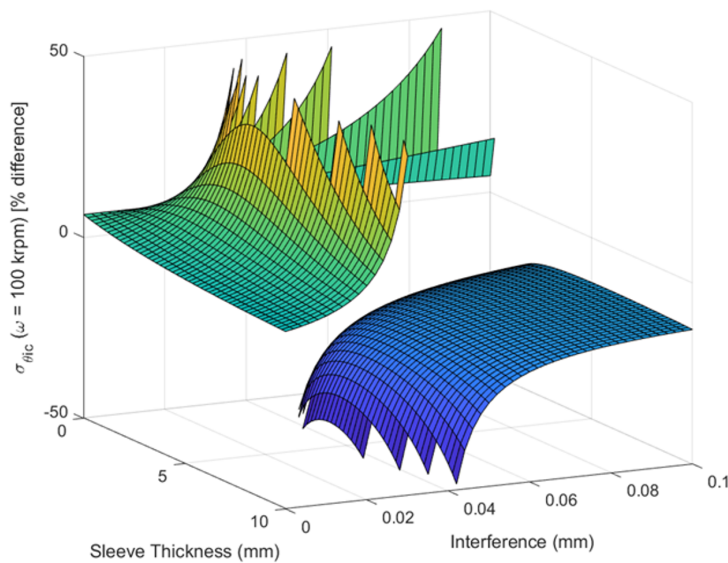
FIGURE 3.13: Percentage difference in circumferential stress at magnet outer surface at maximum speed with a 6 mm magnet inner radius.
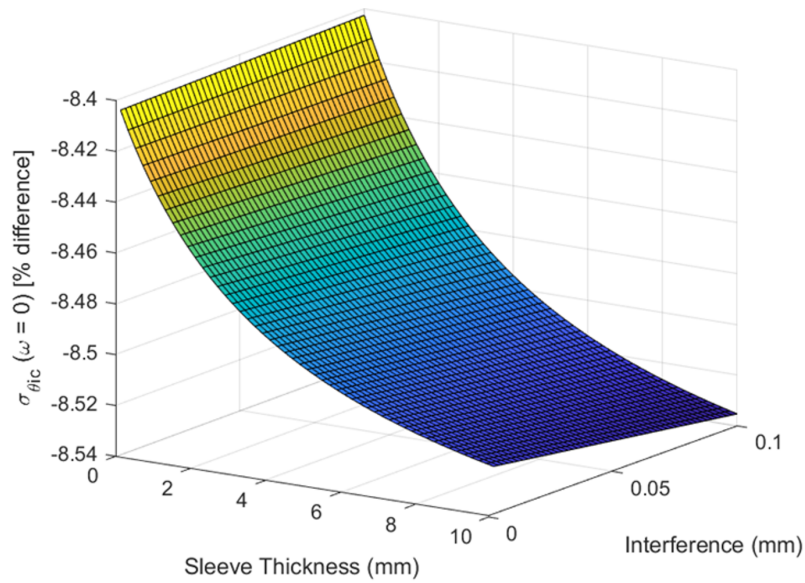
FIGURE 3.14: Percentage difference in circumferential stress at magnet outer surface when stationary with an 8 mm magnet inner radius.
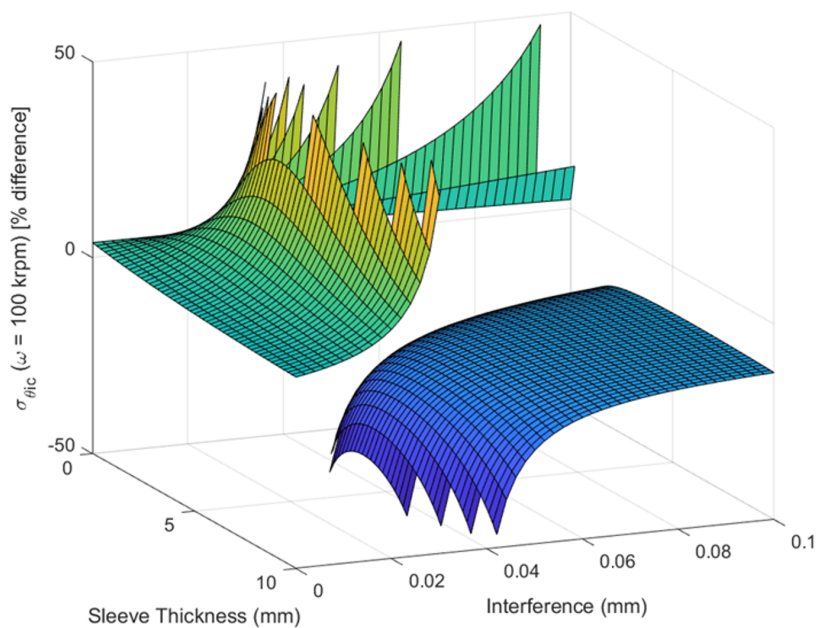
FIGURE 3.15: Percentage difference in circumferential stress at magnet outer surface at maximum speed with an 8 mm magnet inner radius.

When exploring the Von Mises stress at the inner surface of the sleeve, a larger difference was identified between the plane stress and plane strain models, compared to the circumferential stress at the magnet outer surface. Figures 3.16 and 3.17 show the percentage difference between the models for σ_{VMoc}, when stationary and at maximum speed, respectively. The magnet inner radius was set to 4 mm.
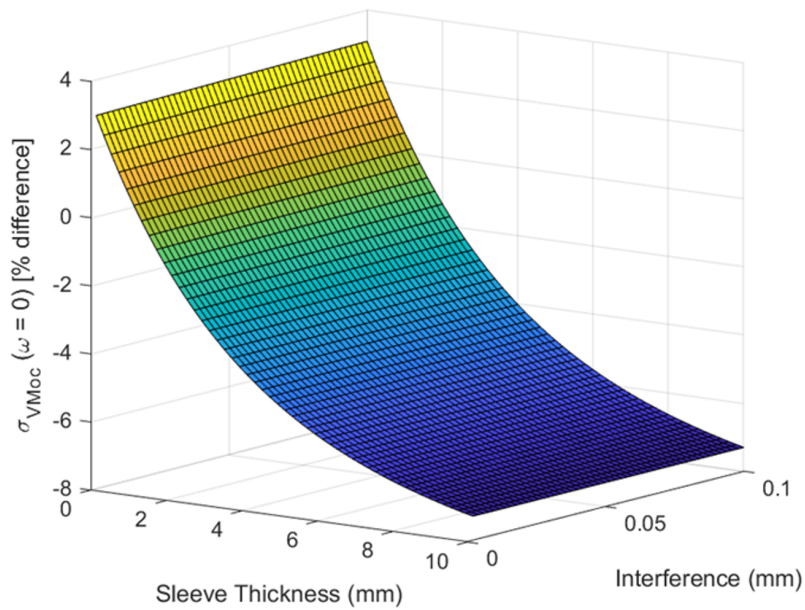
FIGURE 3.16: Percentage difference in Von Mises stress at the sleeve inner surface when stationary.
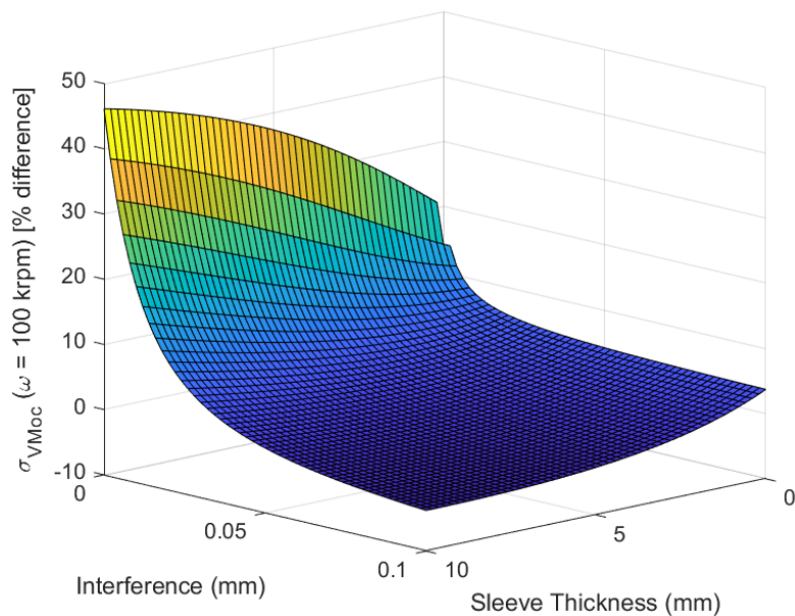
FIGURE 3.17: Percentage difference in Von Mises stress at the sleeve inner surface at maximum speed [153].

The percentage difference between the models when the rotor is stationary is low, with the sleeve thickness dictating most of the change. The thicker the sleeve the larger the difference, as shown in Figure 3.16. The largest difference between the models occurs when the rotor is at speed and has lower levels of interference and a larger sleeve thickness, as shown in Figure 3.17.

Figures 3.18 and 3.19 show that the percentage differences between the plane stress and plane strain models for σ_{VMoc}, are present in different rotor topologies. Figures 3.18 and 3.19 were produced using a magnet inner radius of 6 mm and 8 mm, respectively. The percentage difference peaks were found to reduce as the
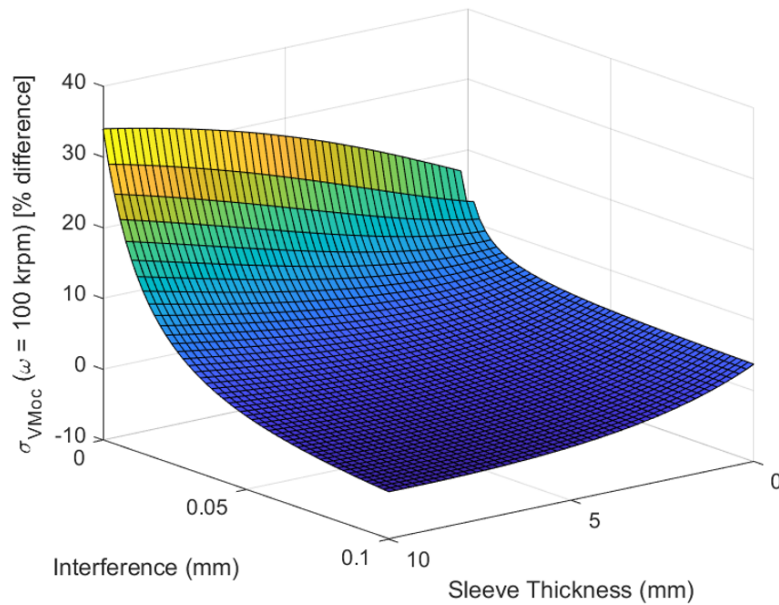
FIGURE 3.18: Percentage difference in Von Mises stress at the sleeve inner surface at maximum speed with a 6 mm magnet inner radius.
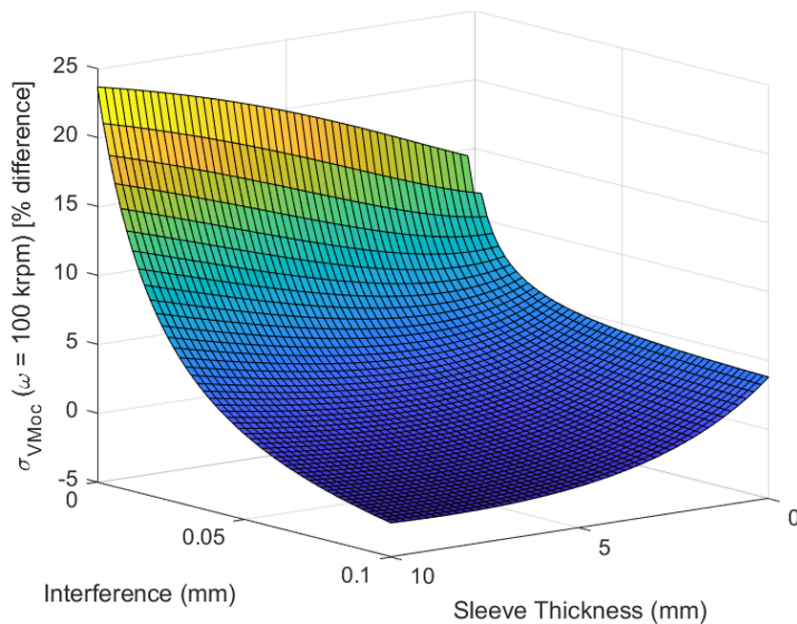
FIGURE 3.19: Percentage difference in Von Mises stress at the sleeve inner surface at maximum speed with an 8 mm magnet inner radius.

magnet inner radius increased. However, the difference between the models is substantial for all topologies explored and reinforces the need for a model that does not incorporate the approximations used in plane stress or plane strain.

3.3.4 Generalised Plane Strain Model

As shown by Barrans [10], the GPS model can be considered accurate away from the rotor ends for relatively long rotors with high levels of friction between the cylinders, which is required for the rotor to operate successfully. It does not include the approximations used in plane stress or the plane strain models. Figures 3.20 and 3.21 show the percentage error in the plane stress and plane strain results respectively, when compared to the GPS results for the stresses $\sigma_{\theta ic}$ and σ_{VMoc}, whilst stationary and at maximum speed. The results were gathered using a magnet inner radius of 4 mm.
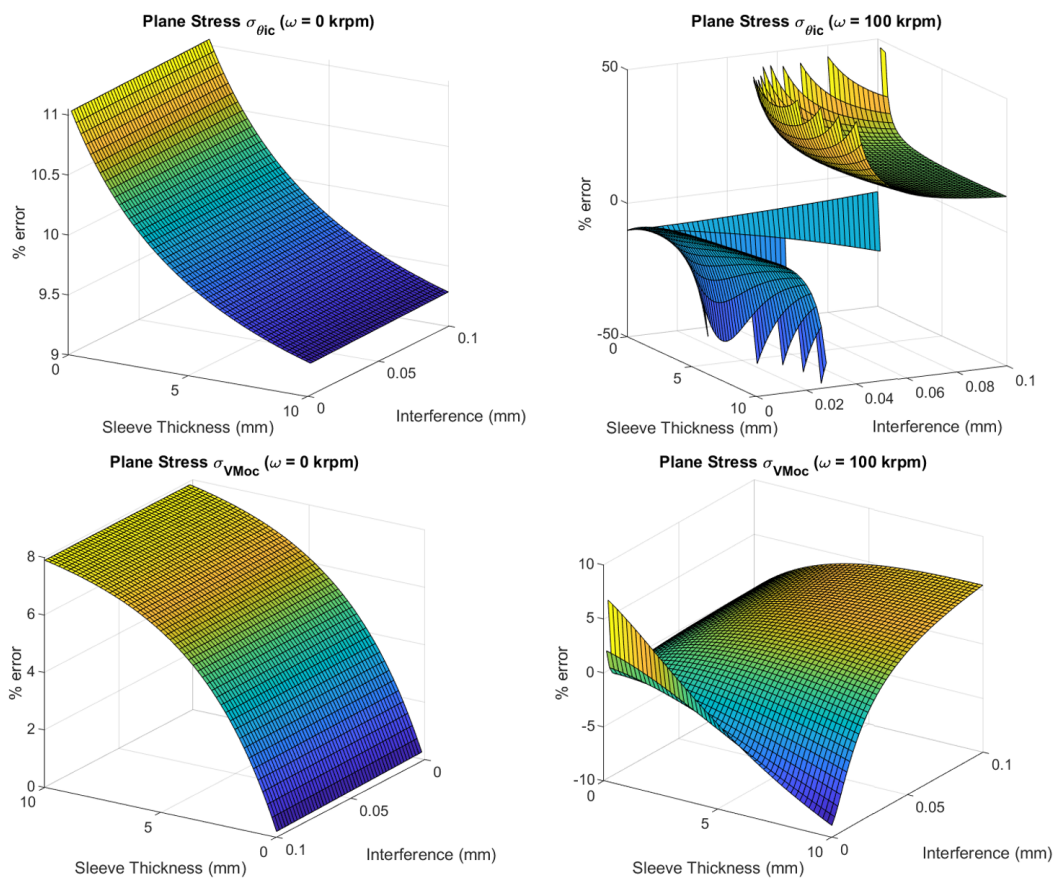
FIGURE 3.20: Percentage errors in the plane stress theory, adapted from Barrans and Mallin [153].

When the rotor is stationary, Figure 3.20 shows that $\sigma_{\theta ic}$ has a significant error across all explored sleeve thicknesses and interference values, but the errors peak as the sleeve thickness reduces. Conversely, the error in σ_{VMoc} increases as the sleeve thickness increases. These conflicting results make it hard to find a rotor topology that will be accurate for both critical stresses explored. When the rotor is at maximum speed significant errors are identified, and the error in σ_{VMoc} is dependent on both the sleeve thickness and interference.
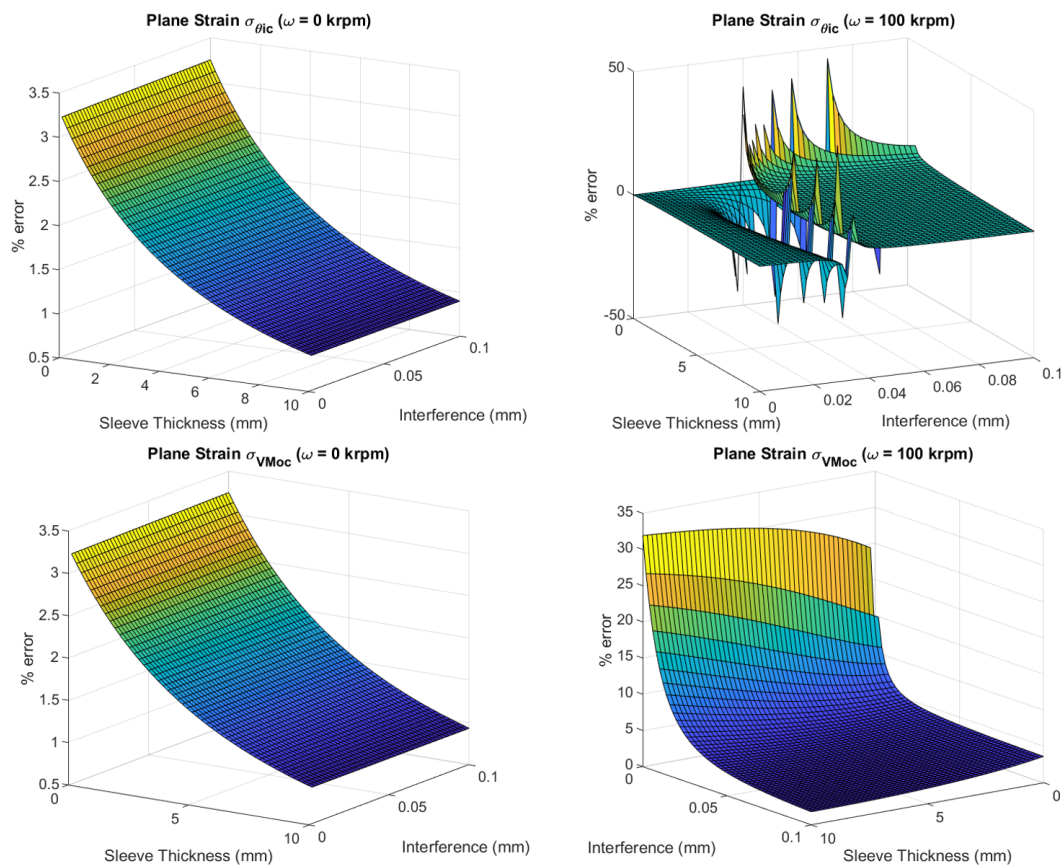
FIGURE 3.21: Percentage errors in the plane strain theory, adapted from Barrans and Mallin [153].

Figure 3.21 shows that when the rotor is stationary, both $\sigma_{\theta ic}$ and σ_{VMoc} percentage errors increase as the sleeve thickness reduces to zero. However, the error is much more significant for the corresponding plane stress results. The main difference appears when speed in introduced to the plane strain model. The Von Mises stress at maximum speed increases as the interference is reduced and the peak is far larger than those found in the plane stress model results. Errors of this magnitude are unsuitable when predicting critical stresses.

Figures 3.22 and 3.23 show the same plane stress and plane strain results respectively, for a rotor with a magnet inner radius of 6 mm, while Figures 3.24 and 3.25 uses a magnet inner radius of 8 mm. These results show that similar error patterns were identified across multiple rotor topologies, with the only significant difference being a reduction in peak percentage error in the plane strain Von Mises results at maximum speed.
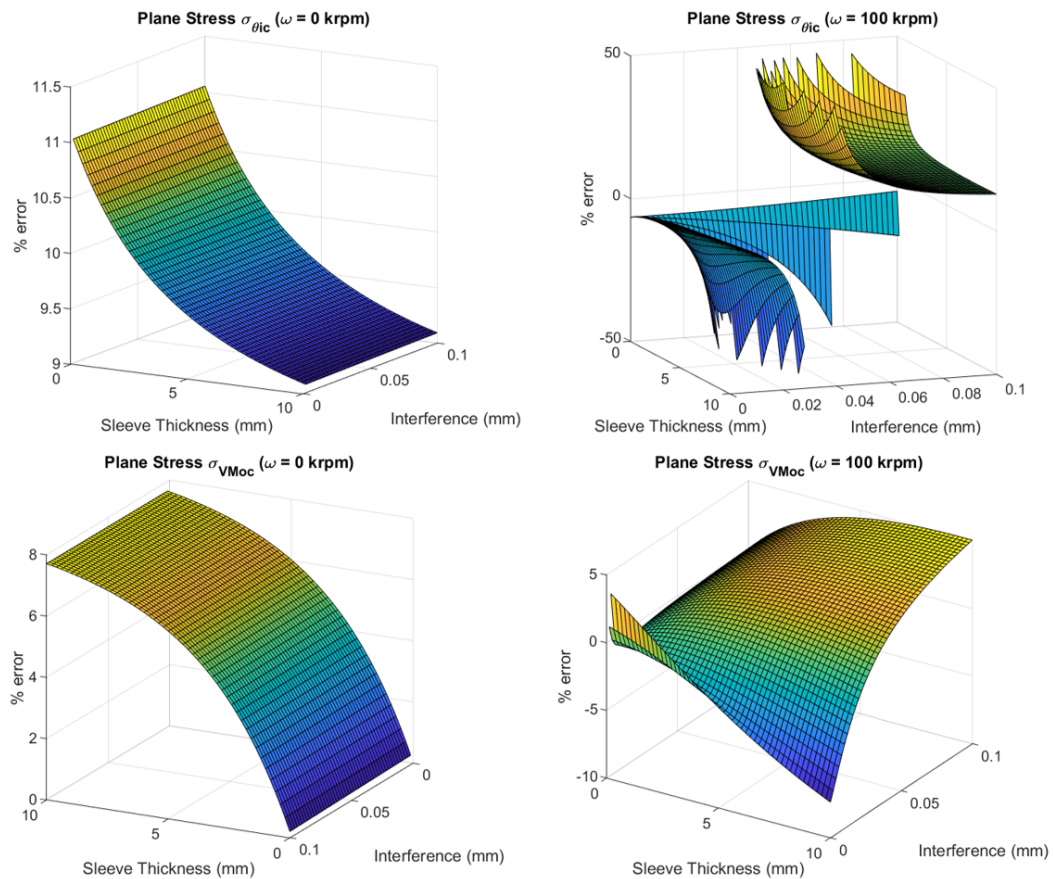
FIGURE 3.22: Percentage errors in the plane stress theory with a rotor magnet inner radius of 6 mm.
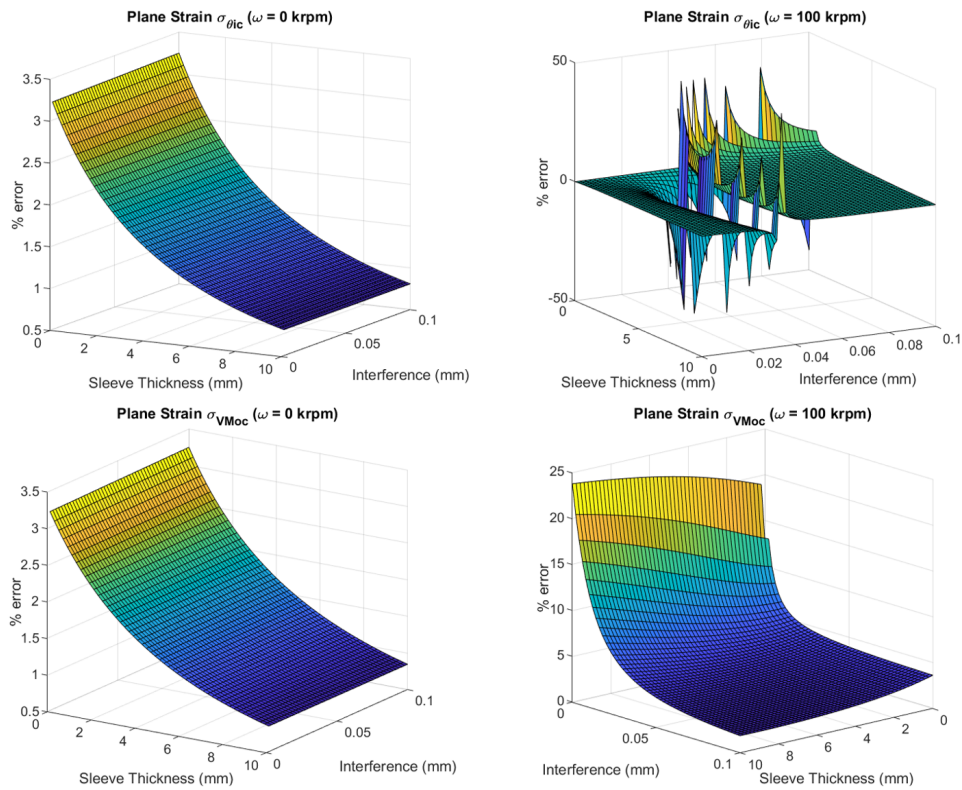
FIGURE 3.23: Percentage errors in the plane strain theory with a rotor magnet inner radius of 6 mm.
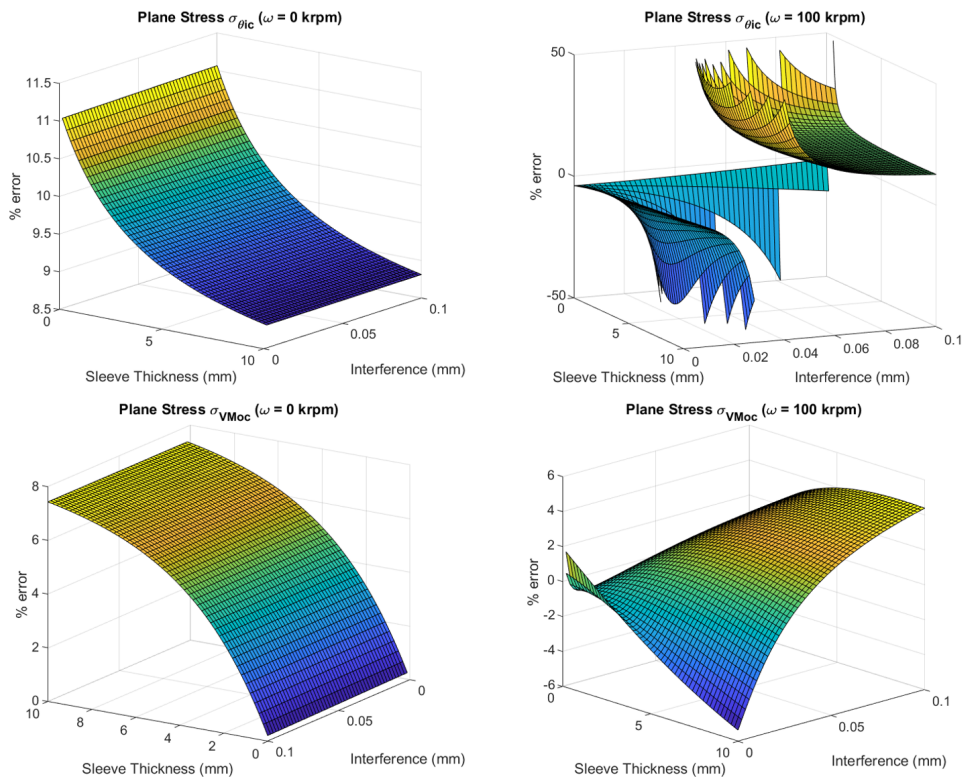
FIGURE 3.24: Percentage errors in the plane stress theory with a rotor magnet inner radius of 8 mm.
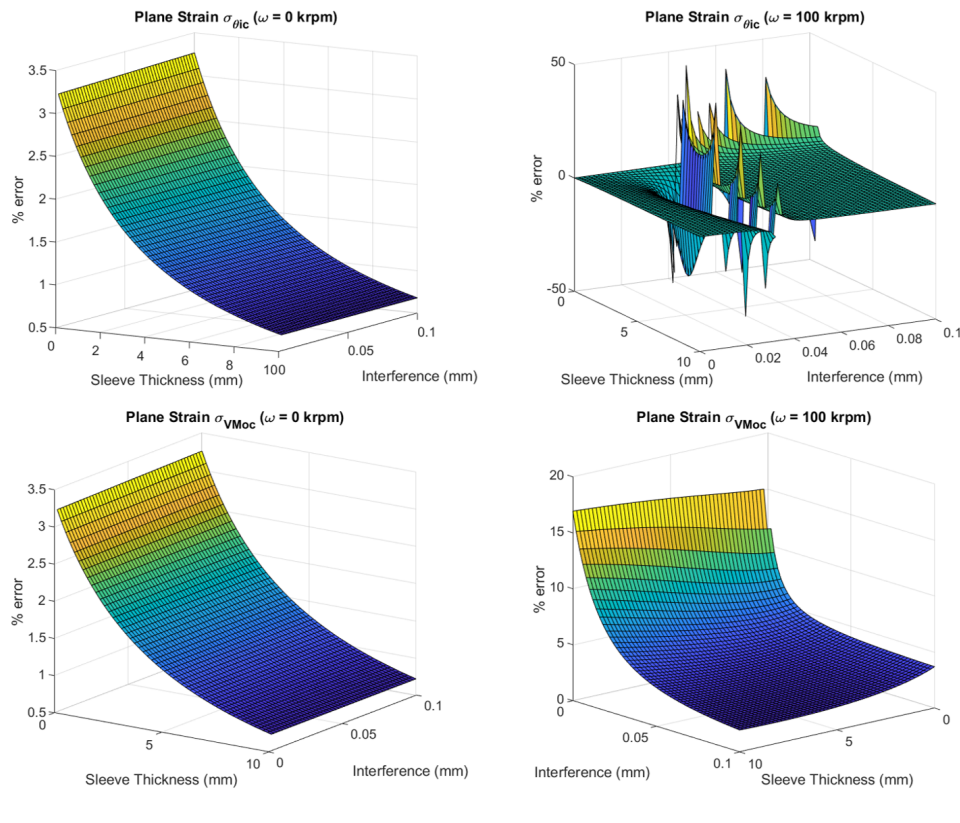
FIGURE 3.25: Percentage errors in the plane strain theory with a rotor
magnet inner radius of 8 mm.

3.4   Summary

Based on the results presented in this chapter, a series of key outcomes were de-
termined, listed below. These outcomes enable decisions to be made regarding the
stress analysis development for three-cylinder rotors.

- Thick cylinder theory is more accurate than the thin cylinder approximation
  by correctly including stress changes through the cylinder wall thickness.

- Ignoring the change in interference due to rotation can cause significant errors
  when predicting stresses.

- As the sleeve thickness reduces, the differences between the plane stress and
  plane strain methods accelerates. This would result in conflicting results be-
  tween the methods for critical stresses when the rotor sleeve is minimised.

- The plane strain results tend to have increased errors compared to the GPS
  as the sleeve thickness is minimised, while the critical plane stress results are
  affected individually by changes in both the sleeve thickness and interference.

- For $\sigma_{\theta ic}$, the plane stress and plane strain results are similar compared to the GPS method when the rotor is stationary. However, at speed, major differences between the three methods are identified for σ_{VMoc}.

- The differences between the three theoretical models are consistent across multiple rotor topologies.

The findings listed above from this chapter highlight three key development areas for the theoretical stress analysis models. These areas are listed below and each represent a significant body of work to incorporate into the analysis models.

- The three theoretical models should be explored for rotors comprising of three compound cylinders. This would represent rotors than include a back iron as well as the retaining sleeve.

- The theoretical models have been developed using the isotropic version of Hooke's law. They are therefore not suitable for anisotropic materials and would require further theoretical development to include them.

- Exploration of the stress changes at the rotor ends would enable the accurate prediction of rotor stresses along the whole length.

4 Three Cylinder Closed Form Analysis Development

4.1 Introduction

Section 3.4 concluded that the two-cylinder GPS analysis method was more accurate than plane stress or plane strain as it did not include the unrealistic assumptions made in those methods. However, Section 3.4 outlined a need for the exploration of closed form analysis techniques for three compound cylinders as some rotors incorporate a rotor or back iron, as shown in Figure 1.5b. As discussed in Section 2.2.6.2, there has been no exploration in the existing literature of three-cylinder closed form analysis for the GPS and plane strain methods, while plane stress has had very little investigation with most opting to solve via finite element analysis (FEA). Therefore, the stress equations for all three models should be derived for three-cylinder rotors. This would then enable comparisons between the models to compliment the two-cylinder rotor findings shown in Chapter 3. The main aspects of this chapter have previously been published by the author. The derivation of the plane stress, plane strain and generalised plane strain (GPS) theories for three-cylinder rotors has been outlined by Mallin and Barrans [154]. However, this chapter explores the derivation of each theory in much greater detail and adds further results by comparing the three-cylinder and two-cylinder theories against each other.

4.2 Three-Cylinder Foundations

As discussed in Section 3.3.2, a MatLab code was generated to enable efficient simulation of the three different stress theories for two-cylinder rotor topologies. For three-cylinder the rotors, the mathematical process is more complex, thus requiring a MatLab code to efficiently simulate three-cylinder rotor topologies for plane stress, plane strain and GPS methodologies. However, with the added complexity, MatLab

Symbolic Math Toolbox was utilised to minimise the risk of trivial errors being made during the deriving and inputting process. The equations were derived by hand and via the math toolbox so the equations could be compared and verified. Visualising the mathematical symbols also reduced the risk of typing errors when inputting the derived equations.

Figure 4.1 shows a three-cylinder compound rotor, similar to the two-cylinder rotor shown in Figure 3.7, where R_{ii} is the inner surface of the inner cylinder; R_{ic} is the outer surface of the inner cylinder; R_{mc} is the inner surface of the magnets; R_{md} is the outer surface of the magnets; R_{od} is the inner surface of the outer cylinder; and R_{oo} is the outer surface of the outer cylinder. The notation is based on the first subscript letter representing the cylinder (inner, middle, or outer) and the second subscript letter representing the radial location within the compound cylinder. The inner and outer common radii are given the subscripts c and d, respectively.
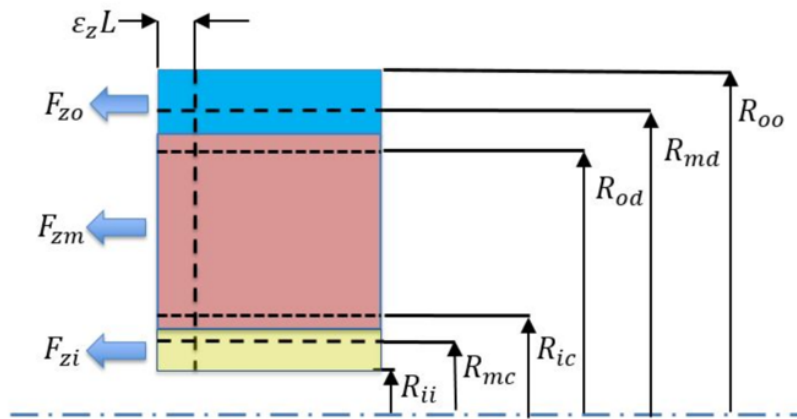
FIGURE 4.1: Axial effects and boundary notation on a three-cylinder rotor axial cross section [154].

F_{zi}, F_{zm}, and F_{zo} are the external axial forces acting on the inner middle and outer cylinder, respectively, while $\varepsilon_z L$ is the change in axial length, as defined in Section 3.3.1. For such three-cylinder rotor configurations: no radial stress is applied to R_{ii} or R_{oo}; radial stress at R_{ic} and R_{mc} is equal to the interference shrinkage pressure, S_1; and radial stress at R_{md} and R_{od} is equal to the interference shrinkage pressure, S_2. From this, a set of boundary conditions are derived for each cylinder, where r is the variable radial dimension and σ_r is the radial stress. Additional subscripts on σ_r indicate firstly the part that the stress occurs in and secondly the radial position at

which the stress occurs. The boundary conditions are:

$$\text{Inner cylinder: When} \quad r = R_{ii}; \quad \sigma_{rii} = 0$$

$$r = R_{ic}; \quad \sigma_{ric} = -S_1$$

$$\text{Middle cylinder: When} \quad r = R_{mc}; \quad \sigma_{rmc} = -S_1$$

$$r = R_{md}; \quad \sigma_{rmd} = -S_2$$

$$\text{Outer cylinder: When} \quad r = R_{od}; \quad \sigma_{rod} = -S_2$$

$$r = R_{oo}; \quad \sigma_{roo} = 0$$

The boundary conditions are then applied to the corresponding equations for each theoretical approach. The following assumptions are made for the theoretical analyses:

- The radial and circumferential stresses are uniform along the length of the rotor.

- No interactions with the surroundings for the inner and outer surfaces of the rotor.

- The friction between the interfering cylinder surfaces is high enough to prevent axial slip.

- Each cylinder is an isotropic solid body.

As discussed in Section 3.2.3, if the change in interference due to rotation is not included in the analysis, large errors can be induced. Therefore, compatibility conditions must be placed on the analyses. The compatibility conditions are:

At the inner common radius:

$$R_{ic}(1 + \varepsilon_{\theta ic}) = R_{mc}(1 + \varepsilon_{\theta mc}) \tag{4.1}$$

At the outer common radius:

$$R_{md}(1 + \varepsilon_{\theta md}) = R_{od}(1 + \varepsilon_{\theta od}) \tag{4.2}$$

Where ε_θ is the circumferential strain at a specific rotor surface indicated by the notation related to Figure 4.1. As shown in Figure 1.5, surface-mounted permanent

magnet (SPM) rotor designs often used segmented magnets. The theoretical approaches presented here assume the permanent magnet (PM) cylinder is a solid body and cannot predict the interactions between each magnet. Therefore, rotor designs with interpole gaps will not be suitable for the calculations. In these rotors, as shown by Chen et al. [115], the stress in the sleeve spikes at the edges of the magnets. To accommodate this high stress, the sleeve must be strengthened. However, designs without interpole gaps will be suitable for analysis using approaches presented here, despite using segmented magnets. As discussed by Barrans et al. [10] and shown in Section 5.2.2, the magnets must always be held in compression and can therefore be assumed to act as a solid body.

4.3   Plane Stress

To aid readability, equations 3.14 and 3.15 from section 3.2.2 are repeated here as equations 4.3 and 4.4. These equations show the radial, circumferential, and axial stresses for the plane stress approach:

$$\sigma_r = A - \frac{B}{r^2} - \frac{3+\nu}{8}\rho\omega^2 r^2 \tag{4.3}$$

$$\sigma_\theta = A + \frac{B}{r^2} - \frac{1+3\nu}{8}\rho\omega^2 r^2 \tag{4.4}$$

$$\sigma_z = 0 \tag{4.5}$$

The boundary conditions from Section 4.2 are used to identify the radial and circumferential stress equations for the inner, middle, and outer cylinders. By substituting a pair of boundary conditions into equation 4.3, constants A and B are eliminated, and equations 4.3 and 4.4 can then be rewritten in terms of the shrinkage pressures S_1 and S_2. However, in the interest of brevity, the process for the middle cylinder will be outlined, and the resulting radial and circumferential stress equations will be used to determine the corresponding equations for the inner and outer cylinders.

Substituting the middle cylinder boundary conditions into equation 4.3, results in a pair of simultaneous equations 4.6 and 4.7.

$$-S_1 = A - \frac{B}{r^2} - \frac{3+v}{8}\rho\omega^2 R_{mc}^2 \tag{4.6}$$

$$-S_2 = A - \frac{B}{r^2} - \frac{3+v}{8}\rho\omega^2 R_{md}^2 \tag{4.7}$$

Rearranging equations 4.6 and 4.7 for A allows them to be equated and solved for B, given by equation 4.8.

$$B = \frac{R_{mc}^2 R_{md}^2 (S_2 - S_1)}{R_{mc}^2 - R_{md}^2} + \frac{R_{mc}^2 R_{md}^2 (3+v)}{8}\rho\omega^2 \tag{4.8}$$

Equation 4.8 can then be substituted into equation 4.6 and solved for A, given by equation 4.9.

$$A = \frac{R_{mc}^2 S_1 - R_{md}^2 S_2}{R_{md}^2 - R_{mc}^2} + \frac{(R_{mc}^2 + R_{md}^2)(3+v)}{8}\rho\omega^2 \tag{4.9}$$

A and B, from equations 4.8 and 4.9 respectively, are then substituted back into the radial and circumferential stress equations 4.3 and 4.4 to produce the full stress equations in terms of the shrinkage pressures S_1 and S_2. These are given by equations 4.10 and 4.11 respectively.

$$\sigma_{rm} = \frac{\left(S_1 R_{mc}^2 (R_{md}^2 - r^2) - S_2 R_{md}^2 (R_{mc}^2 - r^2)\right)}{r^2 (R_{mc}^2 - R_{md}^2)} \\ - \frac{\rho_m \omega^2}{8}(v_m + 3)\left(\frac{R_{mc}^2 R_{md}^2}{r^2} - R_{mc}^2 - R_{md}^2 + r^2\right) \tag{4.10}$$

$$\sigma_{\theta m} = \frac{\left(S_2 R_{md}^2 (R_{mc}^2 - r^2 l) - S_1 R_{mc}^2 (R_{md}^2 + r^2)\right)}{r^2 (R_{mc}^2 - R_{md}^2)} \\ + \frac{\rho_m \omega^2}{8}\left[(v_m + 3)\left(\frac{R_{mc}^2 R_{md}^2}{r^2} + R_{mc}^2 + R_{md}^2\right) - r^2(3v_m + 1)\right] \tag{4.11}$$

The same process can be followed to determine the corresponding stresses for the inner and outer cylinders. However, equations 4.10 and 4.11 can also be utilised. If $S_1 = 0$, then the middle cylinder is placed under the same conditions as the inner

cylinder. Therefore, by applying $S_1 = 0$, $S_2 = S_1$, and the inner cylinder notations to equations 4.10 and 4.11, the radial and circumferential stress equations for the inner cylinder can be derived, given by equations 4.12 and 4.13.

$$\sigma_{ri} = \frac{S_1 R_{ic}^2}{R_{ic}^2 - R_{ii}^2}\left(\frac{R_{ii}^2}{r^2} - 1\right) - \frac{\rho_i \omega^2}{8}(\nu_i + 3)\left(\frac{R_{ic}^2 R_{ii}^2}{r^2} - R_{ic}^2 - R_{ii}^2 + r^2\right) \tag{4.12}$$

$$\sigma_{\theta i} = \frac{S_1 R_{ic}^2}{R_{ii}^2 - R_{ic}^2}\left(\frac{R_{ii}^2}{r^2} + 1\right) + \frac{\rho_i \omega^2}{8}\left[(\nu_i + 3)\left(\frac{R_{ic}^2 R_{ii}^2}{r^2} + R_{ic}^2 + R_{ii}^2\right) - r^2(3\nu_i + 1)\right] \tag{4.13}$$

Likewise, by applying $S_2 = 0$, $S_1 = S_2$, and the outer cylinder notations to equations 4.10 and 4.11, the radial and circumferential stress equations for the outer cylinder can be derived, given by equations 4.14 and 4.15.

$$\sigma_{ro} = \frac{S_2 R_{od}^2}{R_{od}^2 - R_{oo}^2}\left(\frac{R_{oo}^2}{r^2} - 1\right) - \frac{\rho_o \omega^2}{8}(\nu_o + 3)\left(\frac{R_{od}^2 R_{oo}^2}{r^2} - R_{od}^2 - R_{oo}^2 + r^2\right) \tag{4.14}$$

$$\sigma_{\theta o} = \frac{S_2 R_{od}^2}{R_{oo}^2 - R_{od}^2}\left(\frac{R_{oo}^2}{r^2} + 1\right) + \frac{\rho_o \omega^2}{8}\left[(\nu_o + 3)\left(\frac{R_{od}^2 R_{oo}^2}{r^2} + R_{od}^2 + R_{oo}^2\right) - r^2(3\nu_o + 1)\right] \tag{4.15}$$

Using equations 4.10 and 4.15, the radial and circumferential stress equations for each cylinder surface, outlined in Figure 4.1, can be determined by substituting in the relevant radius notation for r. For example, to determine the radial stress equation at the inner surface of the inner cylinder, R_{ii} can be substituted for r in equation 4.12. Equations 4.16 and 4.27 show the simplified radial and circumferential stress equations for each cylinder surface.

$$\sigma_{rii} = 0 \tag{4.16}$$

$$\sigma_{\theta ii} = \frac{2S_1 R_{ic}^2}{R_{ii}^2 - R_{ic}^2} + \frac{\rho_i \omega^2}{4}\left(R_{ii}^2 + 3R_{ic}^2 + \nu_i(R_{ic}^2 - R_{ii}^2)\right) \tag{4.17}$$

$$\sigma_{ric} = -S_1 \tag{4.18}$$

$$\sigma_{\theta ic} = \frac{S_1(R_{ic}^2 + R_{ii}^2)}{R_{ii}^2 - R_{ic}^2} + \frac{\rho_i \omega^2}{4}\left(3R_{ii}^2 + R_{ic}^2 + \nu_i(R_{ii}^2 - R_{ic}^2)\right) \tag{4.19}$$

$$\sigma_{rmc} = -S_1 \tag{4.20}$$

$$\sigma_{\theta mc} = \frac{-S_1(R_{md}^2 + R_{mc}^2)}{R_{mc}^2 - R_{md}^2} + \frac{\rho_m \omega^2}{4}\left(R_{mc}^2 + 3R_{md}^2 + \nu_m(R_{md}^2 - R_{mc}^2)\right) \tag{4.21}$$

$$\sigma_{rmd} = -S_2 \tag{4.22}$$

$$\sigma_{\theta md} = \frac{S_2(R_{mc}^2 - R_{md}^2) - 2S_1 R_{mc}^2}{R_{mc}^2 - R_{md}^2} + \frac{\rho_m \omega^2}{4}\left(3R_{mc}^2 + R_{md}^2 + v_m(R_{mc}^2 - R_{md}^2)\right) \tag{4.23}$$

$$\sigma_{rod} = -S_2 \tag{4.24}$$

$$\sigma_{\theta od} = \frac{S_2(R_{od}^2 + R_{oo}^2)}{R_{oo}^2 - R_{od}^2} + \frac{\rho_o \omega^2}{4}\left(R_{od}^2 + 3R_{oo}^2 + v_o(R_{oo}^2 - R_{od}^2)\right) \tag{4.25}$$

$$\sigma_{roo} = 0 \tag{4.26}$$

$$\sigma_{\theta oo} = \frac{2S_2 R_{od}^2}{R_{oo}^2 - R_{od}^2} + \frac{\rho_o \omega^2}{4}\left(3R_{od}^2 + R_{oo}^2 + v_o(R_{od}^2 - R_{oo}^2)\right) \tag{4.27}$$

To apply the compatibility conditions shown in equations 4.1 and 4.2, the circumferential strain equations must be derived for each interfering surface location. Therefore, the corresponding radial and circumferential stress equations for a specific radial surface are substituted into equation 3.7. Equations 4.28 - 4.31 give the circumferential strain equations for R_{ic}, R_{mc}, R_{md}, and R_{od}, respectively.

$$\varepsilon_{\theta ic} = \frac{S_1}{E_i}\left(\frac{R_{ii}^2 + R_{ic}^2}{R_{ii}^2 - R_{ic}^2} + v_i\right) + \frac{\rho_i \omega^2}{4E_i}\left(R_{ic}^2 + 3R_{ii}^2 + v_i(R_{ii}^2 - R_{ic}^2)\right) + \Delta_T \alpha_i \tag{4.28}$$

$$\varepsilon_{\theta mc} = \frac{2R_{md}^2(S_1 - S_2)}{E_m(R_{md}^2 - R_{mc}^2)} + \frac{S_1(v_m - 1)}{E_m} + \frac{\rho_m \omega^2}{4E_m}\left(R_{mc}^2 + 3R_{md}^2 + v_m(R_{md}^2 - R_{mc}^2)\right) + \Delta_T \alpha_m \tag{4.29}$$

$$\varepsilon_{\theta md} = \frac{2R_{mc}^2(S_2 - S_1)}{E_m(R_{mc}^2 - R_{md}^2)} + \frac{S_2(v_m - 1)}{E_m} + \frac{\rho_m \omega^2}{4E_m}\left(R_{md}^2 + 3R_{mc}^2 + v_m(R_{mc}^2 - R_{md}^2)\right) + \Delta_T \alpha_m \tag{4.30}$$

$$\varepsilon_{\theta od} = \frac{S_2}{E_o}\left(\frac{R_{oo}^2 + R_{od}^2}{R_{oo}^2 - R_{od}^2} + v_o\right) + \frac{\rho_o \omega^2}{4E_o}\left(R_{od}^2 + 3R_{oo}^2 + v_o(R_{oo}^2 - R_{od}^2)\right) + \Delta_T \alpha_o \tag{4.31}$$

Substituting equations 4.28 - 4.31 into equations 4.1 and 4.2 leaves two unknown values to be determined, S_1 and S_2, and can be written in the following format:

$$\begin{bmatrix} A & B \\ D & E \end{bmatrix} \begin{bmatrix} S_1 \\ S_2 \end{bmatrix} = \begin{bmatrix} C \\ F \end{bmatrix} \tag{4.32}$$

Where:

$$A = \frac{R_{ic}}{E_i}\left(\frac{2R_{ii}^2}{R_{ic}^2 - R_{ii}^2} + (1 - v_i)\right) - \frac{R_{mc}}{E_m}\left(\frac{2R_{md}^2}{R_{mc}^2 - R_{md}^2} + (1 - v_m)\right) \tag{4.33}$$

$$B = \frac{2R_{mc}R_{md}^2}{E_m(R_{mc}^2 - R_{md}^2)} \tag{4.34}$$

$$C = R_{ic}\left[\frac{\rho_i\omega^2}{4E_i}\left(R_{ic}^2 + 3R_{ii}^2 + v_i(R_{ii}^2 - R_{ic}^2)\right) + \Delta_T\alpha_i + 1\right]$$
$$- R_{mc}\left[\frac{\rho_m\omega^2}{4E_m}\left(R_{mc}^2 + 3R_{md}^2 + v_m(R_{md}^2 - R_{mc}^2)\right) + \Delta_T\alpha_m + 1\right] \tag{4.35}$$

$$D = \frac{2R_{md}R_{mc}^2}{E_m(R_{md}^2 - R_{mc}^2)} \tag{4.36}$$

$$E = \frac{R_{od}}{E_o}\left(\frac{2R_{oo}^2}{R_{od}^2 - R_{oo}^2} + (1 - v_o)\right) - \frac{R_{md}}{E_m}\left(\frac{2R_{mc}^2}{R_{md}^2 - R_{mc}^2} + (1 - v_m)\right) \tag{4.37}$$

$$F = R_{od}\left[\frac{\rho_o\omega^2}{4E_o}\left(R_{od}^2 + 3R_{oo}^2 + v_o(R_{oo}^2 - R_{od}^2)\right) + \Delta_T\alpha_o + 1\right]$$
$$- R_{md}\left[\frac{\rho_m\omega^2}{4E_m}\left(R_{md}^2 + 3R_{mc}^2 + v_m(R_{mc}^2 - R_{md}^2)\right) + \Delta_T\alpha_m + 1\right] \tag{4.38}$$

Once the values of S_1 and S_2 have been determined using equation 4.32, they can then be substituted back into the stress equations 4.16 and 4.27. This enables the radial and circumferential stress values to be found at specific rotor surfaces.

4.4 Plane Strain

To aid readability, equations 3.18, 3.19 and 3.20 from section 3.2.3 are repeated here as equations 4.39, 4.40, and 4.41, respectively. These equations give the radial, circumferential, and axial stresses for the plane strain approach:

$$\sigma_r = A - \frac{B}{r^2} - \frac{3 - 2v}{8(1 - v)}\rho\omega^2 r^2 \tag{4.39}$$

$$\sigma_\theta = A + \frac{B}{r^2} - \frac{1 + 2v}{8(1 - v)}\rho\omega^2 r^2 \tag{4.40}$$

$$\sigma_z = v(\sigma_r + \sigma_\theta) - E\Delta T\alpha \tag{4.41}$$

The same process, outlined in Section 4.3 for the derivation of the plane stress approach, was followed for the plane strain approach, however there is the addition of the axial stress equation to include. The boundary conditions, shown in Section 4.2, are used to identify the radial, circumferential, and axial stress equations for the inner, middle, and outer cylinders, respectively. Substituting a pair of boundary conditions into the radial stress equation 4.39 enables the constants A and B

to be identified, producing radial and circumferential stress equations in terms of the shrinkage pressures, S_1 and S_2. The completed radial and circumferential stress equations are then substituted into equation 4.41 to derive the axial stress equation.

Focussing on the middle cylinder, as in Section 4.3, substituting the middle cylinder boundary conditions from Section 4.2 into equation 4.39, produces the pair of simultaneous equations 4.42 and 4.43.

$$-S_1 = A - \frac{B}{R_{mc}^2} - \frac{3 - 2\nu}{8(1 - \nu)}\rho\omega^2 R_{mc}^2 \tag{4.42}$$

$$-S_2 = A - \frac{B}{R_{md}^2} - \frac{3 - 2\nu}{8(1 - \nu)}\rho\omega^2 R_{md}^2 \tag{4.43}$$

Rearranging equations 4.42 and 4.43 for A allows the constant B to be identified, which can then be substituted back into equation 4.42 to identify A. The equations for B and A are shown in equations 4.44 and 4.45, respectively.

$$B = \frac{R_{mc}^2 R_{md}^2 (S_1 - S_2)}{R_{md}^2 - R_{mc}^2} + \frac{\rho\omega^2 (2\nu - 3)}{8(\nu - 1)} R_{mc}^2 R_{md}^2 \tag{4.44}$$

$$A = \frac{R_{mc}^2 S_1 - R_{md}^2 S_2}{R_{md}^2 - R_{mc}^2} + \frac{\rho\omega^2 (2\nu - 3)}{8(\nu - 1)} (R_{mc}^2 + R_{md}^2) \tag{4.45}$$

Using equations 4.44 and 4.45, A and B are substituted into the radial and circumferential stress equations 4.39 and 4.40, respectively. The radial and circumferential stress equations in terms of S_1 and S_2 are shown in equations 4.46 and 4.47 respectively.

$$\sigma_{rm} = \frac{\left(S_1 R_{mc}^2 (R_{md}^2 - r^2) - S_2 R_{md}^2 (R_{mc}^2 - r^2)\right)}{r^2 (R_{mc}^2 - R_{md}^2)} \\ - \frac{\rho_m \omega^2}{8(\nu_m - 1)}(2\nu_m - 3)\left(\frac{R_{mc}^2 R_{md}^2}{r^2} - R_{mc}^2 - R_{md}^2 + r^2\right) \tag{4.46}$$

$$\sigma_{\theta m} = \frac{\left(S_2 R_{md}^2 (R_{mc}^2 + r^2) - S_1 R_{mc}^2 (R_{md}^2 + r^2)\right)}{r^2 (R_{mc}^2 - R_{md}^2)} \\ + \frac{\rho_m \omega^2}{8(\nu_m - 1)}\left[(2\nu_m - 3)\left(\frac{R_{mc}^2 R_{md}^2}{r^2} + R_{mc}^2 + R_{md}^2\right) + r^2(2\nu_m + 1)\right] \tag{4.47}$$

To derive the axial stress equation, equations 4.46 and 4.47 are substituted into equation 4.41. This produces:

$$\sigma_{zm} = \frac{2\nu_m(S_1 R_{mc}^2 - S_2 R_{md}^2)}{R_{md}^2 - R_{mc}^2} + \frac{\nu_m \rho_m \omega^2}{4(1-\nu_m)}\left((3-2\nu_m)(R_{md}^2 + R_{mc}^2) - 2r^2\right) - \Delta_T \alpha_m E_m$$

(4.48)

Using equations 4.46 - 4.48, the radial, circumferential, and axial stress equations for the inner and outer surface of the middle cylinder, R_{mc} and R_{md}, can be found and are given by equations 4.49 - 4.54.

$$\sigma_{rmc} = -S_1$$

(4.49)

$$\sigma_{\theta mc} = \frac{2 S_2 R_{md}^2 - S_1(R_{md}^2 + R_{mc}^2)}{R_{mc}^2 - R_{md}^2} + \frac{\rho_m \omega^2}{4(1-\nu_m)}\left(3 R_{md}^2 + R_{mc}^2 - 2\nu_m(R_{md}^2 + R_{mc}^2)\right)$$

(4.50)

$$\sigma_{zmc} = \frac{2\nu_m(S_1 R_{mc}^2 - S_2 R_{md}^2)}{R_{md}^2 - R_{mc}^2} + \frac{\nu_m \rho_m \omega^2}{4(1-\nu_m)}\left(3 R_{md}^2 + R_{mc}^2 - 2\nu_m(R_{md}^2 + R_{mc}^2)\right) - \Delta_T \alpha_m E_m$$

(4.51)

$$\sigma_{rmd} = -S_2$$

(4.52)

$$\sigma_{\theta md} = \frac{S_2(R_{md}^2 + R_{mc}^2) - 2 S_1 R_{mc}^2}{R_{mc}^2 - R_{md}^2} + \frac{\rho_m \omega^2}{4(1-\nu_m)}\left(3 R_{mc}^2 + R_{md}^2 - 2\nu_m(R_{md}^2 + R_{mc}^2)\right)$$

(4.53)

$$\sigma_{zmd} = \frac{2\nu_m(S_1 R_{mc}^2 - S_2 R_{md}^2)}{R_{md}^2 - R_{mc}^2} + \frac{\nu_m \rho_m \omega^2}{4(1-\nu_m)}\left(3 R_{mc}^2 + R_{md}^2 - 2\nu_m(R_{md}^2 + R_{mc}^2)\right) - \Delta_T \alpha_m E_m$$

(4.54)

The corresponding stress equations for the inner and outer cylinders can be derived in a similar fashion and are shown below by equations 4.55 - 4.66.

$$\sigma_{rii} = 0$$

(4.55)

$$\sigma_{\theta ii} = \frac{2 S_1 R_{ic}^2}{R_{ii}^2 - R_{ic}^2} + \frac{\rho_i \omega^2}{4(1-\nu_i)}\left(R_{ii}^2 + 3 R_{ic}^2 - 2\nu_i(R_{ic}^2 + R_{ii}^2)\right)$$

(4.56)

$$\sigma_{zii} = \frac{2\nu_i S_1 R_{ic}^2}{R_{ii}^2 - R_{ic}^2} + \frac{\nu_i \rho_i \omega^2}{4(1-\nu_i)}\left(R_{ii}^2 + 3 R_{ic}^2 - 2\nu_i(R_{ic}^2 + R_{ii}^2)\right) - \Delta_T \alpha_i E_i$$

(4.57)

$$\sigma_{ric} = -S_1$$

(4.58)

$$\sigma_{\theta ic} = \frac{S_1(R_{ic}^2 + R_{ii}^2)}{R_{ii}^2 - R_{ic}^2} + \frac{\rho_i \omega^2}{4(1-\nu_i)}\left(3 R_{ii}^2 + R_{ic}^2 - 2\nu_i(R_{ii}^2 + R_{ic}^2)\right)$$

(4.59)

$$\sigma_{zic} = \frac{2\nu_i S_1 R_{ic}^2}{R_{ii}^2 - R_{ic}^2} + \frac{\nu_i \rho_i \omega^2}{4(1 - \nu_i)} \left(3R_{ii}^2 + R_{ic}^2 - 2\nu_i (R_{ii}^2 + R_{ic}^2) \right) - \Delta_T \alpha_i E_i \tag{4.60}$$

$$\sigma_{rod} = -S_2 \tag{4.61}$$

$$\sigma_{\theta od} = \frac{S_2(R_{od}^2 + R_{oo}^2)}{R_{oo}^2 - R_{od}^2} + \frac{\rho_o \omega^2}{4(1 - \nu_o)} \left(R_{od}^2 + 3R_{oo}^2 - 2\nu_o (R_{oo}^2 + R_{od}^2) \right) \tag{4.62}$$

$$\sigma_{zod} = \frac{2\nu_o S_2 R_{od}^2}{R_{oo}^2 - R_{od}^2} + \frac{\nu_o \rho_o \omega^2}{4(1 - \nu_o)} \left(R_{od}^2 + 3R_{oo}^2 - 2\nu_o (R_{oo}^2 + R_{od}^2) \right) - \Delta_T \alpha_o E_o \tag{4.63}$$

$$\sigma_{roo} = 0 \tag{4.64}$$

$$\sigma_{\theta oo} = \frac{2S_2 R_{od}^2}{R_{oo}^2 - R_{od}^2} + \frac{\rho_o \omega^2}{4(1 - \nu_o)} \left(3R_{od}^2 + R_{oo}^2 - 2\nu_o (R_{od}^2 + R_{oo}^2) \right) \tag{4.65}$$

$$\sigma_{zoo} = \frac{2\nu_o S_2 R_{od}^2}{R_{oo}^2 - R_{od}^2} + \frac{\nu_o \rho_o \omega^2}{4(1 - \nu_o)} \left(3R_{od}^2 + R_{oo}^2 - 2\nu_o (R_{od}^2 + R_{oo}^2) \right) - \Delta_T \alpha_o E_o \tag{4.66}$$

To apply the compatibility conditions shown in equations 4.1 and 4.2, the circumferential strain equations for each interfering surface location are required. Therefore, the corresponding radial, circumferential, and axial stress equations are substituted into equation 3.7. For R_{mc}, equations 4.49 - 4.51 are substituted into equation 3.7, while equations 4.52 - 4.54 are used for R_{md}. The same process is applied to the corresponding equations for the inner and outer cylinders. Equations 4.67 - 4.70 give the circumferential strain equations for R_{ic}, R_{mc}, R_{md}, and R_{od}, respectively.

$$\varepsilon_{\theta ic} = \frac{(\nu_i + 1) \left[S_1 \left(R_{ic}^2 (1 - 2\nu_i) + R_{ii}^2 \right) \right]}{E_i (R_{ii}^2 - R_{ic}^2)}$$
$$+ \frac{\rho_i \omega^2}{4E_i} (\nu_i + 1) \left(3R_{ii}^2 + R_{ic}^2 - 2\nu_i (R_{ic}^2 + R_{ii}^2) \right) + \Delta_T \alpha_i \tag{4.67}$$

$$\varepsilon_{\theta mc} = \frac{(\nu_m + 1) \left[2S_2 R_{md}^2 (\nu_m - 1) + S_1 \left(R_{mc}^2 (1 - 2\nu_m) + R_{md}^2 \right) \right]}{E_m (R_{md}^2 - R_{mc}^2)}$$
$$+ \frac{\rho_m \omega^2}{4E_m} (\nu_m + 1) \left(3R_{md}^2 + R_{mc}^2 - 2\nu_m (R_{mc}^2 + R_{md}^2) \right) + \Delta_T \alpha_m \tag{4.68}$$

$$\varepsilon_{\theta md} = \frac{(\nu_m + 1) \left[2S_1 R_{mc}^2 (\nu_m - 1) + S_2 \left(R_{md}^2 (1 - 2\nu_m) + R_{mc}^2 \right) \right]}{E_m (R_{mc}^2 - R_{md}^2)}$$
$$+ \frac{\rho_m \omega^2}{4E_m} (\nu_m + 1) \left(3R_{mc}^2 + R_{md}^2 - 2\nu_m (R_{md}^2 + R_{mc}^2) \right) + \Delta_T \alpha_m \tag{4.69}$$

$$\varepsilon_{\theta od} = \frac{(\nu_o + 1)\left[S_2\left(R_{od}^2(1 - 2\nu_o) + R_{oo}^2\right)\right]}{E_o(R_{oo}^2 - R_{od}^2)}$$
$$+ \frac{\rho_o \omega^2}{4E_o}(\nu_o + 1)\left(3R_{oo}^2 + R_{od}^2 - 2\nu_o(R_{od}^2 + R_{oo}^2)\right) + \Delta_T \alpha_o \tag{4.70}$$

Submitting equations 4.67 - 4.70 into equations 4.1 and 4.2 leaves two unknown values to be determined, S_1 and S_2, and can be written in the following format:

$$\begin{bmatrix} A & B \\ D & E \end{bmatrix} \begin{bmatrix} S_1 \\ S_2 \end{bmatrix} = \begin{bmatrix} C \\ F \end{bmatrix} \tag{4.71}$$

Where:

$$A = \frac{R_{ic}(\nu_i + 1)\left(R_{ic}^2(1 - 2\nu_i) + R_{ii}^2\right)}{E_i(R_{ic}^2 - R_{ii}^2)} + \frac{R_{mc}(\nu_m + 1)\left(R_{mc}^2(1 - 2\nu_m) + R_{md}^2\right)}{E_m(R_{md}^2 - R_{mc}^2)} \tag{4.72}$$

$$B = \frac{2R_{mc}R_{md}^2(\nu_m^2 - 1)}{E_m(R_{md}^2 - R_{mc}^2)} \tag{4.73}$$

$$C = R_{ic}(\nu_i + 1)\left[\frac{\omega^2 \rho_i}{4E_i}\left(3R_{ii}^2 + R_{ic}^2 - 2\nu_i(R_{ii}^2 + R_{ic}^2)\right) + \Delta_T \alpha_i\right] + R_{ic}$$
$$- R_{mc}(\nu_m + 1)\left[\frac{\omega^2 \rho_m}{4E_m}\left(3R_{mc}^2 + R_{md}^2 - 2\nu_m(R_{md}^2 + R_{mc}^2)\right) + \Delta_T \alpha_m\right] - R_{mc} \tag{4.74}$$

$$D = \frac{2R_{md}R_{mc}^2(\nu_m^2 - 1)}{E_m(R_{mc}^2 - R_{md}^2)} \tag{4.75}$$

$$E = \frac{R_{od}(\nu_o + 1)\left(R_{od}^2(1 - 2\nu_o) + R_{oo}^2\right)}{E_o(R_{od}^2 - R_{oo}^2)} + \frac{R_{md}(\nu_m + 1)\left(R_{md}^2(1 - 2\nu_m) + R_{mc}^2\right)}{E_m(R_{mc}^2 - R_{md}^2)} \tag{4.76}$$

$$F = R_{od}(\nu_o + 1)\left[\frac{\omega^2 \rho_o}{4E_o}\left(3R_{oo}^2 + R_{od}^2 - 2\nu_o(R_{oo}^2 + R_{od}^2)\right) + \Delta_T \alpha_o\right] + R_{od}$$
$$- R_{md}(\nu_m + 1)\left[\frac{\omega^2 \rho_m}{4E_m}\left(3R_{md}^2 + R_{mc}^2 - 2\nu_m(R_{mc}^2 + R_{md}^2)\right) + \Delta_T \alpha_m\right] - R_{md} \tag{4.77}$$

Once the values of S_1 and S_2 have been determined using equation 4.71, they can be substituted back into equations 4.49 - 4.54, or the corresponding equations for the inner and outer cylinders. Therefore, determining the radial, circumferential, and axial stress values at a specified rotor surface.

4.5 Generalised Plane Strain

For the generalised plane strain method, the initial radial and circumferential stress equations shown by equations 4.39 and 4.40 are applicable. However, the axial stress equation differs from the plane strain theory, as shown in Section 3.2.4. The axial stress equation is given by equation 3.22 and is repeated here as equation 4.78, to aid readability.

$$\sigma_z = \frac{-r^2 v \rho \omega^2}{2(1-v)} + C \qquad (4.78)$$

To eliminate the constants from equations 4.39 and 4.40 the same process is followed as shown in in Section 4.4 for the radial and circumferential stress equations. Therefore, equations 4.46 and 4.47 represent the radial and circumferential stress equations for the GPS method. For the axial stress equation, the same process as described in Section 3.2.4 is required. As in the previous sections, the middle cylinder will be focussed on during the theory development.

To eliminate constant C, the axial force in the cylinder must be incorporated into the equation. There must be equilibrium between the internal and external axial forces, expressed by equation 4.79. The external axial force, F_{zm}, is calculated by integrating the axial stress through the cylinder cross section.

$$F_{zm} = 2\pi \int_{R_{mc}}^{R_{md}} r\sigma_z dr \qquad (4.79)$$

By substituting equation 4.78 into equation 4.79, constant C can be determined when carrying out the integration and is shown below.

$$C = \frac{F_{zm}}{\pi(R_{md}^2 - R_{mc}^2)} + \frac{v_m \rho_m \omega^2}{4(1-v_m)}(R_{md}^2 + R_{mc}^2) \qquad (4.80)$$

Constant C can be substituted back into equation 4.78 to eliminate it. Equation 4.81 shows the axial stress equation in terms of the axial force.

$$\sigma_{zm} = \frac{F_{zm}}{\pi(R_{md}^2 - R_{mc}^2)} + \frac{v_m \rho_m \omega^2}{4(1-v_m)}(R_{md}^2 + R_{mc}^2 - 2r^2) \qquad (4.81)$$

The same assumptions discussed in Section 3.2.4 are applied, while the equilibrium and compatibility conditions outlined in Section 3.3.1 are adapted for three cylinders rather than two cylinders. Therefore, the equilibrium and compatibility conditions are:

A. At an interface between the cylinders, there must be force equilibrium in the radial direction.

B. At an interface between the cylinders, there must be circumferential strain compatibility.

C. Assuming sufficient friction, there must be axial strain compatibility between all cylinders. This can be written as:

$$\varepsilon_{zi} = \varepsilon_{zm} = \varepsilon_{zo} \tag{4.82}$$

Where ε_{zi}, ε_{zm}, and ε_{zo} are the axial strains of the inner, middle, and outer cylinders, respectively.

D. There must be axial force equilibrium between the three cylinders. Referencing Figure 4.1, this can be written as:

$$F_{zi} + F_{zm} + F_{zo} = 0 \tag{4.83}$$

$$F_{zm} = -(F_{zi} + F_{zo}) \tag{4.84}$$

Condition *A* is achieved via the use of shrinkage pressures S_1 and S_2 and is applied with the boundary conditions outlined in Section 4.2. Condition *B* requires the application of equations 4.1 and 4.2. Using equations 4.46, 4.47, and 4.81 the radial, circumferential, and axial stress equations are produced for R_{mc} and R_{md}, shown in equations 4.85 - 4.87 and 4.88 - 4.90, respectively. The same process is followed for the inner and outer cylinders.

$$\sigma_{rmc} = -S_1 \tag{4.85}$$

$$\sigma_{\theta mc} = \frac{2S_2 R_{md}^2 - S_1(R_{md}^2 + R_{mc}^2)}{R_{mc}^2 - R_{md}^2} + \frac{\rho_m \omega^2}{4(1 - \nu_m)}\left(3R_{md}^2 + R_{mc}^2 - 2\nu_m(R_{md}^2 + R_{mc}^2)\right) \tag{4.86}$$

$$\sigma_{zmc} = \frac{F_{zm}}{\pi(R_{md}^2 - R_{mc}^2)} + \frac{\nu_m \rho_m \omega^2}{4(1 - \nu_m)}(R_{md}^2 - R_{mc}^2) \tag{4.87}$$

$$\sigma_{rmd} = -S_2 \tag{4.88}$$

$$\sigma_{\theta md} = \frac{S_2(R_{md}^2 + R_{mc}^2) - 2S_1 R_{mc}^2}{R_{mc}^2 - R_{md}^2} + \frac{\rho_m \omega^2}{4(1 - \nu_m)}\left(3R_{mc}^2 + R_{md}^2 - 2\nu_m(R_{md}^2 + R_{mc}^2)\right) \tag{4.89}$$

$$\sigma_{zmd} = \frac{F_{zm}}{\pi(R_{md}^2 - R_{mc}^2)} + \frac{\nu_m \rho_m \omega^2}{4(1 - \nu_m)}(R_{mc}^2 - R_{md}^2) \tag{4.90}$$

By substituting into the Hooke's law equation 3.7, the circumferential strain equations can be found. Equations 4.91 - 4.94 show the circumferential strain equations for R_{ic}, R_{mc}, R_{md}, and R_{od}, respectively.

$$\begin{aligned}\varepsilon_{\theta_{ic}} &= \frac{\pi S_1\left(R_{ic}^2(1 - \nu_i) + R_{ii}^2(1 + \nu_i)\right) + \nu_i F_{zi}}{E_i \pi(R_{ii}^2 - R_{ic}^2)} \\ &+ \frac{\omega^2 \rho_i}{4E_i}\left(R_{ic}^2(1 - \nu_i) + R_{ii}^2(3 + \nu_i)\right) + \Delta T \alpha_i\end{aligned} \tag{4.91}$$

$$\begin{aligned}\varepsilon_{\theta_{mc}} &= \frac{\pi\left[2S_2 R_{md}^2 - S_1\left(R_{mc}^2(1 - \nu_m) + R_{md}^2(1 + \nu_m)\right)\right] + \nu_m F_{zm}}{E_m \pi(R_{mc}^2 - R_{md}^2)} \\ &+ \frac{\omega^2 \rho_m}{4E_m}\left(R_{mc}^2(1 - \nu_m) + R_{md}^2(3 + \nu_m)\right) + \Delta T \alpha_m\end{aligned} \tag{4.92}$$

$$\begin{aligned}\varepsilon_{\theta_{md}} &= \frac{\pi\left[2S_1 R_{mc}^2 - S_2\left(R_{md}^2(1 - \nu_m) + R_{mc}^2(1 + \nu_m)\right)\right] + \nu_m F_{zm}}{E_m \pi(R_{md}^2 - R_{mc}^2)} \\ &+ \frac{\omega^2 \rho_m}{4E_m}\left(R_{md}^2(1 - \nu_m) + R_{mc}^2(3 + \nu_m)\right) + \Delta T \alpha_m\end{aligned} \tag{4.93}$$

$$\begin{aligned}\varepsilon_{\theta_{od}} &= \frac{\pi S_2\left(R_{od}^2(1 - \nu_o) + R_{oo}^2(1 + \nu_o)\right) - \nu_o F_{zo}}{E_o \pi(R_{oo}^2 - R_{od}^2)} \\ &+ \frac{\omega^2 \rho_o}{4E_o}\left(R_{od}^2(1 - \nu_o) + R_{oo}^2(3 + \nu_o)\right) + \Delta T \alpha_o\end{aligned} \tag{4.94}$$

However, to apply condition D at this stage, equation 4.84 is substituted into equations 4.92 and 4.93 to eliminate F_{zm} from the middle cylinder equations, ensuring there are fewer variables to calculate. Therefore, the circumferential strain equations for R_{mc} and R_{md} are shown in equations 4.95 and 4.96, respectively.

$$\varepsilon_{\theta_{mc}} = \frac{\pi\left[2S_2R_{md}^2 - S_1\left(R_{mc}^2(1 - \nu_m) + R_{md}^2(1 + \nu_m)\right)\right] - \nu_m(F_{zi} + F_{zo})}{E_m\pi(R_{mc}^2 - R_{md}^2)}$$
$$+ \frac{\omega^2\rho_m}{4E_m}\left(R_{mc}^2(1 - \nu_m) + R_{md}^2(3 + \nu_m)\right) + \Delta T\alpha_m \tag{4.95}$$

$$\varepsilon_{\theta_{md}} = \frac{\pi\left[2S_1R_{mc}^2 - S_2\left(R_{md}^2(1 - \nu_m) + R_{mc}^2(1 + \nu_m)\right)\right] - \nu_m(F_{zi} + F_{zo})}{E_m\pi(R_{md}^2 - R_{mc}^2)}$$
$$+ \frac{\omega^2\rho_m}{4E_m}\left(R_{md}^2(1 - \nu_m) + R_{mc}^2(3 + \nu_m)\right) + \Delta T\alpha_m \tag{4.96}$$

To complete condition *B*, equations 4.91 and 4.95 are substituted into equation 4.1 while equations 4.94 and 4.96 are substituted into equation 4.2. This results in 4.97 and 4.98 for interfaces *c* and *d*, respectively.

$$S_1\Bigg[R_{ic}E_m(R_{md}^2 - R_{mc}^2)\left(R_{ic}^2(1 - \nu_i) + R_{ii}^2(1 + \nu_i)\right)$$
$$- R_{mc}E_i(R_{ii}^2 - R_{ic}^2)\left(R_{md}^2(1 + \nu_m) + R_{mc}^2(1 - \nu_m)\right)\Bigg] + S_2\Bigg[2R_{md}^2R_{mc}E_i(R_{ii}^2 - R_{ic}^2)\Bigg]$$
$$- \frac{F_{zo}}{\pi}\Bigg[R_{mc}E_i\nu_m(R_{ii}^2 - R_{ic}^2)\Bigg] + \frac{F_{zi}}{\pi}\Bigg[R_{ic}E_m\nu_i(R_{md}^2 - R_{mc}^2) - R_{mc}E_i\nu_m(R_{ii}^2 - R_{ic}^2)\Bigg]$$
$$= (R_{ii}^2 - R_{ic}^2)(R_{md}^2 - R_{mc}^2)\Bigg[\frac{R_{mc}E_i\rho_m\omega^2}{4}\left(R_{md}^2(3 + \nu_m) + R_{mc}^2(1 - \nu_m)\right)$$
$$- \frac{R_{ic}E_m\rho_i\omega^2}{4}\left(R_{ii}^2(3 + \nu_i) + R_{ic}^2(1 - \nu_i)\right)$$
$$+ E_mE_i\left(R_{mc}(1 + \Delta T\alpha_m) - R_{ic}(1 + \Delta T\alpha_i)\right)\Bigg]$$

$$\tag{4.97}$$

$$S_2\Bigg[R_{md}E_o(R_{oo}^2 - R_{od}^2)\left(R_{mc}^2(1 + \nu_m) + R_{md}^2(1 - \nu_m)\right)$$
$$- R_{od}E_m(R_{mc}^2 - R_{md}^2)\left(R_{od}^2(1 - \nu_o) + R_{oo}^2(1 + \nu_o)\right)\Bigg] - S_1\Bigg[2R_{mc}^2R_{md}E_o(R_{oo}^2 - R_{od}^2)\Bigg]$$
$$- \frac{F_{zi}}{\pi}\Bigg[2R_{md}E_o\nu_m(R_{oo}^2 - R_{od}^2)\Bigg] - \frac{F_{zo}}{\pi}\Bigg[R_{md}E_o\nu_m(R_{oo}^2 - R_{od}^2) + R_{od}E_m\nu_o(R_{mc}^2 - R_{md}^2)\Bigg]$$
$$= (R_{oo}^2 - R_{od}^2)(R_{mc}^2 - R_{md}^2)\Bigg[\frac{R_{od}E_m\rho_o\omega^2}{4}\left(R_{oo}^2(3 + \nu_o) + R_{od}^2(1 - \nu_o)\right)$$
$$- \frac{R_{md}E_o\rho_m\omega^2}{4}\left(R_{mc}^2(3 + \nu_m) + R_{md}^2(1 - \nu_m)\right)$$
$$+ E_mE_o\left(R_{od}(1 + \Delta T\alpha_o) - R_{md}(1 + \Delta T\alpha_m)\right)\Bigg]$$

$$\tag{4.98}$$

To enforce condition C, the axial strain equations for the inner, middle, and outer cylinders must be derived. For the middle cylinder, equations 4.46, 4.47, and 4.81 are substituted into Hooke's law equation 3.8, producing equation 4.99 shown below. The corresponding equations for the inner and outer cylinders are used in the same process to produce the axial strain equations for the inner outer cylinders which are shown in equations 4.100 and 4.101 respectively.

$$\varepsilon_{zm} = \frac{1}{E_m}\left(\frac{F_{zm}}{\pi(R_{md}^2 - R_{mc}^2)} - \frac{2\nu_m(S_1 R_{mc}^2 - S_2 R_{md}^2)}{R_{md}^2 - R_{mc}^2} - \frac{\omega^2 \rho_m \nu_m(R_{md}^2 + R_{mc}^2)}{2}\right) + \Delta T \alpha_m$$

(4.99)

$$\varepsilon_{zi} = \frac{1}{E_i}\left(\frac{F_{zi}}{\pi(R_{ic}^2 - R_{ii}^2)} - \frac{2\nu_m S_1 R_{ic}^2}{R_{ii}^2 - R_{ic}^2} - \frac{\omega^2 \rho_i \nu_i(R_{ic}^2 + R_{ii}^2)}{2}\right) + \Delta T \alpha_i$$

(4.100)

$$\varepsilon_{zo} = \frac{1}{E_o}\left(\frac{F_{zo}}{\pi(R_{oo}^2 - R_{od}^2)} - \frac{2\nu_o S_2 R_{od}^2}{R_{oo}^2 - R_{od}^2} - \frac{\omega^2 \rho_o \nu_o(R_{oc}^2 + R_{oo}^2)}{2}\right) + \Delta T \alpha_o$$

(4.101)

Ensuring that condition D is satisfied requires equation 4.84 to be substituted into equation 4.99, producing equation 4.102.

$$\varepsilon_{zm} = \frac{1}{E_m}\left(\frac{-(F_{zi} + F_{zo})}{\pi(R_{md}^2 - R_{mc}^2)} - \frac{2\nu_m(S_1 R_{mc}^2 - S_2 R_{md}^2)}{R_{md}^2 - R_{mc}^2} - \frac{\omega^2 \rho_m \nu_m(R_{md}^2 + R_{mc}^2)}{2}\right) + \Delta T \alpha_m$$

(4.102)

To enforce condition C, equation 4.82 is first split into equations 4.103 and 4.104.

$$\varepsilon_{zi} = \varepsilon_{zm}$$ (4.103)

$$\varepsilon_{zm} = \varepsilon_{zo}$$ (4.104)

Equations 4.100 - 4.102 are then substituted into equations 4.103 and 4.104 to enforce condition C and produce equations 4.105 and 4.106 respectively.

$$\begin{aligned}
&S_1\left[2\left(\nu_i E_m R_{ic}^2(R_{mc}^2 - R_{md}^2) - \nu_m E_i R_{mc}^2(R_{ic}^2 - R_{ii}^2)\right)\right] + S_2\left[2\nu_m E_i R_{md}^2(R_{ic}^2 - R_{ii}^2)\right] \\
&- \frac{F_{zo}}{\pi}\left[E_i(R_{ic}^2 - R_{ii}^2)\right] + \frac{F_{zi}}{\pi}\left[E_m(R_{mc}^2 - R_{md}^2) - E_i(R_{ic}^2 - R_{ii}^2)\right] \\
&= (R_{ic}^2 - R_{ii}^2)(R_{mc}^2 - R_{md}^2)\left[\frac{\omega^2}{2}\left(\rho_i \nu_i E_m(R_{ii}^2 + R_{ic}^2) - \rho_m \nu_m E_i(R_{mc}^2 + R_{md}^2)\right)\right. \\
&\left. + E_m E_i \Delta T(\alpha_m - \alpha_i)\right]
\end{aligned}$$

(4.105)

$$S_2 \left[2 \left(\nu_m E_o R_{md}^2 (R_{od}^2 - R_{oo}^2) + \nu_o E_m R_{od}^2 (R_{mc}^2 - R_{md}^2) \right) \right] - S_1 \left[2\nu_m E_o R_{mc}^2 (R_{od}^2 - R_{oo}^2) \right]$$

$$- \frac{F_{zi}}{\pi} \left[E_o (R_{od}^2 - R_{oo}^2) \right] - \frac{F_{zo}}{\pi} \left[E_m (R_{mc}^2 - R_{md}^2) + E_o (R_{od}^2 - R_{oo}^2) \right]$$

$$= (R_{od}^2 - R_{oo}^2)(R_{mc}^2 - R_{md}^2) \left[\frac{\omega^2}{2} \left(\rho_o \nu_o E_m (R_{od}^2 + R_{oo}^2) - \rho_m \nu_m E_o (R_{mc}^2 + R_{md}^2) \right) \right.$$

$$\left. + E_m E_o \Delta T (\alpha_m - \alpha_o) \right]$$

$$\tag{4.106}$$

Equations 4.97, 4.98, 4.105, and 4.106 use the derived GPS stress and strain equations while implementing the four equilibrium and compatibility conditions, A, B, C, and D. The axial force for the middle cylinder, F_{zm}, has been eliminated, leaving four unknown variables to determine: S_1; S_2; F_{zi}; and F_{zo}. Equations 4.97, 4.98, 4.105, and 4.106 can therefore be written as:

$$\begin{bmatrix} F & G & H & I \\ K & L & M & N \\ P & Q & R & T \\ V & W & X & Y \end{bmatrix} \begin{bmatrix} F_{zo} \\ F_{zi} \\ S_2 \\ S_1 \end{bmatrix} = \begin{bmatrix} J \\ O \\ U \\ Z \end{bmatrix} \tag{4.107}$$

Where:

$$F = -\frac{1}{\pi} \left[R_{mc} E_i \nu_m (R_{ii}^2 - R_{ic}^2) \right] \tag{4.108}$$

$$G = \frac{1}{\pi} \left[R_{ic} E_m \nu_i (R_{mc}^2 - R_{md}^2) - R_{mc} E_i \nu_m (R_{ii}^2 - R_{ic}^2) \right] \tag{4.109}$$

$$H = 2R_{md}^2 R_{mc} E_i (R_{ii}^2 - R_{ic}^2) \tag{4.110}$$

$$I = R_{ic} E_m (R_{md}^2 - R_{mc}^2) \left(R_{ic}^2 (1 - \nu_i) + R_{ii}^2 (1 + \nu_i) \right)$$

$$- R_{mc} E_m (R_{ii}^2 - R_{ic}^2) \left(R_{md}^2 (1 + \nu_m) + R_{mc}^2 (1 - \nu_m) \right) \tag{4.111}$$

$$J = (R_{ii}^2 - R_{ic}^2)(R_{md}^2 - R_{mc}^2) \left[\frac{R_{mc} E_i \rho_m \omega^2}{4} \left(R_{md}^2 (3 + \nu_m) + R_{mc}^2 (1 - \nu_m) \right) \right.$$

$$- \frac{R_{ic} E_m \rho_i \omega^2}{4} \left(R_{ii}^2 (3 + \nu_i) + R_{ic}^2 (1 - \nu_i) \right)$$

$$\left. + E_m E_i \left(R_{mc} (1 + \Delta T \alpha_m) - R_{ic} (1 + \Delta T \alpha_i) \right) \right] \tag{4.112}$$

$$K = -\frac{1}{\pi}\left[R_{md}E_o\nu_m(R_{oo}^2 - R_{od}^2) + R_{od}E_m\nu_o(R_{mc}^2 - R_{md}^2)\right]$$

(4.113)

$$L = -\frac{1}{\pi}\left[2R_{md}E_o\nu_m(R_{oo}^2 - R_{od}^2)\right]$$

(4.114)

$$M = R_{md}E_o(R_{oo}^2 - R_{od}^2)\left(R_{mc}^2(1 + \nu_m) + R_{md}^2(1 - \nu_m)\right)$$
$$- R_{od}E_m(R_{mc}^2 - R_{md}^2)\left(R_{od}^2(1 - \nu_o) + R_{oo}^2(1 + \nu_o)\right)$$

(4.115)

$$N = 2R_{mc}^2 R_{md}E_o(R_{oo}^2 - R_{od}^2)$$

(4.116)

$$O = (R_{oo}^2 - R_{od}^2)(R_{mc}^2 - R_{md}^2)\left[\frac{R_{od}E_m\rho_o\omega^2}{4}\left(R_{oo}^2(3 + \nu_o) + R_{od}^2(1 - \nu_o)\right)\right.$$
$$- \frac{R_{md}E_o\rho_m\omega^2}{4}\left(R_{mc}^2(3 + \nu_m) + R_{md}^2(1 - \nu_m)\right)$$
$$\left. + E_m E_o\left(R_{od}(1 + \Delta T\alpha_o) - R_{md}(1 + \Delta T\alpha_m)\right)\right]$$

(4.117)

$$P = -\frac{1}{\pi}\left[E_i(R_{ic}^2 - R_{ii}^2)\right]$$

(4.118)

$$Q = \frac{1}{\pi}\left[E_m(R_{mc}^2 - R_{md}^2) - E_i(R_{ic}^2 - R_{ii}^2)\right]$$

(4.119)

$$R = 2\nu_m E_i R_{md}^2(R_{ic}^2 - R_{ii}^2)$$

(4.120)

$$T = 2\left[\nu_i E_m R_{ic}^2(R_{mc}^2 - R_{md}^2) - \nu_m E_i R_{mc}^2(R_{ic}^2 - R_{ii}^2)\right]$$

(4.121)

$$U = (R_{ic}^2 - R_{ii}^2)(R_{mc}^2 - R_{md}^2)\left[\frac{\omega^2}{2}\left(\rho_i\nu_i E_m(R_{ii}^2 + R_{ic}^2) - \rho_m\nu_m E_i(R_{mc}^2 + R_{md}^2)\right)\right.$$
$$\left. + E_m E_i \Delta T(\alpha_m - \alpha_i)\right]$$

(4.122)

$$V = -\frac{1}{\pi}\left[E_m(R_{mc}^2 - R_{md}^2) + E_o(R_{od}^2 - R_{oo}^2)\right]$$

(4.123)

$$W = -\frac{1}{\pi}\left[E_o(R_{od}^2 - R_{oo}^2)\right]$$

(4.124)

$$X = 2\left[\nu_m E_o R_{md}^2(R_{od}^2 - R_{oo}^2) + \nu_o E_m R_{od}^2(R_{mc}^2 - R_{md}^2)\right]$$

(4.125)

$$Y = -2\nu_m E_o R_{mc}^2(R_{od}^2 - R_{oo}^2)$$

(4.126)

$$Z = (R_{od}^2 - R_{oo}^2)(R_{mc}^2 - R_{md}^2)\left[\frac{\omega^2}{2}\left(\rho_o\nu_o E_m(R_{od}^2 + R_{oo}^2) - \rho_m\nu_m E_o(R_{mc}^2 + R_{md}^2)\right)\right.$$
$$\left. + E_m E_o \Delta T(\alpha_m - \alpha_o)\right]$$

(4.127)

The unknown terms can then be found by inverting the matrix. Having determined these terms, stresses at any location can be found by referring to equations 4.46, 4.47, and 4.81 and their equivalents for the inner and outer cylinders.

4.6 Results

4.6.1 Background

Determining whether the three-cylinder analyses from Section 4.5 had been successfully derived required a comparison against the corresponding, established two-cylinder theory. By simulating a two-cylinder rotor within the three-cylinder theories, results can be compared across the two-cylinder and three-cylinder theories. Matching results would verify the correct derivation of the three-cylinder theory. The method was used to verify the plane stress, plane strain, and GPS methodologies.

To achieve this, the inner and middle cylinders in the three-cylinder theories represented the inner and outer cylinders of the two-cylinder theory. The shrinkage pressure, S_2, was removed to avoid the outer cylinder affecting the stress results and the condition shown in equation 4.2 was also removed from the equations for all three theories. For the GPS theory, the outer cylinder terms were removed from equations 4.82 and 4.84.

Three rotor topologies were compared at the following four operating conditions to confirm the accuracy of the derived three-cylinder theories:

- Stationary and ambient temperature.
- Maximum speed and ambient temperature.
- Stationary at maximum temperature.
- Maximum speed and temperature.

The materials used for the inner and middle cylinders were 416 stainless steel and neodymium magnet (NdFeB). The material properties were taken from Burnand et al. [11] and are shown in Table 4.1, while the three rotor topology parameters are detailed in Table 4.2. The rotor speed was limited by point at which the rotor separated due to excessive centrifugal forces.

Material Property	Inner Cylinder	Middle Cylinder
Young's Modulus (*GPa*)	215	160
Poisson's Ratio	0.29	0.24
Density (*kg/m³*)	7700	7500
Coefficient of Thermal Expansion (*K⁻¹*)	1×10^{-5}	5×10^{-6}

TABLE 4.1: Material properties for each cylinder.

Rotor Element	Thin Rotor Model	Medium Rotor Model	Thick Rotor Model
R_{ii} (*mm*)	3	5	7
R_{ic} (*mm*)	5.002	10.004	14.006
R_{mc} (*mm*)	5	10	14
R_{md} (*mm*)	8	15	21
Inner Cylinder Thickness (*mm*)	2.002	5.004	7.006
Middle Cylinder Thickness (*mm*)	3	5	7
Interference at c (*mm*)	0.002	0.004	0.006
Maximum Temperature (*ᵒC*)	100	100	100
Maximum Speed (*rpm*)	80	60	40

TABLE 4.2: Model Rotor Parameters.

For the results tables, a percentage difference to the two-cylinder result was calculated for each three-cylinder results, to enable easy comparison across each theory. Percentage difference results were also colour coded to highlight how close they were to the two-cylinder results. Dark green indicates a difference of less than 1% and the colour changes from green to yellow, then red as the difference increases. Red indicates a difference of 50% or more.

Results may not be identical due to the use of a common radius in the two-cylinder equations. A common radius between the inner and middle cylinders is determined by averaging the interference at c. However, in the three-cylinder equations, the specific rotor dimensions for the inner and middle cylinder surfaces at c are used.

4.6.2 Plane Stress

The results used to compare the three-cylinder and two-cylinder plane stress theories were the interference pressure, S_1; the circumferential stress at each cylinder

surface, $\sigma_{\theta ii}$, $\sigma_{\theta ic}$, $\sigma_{\theta mc}$, and $\sigma_{\theta md}$; and the Von Mises stress at each cylinder surface, σ_{VMii}, σ_{VMic}, σ_{VMmc}, and σ_{VMmd}. These stresses are critical to the rotor design and must be accurately predicted. As plane stress assumes axial stress is zero, the axial stresses at each surface have not been included. The results are shown in Tables 4.3 - 4.5, which represent the thin, medium, and thick rotor topologies, respectively. The results show the percentage difference in stress values produced by the three-cylinder equations compared to the two-cylinder equations.

Tables 4.3 - 4.5 shows that the three-cylinder plane stress equations were derived correctly as the stress results were very closely aligned with the two-cylinder plane stress results. Over 97% of the results across all topologies and operating conditions were within 0.1% of the two-cylinder results. Although the results are extremely similar, there is a trend showing the accuracy of the results appears to decrease as

Stress	$\omega(0krpm)$ $\Delta T(0^oC)$	$\omega(0krpm)$ $\Delta T(100^oC)$	$\omega(80krpm)$ $\Delta T(0^oC)$	$\omega(80krpm)$ $\Delta T(100^oC)$
S_1	0.04	0.04	0.05	0.06
$\sigma_{\theta ii}$	0.01	0.01	0.03	0.04
$\sigma_{\theta ic}$	0.00	0.00	0.02	0.03
$\sigma_{\theta mc}$	0.00	0.00	0.00	0.01
$\sigma_{\theta md}$	0.03	0.03	0.02	0.01
σ_{VMii}	0.01	0.01	0.03	0.04
σ_{VMic}	0.00	0.00	0.03	0.03
σ_{VMmc}	0.01	0.01	0.01	0.02
σ_{VMmd}	0.03	0.03	0.02	0.01

TABLE 4.3: Percentage difference between plane stress results for three and two cylinder theories for thin rotor topology.

Stress	$\omega(0krpm)$ $\Delta T(0^oC)$	$\omega(0krpm)$ $\Delta T(100^oC)$	$\omega(60krpm)$ $\Delta T(0^oC)$	$\omega(60krpm)$ $\Delta T(100^oC)$
S_1	0.04	0.04	0.09	0.09
$\sigma_{\theta ii}$	0.02	0.02	0.02	0.11
$\sigma_{\theta ic}$	0.02	0.02	0.03	0.09
$\sigma_{\theta mc}$	0.01	0.01	0.00	0.02
$\sigma_{\theta md}$	0.04	0.04	0.02	0.00
σ_{VMii}	0.02	0.02	0.02	0.11
σ_{VMic}	0.02	0.02	0.01	0.09
σ_{VMmc}	0.00	0.00	0.01	0.03
σ_{VMmd}	0.04	0.04	0.02	0.00

TABLE 4.4: Percentage difference between plane stress results for three and two cylinder theories for medium rotor topology.

Stress	$\omega(0krpm)$ $\Delta T(0^oC)$	$\omega(0krpm)$ $\Delta T(100^oC)$	$\omega(40krpm)$ $\Delta T(0^oC)$	$\omega(40krpm)$ $\Delta T(100^oC)$
S_1	0.04	0.04	0.08	0.09
$\sigma_{\theta ii}$	0.03	0.03	0.02	0.09
$\sigma_{\theta ic}$	0.02	0.02	1.34	0.08
$\sigma_{\theta mc}$	0.01	0.01	0.00	0.02
$\sigma_{\theta md}$	0.04	0.04	0.02	0.01
σ_{VMii}	0.03	0.03	0.02	0.09
σ_{VMic}	0.02	0.02	0.05	0.08
σ_{VMmc}	0.00	0.00	0.01	0.03
σ_{VMmd}	0.04	0.04	0.02	0.01

TABLE 4.5: Percentage difference between plane stress results for three and two cylinder theories for thick rotor topology.

speed and temperature effects are incorporated. This is likely due to these factors exacerbating any difference due not using a common radius like the two-cylinder equations, as discussed in Section 4.6.1.

4.6.3   Plane Strain

The same results were extracted for the plane strain comparisons, shown in Tables 4.6 - 4.8 which represent the thin, medium, and thick rotor topologies, respectively. However, as plane strain acknowledges the presence of axial stress, the axial stresses at each cylinder surface, σ_{zii}, σ_{zic}, σ_{zmc}, and σ_{zmd}, were also included.

Stress	$\omega(0krpm)$ $\Delta T(0^oC)$	$\omega(0krpm)$ $\Delta T(100^oC)$	$\omega(80krpm)$ $\Delta T(0^oC)$	$\omega(80krpm)$ $\Delta T(100^oC)$
S_1	0.04	0.06	0.05	0.09
$\sigma_{\theta ii}$	0.01	0.04	0.02	0.07
$\sigma_{\theta ic}$	0.00	0.03	0.02	0.06
$\sigma_{\theta mc}$	0.00	0.02	0.01	0.04
$\sigma_{\theta md}$	0.03	0.01	0.02	0.01
σ_{zii}	0.01	0.01	0.02	0.01
σ_{zic}	0.01	0.01	0.03	0.01
σ_{zmc}	0.03	0.00	0.01	0.00
σ_{zmd}	0.03	0.00	0.02	0.00
σ_{VMii}	0.01	0.01	0.02	0.01
σ_{VMic}	0.01	0.01	0.00	0.01
σ_{VMmc}	0.01	0.02	0.01	0.03
σ_{VMmd}	0.03	0.00	0.02	0.00

TABLE 4.6: Percentage difference between plane strain results for three and two cylinder theories for thin rotor topology.

Stress	$\omega(0krpm)$ $\Delta T(0^oC)$	$\omega(0krpm)$ $\Delta T(100^oC)$	$\omega(60krpm)$ $\Delta T(0^oC)$	$\omega(60krpm)$ $\Delta T(100^oC)$
S_1	0.04	0.06	0.09	0.13
$\sigma_{\theta ii}$	0.02	0.05	0.02	0.15
$\sigma_{\theta ic}$	0.02	0.04	0.06	0.13
$\sigma_{\theta mc}$	0.01	0.02	0.00	0.05
$\sigma_{\theta md}$	0.04	0.01	0.02	0.02
σ_{zii}	0.02	0.01	0.02	0.01
σ_{zic}	0.02	0.01	4.53	0.01
σ_{zmc}	0.04	0.00	0.00	0.01
σ_{zmd}	0.04	0.00	0.02	0.01
σ_{VMii}	0.02	0.01	0.02	0.00
σ_{VMic}	0.00	0.01	0.01	0.01
σ_{VMmc}	0.00	0.02	0.01	0.05
σ_{VMmd}	0.04	0.00	0.02	0.01

TABLE 4.7: Percentage difference between plane strain results for three and two cylinder theories for medium rotor topology.

Stress	$\omega(0krpm)$ $\Delta T(0^oC)$	$\omega(0krpm)$ $\Delta T(100^oC)$	$\omega(40krpm)$ $\Delta T(0^oC)$	$\omega(40krpm)$ $\Delta T(100^oC)$
S_1	0.04	0.06	0.08	0.12
$\sigma_{\theta ii}$	0.03	0.05	0.04	0.13
$\sigma_{\theta ic}$	0.02	0.04	0.20	0.12
$\sigma_{\theta mc}$	0.01	0.02	0.00	0.05
$\sigma_{\theta md}$	0.04	0.01	0.02	0.02
σ_{zii}	0.03	0.01	0.04	0.01
σ_{zic}	0.03	0.01	0.11	0.01
σ_{zmc}	0.04	0.00	0.00	0.01
σ_{zmd}	0.04	0.00	0.02	0.01
σ_{VMii}	0.03	0.01	0.04	0.00
σ_{VMic}	0.00	0.01	0.03	0.01
σ_{VMmc}	0.00	0.02	0.01	0.04
σ_{VMmd}	0.04	0.01	0.02	0.01

TABLE 4.8: Percentage difference between plane strain results for three and two cylinder theories for thick rotor topology.

The percentage differences between the two-cylinder and three-cylinder plane strain theories show that the three-cylinder equations have been derived correctly. Over 99% of all results across three topologies and four operating conditions were within 0.2% of the two-cylinder results. Only one results stands out as an outlier, shown clearly in Table 4.7. At 4.53% away from the two-cylinder theory, it is much further away than all other results. However, this is due to the stress result being predicted to be at least two orders of magnitude smaller than all other stress results

sampled. Therefore, while the stress value difference between the two-cylinder and three-cylinder equations is small, the percentage difference is made worse due to the small stress numerical value.

4.6.4 Generalised Plane Strain

The GPS results are shown in Tables 4.9 - 4.11, which represent the thin, medium, and thick rotor topologies, respectively. GPS theory acknowledges the existence of

Stress	$\omega(0krpm)$ $\Delta T(0^oC)$	$\omega(0krpm)$ $\Delta T(100^oC)$	$\omega(80krpm)$ $\Delta T(0^oC)$	$\omega(80krpm)$ $\Delta T(100^oC)$
S_1	0.03	0.03	0.04	0.04
$\sigma_{\theta ii}$	0.01	0.01	0.00	0.01
$\sigma_{\theta ic}$	0.00	0.00	0.00	0.00
$\sigma_{\theta od}$	0.00	0.00	0.00	0.00
$\sigma_{\theta oo}$	0.03	0.03	0.03	0.03
σ_{zii}	0.01	0.01	0.03	0.01
σ_{zic}	0.01	0.01	0.01	0.01
σ_{zod}	0.02	0.02	0.02	0.02
σ_{zoo}	0.02	0.02	0.01	0.02
σ_{VMii}	0.01	0.01	0.00	0.00
σ_{VMic}	0.00	0.04	0.05	0.04
σ_{VMod}	0.01	0.01	0.00	0.01
σ_{VMoo}	0.03	0.02	0.03	0.02

TABLE 4.9: Percentage difference between GPS results for three and two cylinder theories for thin rotor topology.

Stress	$\omega(0krpm)$ $\Delta T(0^oC)$	$\omega(0krpm)$ $\Delta T(100^oC)$	$\omega(60krpm)$ $\Delta T(0^oC)$	$\omega(60krpm)$ $\Delta T(100^oC)$
S_1	0.04	0.04	0.06	0.04
$\sigma_{\theta ii}$	0.02	0.02	0.03	0.02
$\sigma_{\theta ic}$	0.02	0.02	0.02	0.02
$\sigma_{\theta od}$	0.01	0.01	0.00	0.00
$\sigma_{\theta oo}$	0.04	0.04	0.03	0.03
σ_{zii}	0.01	0.01	0.06	0.01
σ_{zic}	0.01	0.01	0.01	0.01
σ_{zod}	0.01	0.01	0.01	0.01
σ_{zoo}	0.01	0.01	0.05	0.01
σ_{VMii}	0.03	0.02	0.01	0.01
σ_{VMic}	0.03	0.05	0.01	0.04
σ_{VMod}	0.00	0.01	0.00	0.00
σ_{VMoo}	0.04	0.02	0.02	0.03

TABLE 4.10: Percentage difference between GPS results for three and two cylinder theories for medium rotor topology.

Stress	$\omega(0krpm)$ $\Delta T(0^oC)$	$\omega(0krpm)$ $\Delta T(100^oC)$	$\omega(40krpm)$ $\Delta T(0^oC)$	$\omega(40krpm)$ $\Delta T(100^oC)$
S_1	0.04	0.04	0.05	0.04
$\sigma_{\theta ii}$	0.02	0.02	0.06	0.02
$\sigma_{\theta ic}$	0.02	0.02	0.07	0.02
$\sigma_{\theta od}$	0.01	0.01	0.00	0.01
$\sigma_{\theta oo}$	0.04	0.04	0.03	0.03
σ_{zii}	0.01	0.01	0.04	0.01
σ_{zic}	0.01	0.01	0.01	0.01
σ_{zod}	0.01	0.01	0.01	0.01
σ_{zoo}	0.01	0.01	0.03	0.01
σ_{VMii}	0.03	0.02	0.01	0.00
σ_{VMic}	0.03	0.05	0.03	0.04
σ_{VMod}	0.00	0.01	0.00	0.00
σ_{VMoo}	0.04	0.03	0.03	0.03

TABLE 4.11: Percentage difference between GPS results for three and two cylinder theories for thick rotor topology.

axial stress, like plane strain theory, as discussed in Section 4.6.3. Therefore, the same critical stresses extracted for the plane strain comparison, were used to compare the three-cylinder to the two-cylinder GPS equations.

The percentage differences between the three-cylinder and two-cylinder equations for the GPS theory are slightly smaller than either the plane stress or plane strain results. With 100% of results within 0.1% of the two-cylinder results, the derivation of the three-cylinder equations has been shown to have been completed successfully. There appears to be a trend of the percentage difference GPS results worsening marginally with thicker rotor topologies. However, this will be due to the increased interference level in the thick rotor topology, thus creating a larger difference to the common radius used in the two-cylinder equations. To test the effect the increased interference level has on the disparity between the three and two-cylinder methodologies, the use of R_{ic} and R_{mc} was removed from the three-cylinder theory. Both terms were replaced with a common radius, R_c, of 14.003 mm and the comparison of the GPS theory for the thick rotor was repeated, shown below in Table 4.12. By removing the use of a common radius from the two-cylinder theory, the results difference between the two-cylinder and three-cylinder GPS methodologies has been eliminated. This further proves that the three-cylinder theory has been correctly derived.

Stress	$\omega(0krpm)$ $\Delta T(0^oC)$	$\omega(0krpm)$ $\Delta T(100^oC)$	$\omega(40krpm)$ $\Delta T(0^oC)$	$\omega(40krpm)$ $\Delta T(100^oC)$
S_1	0.00	0.00	0.00	0.00
$\sigma_{\theta ii}$	0.00	0.00	0.00	0.00
$\sigma_{\theta ic}$	0.00	0.00	0.00	0.00
$\sigma_{\theta od}$	0.00	0.00	0.00	0.00
$\sigma_{\theta oo}$	0.00	0.00	0.00	0.00
σ_{zii}	0.00	0.00	0.00	0.00
σ_{zic}	0.00	0.00	0.00	0.00
σ_{zod}	0.00	0.00	0.00	0.00
σ_{zoo}	0.00	0.00	0.00	0.00
σ_{VMii}	0.00	0.00	0.00	0.00
σ_{VMic}	0.00	0.00	0.00	0.00
σ_{VMod}	0.00	0.00	0.00	0.00
σ_{VMoo}	0.00	0.00	0.00	0.00

TABLE 4.12: Percentage difference between GPS results for three and two cylinder theories for thick rotor topology.

4.7 Summary

After deriving and comparing the three-cylinder models for GPS, plane strain, and plane stress, the key outcomes of this chapter were extracted and compiled below. The listed outcomes enable the project to progress to the next stage with confidence in the current work.

- The plane stress, plane strain, and GPS methodologies have all been successfully derived for the use of three-cylinder rotors.

- The accuracies of each methodology derived for three-cylinder rotors have been verified against the corresponding two-cylinder theory.

- The difference between the two- and three-cylinder theories increases marginally with rotor thickness due to the higher levels of interference. However, the effect is minimal and the three-cylinder theory remained within 0.1% of the two-cylinder theory.

- The derived three-cylinder plane stress, plane strain, and GPS equations can be compared against FEA simulations with confidence that they are correctly predicting rotor stresses with respect to the assumptions used in the theory.

5 Finite Element Analysis

5.1 Introduction

After successfully deriving equations for three-cylinder stress analysis across plane stress, plane strain, and generalised plane strain (GPS) methodologies, finite element analysis (FEA) simulations were required to assess the accuracy of each method. For the theory to be used with confidence, the results must closely align with FEA simulations. Much of the work completed in this chapter have previously been published by the author. Sections 5.2.1 and 5.3 have previously been outlined by Mallin and Barrans [154] where most of the tables, figures and text appears. However, this chapter is augmented with further figures and text content to explore the work in greater detail. Sections 5.2.2 and 5.2.3 have also been added to supplement the published work in this chapter.

5.2 Finite Element Analysis Model

5.2.1 Model Set Up

To investigate the accuracy and possible limitations of the theoretical approaches, a range of finite element analyses were carried out on six rotors with the material properties and dimensions shown in Tables 5.1 and 5.2, respectively. The materials used for the inner and middle cylinders remained the same from Chapter 4 while grade 5 titanium was used for the outer cylinder, taken from Burnand et al. [11]. Long and short versions of a rotor topology were selected recognizing that, as demonstrated by Barrans et al. [10], the length to diameter ratio of the rotor can have a significant effect on the stress distribution. The short rotor aspect ratios, defined as length to outer radius ratio, were 2, 2.1, and 2.2 for the thin, medium, and thick rotor topologies, respectively. The long rotor aspect ratios were, 7, 7.4, and 7.4 for the thin, medium, and thick rotor topologies, respectively. Where the thin, medium, and thick rotor topologies refer to the total wall thickness between R_{ii} and R_{oo}. However,

the ratios of the individual cylinder thicknesses within each rotor have little variation across the three topologies. This decision ensured that the significant differences between each model were either the thickness or the length and the results were not adversely affected by having many differences between each model e.g., a rotor topology having a larger middle cylinder ratio could affect the rotor behaviour compared to other models. Therefore, when comparing the results, the effect of the rotor thickness or length could be accurately determined.

Material Property	Inner Rotor Cylinder	Middle Rotor Cylinder	Outer Rotor Cylinder
Young's Modulus (GPa)	215	160	114
Poisson's Ratio	0.29	0.24	0.36
Density (kg/m^3)	7700	7500	4400
Coefficient of Thermal Expansion (K^{-1})	1×10^{-5}	5×10^{-6}	9×10^{-6}

TABLE 5.1: Material properties for each cylinder.

Rotor Element	Thin Rotor Model	Medium Rotor Model	Thick Rotor Model
R_{ii} (mm)	3	5	7
R_{ic} (mm)	5.002	10.004	14.006
R_{mc} (mm)	5	10	14
R_{md} (mm)	8.04	15.11	21.19
R_{od} (mm)	8	15	21
R_{oo} (mm)	10	19	27
Short Rotor Length (mm)	20	40	60
Long Rotor Length (mm)	70	140	200
Inner Cylinder Thickness (mm)	2.002	5.004	7.006
Middle Cylinder Thickness (mm)	3.04	5.11	7.19
Outer Cylinder Thickness (mm)	2	4	6
Interference at c (mm)	0.002	0.004	0.006
Interference at d (mm)	0.04	0.11	0.19
Maximum Temperature ($^o C$)	100	100	100
Maximum Speed (rpm)	80	70	60

TABLE 5.2: Model Rotor Parameters.

The rotors were defined as running at 60 - 80 krpm, with a 100^oC temperature rise whilst both stationary and at full speed. The rotor speeds were limited by the centrifugal forces causing rotor separation. Preliminary checks using the theoretical analyses developed in Chapter 4 ensured that the selected rotors would operate at the speed and temperature range without failing due to excessive stress or cylinder

separation. The material properties were taken from Burnand et al. [11] and used in all cases. The materials used for the inner, middle, and outer cylinders was Stainless Steel 416 , Neodymium, and Titanium Grade 5. The outer sleeve is required to be low density to avoid excessive centrifugal forces, but it must also have a high yield stress to withstand the rotor stresses and maintain magnet compression.

Based on the findings in Section 2.3.3, an axisymmetric model was selected for the analyses. A 2D radial section analysis would not have been suitable as the change in stresses along the axis could not have been simulated. This would have made it impossible to explore the *end-effect* discussed by Barrans et al. [10]. Barrans et al. [10] states that at the free end of the rotor, the behaviour switches from being in GPS to a state of plane stress. As axisymmetric behaviour is true while the magnets are held in compression, a full 3D FEA model would have yielded no further information regarding the stress and strain distribution and would therefore have been inefficient. Recognising the axial symmetry present, only half of the rotor length was modelled, and an axial displacement constraint applied. Figure 5.1 shows one of the FEA models with three cylinders and the axial symmetry and displacement conditions in place. The dashed line represents the rotor axis.
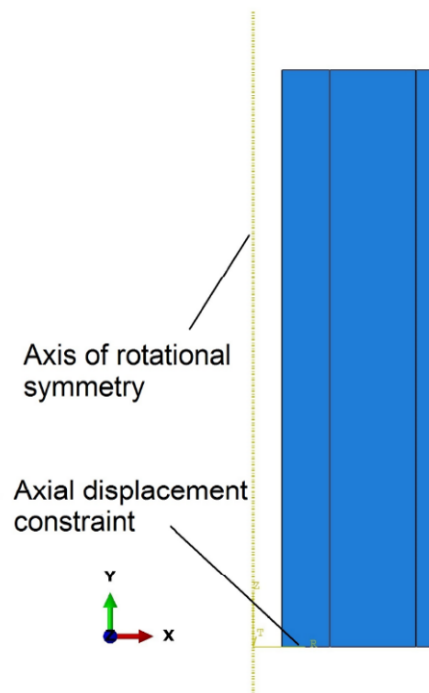
FIGURE 5.1: Three cylinder axisymmetric FEA Model.

Once the rotor was created, the simulation conditions were specified. An interference fit with *small sliding* condition was applied to surfaces *c* and *d*. The small sliding formulation assumes that there is no significant tangential motion between the two surfaces and is appropriate in this case. During the first analysis step, the interfering surfaces were moved to a common radius. Since the surfaces cannot intersect, *hard* contact was specified between the surfaces. In the tangential direction, a coefficient of friction of 1 was specified. Separation of the surfaces was allowed as this enabled the FEA to predict when the centrifugal force from rotation would become too large for the rotor to withstand.

5.2.2 Model Justification

In an axisymmetric FEA model, the inner, middle, and outer cylinders are modelled as solid parts but as shown in Section 1.1.2, magnets are often segmented in practice. However, as discussed by Barrans et al. [10], the behaviour of the rotor is axisymmetric while a compressive stress is maintained in the circumferential direction, within the magnets. If the magnets are held in compression then they act as a solid cylinder, justifying the implementation of solid cylinders in the model. To show that this is the case during rotor operation, FEA was used to simulate the behaviour of segmented magnets, shown in Figure 5.2.
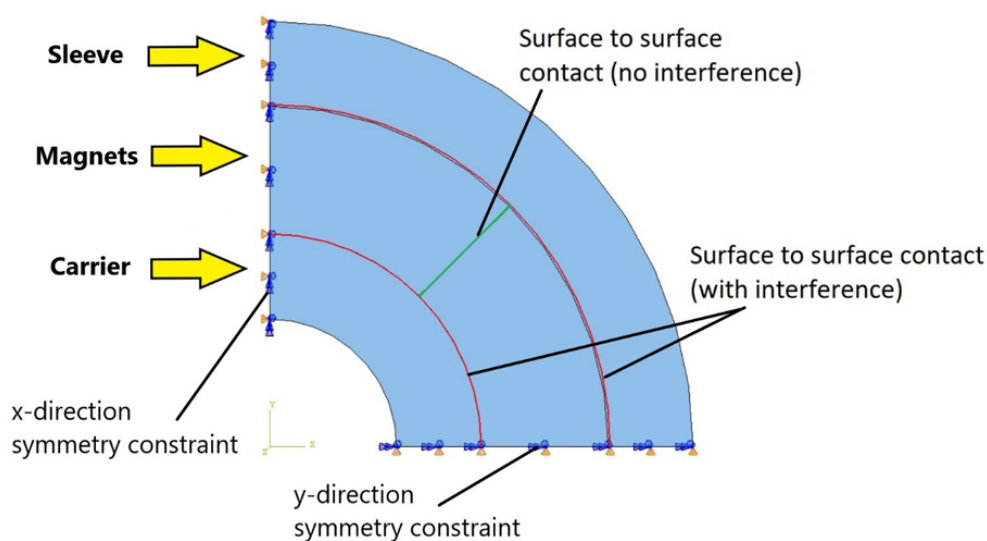
FIGURE 5.2: FEA setup for a 2D radial section model to investigate segment magnet behaviour.

The thin rotor topology detailed in Table 5.2 was used with the cylinder material properties from Table 5.1. To explore the behaviour of segmented magnets, a 2D radial section was used. This is suitable as the axial strain behaviour is not being investigated. A quarter model was used with the appropriate boundary conditions required to simulate the full rotor. The symmetry constraints which restrict movement in the x and y directions allow the rotor components to move radially but ensure that the quarter model behaves as a full rotor. The red lines between the sleeve, magnets, and carrier represent where surface to surface contact was specified with interference. The green line between the segmented magnets represents surface to surface contact with no interference.

The contact settings outlined in Section 5.2.1 were used in the model. The rotor speed was increased until the magnets separated to enable the monitoring of the rotor behaviour during separation. Figure 5.3 shows the contact pressure during the four increments prior to and including magnet separation, where figures *a*, *b*, *c*, and *d* represent 53.6%, 66.1%, 81.4% and 100% of the rotor speed.

(A) Three increments prior to rotor separation.

(B) Two increments prior to rotor separation.

(C) One increment prior to rotor separation.

(D) The moment magnets separate.
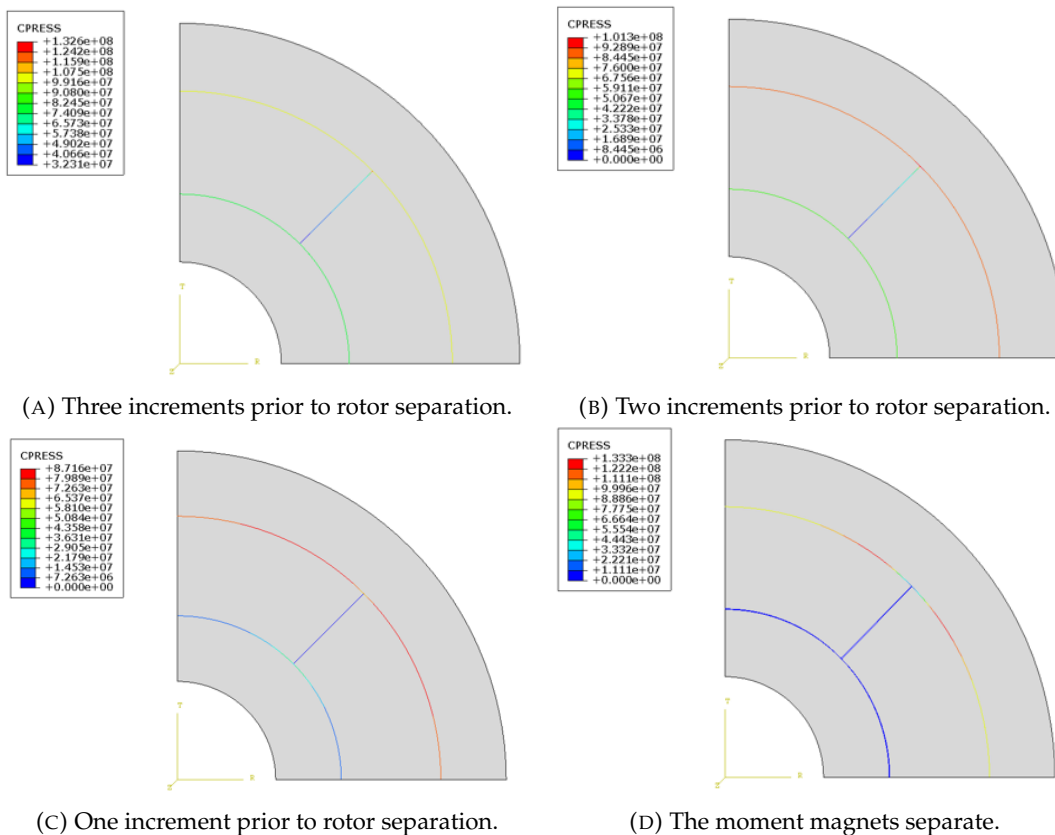
FIGURE 5.3: FEA results - Contact pressures (Pa) at component interfaces.

As seen in Figure 5.3a, contact pressures are present in all locations, between the three cylinders and the segmented magnets. Figure 5.3b shows a loss of contact pressure appearing at the interface between the segmented magnets, occurring at the base of the magnets. However, contact pressures are still maintained at interference locations *c* and *d*. Figure 5.3c shows a significant reduction in contact pressure at interference locations *c* and *d*, but the pressure is still present. However, there is a total loss of contact pressure between the segmented magnets, along the whole interface, signalling the rotor is just beginning to separate. Finally, Figure 5.3d shows a complete loss of contact pressure at interference location *c* and the deformed shape of the model highlights the magnets separate from each other and the inner cylinder. The results shown in Figures 5.4 and 5.5 correspond to the respective increments shown in Figure 5.3. Figures 5.4 and 5.5 show the development of circumferential stress and the Von Mises stress, respectively, throughout the four increments leading to rotor separation.

(A) Three increments prior to rotor separation.

(B) Two increments prior to rotor separation.

(C) One increment prior to rotor separation.

(D) The moment magnets separate.
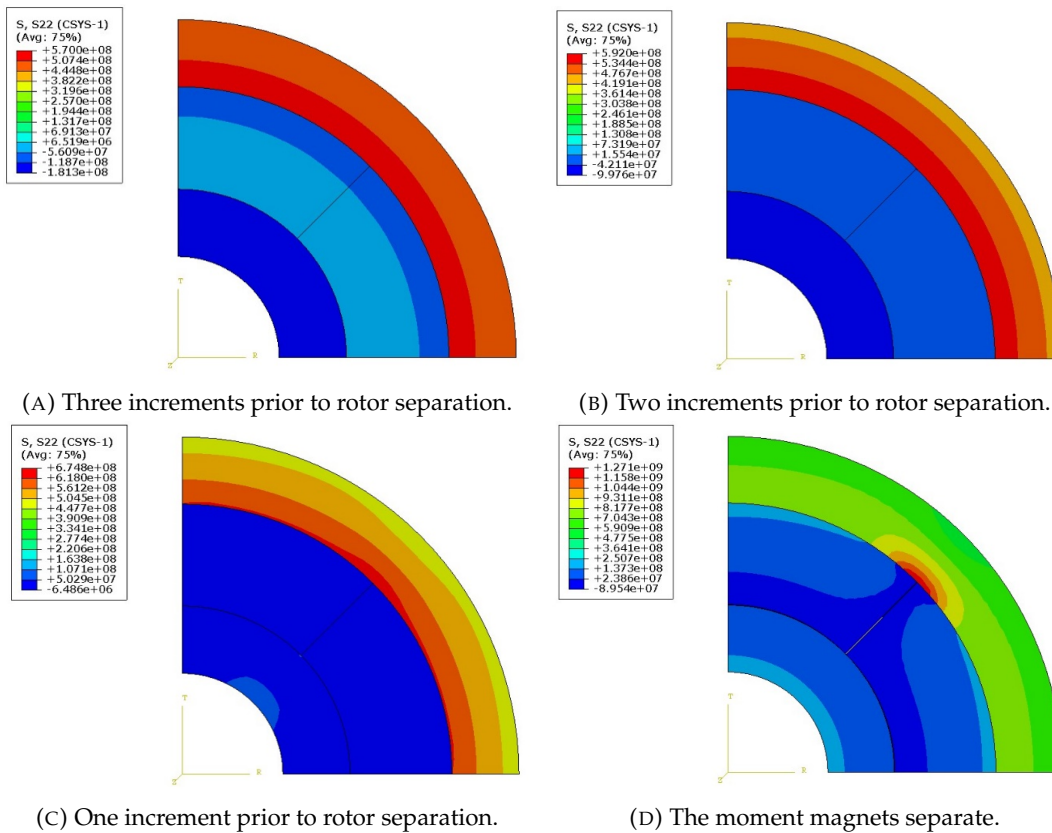
FIGURE 5.4: FEA results - Circumferential stress (Pa) within rotor components.

As shown in Figures 5.4a and 5.4b the rotor behaviour is axisymmetric as the magnets are held in compression in the circumferential direction. Figure 5.4c shows the magnets are still held in compression, however the magnitude of the compressive stress is significantly reduced. As discussed regarding Figure 5.3c, this stage is just as the magnets lose contact pressure at the interface between them. In Figure 5.4c, the outer cylinder starts to lose the axisymmetric behaviour as the stress distribution changes at the segmented magnet interface. The next step from Figure 5.4d shows most of the magnets now in tension, causing failure, and this coincides with a complete loss of axisymmetric behaviour as the stress concentrates around the segmented magnet interface. This study shows that axisymmetric behaviour is maintained while the magnets are held in circumferential compression.

(A) Three increments prior to rotor separation.

(B) Two increments prior to rotor separation.

(C) One increment prior to rotor separation.

(D) The moment magnets separate.
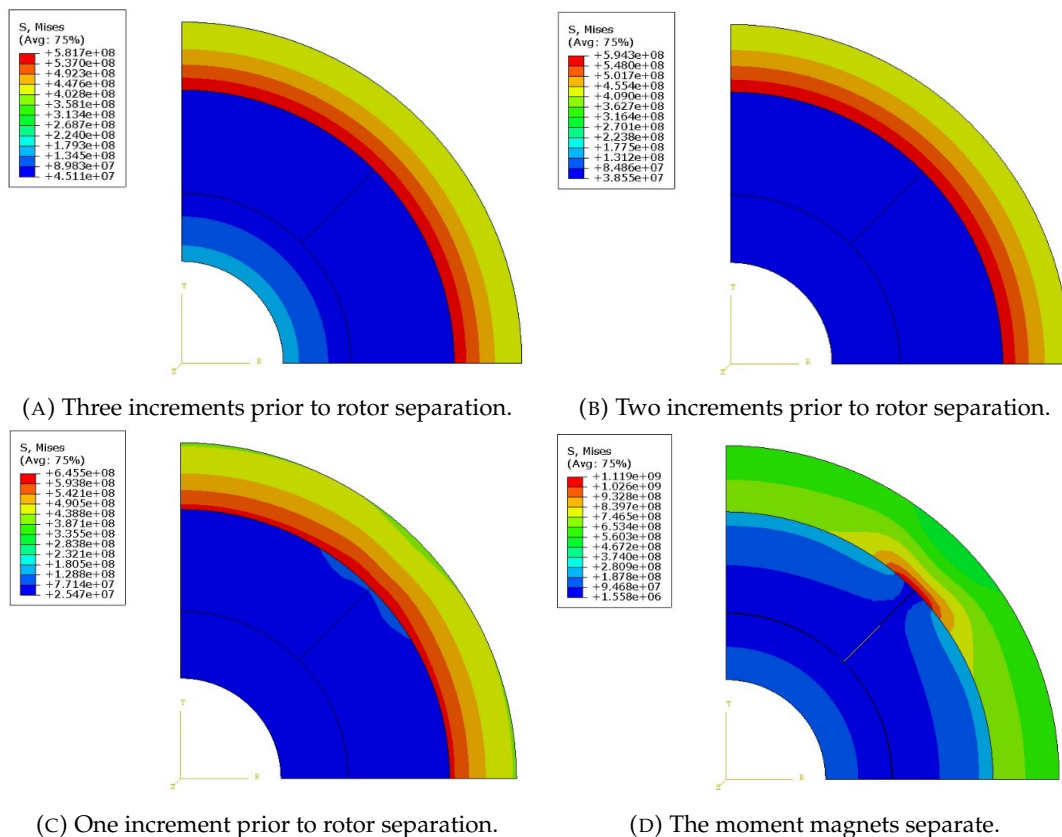
FIGURE 5.5: FEA results - Von Mises stress (Pa) within rotor components.

The Von Mises stress distributions shown in Figure 5.5 reinforces the assumption of axisymmetric behaviour while the magnets are held in circumferential compression. Figures 5.5a and 5.5b show axisymmetric behaviour, as seen in the corresponding studies in Figure 5.4. Figure 5.5c shows signs of loss of the axisymmetric

behaviour as the magnets lose contact pressure between them. Finally, Figure 5.5d shows a complete loss of axisymmetric stress behaviour as the magnets separate and go into tension. It is also seen in Figure 5.5d that as the magnets separate, significant stress concentrations appear at the magnet interface which would cause the failure of the outer cylinder. Therefore, a rotor with segmented magnets can only successfully operate while the magnets are held in compression. Figures 5.4 and 5.5 show that while the magnets are in compression, the rotor behaves axisymmetric, validating the use of an axisymmetric FEA model.

5.2.3 Convergence Study

Before conducting the FEA analyses to compare to the theoretical analyses, a convergence study was conducted to ensure that accurate results were efficiently extracted. The convergence study was completed using the thin long rotor topology from Table 5.2. With reference to Figure 5.1, the initial mesh created was 18 elements through the rotor thickness and 18 elements along the rotor length, producing 324 elements.

Seven meshes were used to carry out the convergence study, shown in Figures 5.6 and 5.7, where the initial mesh using 324 elements, was known as x. Based on
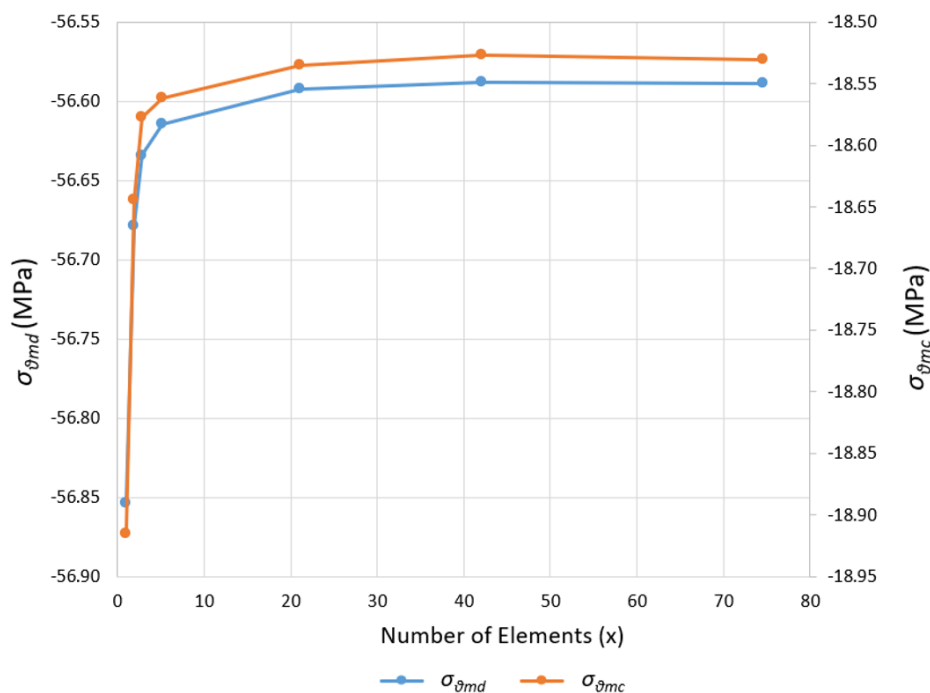
FIGURE 5.6: Mesh convergence study for $\sigma_{\theta mc}$ and $\sigma_{\theta md}$.
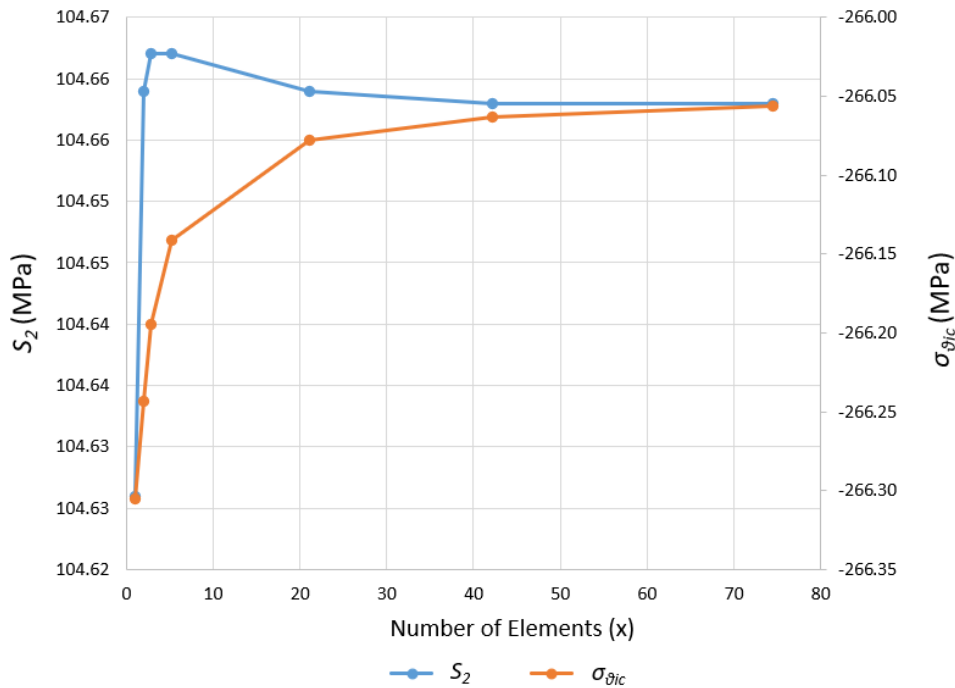
FIGURE 5.7: Mesh convergence study for S_2 and $\sigma_{\theta ic}$.

the number of elements, the refined meshes were then referred to as multiples of the initial mesh and were approximately $2x$, $3x$, $5x$, $20x$, $40x$, and $75x$, respectively.

Four critical stresses were selected to show successful convergence of the results and to select a suitable mesh density for the FEA analyses going forward. The circumferential stress in the middle cylinder at interference locations c, $\sigma_{\theta mc}$, and d, $\sigma_{\theta md}$, were extracted and are shown in the convergence study in Figure 5.6. For the convergence study shown in Figure 5.7, the shrinkage pressure, S_2, and the circumferential stress in the inner cylinder at interference location c, $\sigma_{\theta ic}$, were extracted.

As the mesh is refined, the stresses and shrinkage pressure in Figures 5.6 and 5.7 converge. The most efficient point at which all stresses converged with the lowest mesh density, was with a mesh density of circa $40x$. Therefore, when completing the FEA simulations going forward, the mesh density of $40x$ was used to ensure the results were accurate and obtained efficiently.

5.3 Finite Element Analysis Results

5.3.1 Results

As discussed in Section 5.2.1, six rotor topologies were investigated to provide a comprehensive range of FEA results to compare against the theoretical stress results. This would enable a robust verification of the theoretical models whilst also exposing any limitations of the theories. Each of the six rotor topologies were simulated at four operating conditions to ensure that the results were consistent across all and were not limited by an operating condition. These were:

- Stationary and ambient temperature.

- Maximum speed and ambient temperature.

- Stationary at maximum temperature.

- Maximum speed and temperature.

The maximum temperature used for all models was 100 ^{o}C while the maximum speed was determined by retaining the magnets in circumferential compression and ensuing the cylinders did not separate. For the thin, medium, and thick rotors, the maximum speeds were 80 krpm, 70 krpm, and 60 krpm, respectively.

Before comparing results to the theoretical stress analyses, the axial stress and strain results were explored. Figure 5.8 shows the axial strain results for the long

(A) Thin long rotor.   (B) Medium long rotor.   (C) Thick long rotor.
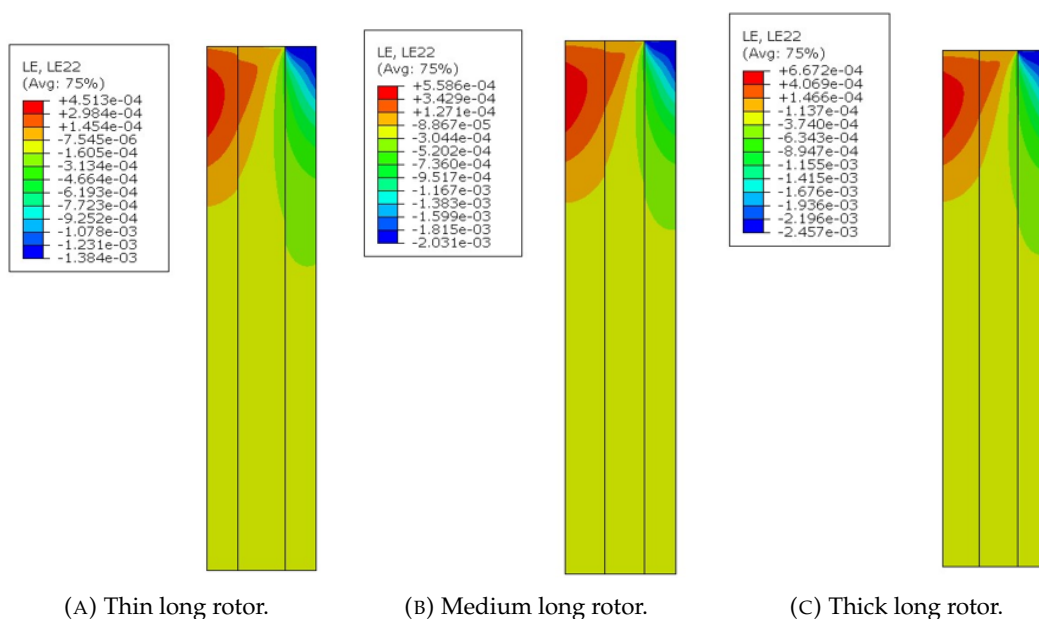
FIGURE 5.8: Long rotor FEA axial strain results.

thin, medium, and thick rotor topologies at maximum speed. As discussed in Section 2.2.1, an assumption made by the GPS theory is that axial strain is constant in the rotor cylinders.

Figure 5.8 shows that the axial strain is constant and compressive for most of the rotor cylinder length and changes towards the free end of the rotor, known as the *end-effect*. Therefore, the assumption in GPS that the axial strain is present and constant, is applicable to most of the rotor length. In turn, this renders the plane strain assumption that axial strain does not exist, incorrect. The end-effect is discussed by Barrans et al. [10] which states that at the free end of the rotor, the rotor changes from being in a state of GPS, to a state of plane stress. This can be seen in Figure 5.9 where the axial stress tends to zero towards the free end of the rotor. Barrans et al. [10] demonstrates that this phenomenon is due to axial load transfer between the cylinders caused by the friction between them. However, Barrans et al. [10] states that once this axial load has transferred, the cylinders behave as if locked together in the main body of the rotor away from the free ends. Figure 5.8 shows this to be true as the axial strain is the same across the inner, middle, and outer cylinders away from the free end. This validates the axial strain compatibility assumption made in the GPS theory with equation 4.82, and therefore also validates the axial force equilibrium condition from equation 4.84.

(A) Thin long rotor.   (B) Medium long rotor.   (C) Thick long rotor.
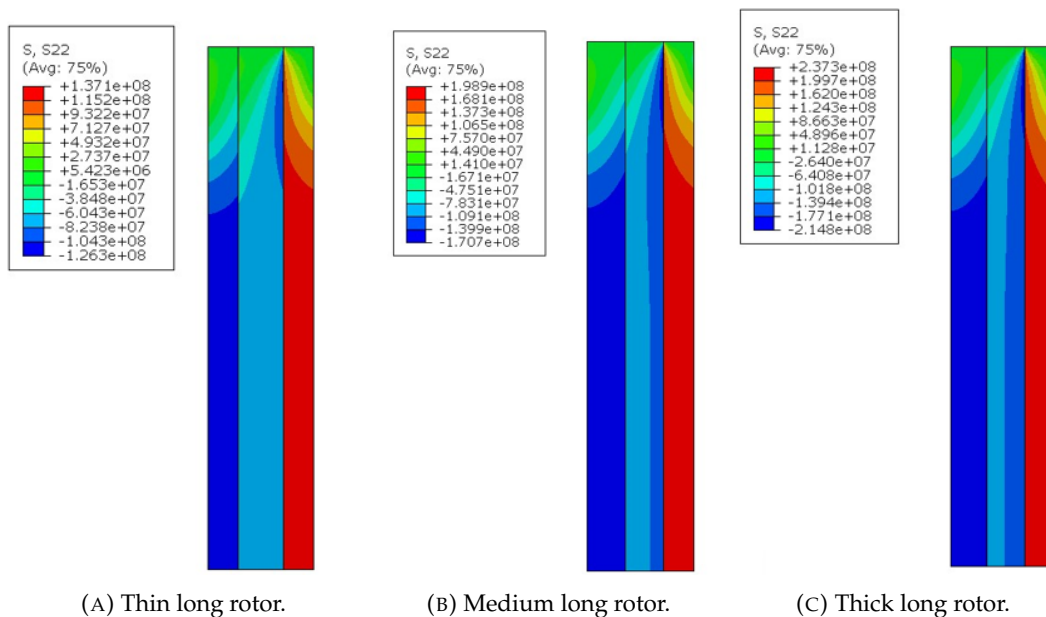
FIGURE 5.9: Long rotor FEA axial stress results.

Figure 5.9 shows the axial stress results for the corresponding rotors shown in Figure 5.8, highlighting the change in axial stress due to the end-effect. However, this also highlights a problem with the plane stress theory. Plane stress assumes that axial stress is zero, but this is not true for most of the rotor. Figures 5.8 and 5.8 show that assumptions regarding axial strain and axial stress, made by both the plane strain and plane stress theories, respectively, are incorrect. The GPS assumptions regarding axial strain compatibility and axial force equilibrium, are shown to be correct for the main body of the rotor.

A limitation to the GPS theory was identified when exploring the corresponding short versions of the rotors from Table 5.2. Figure 5.10 shows the axial strain results for the short rotor simulations. Unlike the long rotor versions, the end-effect dominates the whole length of the short rotors. Therefore, the assumptions made by the GPS theory that axial strain is constant in the cylinders and there is axial strain compatibility between them, is incorrect for short rotors. This shows the GPS theory will be limited to long rotors only.

(A) Thin short rotor.   (B) Medium short rotor.   (C) Thick short rotor.
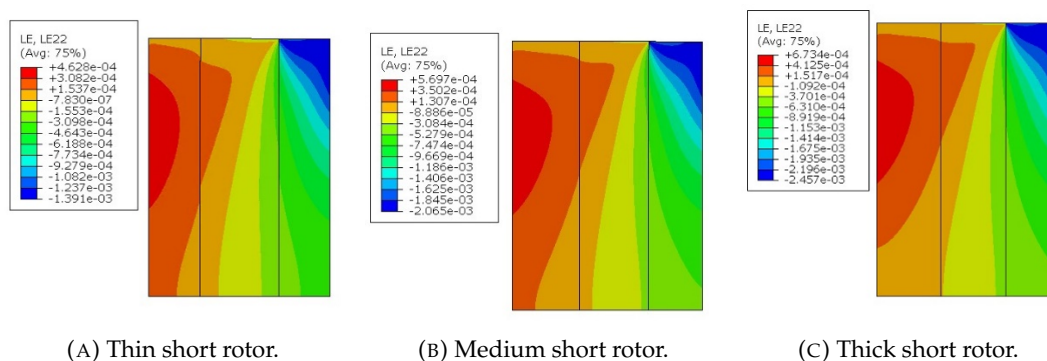
FIGURE 5.10: Short rotor FEA axial strain results.

For the comparison of FEA results to the theoretical analyses, a range of critical stresses were chosen to compare across the four operating conditions discussed earlier in this section. An example of the probed FEA results for the thin long rotor topology at all operating conditions is shown in Table 5.3.

The probed stress components were: contact pressures at c and d (S_1 and S_2); circumferential stresses (σ_θ); axial stresses (σ_z); and Von Mises stresses (σ_{VM}). The circumferential, axial and Von Mises stress were all probed at each cylinder surface and are notated using the surface notation from Figure 4.1. These stresses were selected because: S_1 and S_2 show if the cylinder has remained in compression during

Stress (MPa)	$\omega(0krpm)$ $\Delta T(0^oC)$	$\omega(0krpm)$ $\Delta T(100^oC)$	$\omega(80krpm)$ $\Delta T(0^oC)$	$\omega(80krpm)$ $\Delta T(100^oC)$
S_1	116.2	138.8	106.0	128.5
S_2	115.5	108.8	111.4	104.7
$\sigma_{\theta ii}$	-359.9	-428.8	-316.0	-385.0
$\sigma_{\theta ic}$	-247.4	-294.7	-219.3	-266.7
$\sigma_{\theta mc}$	-112.0	-39.76	-91.33	-19.10
$\sigma_{\theta md}$	-113.3	-69.61	-100.1	-56.41
$\sigma_{\theta od}$	525.5	494.1	536.2	504.9
$\sigma_{\theta oo}$	412.9	388.3	419.3	394.6
σ_{zii}	-128.4	-201.5	-124.3	-197.3
σ_{zic}	-128.5	-201.5	-126.0	-199.1
σ_{zmc}	-72.03	-19.29	-71.04	-18.30
σ_{zmd}	-71.98	-19.25	-74.24	-21.50
σ_{zod}	136.2	110.7	137.0	111.5
σ_{zoo}	136.1	110.6	133.8	108.3
σ_{VMii}	313.6	368.6	273.6	330.6
σ_{VMic}	125.8	136.7	105.2	120.5
σ_{VMmc}	42.28	110.0	30.42	109.2
σ_{VMmd}	42.20	77.35	32.55	71.80
σ_{VMod}	557.4	526.6	564.0	533.4
σ_{VMoo}	365.2	347.2	371.6	353.8

TABLE 5.3: Example of FEA probed results for thin long rotor.

the simulation; circumferential stresses are critical to magnet failure; axial stresses are calculated differently across theoretical methods; and Von Mises stresses can be compared directly to the material yield stress to predict rotor failure due to excessive stress.

The FEA results presented in the following section were compared against the results from each theoretical analysis. Results were probed from the plane of axial symmetry, where end-effect not accounted for in the theoretical approaches will be minimal. A percentage difference to the FEA was calculated for each result, to enable easy comparison across analyses. Percentage difference results were also colour coded to highlight which results were close to the FEA, as in Section 4.6.1. Dark green indicates a difference of less than 1% and the colour changes from green to yellow, then red as the difference increases. Red indicates a difference of 50% or more.

5.3.2 Long Rotor Comparison against Closed Form Analyses

Table 5.4 shows the GPS results for the thin long rotor. To present the results graphically, a histogram was plotted to display the frequency that a result occurred, shown in Figure 5.11. The range of results were split into bins and the number of results

falling into each bin was tallied, showing how the differences to the FEA results are distributed. For the thin long rotor, 76% of the GPS results are within ±1% of the FEA results, while 86% fall within ±2% of the FEA. This accuracy is similar across all operating conditions, showing GPS is a robust analysis method for thin long rotors.

Stress	$\omega(0krpm)$ $\Delta T(0^oC)$	$\omega(0krpm)$ $\Delta T(100^oC)$	$\omega(80krpm)$ $\Delta T(0^oC)$	$\omega(80krpm)$ $\Delta T(100^oC)$
S_1	0.63	0.38	0.71	0.43
S_2	0.28	0.19	0.33	0.23
$\sigma_{\theta ii}$	1.52	1.46	1.62	1.52
$\sigma_{\theta ic}$	0.42	0.35	0.53	0.43
$\sigma_{\theta mc}$	1.16	2.15	1.35	4.03
$\sigma_{\theta md}$	0.99	1.81	1.19	2.35
$\sigma_{\theta od}$	0.43	0.52	0.44	0.53
$\sigma_{\theta oo}$	0.25	0.16	0.25	0.16
σ_{zii}	0.02	0.06	0.03	0.05
σ_{zic}	0.04	0.04	0.01	0.06
σ_{zmc}	0.08	0.08	0.10	0.01
σ_{zmd}	0.02	0.30	0.03	0.46
σ_{zod}	0.10	0.22	0.13	0.25
σ_{zoo}	0.24	0.37	0.22	0.34
σ_{VMii}	2.37	2.31	2.50	2.38
σ_{VMic}	0.24	0.17	0.29	0.24
σ_{VMmc}	2.38	0.77	2.54	0.74
σ_{VMmd}	2.33	0.83	2.88	0.77
σ_{VMod}	0.77	0.85	0.78	0.85
σ_{VMoo}	0.49	0.40	0.48	0.38

TABLE 5.4: GPS thin long rotor results compared to FEA.
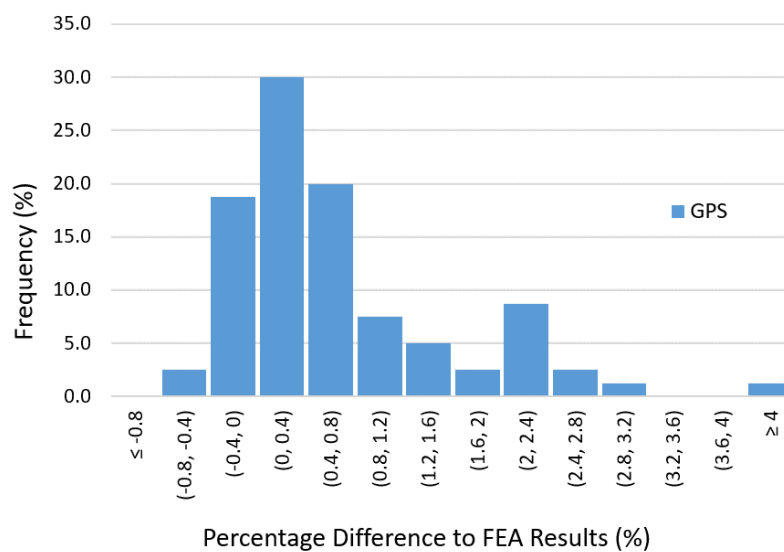
FIGURE 5.11: Thin long rotor - GPS results compared to FEA histogram.

Tables 5.5 and 5.6 show the same results for the plane strain and plane stress, respectively. They are then compared in Figure 5.12. Table 5.5 shows that the plane strain theory has similarly accurate results as GPS, for the circumferential stresses,

Stress	$\omega(0krpm)$ $\Delta T(0^oC)$	$\omega(0krpm)$ $\Delta T(100^oC)$	$\omega(80krpm)$ $\Delta T(0^oC)$	$\omega(80krpm)$ $\Delta T(100^oC)$
S_1	0.60	0.50	0.68	0.55
S_2	0.49	1.19	0.63	1.11
$\sigma_{\theta ii}$	1.50	1.58	1.59	1.65
$\sigma_{\theta ic}$	0.40	0.47	0.50	0.56
$\sigma_{\theta mc}$	1.91	11.10	2.63	21.83
$\sigma_{\theta md}$	1.50	3.37	2.00	3.64
$\sigma_{\theta od}$	0.64	0.86	0.72	0.74
$\sigma_{\theta oo}$	0.04	1.53	0.03	1.43
σ_{zii}	17.51	69.41	25.08	66.48
σ_{zic}	17.53	69.38	24.71	65.90
σ_{zmc}	23.00	532.23	32.29	526.08
σ_{zmd}	22.95	533.62	30.77	448.30
σ_{zod}	9.06	68.36	12.48	63.63
σ_{zoo}	9.22	68.31	12.86	65.43
σ_{VMii}	3.80	7.69	4.55	10.09
σ_{VMic}	9.09	34.24	14.19	47.94
σ_{VMmc}	42.23	12.25	75.24	1.32
σ_{VMmd}	42.38	36.54	73.12	19.65
σ_{VMod}	0.74	2.62	0.71	2.56
σ_{VMoo}	0.86	5.44	1.00	5.05

TABLE 5.5: Plane strain thin long rotor results compared to FEA.

Stress	$\omega(0krpm)$ $\Delta T(0^oC)$	$\omega(0krpm)$ $\Delta T(100^oC)$	$\omega(80krpm)$ $\Delta T(0^oC)$	$\omega(80krpm)$ $\Delta T(100^oC)$
S_1	9.98	12.55	10.66	13.31
S_2	9.60	8.40	9.86	8.63
$\sigma_{\theta ii}$	9.18	11.61	10.21	12.74
$\sigma_{\theta ic}$	10.16	12.57	11.25	13.73
$\sigma_{\theta mc}$	7.18	27.53	8.90	56.75
$\sigma_{\theta md}$	8.06	3.96	9.65	3.94
$\sigma_{\theta od}$	9.46	8.10	9.30	7.96
$\sigma_{\theta oo}$	10.07	8.71	9.74	8.38
σ_{VMii}	4.23	2.83	3.70	1.60
σ_{VMic}	53.06	63.34	60.33	65.36
σ_{VMmc}	146.70	4.06	194.21	8.54
σ_{VMmd}	147.15	15.34	194.33	16.31
σ_{VMod}	3.89	2.91	3.62	2.67
σ_{VMoo}	1.67	2.09	1.82	2.19

TABLE 5.6: Plane stress thin long rotor results compared to FEA.
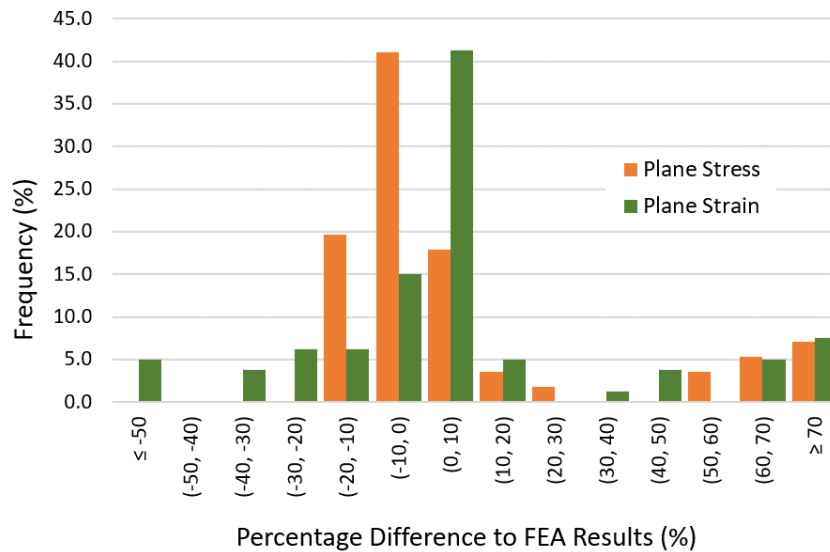
FIGURE 5.12: Thin long rotor - Plane strain and plane stress results compared to FEA histogram.

when the rotor is stationary or at speed. However, the axial stress results are much less accurate and when temperature is increased, the accuracy is affected further. This is due to plane strain assuming there is no axial strain in the rotor. Effectively, this places the rotor between rigid bodies, inducing compressive stress, affecting the results. The inaccuracies with the axial stress are then carried over into the Von Mises stress. Figure 5.12 shows both plane stress and plane strain produce much larger differences than the GPS for thin long rotors. The axial stress results were not included for plane stress as the theory assumes axial stress to be zero.

Prior to running the medium and thick long rotor models at the maximum speeds discussed in Section 5.3.1, they were simulated at 80 krpm like the thin rotor model. The results are shown in Tables 5.7 and 5.8. It is important to note that the FEA simulation for both the medium and thick long rotors, predicted the cylinders would separate at c at 80 krpm. This only occurred at the rotor ends and only at full operating speed with no elevated temperature. At operating speed with elevated temperature, the pressure at c at the rotor ends was also significantly reduced. This appears to have affected the accuracy of S_1 and S_2, causing the circumferential stresses to also lose accuracy, which then has a knock-on effect on the Von Mises stresses. However, when stationary, the accuracy shown in the thin model in Tables 5.4 is closely replicated with the medium and thick versions in Tables 5.7 and 5.8.

Stress	$\omega(0krpm)$ $\Delta T(0^oC)$	$\omega(0krpm)$ $\Delta T(100^oC)$	$\omega(80krpm)$ $\Delta T(0^oC)$	$\omega(80krpm)$ $\Delta T(100^oC)$
S_1	1.00	0.75	7.82	6.60
S_2	0.41	0.32	2.94	2.94
$\sigma_{\theta ii}$	2.05	1.99	13.41	11.55
$\sigma_{\theta ic}$	0.83	0.77	10.46	8.94
$\sigma_{\theta mc}$	1.47	2.38	18.52	115.84
$\sigma_{\theta md}$	1.38	2.18	10.57	18.43
$\sigma_{\theta od}$	0.50	0.58	0.56	0.50
$\sigma_{\theta oo}$	0.25	0.16	1.04	0.98
σ_{zii}	0.02	0.09	2.11	1.59
σ_{zic}	0.02	0.06	0.93	0.75
σ_{zmc}	0.07	0.06	0.43	1.23
σ_{zmd}	0.05	0.11	1.60	3.11
σ_{zod}	0.16	0.26	0.12	0.05
σ_{zoo}	0.38	0.50	1.44	1.68
σ_{VMii}	3.09	3.04	14.89	12.42
σ_{VMic}	1.21	0.72	20.34	8.98
σ_{VMmc}	2.75	1.18	3.74	0.84
σ_{VMmd}	3.10	1.43	9.29	3.19
σ_{VMod}	0.91	0.98	0.33	0.38
σ_{VMoo}	0.52	0.43	1.40	1.35

TABLE 5.7: GPS medium long rotor results compared to FEA.

Stress	$\omega(0krpm)$ $\Delta T(0^oC)$	$\omega(0krpm)$ $\Delta T(100^oC)$	$\omega(80krpm)$ $\Delta T(0^oC)$	$\omega(80krpm)$ $\Delta T(100^oC)$
S_1	1.23	0.98	25.36	21.88
S_2	0.48	0.39	8.62	8.78
$\sigma_{\theta ii}$	2.01	1.94	47.29	39.76
$\sigma_{\theta ic}$	1.13	1.06	37.59	31.99
$\sigma_{\theta mc}$	1.75	2.58	73.02	1709.51
$\sigma_{\theta md}$	1.60	2.19	33.08	54.66
$\sigma_{\theta od}$	0.39	0.48	2.85	2.85
$\sigma_{\theta oo}$	0.19	0.10	2.55	2.53
σ_{zii}	0.04	0.11	6.55	5.01
σ_{zic}	0.02	0.06	2.73	2.17
σ_{zmc}	0.08	0.02	1.51	2.92
σ_{zmd}	0.06	0.06	4.49	7.20
σ_{zod}	0.18	0.29	1.01	1.01
σ_{zoo}	0.48	0.60	4.13	4.62
σ_{VMii}	2.78	2.71	47.28	37.57
σ_{VMic}	1.84	1.48	58.29	16.46
σ_{VMmc}	3.52	1.43	15.50	3.03
σ_{VMmd}	3.75	2.17	2.21	3.96
σ_{VMod}	0.77	0.85	0.96	0.95
σ_{VMoo}	0.40	0.31	3.15	3.16

TABLE 5.8: GPS thick long rotor results compared to FEA.

Figure 5.13 shows the end separation at c predicted by the FEA for the medium and thick rotors from Tables 5.7 and 5.8. The thick rotor separates more, and this is shown by the larger difference in S_1, compared to the FEA results. However, excluding the results from the maximum speed simulations, GPS still produces very accurate results for medium and thick long rotors.
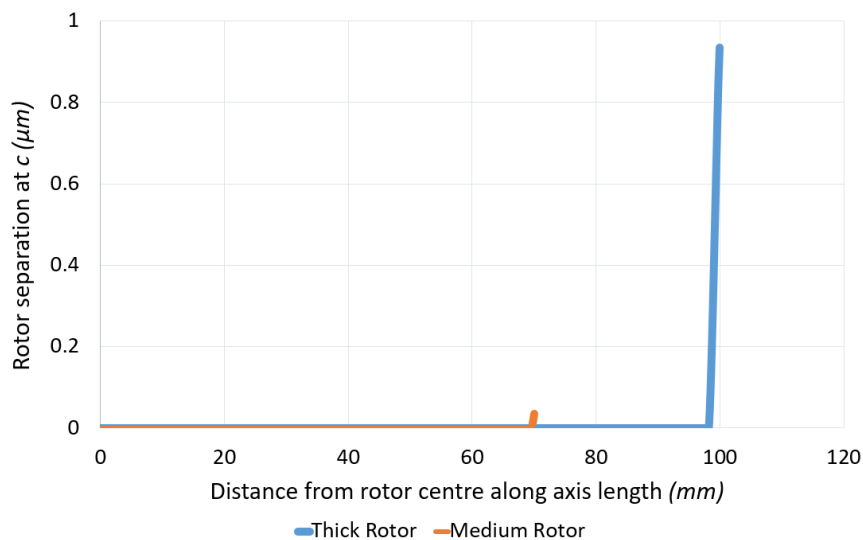
FIGURE 5.13: Rotor end separation at c.

The medium and thick long rotor topologies were then run at a lower speed to avoid separation at the rotor ends and the results accuracy improved greatly. Tables 5.9 and 5.10 show the medium long rotor at 70 krpm and the thick long rotor at 60 krpm, respectively, as discussed in Section 5.3.1. For both the medium and thick rotors, S_1 and S_2 became more accurate, causing the circumferential stresses to become accurate across all operating conditions. This led to very accurate results for all recorded stresses, across all operating ranges.

Figure 5.14 shows the histogram of the GPS results for each rotor without separation at c. The thin rotor has more results concentrated towards 0% and the accuracy then decreases slightly as the rotor thickness increases. The average accuracy shifts further from 0% with each increase in rotor thickness, reducing the probability of obtaining the most accurate results. However, even the thick rotor still has 76% of results falling within a ±2% range and 91% within ±3% of the FEA results.

Stress	$\omega(0krpm)$ $\Delta T(0^oC)$	$\omega(0krpm)$ $\Delta T(100^oC)$	$\omega(70krpm)$ $\Delta T(0^oC)$	$\omega(70krpm)$ $\Delta T(100^oC)$
S_1	1.00	0.75	1.25	0.94
S_2	0.41	0.32	0.54	0.45
$\sigma_{\theta ii}$	2.05	1.99	2.41	2.25
$\sigma_{\theta ic}$	0.83	0.77	1.21	1.06
$\sigma_{\theta mc}$	1.47	2.38	2.04	5.83
$\sigma_{\theta md}$	1.38	2.18	1.92	3.34
$\sigma_{\theta od}$	0.50	0.58	0.51	0.60
$\sigma_{\theta oo}$	0.25	0.16	0.26	0.17
σ_{zii}	0.02	0.09	0.01	0.08
σ_{zic}	0.02	0.06	0.06	0.11
σ_{zmc}	0.07	0.06	0.10	0.01
σ_{zmd}	0.05	0.11	0.07	0.34
σ_{zod}	0.16	0.26	0.21	0.32
σ_{zoo}	0.38	0.50	0.35	0.46
σ_{VMii}	3.09	3.04	3.50	3.28
σ_{VMic}	1.21	0.72	1.55	0.18
σ_{VMmc}	2.75	1.18	2.07	1.01
σ_{VMmd}	3.10	1.43	3.56	1.23
σ_{VMod}	0.91	0.98	0.91	0.99
σ_{VMoo}	0.52	0.43	0.50	0.40

TABLE 5.9: GPS medium long rotor results compared to FEA.

Stress	$\omega(0krpm)$ $\Delta T(0^oC)$	$\omega(0krpm)$ $\Delta T(100^oC)$	$\omega(60krpm)$ $\Delta T(0^oC)$	$\omega(60krpm)$ $\Delta T(100^oC)$
S_1	1.23	0.98	1.61	1.29
S_2	0.48	0.39	0.68	0.59
$\sigma_{\theta ii}$	2.01	1.94	2.55	2.37
$\sigma_{\theta ic}$	1.13	1.06	1.65	1.48
$\sigma_{\theta mc}$	1.75	2.58	2.62	5.48
$\sigma_{\theta md}$	1.60	2.19	2.25	3.35
$\sigma_{\theta od}$	0.39	0.48	0.41	0.50
$\sigma_{\theta oo}$	0.19	0.10	0.19	0.10
σ_{zii}	0.04	0.11	0.04	0.11
σ_{zic}	0.02	0.06	0.07	0.13
σ_{zmc}	0.08	0.02	0.09	0.02
σ_{zmd}	0.06	0.06	0.05	0.24
σ_{zod}	0.18	0.29	0.23	0.34
σ_{zoo}	0.48	0.60	0.47	0.59
σ_{VMii}	2.78	2.71	3.36	3.10
σ_{VMic}	1.84	1.48	2.41	0.88
σ_{VMmc}	3.52	1.43	2.80	0.96
σ_{VMmd}	3.75	2.17	4.63	1.96
σ_{VMod}	0.77	0.85	0.78	0.86
σ_{VMoo}	0.40	0.31	0.37	0.28

TABLE 5.10: GPS thick long rotor results compared to FEA.
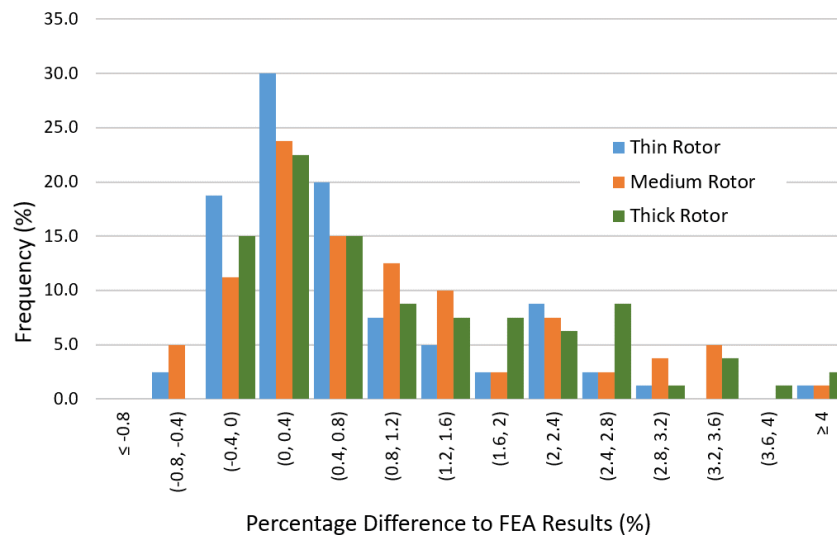
FIGURE 5.14: Long rotors - GPS results compared to FEA histogram.

Tables 5.11 and 5.12 show the plane stress results for the medium and thick long rotors and Figure 5.15 compares those against the respective plane strain results from Tables 5.13 and 5.14. When comparing the GPS medium and thick long rotor results from Figure 5.14 to the corresponding plane stress results in Figure 5.15, we see a similar pattern to the thin rotor results. The medium and thick rotors remaining close, but it appears that the thicker the rotor, the less accurate the results become as the thick rotor results have slightly more occurrences in the higher difference bins.

Stress	$\omega(0krpm)$ $\Delta T(0^oC)$	$\omega(0krpm)$ $\Delta T(100^oC)$	$\omega(70krpm)$ $\Delta T(0^oC)$	$\omega(70krpm)$ $\Delta T(100^oC)$
S_1	9.58	11.40	10.93	12.87
S_2	9.42	8.83	9.92	9.29
$\sigma_{\theta ii}$	8.64	10.31	10.86	12.70
$\sigma_{\theta ic}$	9.73	11.38	12.09	13.83
$\sigma_{\theta mc}$	6.38	13.11	9.64	33.46
$\sigma_{\theta md}$	7.34	1.27	10.30	0.01
$\sigma_{\theta od}$	9.34	8.58	9.08	8.33
$\sigma_{\theta oo}$	10.02	9.26	9.40	8.64
σ_{VMii}	5.05	4.28	3.72	1.80
σ_{VMic}	88.40	111.84	129.46	134.90
σ_{VMmc}	128.91	8.74	155.02	0.54
σ_{VMmd}	139.35	31.04	198.91	33.03
σ_{VMod}	3.96	3.37	3.46	2.90
σ_{VMoo}	1.73	2.03	2.01	2.25

TABLE 5.11: Plane stress medium long rotor results compared to FEA.

Stress	$\omega(0krpm)$ $\Delta T(0^oC)$	$\omega(0krpm)$ $\Delta T(100^oC)$	$\omega(60krpm)$ $\Delta T(0^oC)$	$\omega(60krpm)$ $\Delta T(100^oC)$
S_1	9.30	10.80	10.87	12.51
S_2	9.20	8.74	9.77	9.28
$\sigma_{\theta ii}$	8.60	9.95	11.22	12.75
$\sigma_{\theta ic}$	9.39	10.73	12.20	13.64
$\sigma_{\theta mc}$	5.90	6.06	9.33	12.50
$\sigma_{\theta md}$	6.92	0.92	10.24	3.14
$\sigma_{\theta od}$	9.29	8.66	8.99	8.37
$\sigma_{\theta oo}$	9.81	9.18	9.04	8.41
σ_{VMii}	4.81	4.24	3.16	1.44
σ_{VMic}	89.37	109.28	140.28	141.04
σ_{VMmc}	135.25	26.55	194.42	12.79
σ_{VMmd}	139.42	49.34	220.29	56.44
σ_{VMod}	4.21	3.72	3.61	3.15
σ_{VMoo}	2.00	2.25	2.33	2.52

TABLE 5.12: Plane stress thick long rotor results compared to FEA.

The plane strain results also appear to be closely aligned, but do not follow this pattern as the thick rotor produces a slightly more accurate result spread than the medium rotor. This is because the inaccurate axial stress results produced by the plane strain theory, which fall in the highest difference bin, are less extreme for the thick rotor.
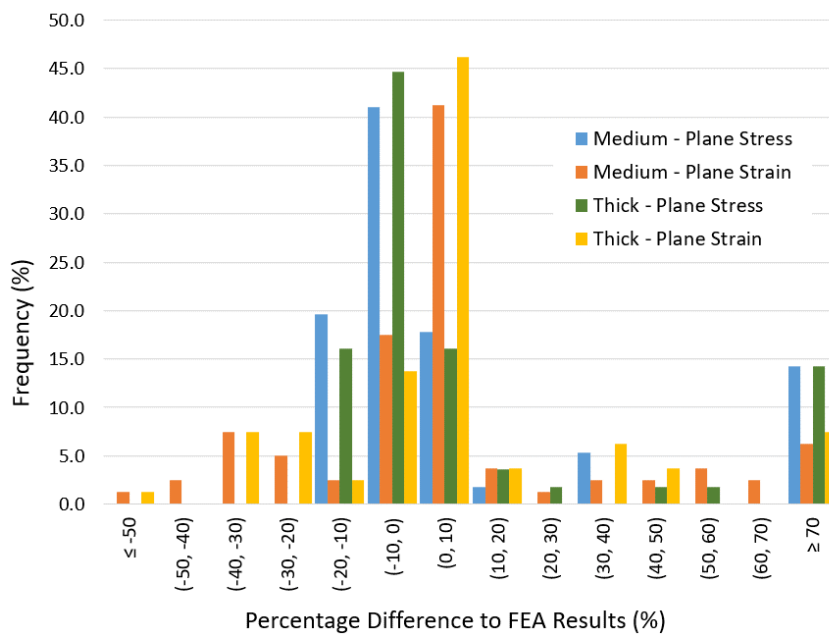
FIGURE 5.15: Medium and thick long rotors - Plane stress and plane strain results compared to FEA histogram.

Stress	$\omega(0krpm)$ $\Delta T(0^oC)$	$\omega(0krpm)$ $\Delta T(100^oC)$	$\omega(70krpm)$ $\Delta T(0^oC)$	$\omega(70krpm)$ $\Delta T(100^oC)$
S_1	0.99	0.76	1.24	0.96
S_2	0.60	0.55	0.90	0.33
$\sigma_{\theta ii}$	2.05	2.01	2.40	2.27
$\sigma_{\theta ic}$	0.83	0.79	1.20	1.07
$\sigma_{\theta mc}$	2.25	4.50	4.01	9.39
$\sigma_{\theta md}$	1.91	1.21	3.08	0.65
$\sigma_{\theta od}$	0.68	0.28	0.83	0.09
$\sigma_{\theta oo}$	0.07	1.02	0.06	0.87
σ_{zii}	17.64	57.64	33.02	50.20
σ_{zic}	17.68	57.58	31.76	48.89
σ_{zmc}	21.48	214.45	38.26	185.21
σ_{zmd}	21.46	214.61	35.38	157.85
σ_{zod}	8.71	42.15	15.03	34.48
σ_{zoo}	8.95	42.01	15.89	36.25
σ_{VMii}	4.56	4.78	6.18	8.49
σ_{VMic}	16.46	23.04	40.16	64.79
σ_{VMmc}	34.74	20.53	65.32	3.78
σ_{VMmd}	38.22	52.34	82.79	25.04
σ_{VMod}	0.88	1.78	0.82	1.72
σ_{VMoo}	0.88	2.77	1.17	2.26

TABLE 5.13: Plane strain medium long rotor results compared to FEA.

Stress	$\omega(0krpm)$ $\Delta T(0^oC)$	$\omega(0krpm)$ $\Delta T(100^oC)$	$\omega(60krpm)$ $\Delta T(0^oC)$	$\omega(60krpm)$ $\Delta T(100^oC)$
S_1	1.23	0.97	1.62	1.28
S_2	0.67	0.27	1.07	0.05
$\sigma_{\theta ii}$	2.01	1.93	2.56	2.36
$\sigma_{\theta ic}$	1.13	1.05	1.66	1.48
$\sigma_{\theta mc}$	2.48	1.33	4.71	0.87
$\sigma_{\theta md}$	2.10	0.04	3.50	1.01
$\sigma_{\theta od}$	0.58	0.18	0.75	0.03
$\sigma_{\theta oo}$	0.00	0.76	0.15	0.57
σ_{zii}	17.41	45.90	35.59	35.80
σ_{zic}	17.46	45.83	34.05	34.65
σ_{zmc}	20.75	123.07	40.00	93.78
σ_{zmd}	20.73	123.14	36.68	81.42
σ_{zod}	9.17	32.87	16.97	23.61
σ_{zoo}	9.50	32.66	18.30	25.08
σ_{VMii}	4.24	2.88	6.19	5.95
σ_{VMic}	16.96	3.86	46.42	39.48
σ_{VMmc}	36.10	28.48	86.84	6.73
σ_{VMmd}	37.55	57.88	95.27	28.10
σ_{VMod}	0.75	1.35	0.68	1.29
σ_{VMoo}	0.78	2.06	1.15	1.48

TABLE 5.14: Plane strain thick long rotor results compared to FEA.

For the medium rotors, only 27% of plane stress results fell within ±5% of the FEA, compared to only 53% of plane strain results falling within the same range. Neither method from Figure 5.15 compares to the accuracy of the GPS results shown in Figure 5.14, which shows 89% of results falling within ±2.5% of the FEA results.

5.3.3 Short Rotor Comparison against Closed Form Analyses

As described in the Section 5.3.1, an end-effect occurs at the rotor ends where axial stress tends to zero. This changes the rotor from a state of GPS to a state of plane stress. When analysing short rotors, it can be seen in Figure 5.10 that the end-effect can affect the whole length of the rotor. The results from all analyses for the thin short rotor can be seen in Tables 5.15 - 5.17, which are then compared in Figure 5.16.

These results show that none of the theoretical approaches can be reliably used for short rotors due to being affected by the end-effect. The plane strain and GPS theories have the largest errors occurring within the axial stress values, leading to significant Von Mises stress errors compared to the FEA. The circumferential stresses and shrinkage pressures also have substantial differences compared to the FEA. The

Stress	$\omega(0krpm)$ $\Delta T(0^oC)$	$\omega(0krpm)$ $\Delta T(100^oC)$	$\omega(80krpm)$ $\Delta T(0^oC)$	$\omega(80krpm)$ $\Delta T(100^oC)$
S_1	6.43	5.67	6.84	5.95
S_2	0.16	0.04	0.13	0.02
$\sigma_{\theta ii}$	9.81	8.73	10.88	9.52
$\sigma_{\theta ic}$	11.48	10.27	12.48	11.00
$\sigma_{\theta mc}$	18.73	40.57	21.77	57.97
$\sigma_{\theta md}$	16.25	24.43	17.68	28.03
$\sigma_{\theta od}$	4.36	4.87	4.23	4.72
$\sigma_{\theta oo}$	4.68	5.30	4.53	5.13
σ_{zii}	90.60	45.48	94.65	46.27
σ_{zic}	46.76	26.65	47.76	26.89
σ_{zmc}	56.08	342.66	55.51	315.89
σ_{zmd}	17.44	45.04	16.74	41.87
σ_{zod}	14.52	19.45	14.31	19.16
σ_{zoo}	30.84	42.81	31.02	43.39
σ_{VMii}	14.13	10.60	15.29	10.94
σ_{VMic}	29.00	22.94	31.68	22.66
σ_{VMmc}	50.27	17.43	56.04	13.29
σ_{VMmd}	0.47	16.00	12.49	22.88
σ_{VMod}	3.61	3.95	3.51	3.84
σ_{VMoo}	2.77	2.73	2.60	2.56

TABLE 5.15: GPS thin short rotor results compared to FEA.

Stress	$\omega(0krpm)$ $\Delta T(0^oC)$	$\omega(0krpm)$ $\Delta T(100^oC)$	$\omega(80krpm)$ $\Delta T(0^oC)$	$\omega(80krpm)$ $\Delta T(100^oC)$
S_1	6.45	5.56	6.88	5.84
S_2	0.04	1.41	0.17	1.32
$\sigma_{\theta ii}$	9.83	8.62	10.91	9.41
$\sigma_{\theta ic}$	11.50	10.16	12.51	10.89
$\sigma_{\theta mc}$	18.12	48.28	20.78	68.42
$\sigma_{\theta md}$	15.83	28.27	17.03	32.24
$\sigma_{\theta od}$	4.58	3.43	4.53	3.40
$\sigma_{\theta oo}$	4.90	3.85	4.83	3.79
σ_{zii}	57.25	146.32	45.87	143.38
σ_{zic}	21.08	114.42	11.25	110.38
σ_{zmc}	20.28	1632.97	5.40	1451.47
σ_{zmd}	36.38	247.23	42.38	217.26
σ_{zod}	24.77	62.28	28.41	56.77
σ_{zoo}	42.55	54.91	47.55	50.61
σ_{VMii}	12.93	5.90	13.61	4.23
σ_{VMic}	22.73	3.62	22.21	14.69
σ_{VMmc}	30.92	28.10	24.87	15.06
σ_{VMmd}	39.80	26.99	89.27	2.01
σ_{VMod}	3.58	5.77	3.45	5.60
σ_{VMoo}	2.39	8.76	2.06	8.15

TABLE 5.16: Plane strain thin short rotor results compared to FEA.

Stress	$\omega(0krpm)$ $\Delta T(0^oC)$	$\omega(0krpm)$ $\Delta T(100^oC)$	$\omega(80krpm)$ $\Delta T(0^oC)$	$\omega(80krpm)$ $\Delta T(100^oC)$
S_1	16.29	17.82	17.36	18.82
S_2	10.00	8.61	10.27	8.83
$\sigma_{\theta ii}$	19.32	20.49	21.25	22.23
$\sigma_{\theta ic}$	20.81	21.83	22.73	23.55
$\sigma_{\theta mc}$	25.42	25.81	29.68	36.67
$\sigma_{\theta md}$	23.76	22.84	26.50	26.91
$\sigma_{\theta od}$	5.91	4.12	5.88	4.12
$\sigma_{\theta oo}$	5.63	3.73	5.41	3.53
σ_{VMii}	12.57	10.15	14.30	11.62
σ_{VMic}	8.41	26.09	9.22	28.19
σ_{VMmc}	19.83	21.39	26.14	21.27
σ_{VMmd}	142.66	32.70	221.80	41.83
σ_{VMod}	1.19	0.08	1.00	0.22
σ_{VMoo}	5.00	5.30	4.97	5.20

TABLE 5.17: Plane stress thin short rotor results compared to FEA.

plane stress theory appears to produce a more consistent set of results that avoids many of the large differences found in the plane strain and GPS theories. However, the plane stress method still produces results that are significantly different to the FEA results.
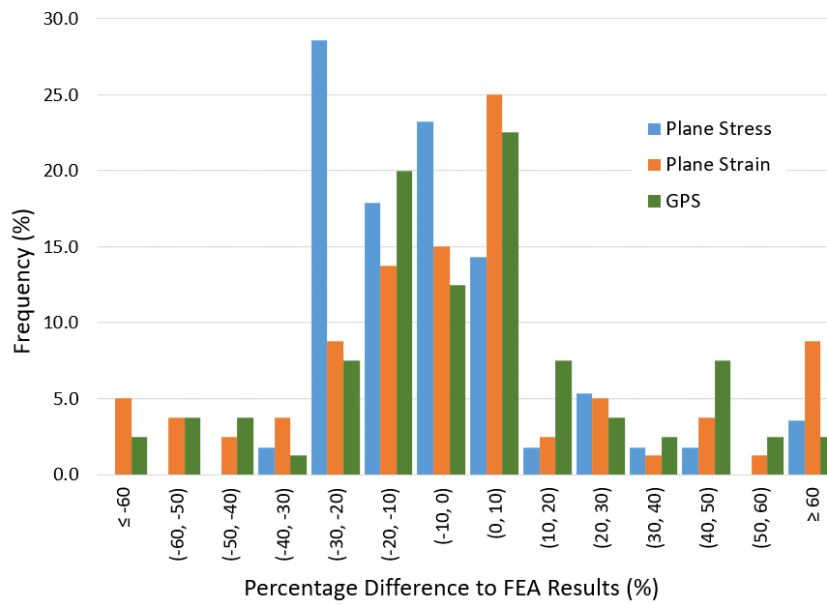
FIGURE 5.16: Thin short rotors - Results compared to FEA histogram.

For thin short rotors, the plane stress approach appears to have the most consistent results with less extreme outliers. This is due to the end-effect essentially creating a state of plane stress in the rotor. Comparing Figure 5.16 with Figure 5.12, the thin long rotor results are slightly more accurate than the thin short rotor results for plane stress, with more results concentrated in the lowest difference bins. When also compared to Figure 5.15, the plane stress theory is shown to be consistent over all tested rotor topologies. However, there are still significant errors that make the results unreliable.

Plane strain appears to have a comparable distribution to GPS in Figure 5.16, but the major axial stress inaccuracies shown in Table 5.16, are concealed in the highest difference bin. Taking this into account, the GPS distribution of Table 5.15 has fewer occurrences in the highest difference bin and is more accurate on average than plane strain, but less accurate than plane stress. 63% of the GPS results fall within ±20% of the FEA, however there are axial stress calculations that are significantly more inaccurate and fall outside of this range. Each theory has circa 40% of results falling outside of ±20% of the FEA. There is also no clear pattern on which results may be accurate or inaccurate.

The unpredictability and unreliability in the GPS results remains for the medium and thick short rotors, as shown by Figure 5.17 which uses the results data from Tables 5.15, Table 5.18, and Table 5.19. For the short rotors, GPS appears to increase in accuracy as the rotor thickness increases, with a higher frequency of the most
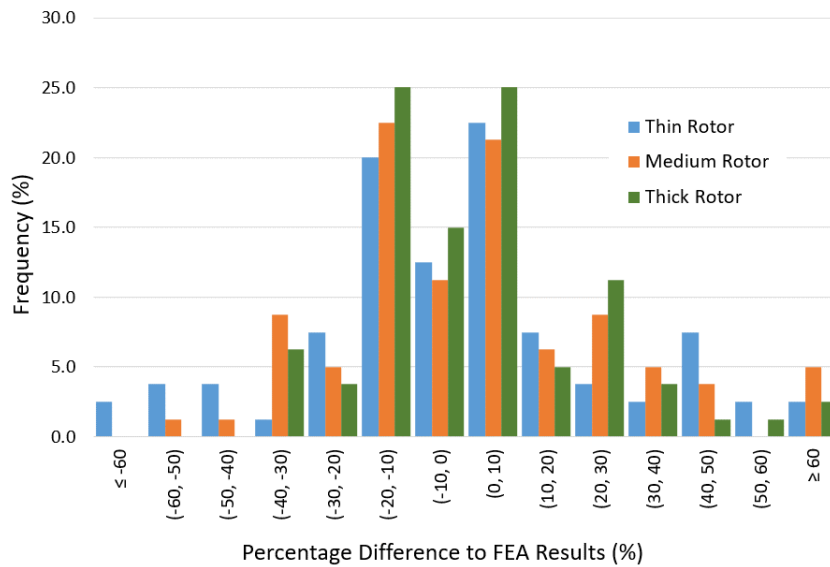
FIGURE 5.17: Short rotors - GPS results compared to FEA histogram.

Stress	$\omega(0krpm)$ $\Delta T(0^oC)$	$\omega(0krpm)$ $\Delta T(100^oC)$	$\omega(70krpm)$ $\Delta T(0^oC)$	$\omega(70krpm)$ $\Delta T(100^oC)$
S_1	5.74	5.52	6.50	6.13
S_2	0.35	0.40	0.26	0.30
$\sigma_{\theta ii}$	10.57	10.10	13.12	12.22
$\sigma_{\theta ic}$	11.72	11.16	13.91	12.98
$\sigma_{\theta mc}$	16.97	30.28	22.31	52.17
$\sigma_{\theta md}$	14.33	20.18	16.75	25.48
$\sigma_{\theta od}$	3.79	4.20	3.59	3.98
$\sigma_{\theta oo}$	4.03	4.52	3.80	4.28
σ_{zii}	71.19	47.01	76.58	48.85
σ_{zic}	28.27	20.56	28.78	20.73
σ_{zmc}	32.93	146.56	32.13	149.41
σ_{zmd}	15.69	30.57	14.54	27.38
σ_{zod}	11.60	14.02	11.24	13.59
σ_{zoo}	25.07	30.89	25.36	31.52
σ_{VMii}	14.42	12.61	16.91	13.89
σ_{VMic}	32.26	30.89	40.22	32.24
σ_{VMmc}	38.53	15.16	37.71	8.26
σ_{VMmd}	8.16	15.98	47.54	28.14
σ_{VMod}	3.14	3.44	3.01	3.30
σ_{VMoo}	2.47	2.61	2.20	2.33

TABLE 5.18: GPS medium short rotor results compared to FEA.

Stress	$\omega(0krpm)$ $\Delta T(0^oC)$	$\omega(0krpm)$ $\Delta T(100^oC)$	$\omega(60krpm)$ $\Delta T(0^oC)$	$\omega(60krpm)$ $\Delta T(100^oC)$
S_1	5.18	5.06	5.99	5.73
S_2	0.43	0.52	0.28	0.38
$\sigma_{\theta ii}$	9.44	9.01	12.28	11.45
$\sigma_{\theta ic}$	10.37	9.90	12.74	11.92
$\sigma_{\theta mc}$	14.26	21.65	19.52	36.55
$\sigma_{\theta md}$	11.93	15.37	14.27	19.67
$\sigma_{\theta od}$	3.51	3.81	3.30	3.58
$\sigma_{\theta oo}$	3.53	3.87	3.29	3.62
σ_{zii}	49.99	36.45	53.98	38.21
σ_{zic}	23.63	18.23	24.20	18.49
σ_{zmc}	26.70	63.56	26.01	63.41
σ_{zmd}	11.79	19.49	10.77	17.28
σ_{zod}	9.44	10.90	9.12	10.53
σ_{zoo}	21.14	24.65	21.53	25.31
σ_{VMii}	12.36	10.98	14.94	12.47
σ_{VMic}	29.11	28.10	37.79	30.07
σ_{VMmc}	36.28	17.85	39.06	9.63
σ_{VMmd}	2.37	9.29	34.99	23.13
σ_{VMod}	2.99	3.21	2.86	3.07
σ_{VMoo}	2.16	2.28	1.89	2.00

TABLE 5.19: GPS thick short rotor results compared to FEA.

accurate results and less extreme results. Mainly the axial stress results improved as rotor thickness increased. However, this improvement did not change the reliability of the model. The GPS results were still unpredictable and unreliable across all rotor thicknesses and therefore cannot be confidently used to predict rotor stresses in short rotors.

The plane strain results for the short rotor topologies are shown in Figure 5.18, taking the results data from Tables 5.16, 5.20, and 5.21. As with the GPS results, the accuracy of the plane strain results increases as the thickness of the rotor increases. However, the thick rotor results are still unreliable, therefore plane strain theory would not be a suitable method to use for short rotors. When compared to the corresponding GPS results from Figure 5.17, the GPS produces more accurate results for the thin, medium, and thick rotor topologies, with fewer results occurring in the extreme bins.

Stress	$\omega(0krpm)$ $\Delta T(0^oC)$	$\omega(0krpm)$ $\Delta T(100^oC)$	$\omega(70krpm)$ $\Delta T(0^oC)$	$\omega(70krpm)$ $\Delta T(100^oC)$
S_1	5.74	5.50	6.51	6.11
S_2	0.17	1.26	0.09	1.07
$\sigma_{\theta ii}$	10.58	10.09	13.12	12.21
$\sigma_{\theta ic}$	11.72	11.14	13.92	12.97
$\sigma_{\theta mc}$	16.34	34.96	20.81	59.05
$\sigma_{\theta md}$	13.88	22.83	15.80	28.35
$\sigma_{\theta od}$	3.98	3.30	3.91	3.26
$\sigma_{\theta oo}$	4.22	3.62	4.13	3.55
σ_{zii}	40.96	131.53	18.26	123.39
σ_{zic}	5.61	89.87	12.16	79.56
σ_{zmc}	4.45	674.82	18.34	611.38
σ_{zmd}	33.75	118.20	44.81	86.62
σ_{zod}	21.12	34.21	27.68	25.82
σ_{zoo}	35.74	24.47	44.77	16.54
σ_{VMii}	13.20	11.13	14.76	9.55
σ_{VMic}	22.06	15.57	17.49	11.46
σ_{VMmc}	19.40	33.36	0.88	12.61
σ_{VMmd}	45.00	45.51	160.40	5.12
σ_{VMod}	3.11	4.25	2.91	4.04
σ_{VMoo}	2.10	5.91	1.51	5.07

TABLE 5.20: Plane strain medium short rotor results compared to FEA.

Stress	$\omega(0krpm)$ $\Delta T(0^oC)$	$\omega(0krpm)$ $\Delta T(100^oC)$	$\omega(60krpm)$ $\Delta T(0^oC)$	$\omega(60krpm)$ $\Delta T(100^oC)$
S_1	5.18	5.06	5.98	5.74
S_2	0.24	1.18	0.11	0.90
$\sigma_{\theta ii}$	9.44	9.02	12.28	11.46
$\sigma_{\theta ic}$	10.37	9.90	12.73	11.93
$\sigma_{\theta mc}$	13.64	24.63	17.88	40.37
$\sigma_{\theta md}$	11.49	17.22	13.22	21.49
$\sigma_{\theta od}$	3.70	3.12	3.65	3.10
$\sigma_{\theta oo}$	3.72	3.19	3.65	3.14
σ_{zii}	23.83	98.86	0.85	87.49
σ_{zic}	2.07	72.32	18.15	59.34
σ_{zmc}	0.50	264.76	24.32	216.60
σ_{zmd}	30.03	79.55	43.53	49.71
σ_{zod}	19.26	25.76	27.34	15.86
σ_{zoo}	32.01	16.55	43.11	6.67
σ_{VMii}	11.12	10.84	12.61	10.05
σ_{VMic}	18.58	26.41	11.07	3.31
σ_{VMmc}	16.23	42.08	10.77	16.51
σ_{VMmd}	35.71	54.95	151.93	13.17
σ_{VMod}	2.96	3.72	2.75	3.51
σ_{VMoo}	1.77	4.71	1.08	3.79

TABLE 5.21: Plane strain thick short rotor results compared to FEA.
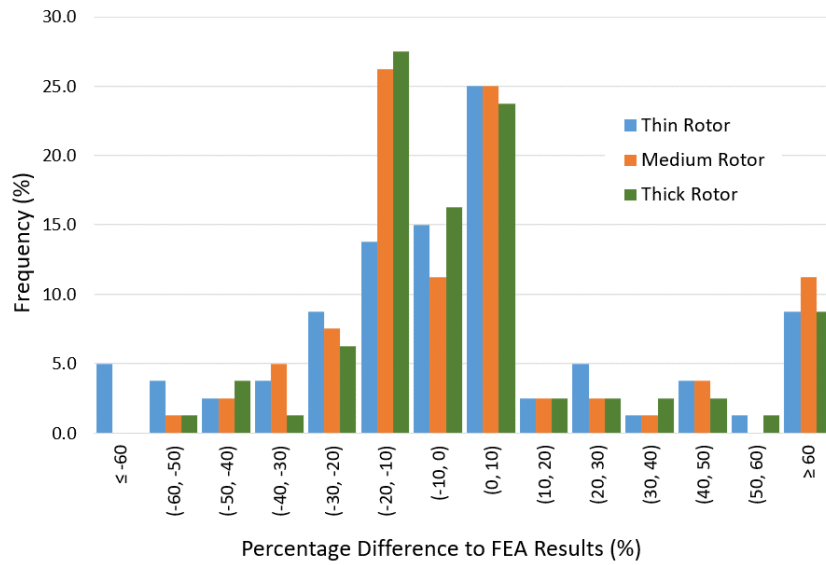
FIGURE 5.18: Short rotors - Plane strain results compared to FEA histogram.

The plane stress results for the short rotor topologies are shown in Figure 5.19, using the results data from Tables 5.17, 5.22, and 5.23. Figure 5.19 shows that plane stress produces the most consistent results across the short rotor topologies compared to plane strain and GPS as the results are more concentrated together. However, all rotor topologies had lower accuracy results than the GPS medium and thick
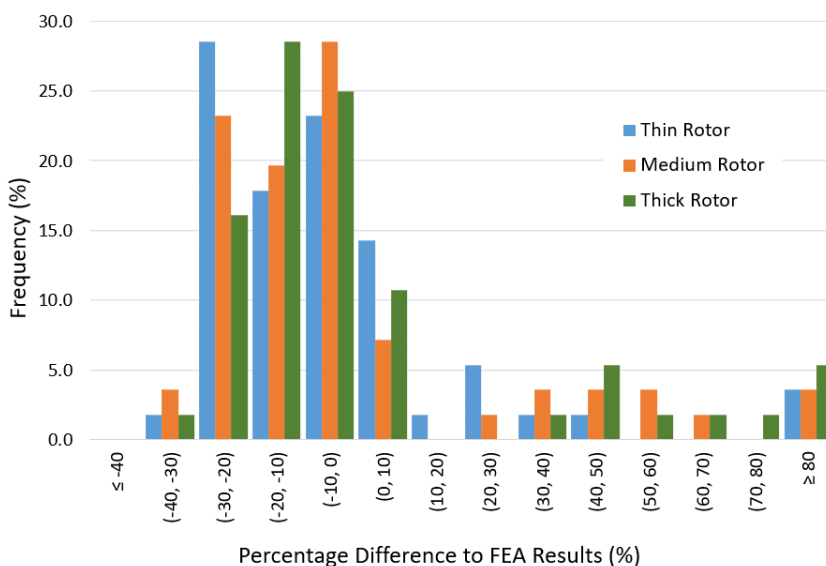
FIGURE 5.19: Short rotors - Plane stress results compared to FEA histogram.

short rotors as many more results occurred between 20% - 30% from the FEA. There-fore, plane stress would also be unsuitable to use for stress analysis of short rotors, despite being more suited to disks and short rotors with the assumption to neglect axial stress. Overall, none of the three stress theory approaches were accurate or reliable enough to use on short rotors.

Stress	$\omega(0krpm)$ $\Delta T(0^oC)$	$\omega(0krpm)$ $\Delta T(100^oC)$	$\omega(70krpm)$ $\Delta T(0^oC)$	$\omega(70krpm)$ $\Delta T(100^oC)$
S_1	15.62	16.91	17.75	18.97
S_2	10.11	9.48	10.64	9.96
$\sigma_{\theta ii}$	19.94	20.94	24.37	25.06
$\sigma_{\theta ic}$	20.97	21.87	25.22	25.80
$\sigma_{\theta mc}$	23.40	22.97	31.20	39.68
$\sigma_{\theta md}$	21.70	20.88	26.73	27.89
$\sigma_{\theta od}$	6.37	5.30	6.30	5.25
$\sigma_{\theta oo}$	6.16	5.00	5.71	4.57
σ_{VMii}	12.80	11.55	16.74	15.13
σ_{VMic}	26.09	45.37	35.08	58.88
σ_{VMmc}	36.94	8.82	55.62	9.67
σ_{VMmd}	151.10	49.85	325.82	68.39
σ_{VMod}	1.83	1.03	1.45	0.68
σ_{VMoo}	4.79	5.14	4.78	5.06

TABLE 5.22: Plane stress medium short rotor results compared to FEA.

Stress	$\omega(0krpm)$ $\Delta T(0^oC)$	$\omega(0krpm)$ $\Delta T(100^oC)$	$\omega(60krpm)$ $\Delta T(0^oC)$	$\omega(60krpm)$ $\Delta T(100^oC)$
S_1	15.04	16.13	17.54	18.58
S_2	10.03	9.57	10.64	10.14
$\sigma_{\theta ii}$	18.86	19.63	24.06	24.53
$\sigma_{\theta ic}$	19.69	20.41	24.63	25.04
$\sigma_{\theta mc}$	20.70	18.99	28.89	32.32
$\sigma_{\theta md}$	19.31	17.94	24.74	24.72
$\sigma_{\theta od}$	6.47	5.63	6.37	5.56
$\sigma_{\theta oo}$	6.45	5.57	5.87	5.00
σ_{VMii}	10.63	9.66	15.10	13.88
σ_{VMic}	31.83	48.29	45.94	67.08
σ_{VMmc}	44.80	2.49	74.55	0.97
σ_{VMmd}	136.22	59.74	313.23	88.93
σ_{VMod}	2.11	1.47	1.63	1.02
σ_{VMoo}	4.62	4.91	4.64	4.86

TABLE 5.23: Plane stress thick short rotor results compared to FEA.

5.4   Summary

This chapter explored the assumptions and accuracy of each theoretical model to determine their suitability in differing scenarios. Understanding the differences between the theories enables the work completed in this project to be applied to the appropriate engineering problems. A summary of the significant findings identified in this chapter is listed below.

- Rotor behaviour was shown to be axisymmetric while the magnets were held in circumferential compression.

- The rotor sleeve rapidly develops major stress concentrations as the magnets go into tension and separate, therefore the rotor will behave axisymmetric when operating successfully.

- The plane stress assumption of negating axial stress was shown to be incorrect even for short rotors.

- The plane strain assumption of negating axial strain was shown to be incorrect.

- Axial strain was shown to be constant throughout a rotor cylinder thickness for longer rotors, verifying the axial strain compatibility condition used in the GPS theory.

- An end-effect is demonstrated to be present at the free end of the rotor where the behaviour changes from GPS to a state of plane stress.

- The end-effect is due to the loss of axial load transfer between the cylinders, caused by the slip between cylinders at the rotor ends. However, this only occurs at the rotor ends whereas most of the rotor corresponds to the axial force equilibrium condition in the GPS theory.

- For long rotors, the GPS theory is much more reliable and accurate than either plane strain or plane stress theories. Over 93% of results were within 3% of the FEA.

- For long rotors, the axial stress results from the plane strain theory were the most compromised due to the incorrect assumption that there is no axial strain in the rotor. These errors then significantly affected the Von Mises stress calculations for the plane strain theory.

- The plane stress results were more consistent than the plane strain results, but still had significant differences from the FEA for the long rotor topologies, where only circa 30% of results fell within 8% of the FEA.

- The GPS theory remains accurate across all operating condition including speed and temperature changes, allowing rotor designs to be optimised using the theory.

- The GPS theory is most accurate for thin long rotors; however, it was still accurate and reliable for the medium and thick rotor topologies.

- The GPS theory is limited by the end-effect and is therefore only suited to long rotors where most of the rotor is in a state of GPS.

- Neither GPS, plane stress, nor plane strain were suitable theories for short rotor topologies.

6 Three Cylinder Rotor & Test Rig Design

6.1 Introduction

Chapter 5 highlighted the accuracy of the theoretical models when compared to finite element analysis (FEA) results. However, the accuracy of the FEA must be established to determine the functionality of these results. Therefore, experimental testing must be conducted requiring the design of a suitable test rig. Much of the work in this chapter has previously been published by the author, outlined by Mallin [157]. However, this chapter discusses the test rig design process in significantly more detail, shown in Section 6.4.

6.2 Instrumentation & Components

6.2.1 Air-handling Devices

Typically, high-speed testing has been done via the use of a high-speed electric machine (HSEM). However, the performance of a HSEM is not relevant to this rig and therefore the complexity can be reduced by using an air turbine to generate rotation, as discussed in Section 2.6.1. Air turbines also allow the mechanical behaviour of the rotor to be measured as it does not require a stator like HSEMs. By utilising an existing turbine, a rotor could be mounted to the turbine shaft to induce rotation. Inspiration was taken from Terdich and Martinez-Botas [16], where a cold gas stand was used. Figure 6.1 shows an electric air compressor the university had access to and an accompanying mounting stand. Using this was deemed a simpler than sourcing and utilising an internal combustion engine, as shown by Gerada et al. [9]. The utilisation of both the compressor and stand reduced the design complexity greatly

and only required the mounting of the test rig to the compressor stand. Figure 6.2 shows a schematic of the airflow in the proposed test rig system.
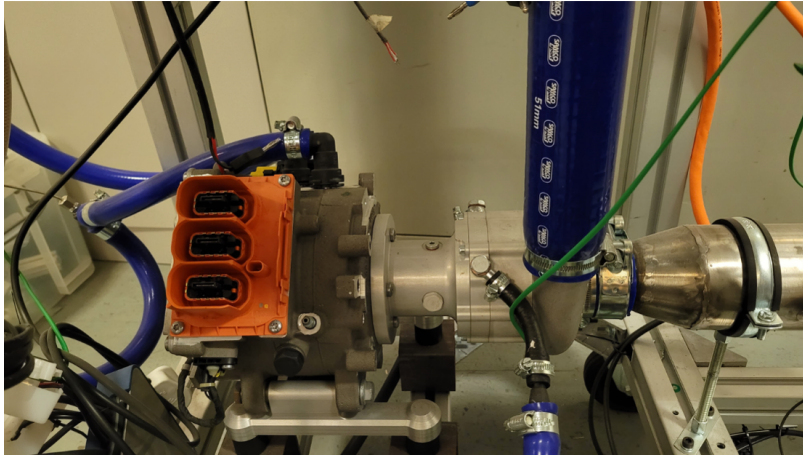
FIGURE 6.1: Electric air compressor.
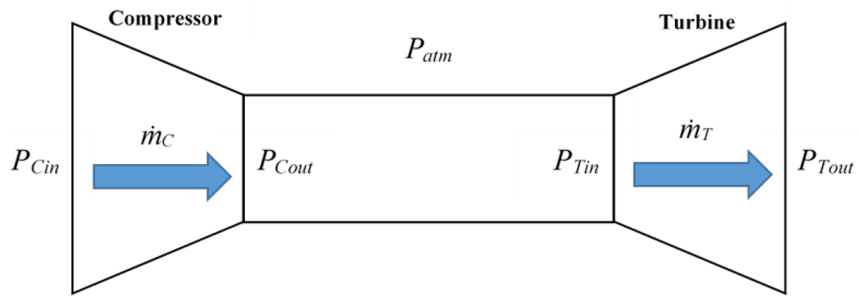
FIGURE 6.2: Electric compressor and turbine air flow chart.

Where P_{Cin}, P_{Cout}, P_{Tin}, P_{Tout} and P_{atm} are the pressures for compressor inlet, compressor outlet, turbine inlet, turbine outlet and atmospheric respectively, while $\dot{m}_C$ and $\dot{m}_T$ are the mass flow rates for the compressor and turbine, respectively. Equations 6.1 - 6.3 show the relationship between the pressures and mass flow rates.

$$P_{Cin} = P_{Tout} = P_{atm} \tag{6.1}$$

$$P_{Cout} = P_{Tin} \tag{6.2}$$

$$\dot{m}_C = \dot{m}_T \tag{6.3}$$

Since the compressor inlet and turbine outlet pressures are the same, while the compressor outlet and turbine inlet are the same, both the compressor and turbine

have the same pressure ratio. Mass flow rate through the compressor must match the flow rate through the turbine. The compressor was fitted with an *EC15* compressor wheel, which provides the airflow highlighted on the compressor map shown in Figure 6.3.

The compressor map shows the airflow and corresponding pressure ratios that the compressor operates within. The *x*-axis plots $\dot{m}_C$ while the *y*-axis plots the ratio between P_{Cout} and P_{Cin}. The compressor delivers a maximum airflow of circa 0.22 kgs^{-1}; therefore, the selected turbine stage should operate within this airflow range to be a good aerodynamic match with the compressor.
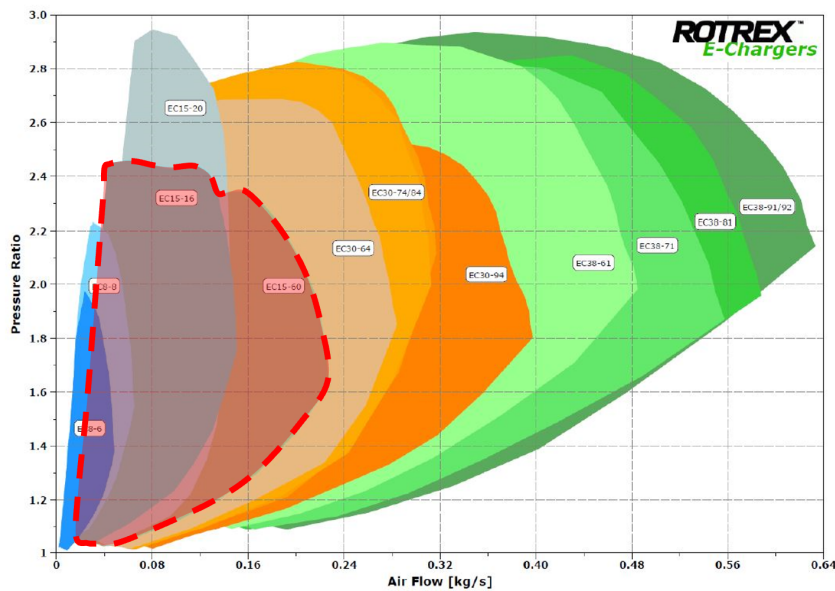
FIGURE 6.3: Compressor map for the university owned electric air compressor, adapted from Rotrex [158].

Being an aerodynamic match to the compressor was not the only selection criteria for the turbine stage. The test requires a rotor to be driven by the turbine stage and therefore, the corresponding shaft and wheel for the turbine stage must have the ability to be easily modified to carry the rotor, have spares available to purchase, and operate at high-speed. Section 6.3 identifies that the test rotor design required a large diameter to produce measurable surface strain and manufacturing constraints meant the test rotor would be short, despite the generalised plane strain (GPS) theory being identified as accurate for long rotors in Chapter 5. Correlating the testing results to finite element analysis (FEA) simulations would still validate the accuracy

of the GPS theory as the analysis correlates with FEA models, shown in Chapter 5.

To replicate the short rotor designs tested in Chapter 5, a minimum length to outer radius aspect ratio of 2 was set. A turbine stage was sought that matched the aerodynamic performance of the compressor, operated at the test rotor design speeds of 80 krpm, and could also carry a 50 mm long rotor on the turbine shaft.

When exploring existing turbine stages and their shaft and wheels, the length of rotor shafts did not vary considerably amongst similar sized turbines and most rotor shafts included a step which would need removing. This would then provide a suitable long, constant diameter shaft to carry the rotor. The primary air turbine choice on site operated at the required speed and had a suitably long shaft. This turbine stage was proceeded with for some time until its lack of spare components caused problems during the design process. Spare components provide the ability to repeat machining processes if an existing part required alterations and was manufactured incorrectly, such as removing the step on the turbine shaft. By manufacturing on site to save costs, the chance of not achieving tight tolerance designs with limited machining capability was relatively high and spares were needed. To mount the rotor onto a turbine shaft, a complete redesign of the bearing housing would be required, therefore only the turbine stage was required to be purchased, reducing costs. A similar sized gas turbine to the primary choice was later sourced with access to individual components. The rotor wheel outer diameter was 56.5 mm and the shaft length capable of carrying a rotor was circa 68 mm. Once the step on the shaft was machined down, it had a diameter of 6 mm.

Figure 6.4 shows the turbine flow chart for the sourced turbine stage. To ensure this replacement air turbine matched the compressor, turbine and compressor flow charts were compared. It was important to match the components to extract strong operating performance. The green 0.57 A/R curve was the air turbine flow for the turbine stage. The performance curve overlaps with the capabilities of the compressor map in Figure 6.3, showing a good aerodynamic match and enabling high performance and rotational speeds.
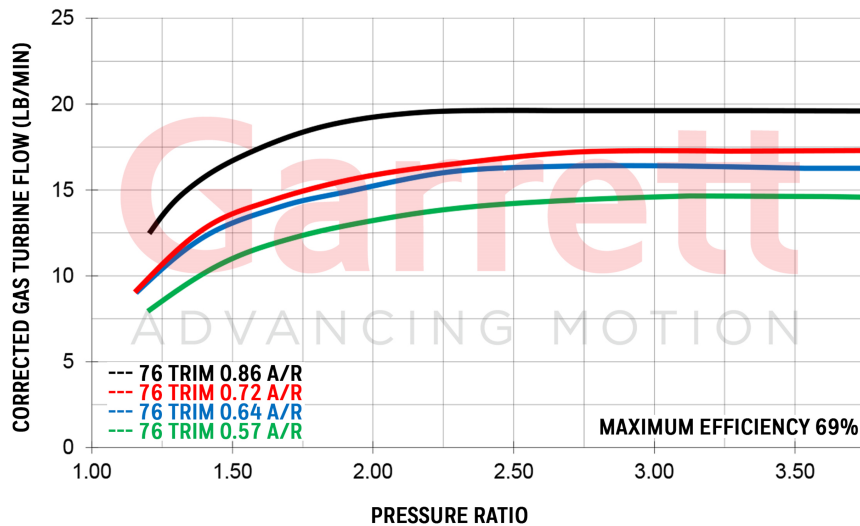
FIGURE 6.4: Air turbine flow chart [159].

6.2.2 Digital Image Correlation

As discussed in Section 2.7, digital image correlation DIC enables the extraction of strain results without any equipment required to be attached to the rotor or test rig. This allows results to be gathered that are not affected by any external factors. Figure 2.7 shows a typical DIC set up where the use of two cameras to view the specimen provides strain analysis in three dimensions. Before setting the cameras, the test specimen will require a speckle pattern. A base layer is used to coat the surface, followed by a contrasting spray to create the speckles. This must be a random pattern so the cameras can identify unique speckles to reference.

When the test specimen and cameras are in place, a reference image is taken. As the test progresses, surface strain will affect the size and position of the speckles. Images taken throughout the test are referenced against the reference image to determine the level of strain taking place. The software then converts this into a visual pattern of surface strain.

For this application, the outer surface of the rotor sleeve is the only visible surface to monitor, therefore any results will have to be validated against the FEA results of the outer surface of the sleeve. The DIC provides a full surface pattern of the strain which will enable the end-effect discussed in Chapter 5 to be visualised.

When testing at speed, a light strobe will be required to capture the same section of the rotor in each image. Each strobe will illuminate the specimen to be visible

to the cameras when the image is recorded. To ensure the timing of the strobe is correct, a rotor speed sensor output can be input into the system during testing. The collection of images will then undergo post processing to determine surface strain value which can then be compared against the FEA results, which will enable the validation of the GPS theoretical analysis results. It must be ensured that the rotor sleeve material will produce enough strain to be detected by the DIC system.

6.2.3   Initial Rig Concept

Considering the instrumentation and components discussed in Section 6.2, the general test rig concept will utilise the university owned compressor and the sourced turbine stage where the compressor is used to deliver high velocity air directly into the turbine volute. This will induce rotation of the turbine wheel and therefore the test rotor which will be carried on the turbine shaft. In a typical turbocharger, the shaft is housed within a bearing housing and is obscured from view. To enable the DIC to measure the surface strain of the test rotor, a bespoke bearing housing will be required to ensure the test rotor is visible during operation.

6.3   Three Cylinder Test Rotor Design

6.3.1   Test Rotor Concept

A concept rotor is shown in Figure 3.1. The carrier is a sliding fit onto the shaft with the interference locations between the carrier and magnets; and the magnets and sleeve, known as radii c and d respectively.

The purpose of the rotor being designed was to allow experimental determination of the strains generated to validate the accuracy of the FEA results from Chapter 5, and therefore the GPS theory. As the focus of the test was to extract strain results, the materials used would not be significant and a wide range of materials could be used in the rotor. Therefore, to avoid the cost and fragility of rare earth magnets, they were replaced with much less expensive, metal *pseudo-magnets*.

It should be noted that the final rotor design in this chapter will not be the most efficient or practical rotor for use in HSEMs. The experiment focusses solely on

the mechanical behaviour of the rotor and consideration is not given to the electromagnetic performance of the test rotor. The rotor is only required to behave as a three-cylinder compound rotor so that the assumptions and compatibility conditions made in the GPS theory are validated as accurate and reliable. Once validated, the GPS theory can be used with confidence within a design process that includes performance considerations, enabling the efficient and successful design of a three-cylinder compound rotor for HSEMs.

6.3.2   Test Rotor Manufacturing & Assembly

To manufacture to rotor the diameter, length, and tolerances of the rotor are important. Without exploring expensive manufacturing techniques, measuring finer than a hundredth of a millimetre when manufacturing components is not possible. Therefore, any tolerance must be specified to at least 10 microns. This could particularly affect the interference levels, which are the smallest measurements of the rotor design but have a major impact on the results.

The diameter and length are related when discussing machining limitations. The machining would be limited by the aspect ratio of the rotor. If the rotor is long and thin, the machines used to manufacture the component are likely to chatter as the machining moves further from the rotor ends. This is due to the component flexing under the pressure applied during cutting. Excessive flexing would destroy the parallelism and tolerances of a rotor component. Given the sensitivity of the results with relation to the interference level between the cylinders, it is likely that the final rotor design will be shorter than the long rotor topologies discussed in Chapter 5.

When assembling a rotor, Binder et al. [25] explores axial pressing and shrink fitting, both capable of being conducted at the university. Binder et al. [25] observed a rotor failure and listed the axial pressing assembly process as harmful to the rotor sleeve strength, although they admit it is difficult to quantify. Wang et al. [110] also state that in HSEMs, the permanent magnets (PMs) have low tensile strength and the tensile load during assembly can be reduced via shrink fitting. The rotor for the design in this paper will enable the assembly method of shrink fitting to avoid the potential negative effects of axial pressing. Therefore, materials must be

selected where the diameters change sufficiently under temperature effects to enable the parts to slide within each other with minimal resistance.

6.3.3 Design Constraints

There are many difficulties in designing a successful rotor for this rig that requires delicate balancing. The rotor design constraints were:

- Pseudo-magnets retained by the sleeve under testing conditions.
- Sleeve outer surface strain differential due to rotation greater than 400 $\mu\varepsilon$.
- Assemble via shrink fitting.
- No yielding under testing condition.
- Interference tolerance at c and d must not have a lower resolution than 10 microns.
- Materials used must be isotropic.
- Carrier inner diameter must be 6 mm.

For a rotor within a HSEM to operate, magnets must remain in compression due to the low tensile strength. However, this condition did not constrain the test rotor design as the pseudo-magnet material could withstand tensile stresses. The focus of the rotor design was to achieve a sufficient outer surface strain. The change in sleeve outer surface strain from stationary to operating conditions had to be large enough to produce accurate DIC results. An experiment conducted by Acciaioli et al. [160] identified a minimum strain value measurement for strain fields under 1000 $\mu\varepsilon$ in the transverse and longitudinal directions. The values were 140 $\mu\varepsilon$ and 400 $\mu\varepsilon$ respectively and were determined by the ability to calculate the Young's modulus and Poisson's ratio of the specimen material accurately. As strain readings fell below these values, variation was exponentially affected. As the rotor surface strain will be measured in both the circumferential and longitudinal directions, 400 $\mu\varepsilon$ was chosen as the minimum required surface strain.

To increase the sleeve outer surface strain, the overall rotor diameter can be increased, thus increasing the centrifugal force. However, an increase in centrifugal force may reduce the interference between the cylinders and risk rotor separation. To maintain retention, the interference levels between the cylinders can be increased.

However, if the interference is increased excessively the rotor may be impossible to assemble by shrink fitting as the temperature differential required to generate the required thermal expansion differential, may be larger than the materials can withstand. Another risk of excessive interference is the rotor yielding under its own compression when stationary.

As discussed in Section 6.3.2, the level of interference between each component must have tolerances limits of at least 10 microns. Based on the turbine stage chosen in Section 6.2, the maximum rotor length was 60 mm due to the turbine shaft length. The turbine shaft also fixed the inner diameter of the inner cylinder at 6 mm once the step on the shaft had been machined down.

6.3.4   Detailed Design Iterations

The developed GPS theory in Chapter 4 was utilised to predict whether a rotor design would be successful during testing. Material specifications, dimensions and operating conditions were the inputs while the key outputs were component stresses, interference pressures S_1 and S_2 at radii c and d respectively, and the sleeve outer surface strain.

The first decision was to select materials in order of stiffness, with the sleeve being the stiffest and the carrier the least stiff rotor cylinder. It was predicted that as the load increased on the rotor, the outer material would deform less than the interfering inner material. Therefore, both c and d should remain in compression. High density materials were selected to attempt to strain the outer sleeve by increasing the centrifugal force, while the high stiffness sleeve material would resist excessive deformation. The chosen materials and the corresponding specifications were idententified via MatWeb [161–163] and are shown in Table 6.1.

Another input, the dimensions, were then determined. To maintain a radius to length aspect ratio of 2, a maximum diameter value of 50 mm was specified. Based on this a medium thickness rotor was chosen, which provided a sensible starting point and ensured the machining was within the university's capacity. The dimensions are specified for the first design iteration in Table 6.2 and the initial test results conducted at rotor speeds of 0-80 krpm are shown in Table 6.3. 80 krpm was chosen

Cylinder component	Material	Poisson's Ratio	Density (kgm^{-3})	Young's Modulus (GPa)	Coefficient of Thermal Expansion	Yield Strength (MPa)	Ultimate Strength (MPa)
Inner	Aluminium 6061-T6	0.33	2700	68.9	2.36×10^{-5}	276	310
Middle	C464 Brass	0.28	8410	100	2.12×10^{-5}	317	476
Outer	304 Stainless Steel	0.29	8000	193	1.73×10^{-5}	210	505

TABLE 6.1: Material selection for first rotor design iteration.

Cylinder component	Inner surface diameter (mm)	Outer surface diameter (mm)	Interference (mm)
Inner	6	12.02	0.01
Middle	12	22.02	
Outer	22	26	0.01

TABLE 6.2: Dimension selection for first rotor design iteration.

Test Speed $(krpm$	Rotor separation?	Sleeve outer surface strain $(\mu\varepsilon)$	Maximum inner cylinder Von Mises stress (MPa)	Maximum middle cylinder Von Mises stress (MPa)	Maximum outer cylinder Von Mises stress (MPa)
0	No	792	167	93	205
50	No	869	145	102	220
80	No	989	111	117	245

TABLE 6.3: First design iteration initial tests.

to represent a realistic high-speed that was within the capability of the components discussed in Section 6.2.

As shown by the initial calculations, the rotor would stay together from stationary to 80 krpm. Most of the rotor stresses were predicted to remain within the yield limits of the material, but the outer sleeve was predicted to plastically deform at both 50 krpm and 80 krpm. With the rotor stationary the sleeve would already be close to yielding. However, the most significant problem was the lack of range for the sleeve outer surface strain. The 77 $\mu\varepsilon$ change, from stationary to 50 krpm would not be reliably detectable by the DIC system and the overall change from stationary to 80 krpm was still under 200 $\mu\varepsilon$.

For the second design iteration, the rotor diameter was substantially increased to maximise the range of sleeve outer surface strain being produced. To combat the extra stresses this would put on the sleeve, the brass and aluminium materials were

switched to the inner and middle cylinders, respectively. The minimum interference remained as a baseline test. Tables 6.4 and 6.5 show the design and test details of the second design iteration.

Cylinder component	Inner surface diameter (*mm*)	Outer surface diameter (*mm*)	Interference (*mm*)
Inner	6	20.02	0.01
Middle	20	40.02	
Outer	40	48	0.01

TABLE 6.4: Dimension selection for second rotor design iteration.

Test Speed (*krpm*	Rotor separation?	Sleeve outer surface strain (*µε*)	Maximum inner cylinder Von Mises stress (*MPa*)	Maximum middle cylinder Von Mises stress (*MPa*)	Maximum outer cylinder Von Mises stress (*MPa*)
0	No	457	96	64	122
50	No	622	33	69	153
80	Yes	-	-	-	-

TABLE 6.5: Second design iteration initial tests.

For this second iteration, the change in sleeve outer surface strain between 0 krpm and 50 krpm was predicted to increase from 77 $\mu\varepsilon$ to 165 $\mu\varepsilon$. Whilst this did not meet the design criteria, the intention of the second iteration was successful. There was also a substantial reduction in the stresses produced in each component, eliminating any yielding at stationary or at an operating speed of 50 krpm. However, the rotor would separate before reaching 80 krpm as the centrifugal forces of the sleeve pulled it from the middle cylinder. The speed limit for the second design iteration was found to be 60 krpm. To combat this in the third design iteration, different material grades were selected. A reduction in sleeve density and an increase in stiffness would reduce centrifugal forces to delay rotor separation, but also may hinder sleeve surface strain. An increase in density and a reduction in stiffness for the inner cylinder would also reduce rotor separation and increase sleeve outer surface strain. Due to supply issues the aluminium was swapped for a similar grade. Tables 6.6 - 6.8 show the design and test details of the third design iteration. The material properties were identified via the material supplier [164–166], MatWeb [167, 168], Davoudinejad et al. [169], and Aalco [170].

Cylinder component	Material	Poisson's Ratio	Density (kgm^{-3})	Young's Modulus (GPa)	Coefficient of Thermal Expansion	Yield Strength (MPa)	Ultimate Strength (MPa)
Inner	CZ121 Brass	0.31	8470	97	2.09×10^{-5}	369	495
Middle	Aluminium 6082-T6	0.33	2700	70	2.40×10^{-5}	260	310
Outer	EN16T Steel	0.3	7800	210	1.20×10^{-5}	680	850

TABLE 6.6: Material selection for third rotor design iteration.

Cylinder component	Inner surface diameter (mm)	Outer surface diameter (mm)	Interference (mm)
Inner	6	20.02	0.01
Middle	20	40.02	
Outer	40	48	0.01

TABLE 6.7: Dimension selection for third rotor design iteration.

Test Speed $(krpm)$	Rotor separation?	Sleeve outer surface strain $(\mu\varepsilon)$	Maximum $\sigma_{VMi}(MPa)$	Maximum $\sigma_{VMm}(MPa)$	Maximum $\sigma_{VMo}(MPa)$
0	No	451	101	66	132
50	No	608	38	71	164
80	Yes	-	-	-	-

TABLE 6.8: Third design iteration initial tests.

The results for the third iteration in Table 6.8 appear very similar to the second iteration results. It is predicted that there would be slight increases in the stresses throughout all three-cylinder components and the sleeve outer surface strain range would slightly decrease. The rotor also separates before reaching 80 krpm. However, the third design would reach 64 krpm instead of the 60 krpm achieved by the second iteration. As the sleeve outer surface strain range did not meet the design criteria, the operating range must be further increased. However, the third design iteration showed that these criteria offset each other. To identify further potential rotor designs, the third design iteration was further explored using different interference levels at radii c and d, known as δ_c and δ_d, respectively. The results are shown in Figures 6.5 – 6.12.
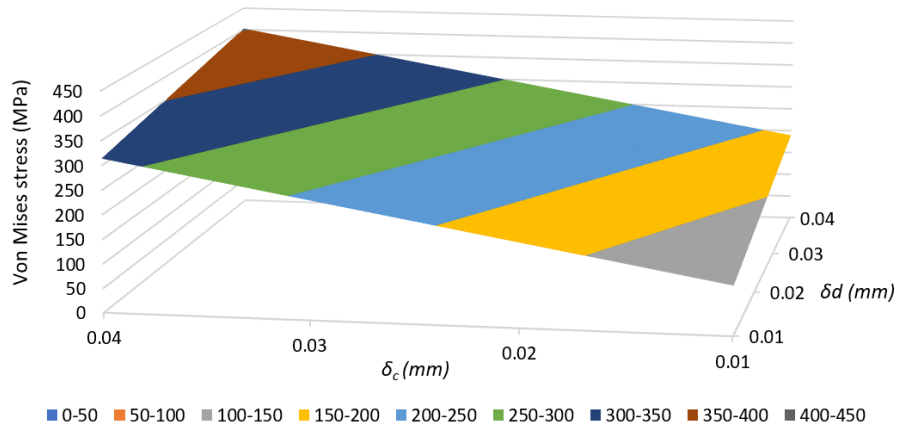
FIGURE 6.5: Inner Cylinder peak Von Mises Stress across various interferences when stationary.
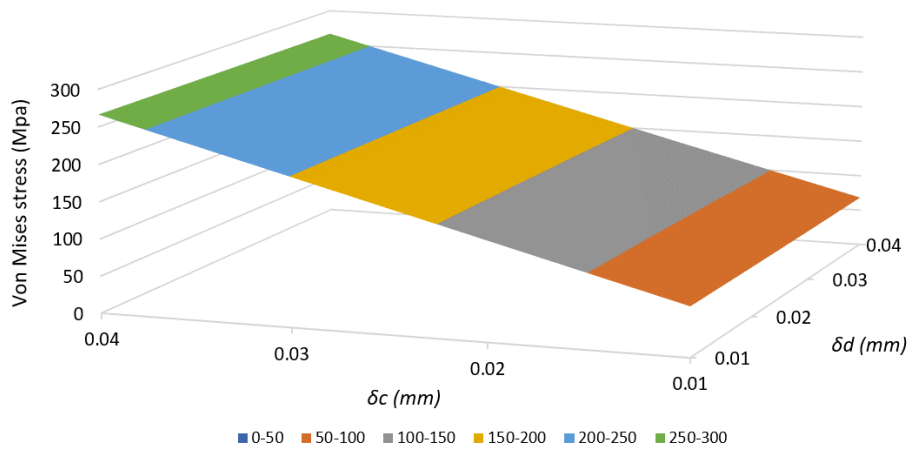
FIGURE 6.6: Middle Cylinder peak Von Mises Stress across various interferences when stationary.
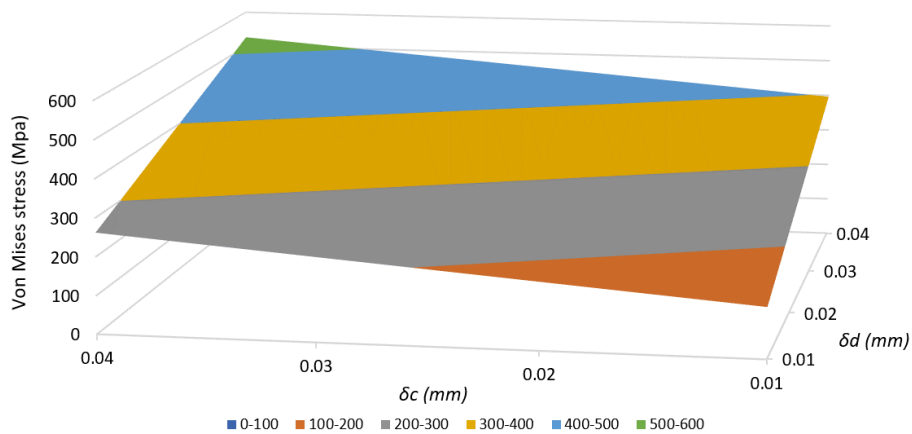
FIGURE 6.7: Outer Cylinder peak Von Mises Stress across various interferences when stationary.

From Figures 6.5 and 6.6, to avoid yielding of the inner and middle cylinders, the following design constraints are required:

$$\delta_d \leq 0.04 - 2(\delta_c - 0.03)$$

$$\delta_c \leq 0.04$$

From Figure 6.7, the outer cylinder remains elastic for all levels of interference.

As shown in Table 6.8, a 50 krpm operating speed did not produce enough change in surface strain to be measured by the DIC system. Therefore, an operating speed of 80 krpm was examined to determine a suitable rotor design. As shown in Figure 6.8, yielding was not predicted in the inner cylinder for any combination
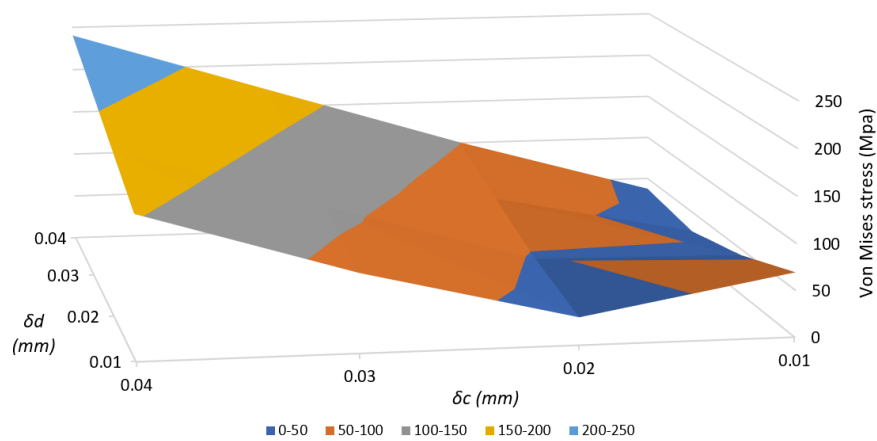
FIGURE 6.8: Inner Cylinder peak Von Mises Stress across various interferences at 80 krpm.
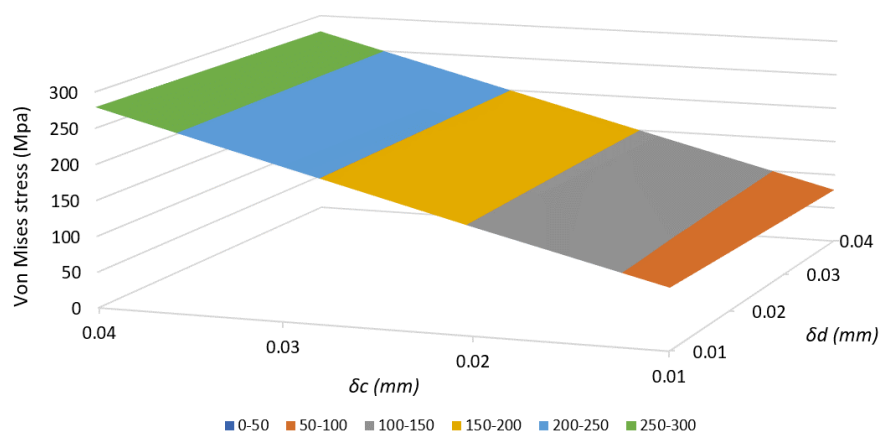
FIGURE 6.9: Middle Cylinder peak Von Mises Stress across various interferences at 80 krpm.
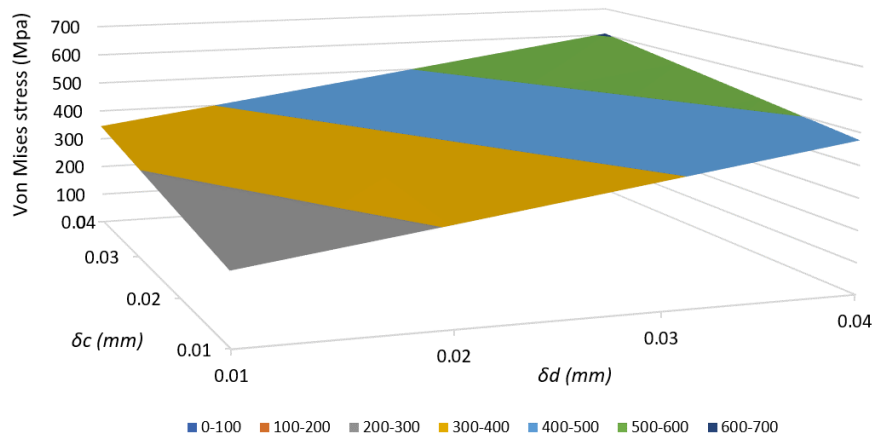
FIGURE 6.10: Outer Cylinder peak Von Mises Stress across various interferences at 80 krpm.

of interferences. For the middle cylinder in Figure 6.9, yielding was predicted when the interference, δ_c was 0.04 mm with any δ_d value. The outer cylinder in Figure 6.10, again shows that all levels of interference remained within the cylinder stress limit. However, rotor separation was predicted by the theory when interference, δ_d was 0.01 mm with a δ_c range of 0.01-0.02 mm.
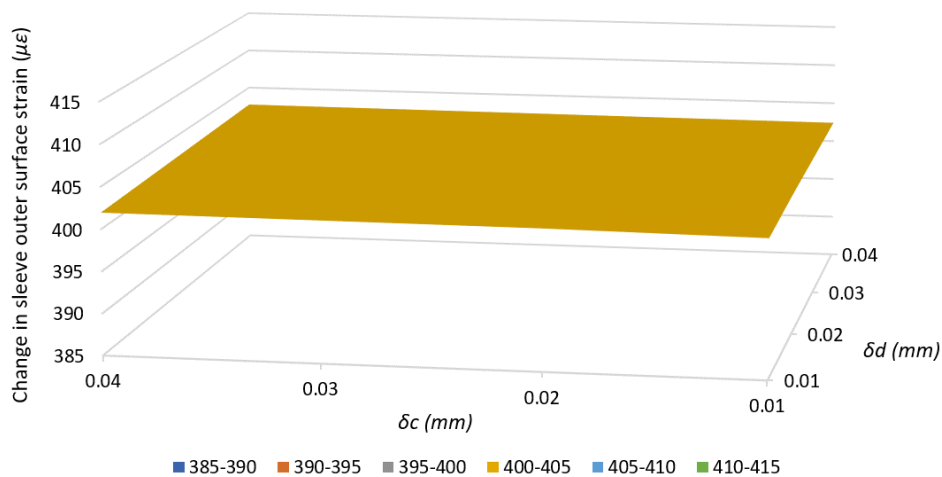
FIGURE 6.11: Change is sleeve outer surface strain from stationary to 80 krpm for various interferences.

Figure 6.12 shows the predicted sleeve strain values produced when stationary. All values are over the 400 $\mu\varepsilon$ limit required to be detected by the DIC system. This would allow strain testing to be achieved at stationary and operating conditions and could be utilised to conduct stationary thermal tests too. Figure 6.11 shows that
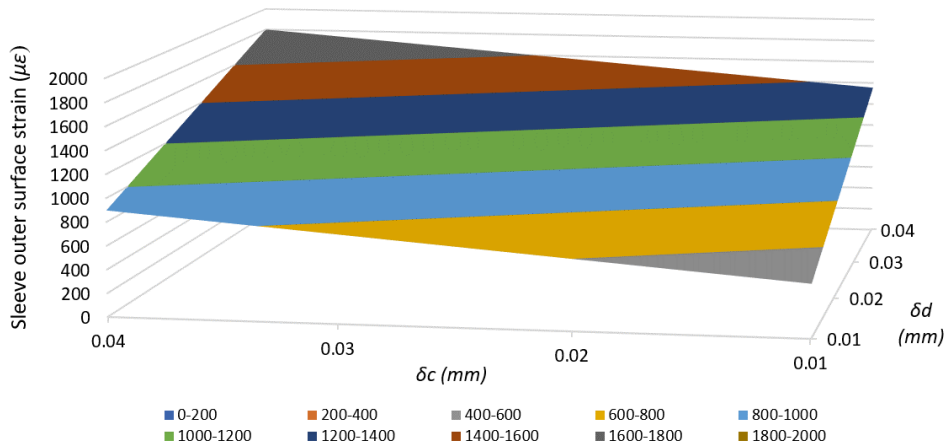
FIGURE 6.12: Sleeve outer surface strain for various interferences when stationary.

the predicted change in sleeve outer surface strain is constant for all interference topologies. Circa 400 $\mu\varepsilon$ is consistently produced, enabling accurate results to be extracted from DIC. The added strain due to rotation is expected to be the same for all interference levels because the materials, rotor size and rotational speed are the same.

6.3.5   Final Design

Based on the design iterations shown in Section 6.3.4, the final rotor design dimensions are shown in Table 6.9. The materials from Table 6.6 will be used. The final rotor design achieves the required change in outer surface strain to be detected by the DIC system and for speeds up to 80 krpm, the rotor is predicted to stay together with no rotor elements yielding, meeting the specified criteria.

Cylinder component	Inner surface diameter (mm)	Outer surface diameter (mm)	Interference (mm)
Inner	6.005 - 6.02	A + interference	+(0.01-0.02)
Middle	20 ±0.1 (A)	B + interference	
Outer	40 ±0.1 (B)	48 - 48.10	+(0.02-0.03)

TABLE 6.9: Dimension selection for final rotor design.

To accurately machine the interference levels between the rotor cylinders, the outer surface diameters of the inner and middle cylinders must be based off the inner diameters of the middle and outer cylinders, respectively. Therefore, Table 6.9 shows the use of the labels *A* and *B* to determine said dimensions. Table 6.10 shows the key tests to ensure the rotor will operate successfully at all potential interference combinations when at speed and at stationary conditions. Nominal dimension values have been used to demonstrate this as it is the interference that will have the major impact on results.

Test Speed (*krpm*)	Interference at *c* (*mm*)	Interference at *d* (*mm*)	Rotor separation?	Sleeve outer surface strain ($\mu\varepsilon$)	Maximum $\sigma_{VMi}(MPa)$	Maximum $\sigma_{VMm}(MPa)$	Maximum $\sigma_{VMo}(MPa)$
0	0.01	0.02	No	752	130	67	220
80	0.01	0.02	No	1154	43	82	304
0	0.01	0.03	No	1054	160	67	308
80	0.01	0.03	No	1456	28	79	390
0	0.02	0.02	No	901	201	133	263
80	0.02	0.02	No	1303	47	146	347
0	0.02	0.03	No	1203	231	133	351
80	0.02	0.03	No	1605	73	144	433

TABLE 6.10: Final design tests.

Table 6.10 shows that at any combination of interference, the change in outer surface strain between 0 krpm and 80 krpm is at least 400 $\mu\varepsilon$. The rotor cylinders are predicted to maintain contact pressure and not separate. All rotor cylinders operate within their yield stress limits comfortably. Therefore, the slight variations in machining tolerances, which does not affect the interference, will no affect the results enough to cause a failure in any of the rotor tests in Table 6.10.

For the shrink fitting process, it is assumed the materials are at 20°C room temperature and are cooled with liquid nitrogen to -196°C. Only the inner and middle cylinders will require shrinking to slide into their larger outer cylinder. Table 6.11 shows that the rotor cylinder diameters will change enough in liquid nitrogen to be assembled via shrink fitting and therefore the rotor design meets all criteria set in Section 6.3.3.

Cylinder component	Material	Coefficient of Thermal Expansion	Temperature change (^{o}C)	Starting diameter (mm)	Change in diameter (mm)	Required change in diameter (mm)
Inner	CZ121 Brass	2.09 $\times 10^{-5}$	-216	19.92 - 20.14	0.09	0.04
Middle	Aluminium 6082-T6	2.40 $\times 10^{-5}$	-216	39.94 - 40.16	0.21	0.06

TABLE 6.11: Shrink fit calculations for final rotor design iteration.

6.4 Test Rig Design

6.4.1 Design Requirements

After reviewing the existing literature and the initial design concept in Section 6.2.3, design constraints were specified to ensure the test rig design operated as intended. The following constraints were applied to the design of the test rig.

- Test rig must operate over 80,000 rpm.

- Rotor must be visible for the DIC system to measure surface strain.

- Existing parts available at the University should be utilised.

- Rotor assembly procedure must minimise presence of residual stress.

- Any machining and testing should be completed in-house at the University.

As discussed in Section 6.2.3, the test rig concept consists of an existing compressor, owned by the university, driving air into the adapted turbine stage which induces rotation of the test rotor. The use of an existing compressor reduces the rig cost and reduces the design requirements to that of only the adjoined turbine stage.

To ensure the testing conditions are comparable to HSEM applications the test rig must operate at 80 krpm. HSEMs operate across a wide range of speeds, which the developed GPS theory from Mallin and Barrans [154] must be validated against. The testing of a high, top speed allows the theory to be evaluated across a large range, improving result reliability. An operating speed of 80 krpm also enables the test rotor, designed in Section 6.3.5, to generate the required outer surface strain for the DIC system to accurately detect results.

To enable strain readings to be made using DIC during high-speed operation, there must be a full visual of the rotor during operation, which is usually obscured by a typical bearing housing. The strain readings will then enable the validation of

FEA and theoretical results. As discussed in Section 2.6.1, a pass or fail criteria is currently used in literature to determine the mechanical analysis success of a tested rotor. This method does not validate any predicted FEA or theoretical stress results.

Any component machining required for the rig should be completed within university resources to minimise project expenditure as the use of external suppliers for one-off components is expensive. Testing is also to be completed on-site requiring the rig to fit within available test cells. To further minimise expenditure, suitable accessible components or other services provided by university should be used.

As the rotor assembly will consist of interfering components, it is important to maintain the material capabilities of each section, post-assembly, by avoiding excessive stressing of the components. This may affect material selection and the amount of interference between each part.

6.4.2   Design Iterations

The turbine stage sourced within the university in Section 6.2 was designed to operate at the required 80 krpm and was suitable to use with the compressor. As the compressor will drive the turbine wheel and the attached test rotor, the compressor stage was unnecessary and was removed, simplifying the rig. However, this would remove the compressor load acting against the turbine and make it more difficult to slow the rotor down. The speed of operation would have to be tightly controlled to avoid over-speed which could cause rotor failure. The initial design iteration is shown in Figure 6.13.

As the compressor will drive the turbine wheel and the attached test rotor, the compressor stage was unnecessary and was removed, simplifying the rig. However, this would remove the compressor load acting against the turbine and make it more difficult to slow the rotor down. The speed of operation would have to be tightly controlled to avoid over-speed which could cause rotor failure.

To visualise the rotor for the DIC cameras, a bespoke acrylic bearing housing was chosen. An acrylic cylinder was held in place between two bolted flanges. This enabled the cameras to see the rotor and ensured an element of safety if the test rig unexpectedly failed. The flange connected to the turbine housing was required to fit very accurately like the standard bearing housing flange would. Therefore, the

(A) Full rig assembly. (B) Bearing housing flange detail.
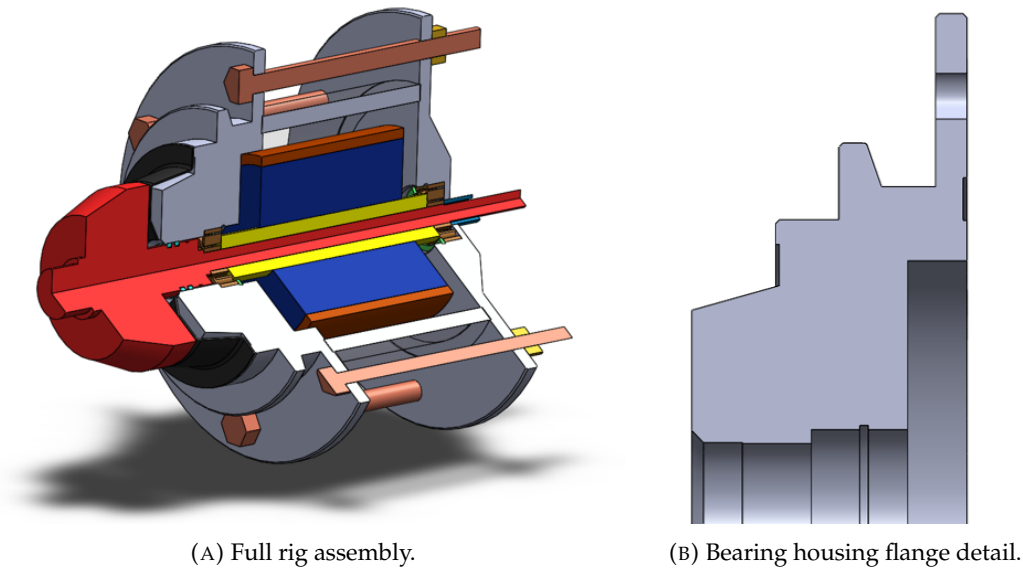
FIGURE 6.13: Section of the first test rig design iteration.

matching bearing housing details were accurately measured and replicated to create
a flange with the same detail. This enabled the air turbine to work as intended
which would maximise performance and reduce potential problems with the design
during operation.

Each flange housed a bearing for the turbine shaft and based on Section 2.6.1,
angular contact ball bearings were chosen for the design. Ball bearings enable a
simple design, but it was important to source angular contact bearings as the axial
load produced by the turbine stage with no compressor stage will be higher than
usual. Each bearing would be retained via a circlip.

To enable rotation, the rotor inner cylinder was designed to be a sliding fit onto
the turbine shaft which was then gripped between the bearings via the compressor
nut. The bearing on the turbine side would then press against the shoulder of the
turbine shaft causing it to rotate as part of the shaft. The standard turbine shaft was
designed to be adapted to a constant 6 mm diameter as a step shaft was incompatible
with the GPS theory, as discussed in Section 6.2.

After designing the first iteration of the test rig, two main issues were later identi-
fied, both with the acrylic housing. After consulting with the DIC system suppliers,
it was informed that a circular housing would cause problems for the cameras as
the light would be acting differently across the field of vision. Secondly, the acrylic
housing forced the rotor bearings to be housed in separate pieces. It was decided

that this could cause alignment issues which would be serious for the rotor speeds being designed for. Figure 6.14 shows the second rig design iteration.

(A) Full bearing housing.

(B) Bearing housing design detail.
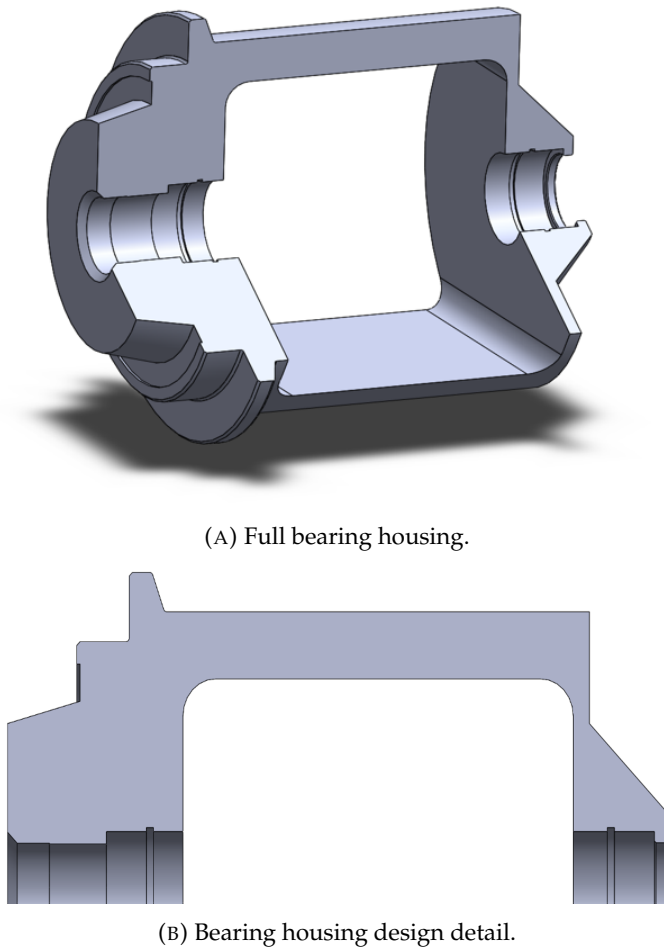
FIGURE 6.14: Section of the second test rig design iteration.

The second design iteration was to introduce a single piece bearing housing rather than using two flanges. This design solved the bearing alignment problem and removed the need for the acrylic housing. However, to ensure the rotor was still visible, a pocket was designed into the bearing housing where the rotor would sit. The detailing from both flanges in the first design, were transferred to the second design with no alterations. To overcome the potential safety issues of having no housing, all testing would be conducted in a test cell.

Despite solving issues with the single piece bearing housing, the second design iteration brought further complications. After consulting with the manufacturing team, it was clear that the University did not have the capabilities to machine the bearing housing. The main problem was the narrow boring diameter through the

centre of the component. Available tooling could not get through the small diameter to machine the grooves and lips required retain and locate the bearings. Considering these issues, Figure 6.15 shows the third test rig design iteration.
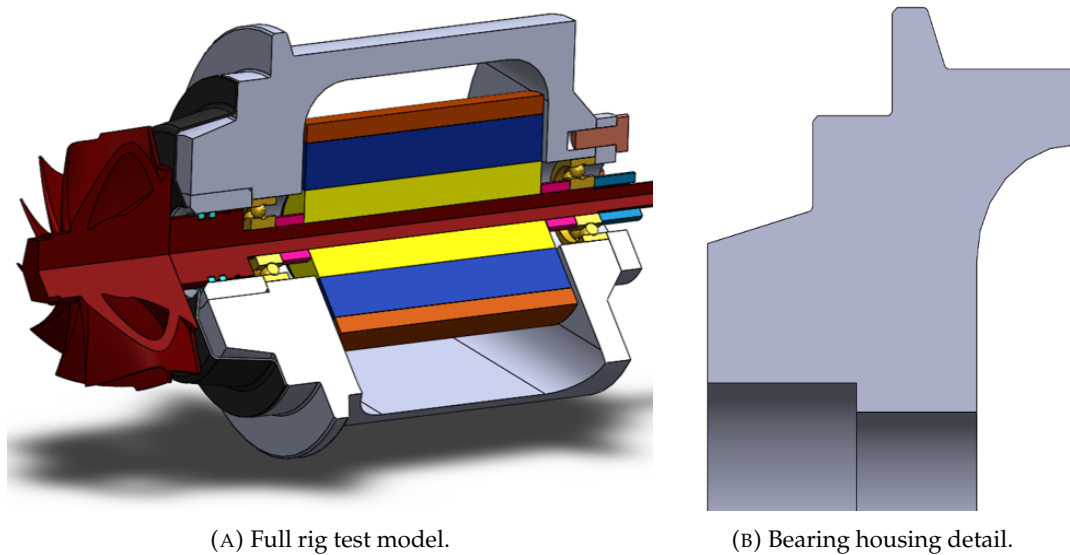
(A) Full rig test model.

(B) Bearing housing detail.

FIGURE 6.15: Section of the third test rig design iteration.

To overcome the machining limitations of the second design iteration, the third design incorporates two additional components. A pressed bush and a bolted plate were utilised at either end of the bearing housing to create the necessary bearing locators while the bearing housing has one main diameter hole throughout the model. This enables the central diameter to be machined in a single job. To remove the need for circlips and their complex grooves, the bearings were specified as interference fit and would be pressed into place. Other minor changes were the introduction of spacers on either side of the rotor. This allowed the rotor cylinders to all be the same length. Figure 6.15b shows a small reduction in unnecessary detailing to reduce machining complexity.

Manufacturing the bearing housing was still a concern to the machinists due to the tight tolerances on the components. Due to the stack up of parts along the rotor shaft, tight tolerances had developed to ensure the compressor nut would tighten them together so the rotor would turn with the shaft. The machinists also had concerns over machining the reduction in diameter of the turbine shaft. The main concern was the reduced diameter would cause serious deflection during machining

and the tolerances required would not be achieved. A recommendation of spare turbine shafts was made. It was at this point that the turbine stage with access to spare components was sourced, as discussed in Section 6.2 which resulted in a redesign of the test rig.

6.4.3   Final Design

After the bearing housing was redesigned for the newly sourced turbine stage, a series of further improvement were made to the design, shown in Figure 6.16. A central bore diameter was used throughout the component to increase manufacturing ease. Two shallow diameters would then be bored at either end to create the press fit bearing locations. A lip remained before the milled pocket to press the bearings against and easily locate them. This change removed the need for the pressed

(A) Complete assembly excluding turbine housing.

(B) Bearing housing detail.

(C) Bearing housing detail.
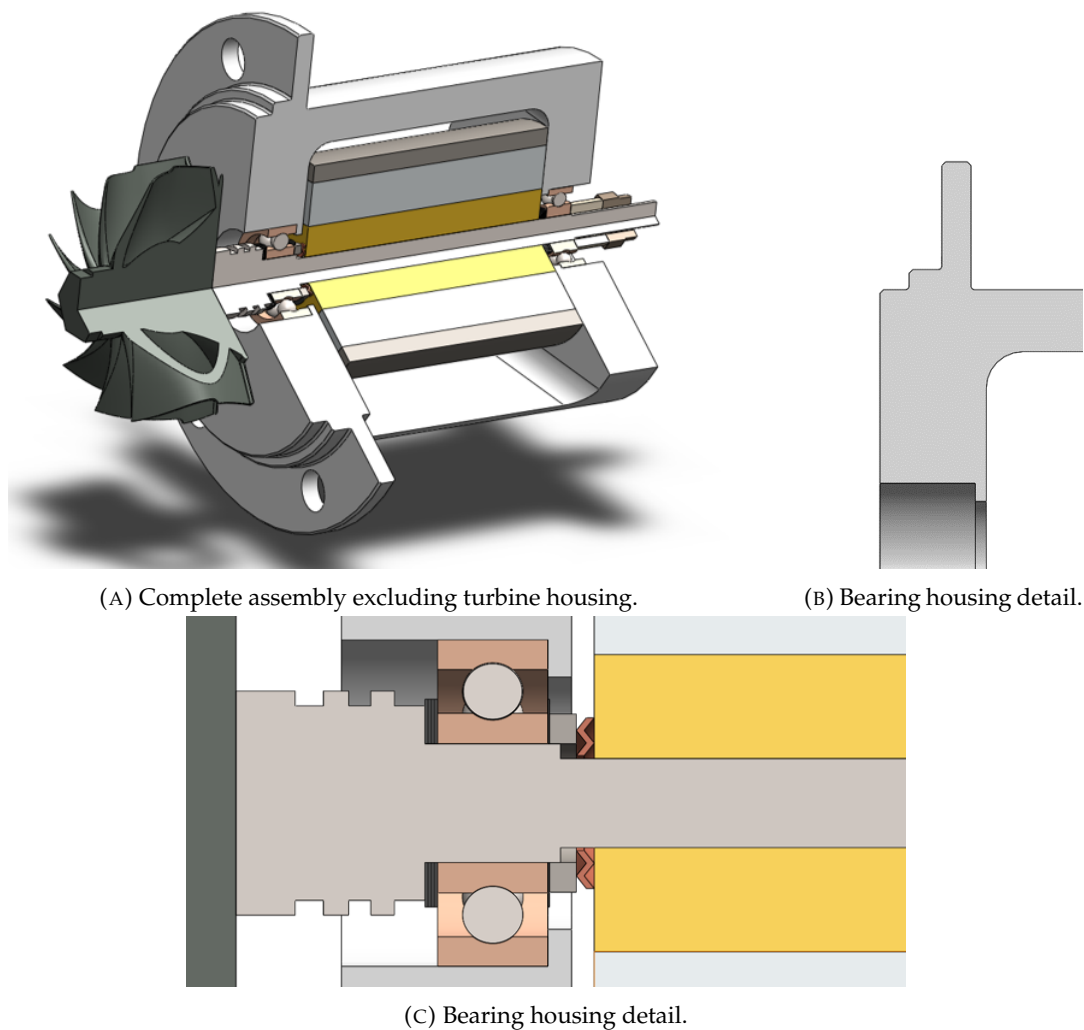
FIGURE 6.16: Spring washer integration detail.

fit bush and bolted plate at either end of the bearing housing shown in Figure 6.15.

To reduce tight tolerances that would be difficult to manufacture with the university's capabilities, shims were input into the design as shown in Figure 6.16c. A series of shims enabled the positional control of the turbine wheel to the turbine housing and the rotor within the milled pocket. This would improve turbine performance as air leakage could be minimised. A major challenge was reducing turbine shaft machining tolerances. To reduce the tolerances along the middle section of the turbine shaft, a step was created at the turbine end, as shown in Figure 6.16a. The bearing at the turbine end was therefore larger and cleared the shaft during assembly. Only tight tolerances were required at the bearing locations on the turbine shaft.

Based on Section 2.6.1, ball bearings were chosen due to their simplicity and low cost. Bearings were identified that could withstand speeds of 80 krpm when appropriately cooled. However, this test rig would not run long enough for the temperature within the components to be an issue. These bearings were chosen over angular contact bearings once their axial load capabilities were identified.

To enable rotation, the rotor was designed to be a sliding fit onto the turbine shaft which was then gripped between the bearings via the compressor nut. However, to ensure the ball bearings operate smoothly, preloading must be applied. To ensure the ball bearings always had an axial load present on them, a spring washer was introduced into the assembly. Having shims enabled the spring washer to be easily placed without affecting much of the design. As shown in Figure 6.16c, this ensured an axial load was present across the bearings while the components along the turbine shaft were still compressed together. These decisions produced a test rig that met all requirements listed in Section 6.4.1.

6.5 Summary

Based on the work carried out in this chapter, a series of outcomes were produced, shown below. These outcomes will help shape the testing and optimisation sections of the project going forward.

- A three-cylinder test rotor was designed that met the initial criteria.

- The design process of a suitable test rotor was slow and gave no guarantee of producing an optimal design.

- The rotor design constraints are conflicting making it difficult to identify suitable rotor designs.

- The rotor shrink fitting assembly will need to be an efficient process to minimise the reversal of the required diameter change.

- A test rig was designed that met the initial criteria with the introduction of shims enabling positional adjustments required due to tolerance constraints.

- A more efficient compound rotor design process is required to efficiently identify the optimal rotor design based on bespoke constraints.

7 Rotor Testing & Results

7.1 Introduction

Chapter 6 detailed the development of the test rotor, test rig design, and the instrumentation required to run validation testing. As the only measurable surface of the test rotor is the outer surface of the sleeve, a test rig design that ensured the surface was visible, was developed. Therefore, Digital Image Correlation (DIC) could be used to measure the surface strain during operation, which could then be validated against finite element analysis (FEA) simulations.

As discussed in Section 6.2.2, the DIC set up required a light strobe to enable strain testing at high speed. Despite the completion of the test rig design and the acquisition of the primary DIC equipment, it was decided that the high-speed testing would fall outside the scope of this project due to the additional workload. Aligning the laser pulse with the high-speed rotation of the rotor is a significant amount of testing work. Therefore, only static strain testing could be achieved which would monitor the magnitude of strain produced due to the interference fit of the rotor cylinders. As discussed in Section 6.3.3, the change in outer surface strain to be suitable for the DIC was at least 400 $\mu\varepsilon$. This was still achievable as the change in outer surface strain was greater due to the cylinder interference than it was due to high-speed rotation, shown in Table 6.10. However, using strain gauges was deemed more appropriate because the test process was now more complex due to it requiring an immediate start, post shrink-fit assembly.

7.2 Test Procedure

7.2.1 Objectives

Acknowledging the testing changed outlined in section 7.1, the testing objectives were:

- Validate the functionality of the test rig design.

- Show that the operating speed meets the design requirements.

- Show that the rotor operates without slip.

- Evaluate the sleeve strain due to interference.

- Use the sleeve strain testing data to validate FEA simulations.

Despite the removal of rotor strain testing at operating speed, the test rig design from Chapter 6 must still be validated and show that it can operate at the required speed outlined in Section 6.4.1. Completing the stationary testing to identify the sleeve strain due to interference ensures that results are obtained that can be used to validate the FEA simulations completed in Chapter 5. This would then therefore validate the accuracy of the generalised plane strain (GPS) analysis developed in Chapter 4.

To meet all objectives listed above, the test procedure was split into the following two components.

- Validation of the test rig functionality.

- Measurement of sleeve strain due to interference.

7.2.2 Test Rig Validation Procedure

To validate the functionality of the test rig, high-speed testing was conducted using a single rotor cylinder mounted onto the rotor shaft. This part of the testing procedure enabled the first three objectives from Section 7.2.1 to be completed.

Figure 7.1 shows the manufactured and sourced components, discussed in Chapter 6, assembled into the test rig shown in Figure 6.16.

As the test had become a verification test for the functionality of the test rig design, only the inner cylinder was assembled onto the rotor shaft. Figure 7.1b shows the spring washer in place to maintain pressure on the rotor. The spring washer was a key aspect of the test rig design and was included to ensure the rotor turned synchronously with the shaft. Assembling the components was difficult with a relatively small clearance between the rotor length and the pocket milled into the housing. As discussed in Section 6.4.3, shims were used to ensure that the design had

(A) Complete assembly. (B) Spring washer detail.
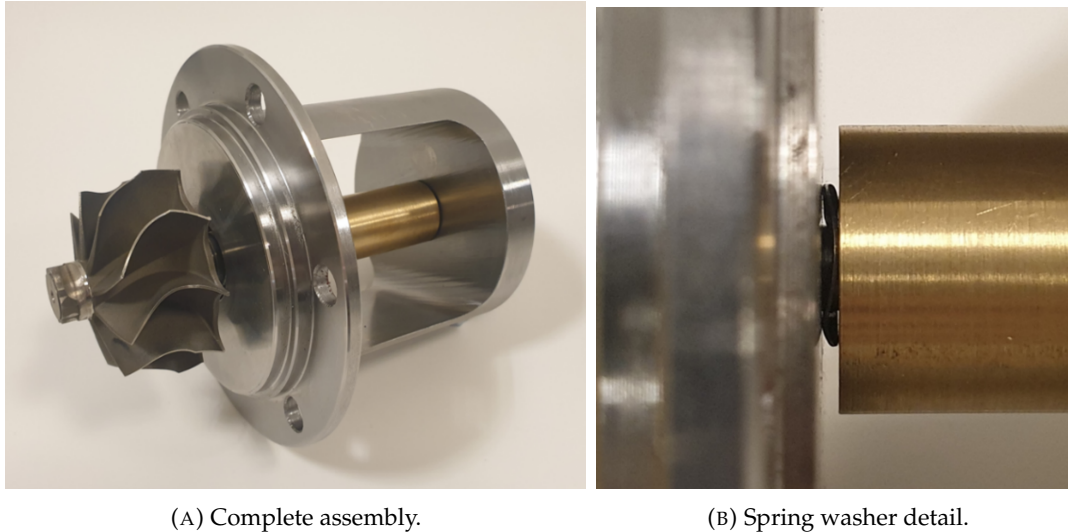
FIGURE 7.1: Assembled test rig.

achievable tolerances, however they were difficult to fit between the rotor and bearing. When tightening the nut at the end of the shaft in Figure 7.2, it was tightened until finger-tight before a further eighth of a turn was added to add a preload to the bearings. Once assembled, the bearing housing discussed in Section 6.2.1 was affixed to the turbine housing, as shown in Figure 7.2.
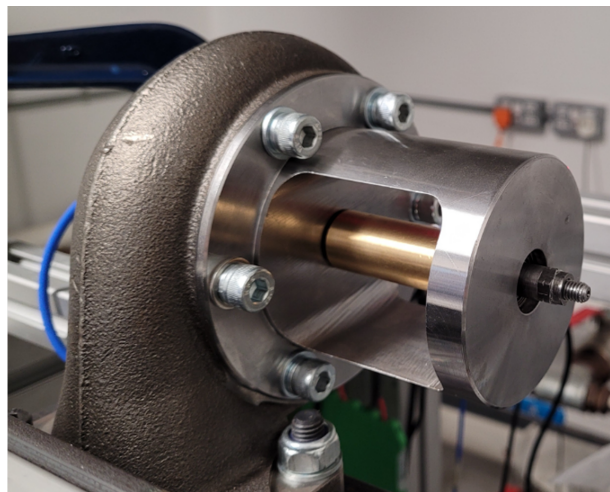
FIGURE 7.2: Test rig assembly showing with turbine housing.

To enable the turbine housing to be connected to the electric compressor, the test rig assembly was attached the existing stand which had the electric compressor already mounted. A speed sensor was then connected using a bracket to measure the speed of the test rotor, as shown in Figure 7.3.

(A) Sensor mounting position.   (B) Laser target surface.
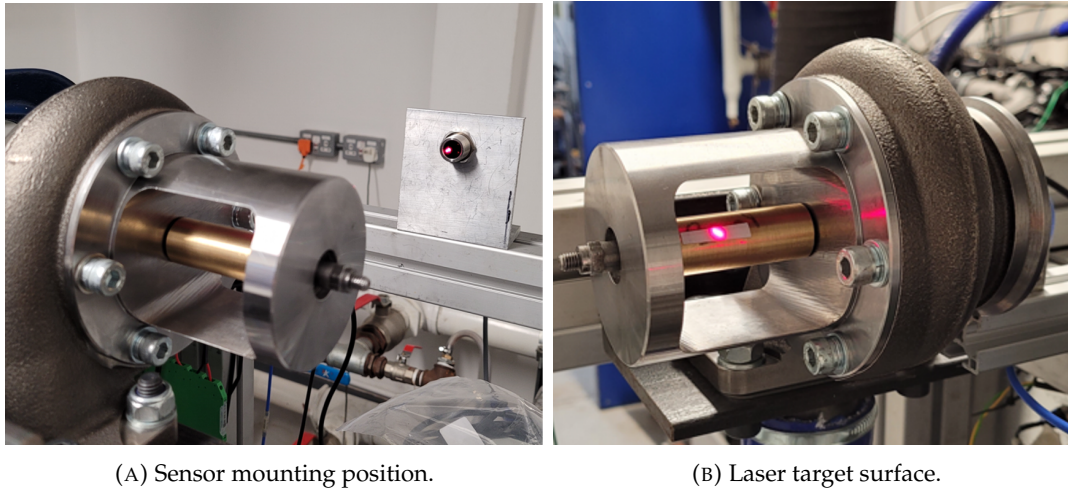
FIGURE 7.3: Laser speed sensor.

The speed sensor used in Figure 7.3 utilised a laser to measure the speed of the rotor. As shown in Figure 7.3b, a strip of reflective tape was adhered to the rotor surface. Therefore, with each turn the laser was reflected and picked up by the sensor before being processed as an output. This enabled the number of revolutions to be determined within the recording period.

When connecting the rig and compressor, the risk of a complete failure during operation was identified and components were added to protect the electric compressor and surrounding equipment. As shown in Figure 7.4, an inverted U-bend was integrated into the connection between the turbine housing and the compressor, while a right-angled pipe was clamped to the turbine outlet.
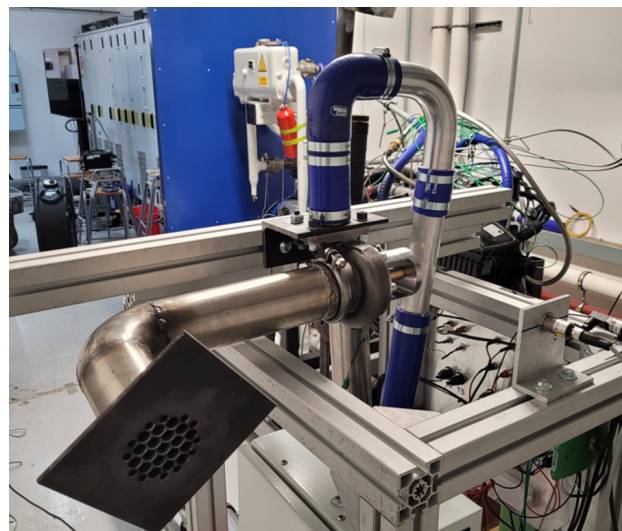
FIGURE 7.4: Test rig set up with safety additions.

The inverted U-bend ensured that if there was a failure during operation, it was much more difficult for shrapnel to travel down into the compressor and cause damage within the machine. The right-angled pipe was also designed to contain and slow shrapnel down so no damage was caused to surrounding equipment within the test cell.

Once all components were in place, the speed sensor was powered and connected to a PicoScope outside of the test cell. A quick manual test ensured the speed sensor output was being picked up on the PicoScope software. Recording was triggered within the software and the operating power of the electric compressor was operated outside of the test cell, starting at 20%. Once the rotor speed had stabilised and remained constant for at least ten seconds, the test was ended, and the compressor power was returned to 0% to preserve the test rig. Despite the bearings being rated to 80 krpm, they were installed dry and therefore were susceptible to generating heat. Stopping between each test run gave the chance for any heat generation to dissipate. For every further test run, the electric compressor speed was then increased in intervals of 10% until a peak operating speed was approached or until the power output of the compressor reached 80%. Limiting the power output to 80% was a safety aspect deployed to protect the electric compressor. Once a full set of results had been gathered, the speed sensor was moved to aim at the compressor nut and the test was repeated to gather the rotor shaft speed.

7.2.3 Strain Gauge Sleeve Strain Measurement Procedure

To enable the final two objectives from Section 7.2.1 to be completed, the outer surface strain of the sleeve required measuring during the shrink fit assembly process. As discussed in Section 7.1, monitoring the sleeve strain due to interference increases the complexity of the testing procedure. The initial plan, to monitor the sleeve strain during rotation, enabled the rotor cylinders to be shrink-fit and allowed to come to room temperature before testing. However, to record the sleeve strain due to interference, the strain recording was required immediately from assembling the rotor components. Due to this, it was deemed more suitable to use temperature compensated strain gauges to measure the sleeve strain. Temperature compensated strain gauges should eliminate the thermal strain effects from the shrink-fit process

and produce results solely due to the interference between the cylinders. To ensure the assembly process was efficient and achieved quickly, it was decided the sleeve would also be heated to gain extra diameter clearance on the middle cylinder than was calculated in Table 6.11.

The first requirement was to measure the accuracy of the steel compensated strain gauges during thermal testing of the rotor sleeve. Therefore, any error could be detected and removed from the strain readings obtained during the shrink-fit assembly, leaving the true strain due to interference. Figure 7.5 shows the strain gauges attached to the centre and both ends of the rotor sleeve. X-Y strain gauges were positioned to measure strains in both the axial and circumferential directions. These were connected to enamelled wire via soldering onto terminal pads. The enamelled wire was required to ensure they could withstand the oven temperatures, whilst they were also secured in place with ceramic adhesive, to prevent damage to the strain gauges or terminal pad connections.
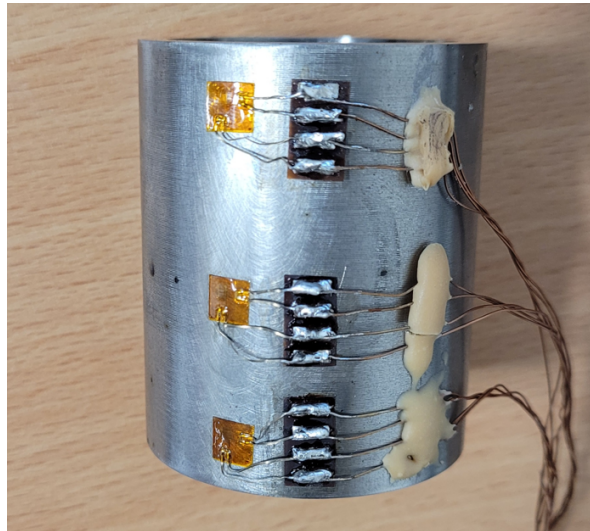
FIGURE 7.5: Rotor sleeve with attached strain gauges.

Using a strain gauge indicator with four outputs, the grids of two strain gauges were connected in a quarter bridge configuration. A strain gauge positioned at the end and the centre of the rotor were used in the test. Once connected, the rotor sleeve was placed in a cold oven. A thermocouple was also placed within the oven, ensuring that it touched the surface of the sleeve to measure the temperature of the material. The arrangement is shown in Figure 7.6.

FIGURE 7.6: Test setup within oven.

The test process consisted of increasing the temperature of the sleeve in increments to ensure the material reached a constant temperature throughout, however the incremental value was not critical. A target temperature of 170°C was set, which would produce close to 1800 $\mu\varepsilon$ and create a total diameter change against the middle cylinder of circa 0.3 mm at d, when combined with the diameter change calculated in Table 6.11. This should create a suitable clearance to assemble the rotor efficiently during the shrink fit process.

Before beginning the test, the strain gauge indicator readings were zeroed and allowed to stand for 15 minutes to ensure there was no drift with the readings which would induce errors into the results. Once the readings were stable, the strain readings were set to automatically record every minute, while the temperature reading was recorded manually using the same intervals. From cold, the oven temperature was increased to 170°C in increments of circa 60°C. With each increment the temperature reading from the thermocouple was allowed to stabilise before the temperature was increased further. Once the target temperature was achieved, the oven was switched off and the strain and temperature readings continued to be recorded until the sleeve had cooled to at least 50°C. Once the test was completed, the components were left to cool fully to room temperature before repeating the test.

The results from this test, shown in Section 7.3.2, show that the steel compensated strain gauges were unsuitable to use to record the sleeve strain during the shrink-fit process. Therefore, it was decided that DIC would be used to record the sleeve strain

due to interference. However, this created procedural problems for the test as it was required to record the sleeve strain immediately after assembling the rotor.

7.2.4 DIC Sleeve Strain Measurement Procedure

As discussed in Section 7.1, the test must begin immediately, post shrink-fit assembly of the rotor. However, when using DIC, this becomes much more difficult. Despite the clearance calculations from Table 6.11 and the additional clearance from heating the sleeve, a mechanical press was acquired to ensure the parts were assembled smoothly and efficiently. It is inevitable that the cold inner cylinders will make contact with the hot sleeve during assembly as the diameter clearance was calculated to only be circa 0.3 mm. When the parts touch, the temperature differential will reduce rapidly and therefore, so will the diameter clearance. It is important that the parts can be aligned accurately, and therefore a mechanical press was available to overcome any build up in resistance during the assembly. Figure 7.7 shows the jig used to locate the rotor sleeve.
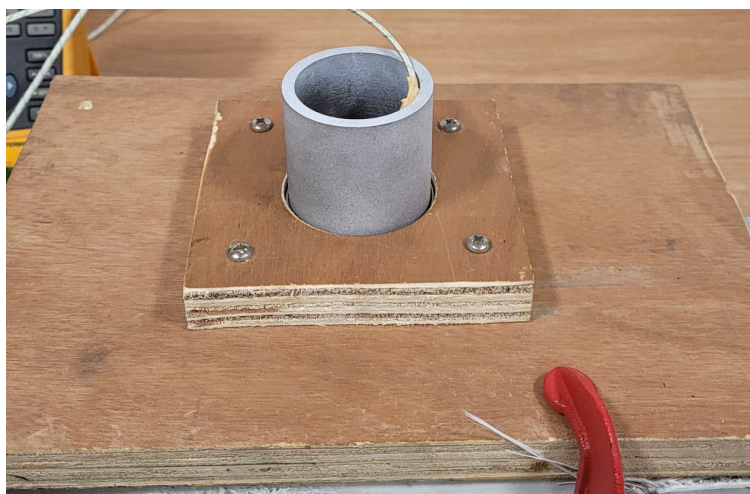
FIGURE 7.7: Sleeve locator jig.

Prior to completing the test measuring strain due to interference, a thermal strain test was required. As the strain due to interference test begins when components are at elevated or reduced temperatures, the strain readings will incorporate both the thermal and interference effects. To be able to eliminate the thermal effects, a purely thermal test was completed. Figure 7.8 shows the DIC setup for the test.
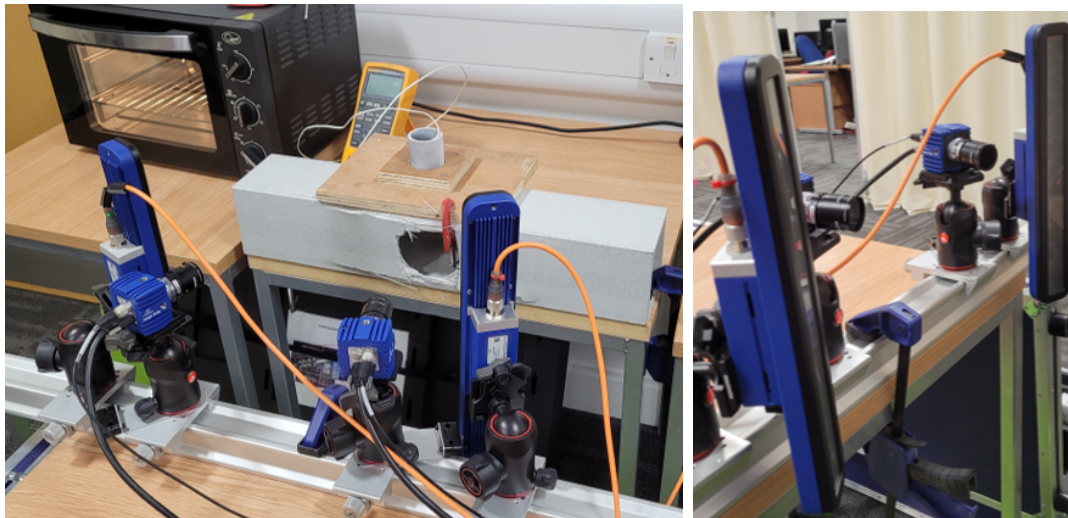
(A) Full test equipment.

(B) DIC camera and light source configuration.

FIGURE 7.8: DIC strain test set up.

As discussed in Section 2.7.1 and shown in Figure 2.7, the DIC test specimen requires a speckle pattern for the cameras to track during the test. To achieve this the rotor sleeve was spray painted white before black spray paint was used lightly to produce a random speckle. The DIC cameras track the change in distance between individual speckles as the rotor sleeve cools from an elevated temperature. Figure 7.9 shows a close-up of the sleeve speckle pattern.

FIGURE 7.9: Sleeve speckle pattern.

To ensure that the DIC was set up correctly to record the sleeve strain immediately from the oven, the locating jig shown in Figure 7.7 was clamped in place. With

the cold sleeve in the jig, the DIC was set up and secured in place. Using the DIC software, the cameras were focussed, and the required light intensity was set, with the system ready to record. Therefore, the rotor sleeve could be placed in the oven and upon removal, could be placed back into the jig locator with the DIC system ready to begin recording immediately. To monitor the temperature of the sleeve, a thermocouple was attached using ceramic adhesive. To ensure the temperature reading was showing the temperature of the sleeve, the thermocouple was secured in contact with the sleeve, as shown in Figure 7.10.

FIGURE 7.10: Thermocouple attachment to rotor sleeve.

Once the DIC cameras and light sources were set up and all equipment were secured, the sleeve was placed in an oven set to 170^oC. The sleeve was left in the oven until the thermocouple reading has stabilised circa the target temperature. The sleeve was then removed from the oven and placed into the secured jig, with the DIC triggered to begin recording. The sleeve temperature was recorded from the Multimeter, shown in Figure 7.8a, at the time the DIC began recording. As the sleeve cooled, the DIC recorded at an image rate of 1 Hz for an hour, by which time the sleeve was approaching room temperature. The final temperature was manually recorded as the last image was recorded.

Following the thermal test, a similar process was followed to use DIC to calculate the sleeve strain due to the shrink-fit assembly. The results from the thermal test

were used to calculate the proportion of strain due to the thermal effect, therefore enabling the strain due to interference to be extracted in the proceeding test. The same process shown in this section was followed for the sleeve, except the thermocouple was attached to the rear outer surface of the sleeve so the inner cylinders could be shrink-fit into the sleeve.

The additional methodology stages to the process discussed above were regarding the shrink-fit process of the rotor. To complete this, liquid nitrogen and an oven were used to reduce or elevate the temperature of components, respectively. Two inner cylinders (inner and middle) were required to be fit with interference into the sleeve, creating a three-layer compound rotor as discussed in Section 6.3.5. Prior to the assembly with the sleeve, the inner and middle cylinders were shrink-fit to each other, shown in Figure 7.11. They were assembled by sliding the inner cylinder into the middle cylinder without the use of the mechanical press.

FIGURE 7.11: Inner and middle cylinder shrink-fit assembly.

This process was repeated to fit the inner and middle cylinder to the sleeve. As shown in Table 6.11 the coefficient of thermal expansion for the middle cylinder was larger than that of the inner cylinder, therefore the assembly shown in Figure 7.11 remained together when placed into liquid nitrogen as one component. Components were removed from the liquid nitrogen simultaneously and the oven simultaneously and were fit together using the locator jig. The mechanical press was not required as the parts slid together with sufficient clearance. The assembled three-cylinder rotor

is shown in Figure 7.12. The DIC was then immediately triggered once assembled to begin the test recording, as before. Once the test was complete the images were processed using the DIC software and final strain results due to interference were extracted by calculating the removal of the thermal effects.
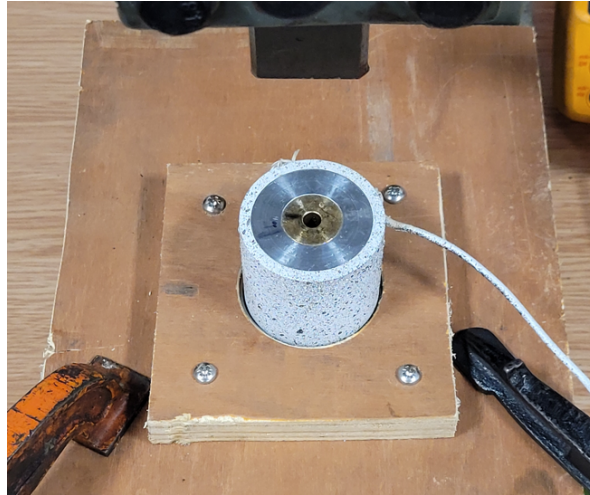
FIGURE 7.12: Complete three-cylinder shrink-fit assembly.

7.3 Results

7.3.1 Test Rig Verification

The speed sensor used on the test rig in Section 7.2.2 output the pulse signal to a PicoScope which was then recorded graphically on the computer. Each test run was recorded and the cycle time between each pulse and the pulse frequency were automatically calculated. Figure 7.13 shows how the results were presented in the PicoScope software with the automatic calculations.

To ensure that the automatically calculated figures were correct, the cycle time was manually calculated within the PicoScope software using a feature that measures the time between two lines. Each line was aligned with the start of consecutive cycles, as shown in Figure 7.14. The cycle time was accurately aligned with the automatic calculation. Therefore, the cycle time could be confidently used to calculate the speed of the rotor in revolutions per minute (rpm) for each test run.
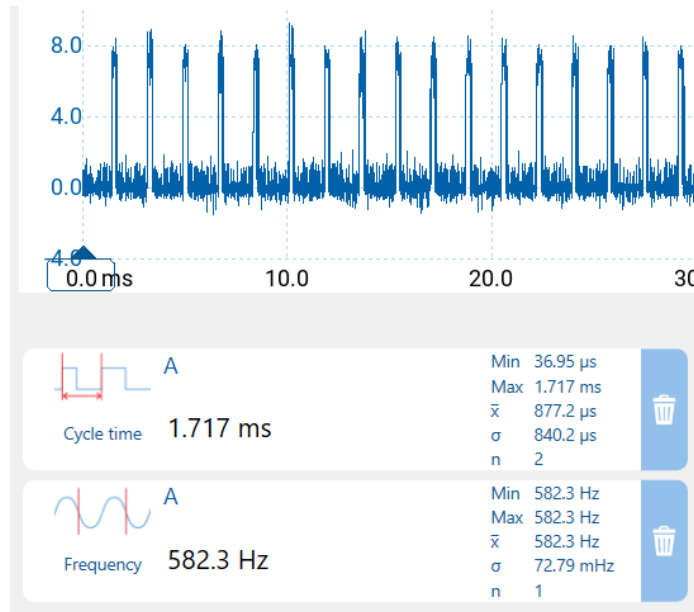
FIGURE 7.13: Speed sensor output recording during rotor testing.
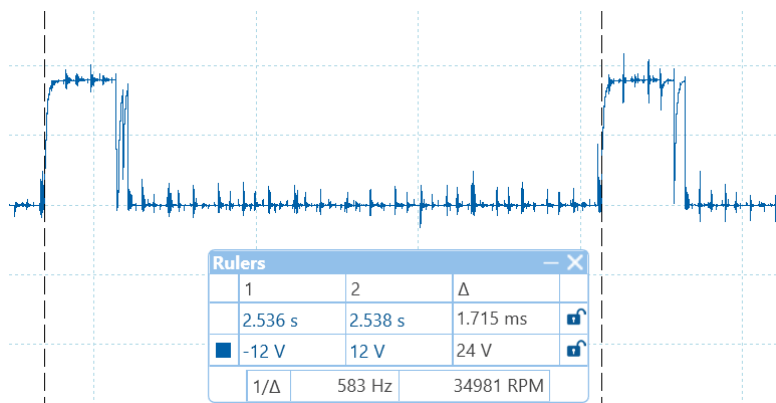
FIGURE 7.14: Manual cycle time measurement between speed sensor pulses.

Table 7.1 shows the results for all test runs completed, while Figure 7.15 presents them graphically.

Electric air compressor power output (%)	Test 1 - Rotor speed (rpm)	Test 2 - Rotor speed (rpm)	Test 3 - Shaft speed (rpm)
20	17641	2615	2611
30	26005	13875	12968
40	31010	25918	20824
50	34161	33122	26910
60	34775	35939	6321
70	-	37058	-

TABLE 7.1: Test rig operating speed results.
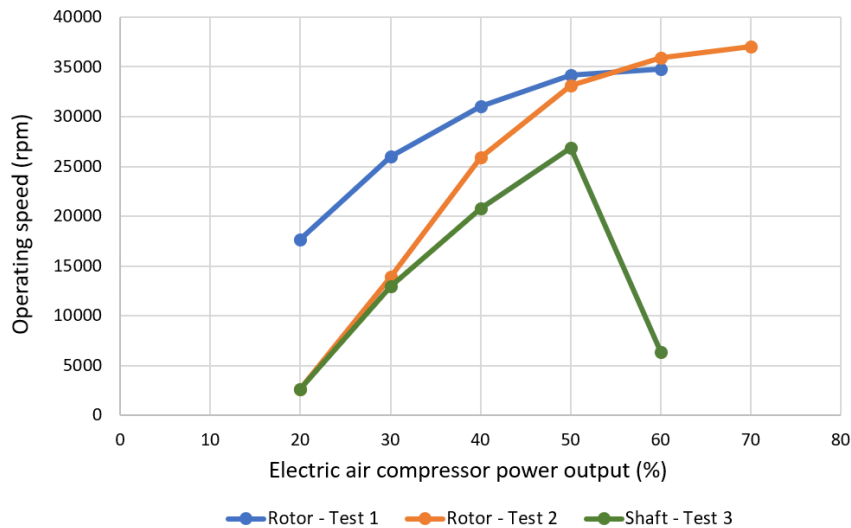
FIGURE 7.15: Test rig operating speed results.

The testing methodology outlined in Section 7.2.2 was used for Test 1, where the speed sensor measured the rotor speed. Due to rotor speed increases clearly stalling at 60% of the electric air compressor output, Test 1 was ended and only achieved a peak rotor speed of circa 35 krpm, far below the intended top speed of the test rig. Once Test 1 was complete, the compressor nut clamping the rotor to the shaft was identified to have become loosened. To ensure that was not the cause of the lower-than-expected peak rotor speed, the test was repeated with the compressor nut given a further eighth of a turn to the tightness specified in Section 7.2.2.

Test 2 shows the extra tightening of the compressor nut had a significant impact on lower powered results. At 20% compressor output, the peak rotor speed was circa 2615 rpm while Test 1 achieved 17641 rpm. This difference will have been caused by the increase in bearing friction generated by the increased preload on the bearings from tightening the compressor nut. However, Test 2 ended up peaking at a similar rotor speed as Test 1, suggesting that was the peak rotor speed for the test rig.

To determine whether the peak rotor speed identified in Tests 1 and 2 were operating without slip, the speed sensor was moved to aim at the compressor nut, therefore recording the shaft speed. As the rotor is designed to be clamped to the rotor shaft, the operating speeds should be synchronous. The compressor nut tightening was repeated from Test 2. At 20% electric compressor power, the shaft speed aligned with the rotor speed from Test 2. At 30% compressor power, the shaft speed

was relatively close the Test 2 results but was now slightly lower. By 40% compressor power, the shaft speed was recording significantly lower speeds than the rotor speed in Test 2. If slip was occurring, then the rotor speed would be expected to be lower than the shaft speed as the shaft is the component being driven by the air flow.

Figure 7.15 shows the shaft speed drift further from the Test 2 rotor speeds as the compressor power output is increased before a dramatic drop off occurred at 60% compressor power. This was a clear indication that the shaft and rotor speed differences between Tests 3 and 2, respectively, had been caused by the increase in bearing friction discussed earlier. Significant heat will have built up between each test run culminating in the bearings seizing at 60% compressor power output.

Due to the bearings seizing in Test 3, it is unknown whether the peak rotor speed was limited by slip in Tests 1 and 2. However, at 20% compressor power the bearings will likely have been sufficiently cool in Test 3 and there were no signs of slip between the rotor and shaft speed. Small differences in the shaft and rotor speed for that test run can be attributed to manually setting the compressor power output with a dial. To assess whether the rotor was limited by slip or other factors such as the bearing system or component balancing, all of which were not optimised, further testing is required. However, the testing completed in this section demonstrates that the test rig is a successful design concept.

7.3.2 Sleeve Strain Gauge Measurements

As discussed in Section 7.2.3, the results from the steel compensated strain gauge testing showed the strain gauges were unsuitable to use to measure the sleeve surface strain during the shrink-fit process. Figure 7.16 shows the results from the four strain arms monitored during the first test.

Figure 7.16 shows that the four gauge grids start at room temperature. The test was a purely thermal test so theoretically the strain gauge readings should remain at zero strain. However, over the first 100^oC temperature change, each reading drifted to circa 50 $\mu\varepsilon$ where it then remained relatively stable for the gauges shown in all gauge grids except the circumferential direction on the centre gauge. The temperature compensation was in effect during this period as without it there would be circa 1200 $\mu\varepsilon$ produced from a 100^oC temperature delta. However, at circa 140^oC for all
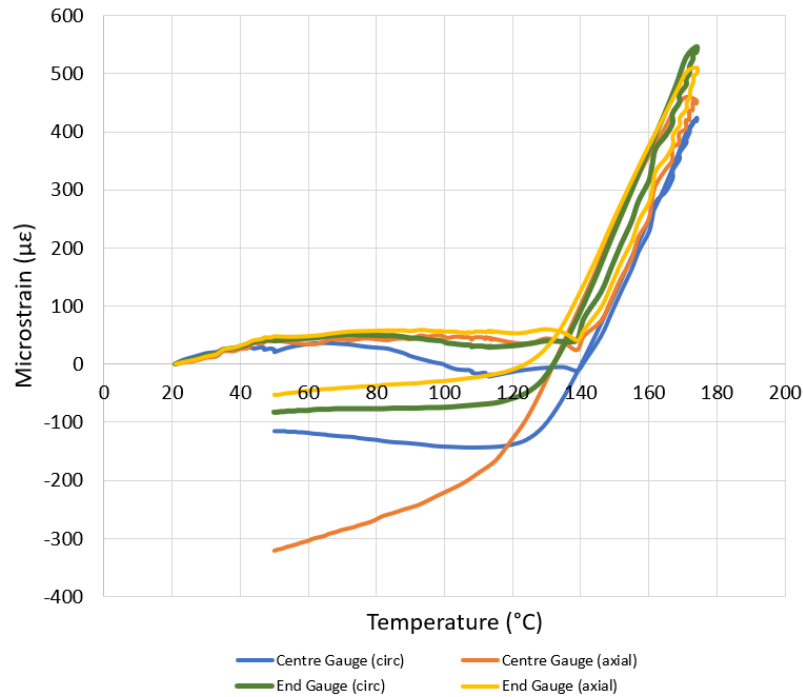
FIGURE 7.16: Test 1 strain gauge results.

gauge grids, the strain gauge stopped operating as expected and a major increase in strain was recorded. Once cooled to 50°C, after reaching the target temperature, the strain gauges did not return to the same strain readings during the temperature increase. Most gauge grids were reading 100 $\mu\varepsilon$ lower, however the axial grid on the centre gauge showed a significantly different final strain reading.

The thermal test was repeated to confirm the results of the initial test were reliable, shown in Figure 7.17. As with the first test, all four gauge grids behaved similarly during each test. A similar increase in strain reading is shown at circa 140°C, as with the first test. However, the increase in strain was non-linear and much higher strain values were recorded as the temperature increased past 140°C. As the temperature was reduced after the target temperature was achieved, the four gauge grids did not return along the same path as they did in Test 1. The final strain readings recorded at 50°C were much further from the readings taken at 50°C at the beginning of the test. This shows that errors were being induced during the test. As aspects of the gauge behaviour in the second test were different to the first test, the gauges were not considered reliable. However, both gauges in each test tests appear to have functional temperature compensation over the first 100°C temperature delta.
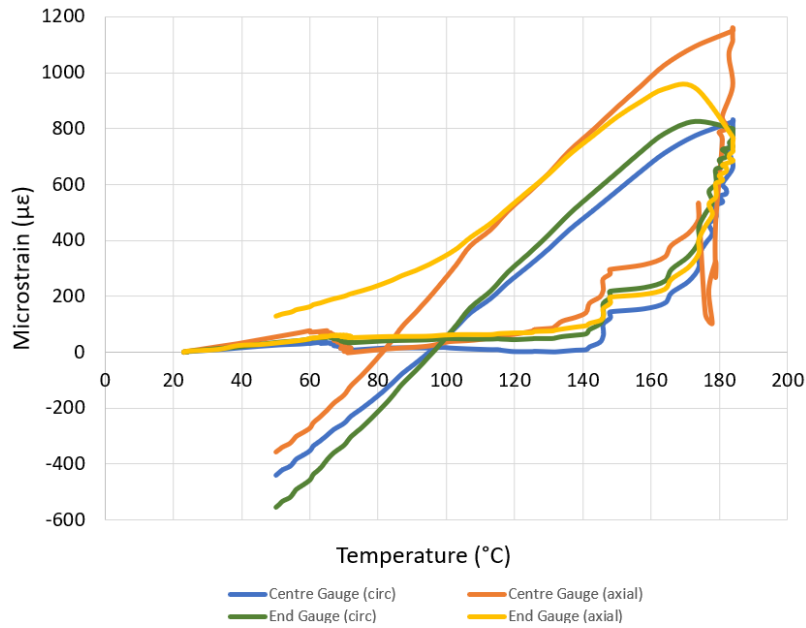
FIGURE 7.17: Test 2 strain gauge results.

The test was repeated a third time for further clarification on the gauge behaviour, shown in Figure 7.18. A significant difference was recorded compared to the first two tests. Figures 7.16 and 7.17 show that the strain gauges operated successfully with reasonable temperature compensation over the first 100^oC temperature delta, providing a potential operating window to use the strain gauges. However, Figure 7.18 shows an approximate 600 $\mu\varepsilon$ change for all four gauge grids at circa 60^oC during the third test. The readings taken prior to this change also did not align with the result from Tests 1 and 2, as they rose to nearly 200 $\mu\varepsilon$, much higher than in the first two tests.

It was later identified that the temperature compensation range and the strain gauge adhesive were both limited to 120^oC, explaining the major changes in strain readings close to this temperature. However, the results in Test 3 meant that no reliable strain gauge behaviour could be concluded from the tests and therefore the strain gauges were deemed unreliable. Therefore, DIC was selected to measure the sleeve strain during the shrink-fit assembly, despite the logistical challenges it created.
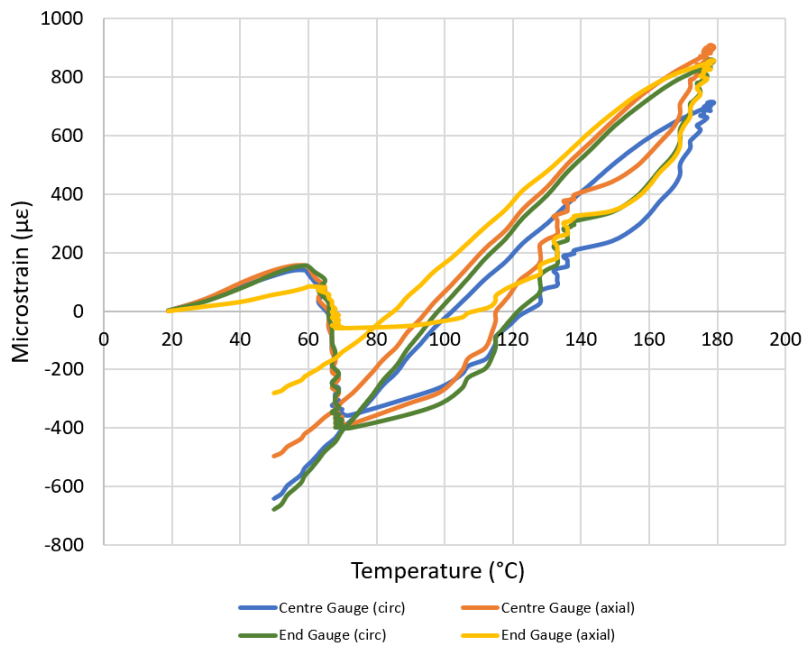
FIGURE 7.18: Test 3 strain gauge results.

7.3.3   DIC Sleeve Strain Results

As discussed in Section 7.2.4, a thermal test using the DIC was initially required to verify that the recorded strain values matched the expected thermal strain. This would then enable the thermal strain to be removed from the shrink-fit results to identify the strain due to interference. Figure 7.19 shows the strain map for the final image taken during the test, showing the strain magnitude as the sleeve cooled.
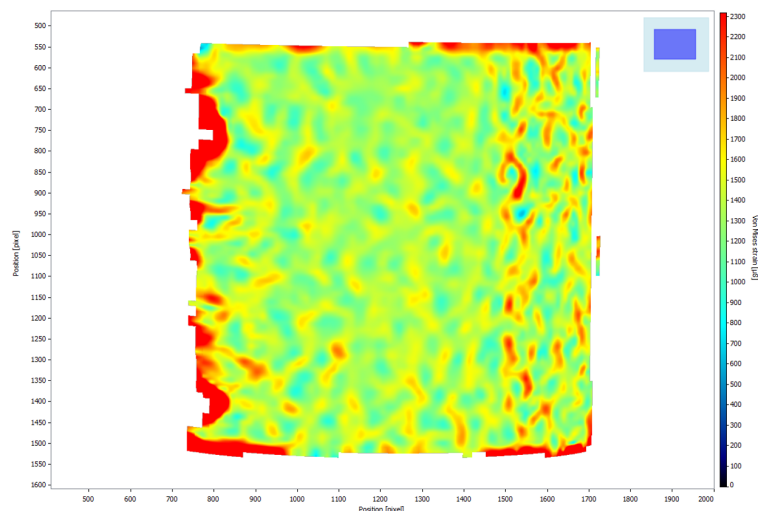
FIGURE 7.19: DIC thermal strain test results.

Theoretically, the strain results should be constant across the rotor sleeve surface, but Figure 7.19 shows variations in the strain pattern. This could be due to the speckle pattern on the specimen which was difficult to apply evenly and reliably. The DIC system also has many other potential sources of error including camera noise or glare, as well as subset size used during the strain calculations. Due to the speckle pattern, it was difficult to apply an optimal subset size across the whole surface, which could have contributed to the strain fluctuations. However, despite this, the centre portion of Figure 7.19 was used to extract results as this was the focus of the DIC cameras.

For the thermal test, the recorded sleeve temperature at the beginning of the test was 159.4^oC, while the final temperature was 27.0^oC. A median value was used to assess the recorded thermal strain by the DIC, circa 1500 $\mu\varepsilon$. Low and high strain variations appear to be circa 1000 $\mu\varepsilon$ and 2000 $\mu\varepsilon$, respectively, while much of the median results appear to fall circa 1400 $\mu\varepsilon$ - 1600 $\mu\varepsilon$. Table 7.2 shows the recorded results against the expected results via hand calculations.

Sleeve Material	Coefficient of Thermal Expansion	Temperature change (^oC)	Calculated strain ($\mu\varepsilon$)	Recorded strain ($\mu\varepsilon$)	Percentage difference to DIC (%)
EN16T Steel	1.20×10^{-5}	132.4	1588.8	1500	5.92

TABLE 7.2: Comparison of DIC recorded sleeve strain against hand calculations.

Table 7.2 shows that the calculated thermal strain only differs from the median DIC strain by 5.92%. It can be considered that the DIC system is measuring much of the rotor as expected based on the median strain values. Therefore, in the shrink-fit test, the strain due to interference can be identified by removing the thermal strain using hand calculations. As discussed in Section 7.2.4, the DIC recorded the sleeve surface strain post shrink-fit assembly. The DIC results are shown in Figure 7.20.

Figure 7.20 shows much greater strain variations than was observed in Figure 7.19. This was likely caused by the condensation that developed on the speckled surface during the test, due to the temperature differential between cold inner cylinders and the warm air on the outside of the rotor sleeve.
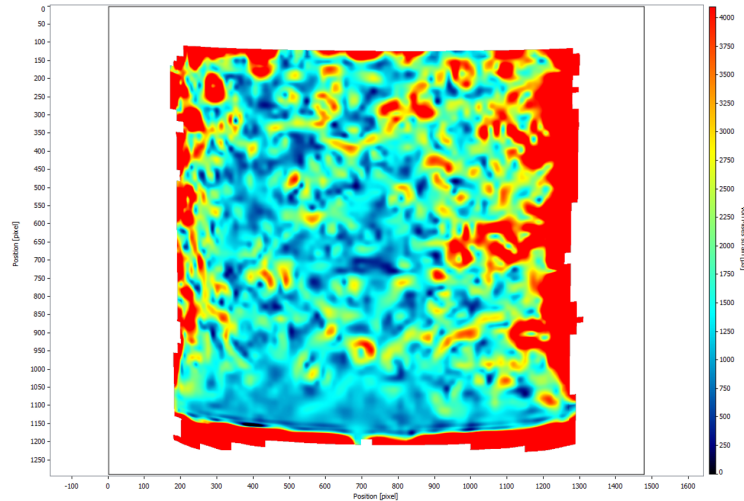
FIGURE 7.20: DIC interference strain test results.

Figure 7.21 shows two DIC strain maps from the shrink-fitting test, 20 seconds apart, approximately 10 minutes into the test. Initially, the strain fluctuations were more aligned with what was observed in the thermal test results. However, 20 seconds later and major strain variations had appeared. Much of the temperature change had already occurred and temperature changes were significantly slower during this period. The development of condensation would interfere with the images taken by the DIC cameras, distorting the results. Despite this, results could still be extracted by using the strain map from Figure 7.21a. While the exact sleeve strain temperature was not recorded at the moment Figure 7.21 was produced, it is known that the temperature range was between 20°C - 30°C. As stated earlier, after
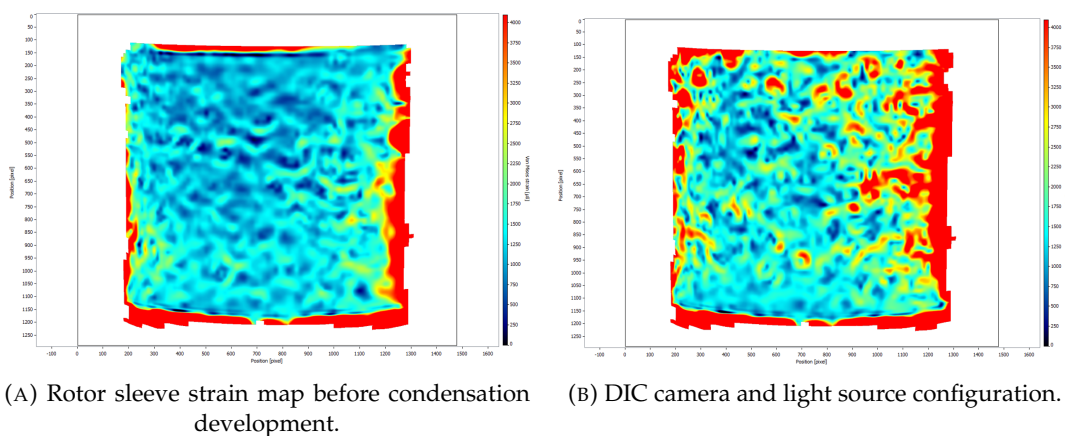
(A) Rotor sleeve strain map before condensation development.

(B) DIC camera and light source configuration.

FIGURE 7.21: Rotor sleeve strain map post condensation development.

10 minutes of the test, much of the cooling had already taken place and further temperature changes were gradual. As the known temperature range is close to room temperature, it can be assumed that complete interference between the components has taken place. Therefore, an interference strain range can be calculated.

The temperature of the sleeve at the beginning of the test had reduced to 89°C, while the final temperature in Figure 7.21a was 20°C - 30°C. The median recorded strain was circa 1000 $\mu\varepsilon$. Table 7.3 shows the recorded results for the interference test with the removal of thermal strain via hand calculations.

Sleeve Material	Coefficient of Thermal Expansion	Temperature change (^{o}C)	Calculated thermal strain ($\mu\varepsilon$)	Recorded strain ($\mu\varepsilon$)	Interference strain ($\mu\varepsilon$)
EN16T Steel	1.20 x10-5	59 - 69	708 - 828	1000	172 - 292

TABLE 7.3: Calculation of test rotor sleeve strain due to interference.

The results from Table 7.3 show that when using the median strain values from Figure 7.21a and removing the calculated thermal strain, the strain due to interference is between 172 $\mu\varepsilon$ - 292 $\mu\varepsilon$. To assess the accuracy of the interference strain result, it was compared to an FEA model using the parameters outlined in Chapter 5, shown in Figure 7.22. The critical rotor surfaces were measured using a coordinate-measuring machine (CMM) to ensure critical dimensions were input correctly within the FEA model. The dimensions used are shown in Table 7.4.

The strain of the outer surface of the sleeve in the FEA model was probed in the centre of the rotor, showing a circumferential strain of 293.9 $\mu\varepsilon$. This result is very close to the strain range calculated in Table 7.3, showing the possibility that the sleeve strain in the test rotor aligns with the confirmed FEA models, adding considerable verification to the accuracy and reliability of the GPS theory derived

Cylinder component	Inner surface diameter (*mm*)	Outer surface diameter (*mm*)	Interference (*mm*)
Inner	6.00	20.0894	0.0181
Middle	20.0713	40.1228	
Outer	40.1114	48.0910	0.0114

TABLE 7.4: Test rotor dimensions.
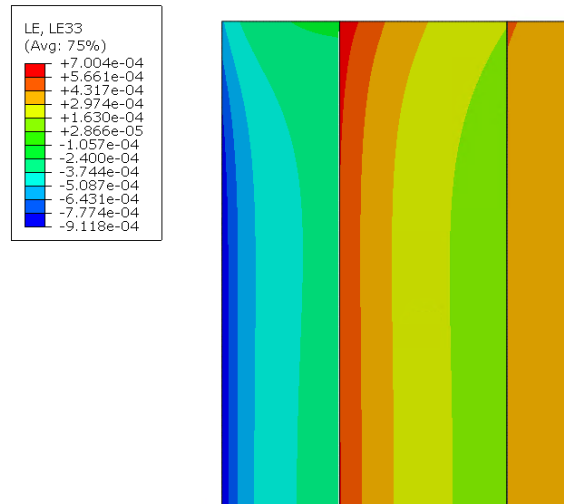
FIGURE 7.22: Test rotor FEA circumferential strain results due to interference.

in Chapter 4. Importantly for future high-speed testing, it also shows that DIC may successfully be used to gather physical strain readings from compound rotors, which can then be used to verify the functionality of a rotor design. However, the results from this section require caution. The fluctuations shown in all DIC strain maps make it difficult to extract definitive results and while they show significant potential for successful rotor analysis, further testing and optimisation of the DIC process is required.

7.4 Summary

The work completed in this chapter proved the testing concept and showed alignment with the FEA results from Chapter 5. However, it also revealed a significant body of work to be completed outside of this project to produce more comprehensive and definitive testing results. The key outcomes from this chapter were extracted and are listed below.

- The functionality and concept of the high-speed test rig was confirmed through achieving 37 krpm peak rotor speed.
- Further testing and test rig development of the bearing system is required to achieve higher speeds and prove the rotor operates without slip.

- Compound rotors can be successfully assembled via shrink-fitting to avoid component damage or stress build up cause by pressing the components together.

- The ability to use DIC to extract strain readings during rotor testing has been proven.

- The limited DIC strain results align with the test rotor FEA results, showing the potential accuracy of the GPS theory against experimental test data.

- Further optimisation of the DIC testing process is required to extract more reliable test results.

- Future shrink-fit assembly DIC testing must be adapted to avoid results being affected by condensation.

8 Rotor Design Optimisation

8.1 Introduction

As Chapter 7 showed alignment between the testing results and the finite element analysis (FEA) results from Chapter 5, the development of an optimisation tool using generalised plane strain (GPS) can take place with confidence in the results. Some sections of the work completed in this chapter have previously been published by Mallin and Barrans [171]. However, the development process and results provide significant expansions to this work, shown in Sections 8.3 and 8.4, respectively.

8.2 Optimisation Tool Elements

8.2.1 Optimisation Requirements

Chapter 4 details the development of the generalised plane strain theory (GPS) for three-cylinder compound rotors. The GPS theory was then used in Chapter 6 to design a rotor for use within the test rig. The theory was used to ensure the rotor would maintain integrity during operating, however it required multiple iterations before identifying a rotor design that satisfied the requirements. Not only is this process inefficient, but it also provides no guarantee that the final rotor design is optimised. Therefore, there is a requirement to develop an optimisation tool that uses the GPS theory. This enables the rotor design process to be automated and produce optimal designs.

As shown in Section 2.4, optimisation for high-speed rotor design includes both the mechanical and electromagnetic aspects of rotor performance. The optimisation parameters can then be applied to both aspects. However, only a limited number of papers included mechanical performance of the rotor in their optimisation model. Almost all papers investigated the optimisation of one criterion and produced a single optimised design. However, the ability to optimise for multiple criteria and produce multiple designs ensures a wider range of factors are considered and provides

results that can be more tailored to the user's requirements. Further to this, robust optimisation was under investigated, therefore papers could have theoretically produced optimised rotor designs that were not possible to manufacture or were too sensitive to manufacturing tolerances which could lead to rotor failure.

From the papers that explored mechanical optimisation, discussed in Section 2.4.1, an optimisation problem can be defined by the following three parameters:

- Criteria.

- Design variables.

- Constraints.

The constraints can then be further broken down into three subcategories:

- Criteria Constraints.

- Design Variable Constraints.

- Functional Constraints.

8.2.2 Multi-Criteria Optimisation Algorithm

As discussed in Section 2.4.3, the Non-dominated Superiority Genetic Algorithm – II (NSGA-II) is a popular multi-criteria optimisation model that uses an evolutionary approach to identifying a Pareto set of results. The method gained popularity due to its superiority and simplicity over other methods. Genetic algorithms use the concept of evolution to progress from a random population set to a Pareto front. Starting with a random population benefits genetic algorithms when compared to optimisation models that optimise from a single point. This process enables genetic algorithms to cope with noisy results and avoids the risk of being stuck in a local optimum, which can happen with single point methods. The algorithm produces a new population with each iteration that is based on the previous population. This enables small improvements to be made with each iteration until the results converge to a Pareto front.

Genetic algorithms are capable of coping with many criteria and design variables providing the capability for rotor design engineers to customise the optimisation model and include a wide range of aspects suited to their needs. As well as

a wide range of criteria and design variables, the genetic algorithm can also cope with a large design space. This enables engineers to explore a wide range of values applied to their criteria and avoid limiting potential designs through a small design space. Within the design space, NGSA-II uses dominance to progress towards a Pareto front, further simplifying the optimisation process. Some other optimisation models produce the feasible set which is a set of every successful design in the optimisation operation. Dominance is not automatically used to identify the Pareto front from the feasible set and must therefore be manually identified by the user, leading to a more complicated process. It has also been highlighted in Section 2.4.3 that NSGA-II can be implemented in MatLab, making it easy for the user to access and operate as MatLab is a common tool used in the engineering industry.

Potential issues with NSGA-II and in particular genetic algorithms, is the computing time required to complete many iterations before achieving a Pareto front. There is also no set limit on the number of iterations and the optimisation model could search continuously for improved feasible designs. Therefore, the user must determine the number of iterations. Too few iterations will result in optimal designs being missed and excessive iterations will result in wasted time being spent trying to identify negligible improvements on the designs currently identified. Also, there is a reliance on the initial random population to identify feasible results which can then be evolved through the optimisation process. It is possible for the algorithm to fail to converge if feasible results are not identified. However, the drawbacks to the algorithm are relatively small considering a long computational time will still be vastly more efficient than performing many FEA studies on potential rotor designs.

8.3 Development of MatLab Optimisation Tool

8.3.1 Introduction

As the optimisation tool is required to improve the type of rotor design methodology used in Chapter 6, the tool will be developed to optimise this rotor design problem. Therefore, the dimensions of the rotor were limited to fit within the cut-out in the test rig bearing housing, allowing a maximum rotor diameter of 56 mm. The rotor

must also slide onto a 6 mm diameter shaft. Other rotor parameters were given a wide range for demonstration purposes of the optimisation tool.

Following the development of the GPS theory in Chapter 4, the equations were input in MatLab to enable quick simulation of different rotor topologies. This allowed results to be acquired that were verified against FEA simulations in Chapter 5, thus enabling the verification against the experimental testing in Chapter 7. As GPS was shown to be much more accurate and reliable than either plane stress or plane strain, the equations were required to be used to create the optimisation tool.

Table 8.1 shows how the parameter names used in the GPS theory were represented in the MatLab code. In the interest of brevity, x represents the any subscript used in the notation system in Chapter 4, i.e., R_{xx} could be R_{ii}, R_{ic}, etc.

An external NSGA-II code was sourced in MatLab format which was then used as the foundation of the optimisation tool developed in this chapter. The GPS theory equations and optimisation parameters were developed to interact with the sourced NSGA-II code to produce an efficient optimisation tool for SPM rotor design.

GPS Theory Notation in Chapter 4	MatLab Input in Optimisation Model
R_{xx}	R_xx
S_x	S_x
F_{zx}	F_zx
E_x	E_x
ν_x	nu_x
ρ_x	rho_x
α_x	alpha_x
ω	omega
Δ_T	Delta_T
$\sigma_{\theta xx}$	sigma_theta_xx
σ_{rxx}	sigma_rxx
σ_{zxx}	sigma_zxx

TABLE 8.1: GPS theory notation conversion to MatLab code.

8.3.2 Optimisation Code Skeleton

Figure 8.1 shows a schematic of the optimisation code and how the NSGA-II code interacts with the files created for the specific optimisation problem presented in this chapter.
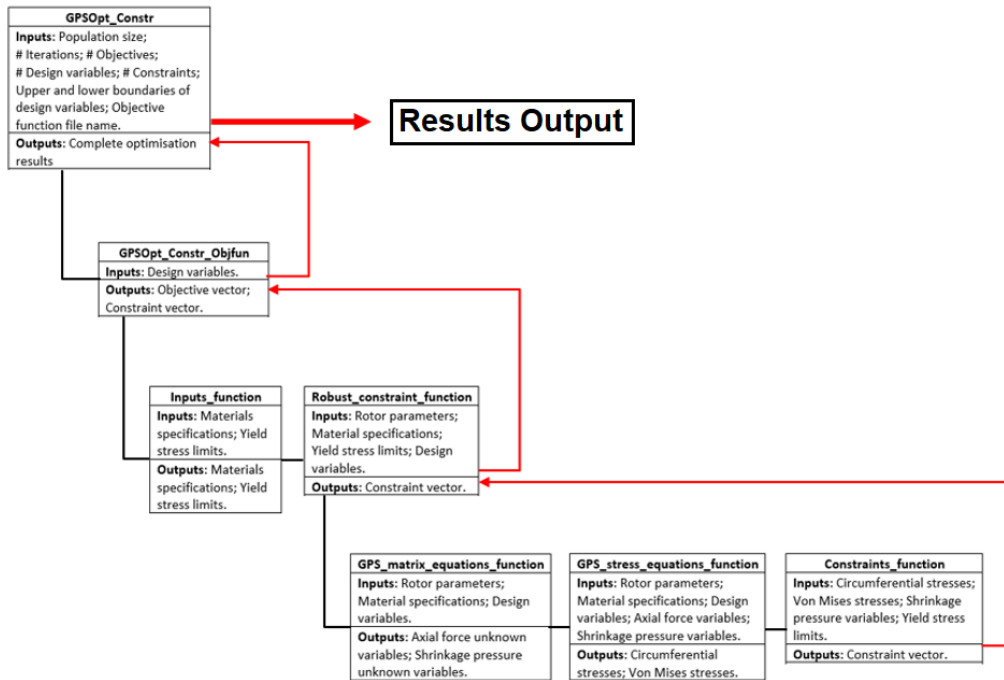
FIGURE 8.1: Skeleton to demonstrate the operation of the optimisation code.

In Figure 8.1, the file name, inputs, and outputs are listed for the main optimisation files. The black lines indicate which functions are called from within a certain file and which order they run in e.g., GPSOpt_Constr_Critfun calls Inputs_function first, followed by Robust_constraint_function. The red lines show the flow of the key outputs required to be able to run the optimisation. The key outputs are the criteria and constraint vectors which begin as empty vectors of zeros. With each design analysis the criteria values and constraint violations populate the respective vectors allowing the optimisation code to interpret and converge the results. The summary of each file is outlined below, while the full code is listed in Appendix B:

GPS_Opt_Constr:

- This is the main file that triggers the optimisation process for the NSGA-II method, using many sub files which do not require alteration.

- The user manually enters the values for the inputs, defining the optimisation parameters.

- The user also defines the file name of the criteria function (GPSOpt_Constr_ Critfun) enabling the code to call said file which is specifically adapted to solve the optimisation problem outlined in this chapter.

GPSOpt_Constr_Critfun:

- The design variables and criteria have been defined for this optimisation problem.

- Extra function files are called within the file to conduct analysis and apply the constraints.

- Values for the design variables between the upper and lower boundaries are automatically input by the optimisation code which enables the rest of the analysis to take place.

- The goal of this file is to output the populated criteria and constraint vectors for the optimisation code to interpret and work towards identifying which design variables produce a successful design.

Inputs_function:

- For ease of use, material specifications are manually defined by the user in this function file and are called into the criteria function file. This also keeps the criteria function concise.

Robust_constraint_function:

- This file operates a loop command to analyse a rotor design at all combinations of potential tolerances and operating conditions with a view to achieving robust optimisation.

- The tolerances of the rotor design parameters are defined by the user.

- Function files are called within the loop to conduct the stress analysis and apply the constraints.

- Constraint violations are stored with each loop and a single violation will trigger a failure for the robust constraint within the constraint vector.

- The goal of this file is to output the populated constraint vector to the criteria function.

GPS_matrix_equations_function:

- This file is used to calculate the axial force and shrinkage pressure variables for each rotor design using equations 4.102 – 4.122, developed in Chapter 4.

- The unknown variables are then output for use within GPS_stress_equations_ function.

GPS_stress_equations_function:

- Equations 4.52, 4.53 and 4.86, derived in Chapter 4, and their equivalents for all rotor cylinders are outlined in this function.
- This file calculates the circumferential, radial, and axial stresses at every cylinder surface of the rotor design which are then used to calculate the Von Mises stresses.
- Relevant stresses are output to then be input into Constraints_function to analyse the success of the rotor design.

Constraints_function:

- The constraints required for the optimisation are defined by the user.
- Any constraint violations are logged in the constraint vector.
- The constraint vector is output into Robust_constraint_function, where the robust condition is applied

8.3.3 Optimisation Parameters

As discussed in Section 8.3.2, GPSOpt_Constr triggers the optimisation process and is the user interface between the externally supplied NSGA-II code files and the user developed files specific to achieving the goals of the optimisation set out in this chapter. The inputs are entered manually by the user and define the optimisation parameters and the results output. Figure 8.2 shows how these inputs are entered into the file.

```
options = nsgaopt();                                          % create default options structure
options.popsize = 500;                                        % populaion size
options.maxGen  = 1000;                                       % max iterations

options.numObj = 3;                                           % number of criterion
options.numVar = 8;                                           % number of design variables
options.numCons = 12;                                         % number of constraints
options.lb = [0.003  0.001  0.000001  0.001  0.000001  0.001  10000    0];    % lower bound of variable x
options.ub = [0.003  0.04  0.001  0.04  0.001  0.03  200000  200];    % upper bound of variable x
options.objfun = @GPSOpt_Constr_Objfun;                       % criteria function handle
options.plotInterval = 100;                                   % interval between two calls of "plotnsga".

result = nsga2(options);                                      % begin the optimization!
```

FIGURE 8.2: Optimisation Parameters .

For the results output, the population size determines the number of new designs the code will introduce into the design space per iteration. The maximum number of iterations determines how many iterations the optimisation process will complete. This gives users control and the value needs to be high enough to allow the results to converge to a Pareto front so the results are not limited. The number of criteria, design variables, and constraints define the optimisation parameters, while the upper and lower value boundaries for each design variable provide limits for the optimisation code to work within. Finally, the criteria function file is named so the code can call the correct file and complete the optimisation. The criteria and constraint vectors are output from the criteria function and that information is used, along with the details input in Figure 8.2, in numerous NSGA-II files that remain constant for any optimisation problem. The files communicate to interpret the results of each iteration, enabling a results convergence and producing a graphical results output for the user.

8.3.4 Design Variables

The criteria function file GPS_Opt_Constr_Critfun is the file adapted by the user to complete the bespoke optimisation problem, defining design variables, criteria, analysis, and constraints. In the optimisation problem discussed in this chapter, multiple function files have been embedded within this criteria function, as shown in Figure 8.1. The goal of the criteria function is to populate and output the criteria and constraint vectors.

Design variables are parameters of the rotor design that are adjusted by the optimisation code until a set that best meets the criteria and satisfies the constraints is identified. The user must provide the range boundaries for the optimisation to operate within, as shown in Figure 8.2. Common design variables used by the existing mechanical optimisation papers were the interference between cylinders and the sleeve thickness for a two-cylinder problem, while one paper also used the magnet thickness as a design variable. However, the optimisation problem in this section is for a three-cylinder rotor. Therefore, there are two interference locations and three-cylinder thickness to consider. To enable simulation at various speeds and temperatures, these factors were also included as design variables. The optimisation code

uses the notation *x(n)* for design variables where n is used to distinguish the different design variables using numbers. Figure 8.3 shows how the cylinder thickness and interference design variables were defined in relation to the cylinder radii while the speed and temperature operating conditions were also outlined.

```
% Design Variables
R_ii = x(1);                    % x(1) = Inner cylinder inner radius (m)
R_ic = R_ii + x(2);             % x(2) = Inner cylinder thickness (m)
R_mc = R_ic - x(3);             % x(3) = Inner cylinder / middle cylinder interference (m)
R_md = R_mc + x(4);             % x(4) = Middle cylinder thickness (m)
R_od = R_md - x(5);             % x(5) = Middle cylinder / outer clyinder interfernce (m)
R_oo = R_od + x(6);             % x(6) = Outer cylinder thickness (m)
omega = x(7) * (2*pi / 60);     % x(7) = Rotor Speed (RPM)
Delta_T = x(8);                 % x(8) = Temperature change (C)
```

FIGURE 8.3: Design variable definitions.

The design variables were used to calculate each rotor cylinder dimension to enable the optimisation code to input the R_{xx} values in the GPS theory shown in Table 8.1. This method ensured that the design variable inputs remained user friendly. Table 8.2 shows the design variable details with boundary ranges and MatLab notations from Figures 8.2 and 8.3, respectively.

Design Variable	Lower boundary	Upper boundary	MatLab notation
Inner radius of inner cylinder (mm)	3	3	x(1)
Inner cylinder thickness (mm)	1	40	x(2)
Middle cylinder thickness (mm)	1	40	x(4)
Outer cylinder thickness (mm)	1	30	x(6)
Inner/middle cylinder interference (mm)	0.001	1	x(3)
Middle/outer cylinder interference (mm)	0.001	1	x(5)
Maximum operating speed (krpm)	10	200	x(7)
Maximum temperature elevation (^{o}C)	0	200	x(8)

TABLE 8.2: Design variable details.

The design variable constraints shown in Table 8.2 are through the application of upper and lower boundary limits. As discussed earlier the rotor is designed to slide onto a 6 mm diameter shaft, therefore the inner radius of the inner cylinder is fixed at 3 mm. The remaining rotor parameters were given wide boundary ranges to avoid limiting the Pareto set. However, the manufacturability was still considered to ensure that the optimal rotor designs were feasible, i.e. a rotor with a cylinder thickness under 1 mm was deemed infeasible to assemble. In Chapter 6, 80 krpm was set as a realistic high-speed value for the rotor. However, the objective then was

to ensure sufficient outer surface strain was generated. For optimisation, the outer surface strain is not a requirement and lower operating speed has been assigned that still ensures the rotor will operate at a reasonable speed.

8.3.5 Criteria

Once the design variables were defined within the criteria function, the criteria could be defined within the same file. The optimisation code uses the notation *y(n)* for criteria where *n* is used to distinguish the different criteria using numbers. This enables the code to populate the empty criteria vector, which is also defined in terms of *y*, as shown in Figure 8.4. The number of zeros is determined by the number of criteria thus enabling all criteria values to be added.

```
y = [0,0,0];            % Criteria vector

% Criteria
y(1) = x(6);            % Outer cylinder thickness
y(2) = x(4)*-1;         % Middle cylinder thickness
y(3) = x(7)*-1;         % Rotor Speed
```

FIGURE 8.4: Multi-criteria selection.

To complete the optimisation process there must be a goal for the optimisation to aim towards, specified as criteria. To show the capability of the optimisation model and to produce a rotor design based on multiple factors, three criteria were used. This also enabled results to be clearly displayed in a three-dimensional (3D) space. To maximise the rotor performance, the criteria were defined as:

- Minimise sleeve thickness (outer cylinder).
- Maximise magnet thickness (middle cylinder).
- Maximise operating speed.

Decreasing the sleeve thickness reduces the effective air gap between the stator and the magnets, which leads to better electromagnetic performance and an increase in operating speed. Increasing the magnet thickness improves the electromagnetic performance by providing a stronger magnet interaction with the stator. Having an increased operating speed enables the rotor to produce a higher power output.

Maximising these factors will produce rotor designs with optimal performance. Figure 8.4 shows the how the criteria were specified within the optimisation tool. The optimisation code operates to minimise all chosen criteria; however, this can easily be used to maximise a criterion by assigning it a negative value. As all criteria are design variables, the criteria constraints are applied through the upper and lower boundaries discussed in Section 8.3.4. It is important to ensure that the constraints placed on the criteria do not limit the optimisation unnecessarily but do retain the feasibility of the design.

8.3.6 Rotor Properties Input

As shown in Figure 8.1, the material properties and yield stress limits for each rotor cylinder are called from a separate function Inputs_function within the constrain function file. This improves the ease of use for the user and ensures the criteria function remains concise. The properties listed in this section have been assumed to be fixed values.

The rotor properties must be specified to enable the optimisation model to apply the GPS analysis equations further on in the optimisation process. The rotor properties are input manually, enabling the user to input the desired materials relevant to their situation. They are then output into the criteria function file. Figure 8.5 shows how the inputs were defined within the Inputs_function file, where σ_x_allow is the allowable stress for the inner, middle, and outer cylinders.

```
alpha_i = 0.000010 ;            % coefficient of thermal expansion for inner cylinder
alpha_m = 0.000005 ;            % coefficient of thermal expansion for middle cylinder
alpha_o = 0.000009 ;            % coefficient of thermal expansion for outer cylinder
nu_i = 0.29 ;                   % Poisson's ratio for inner cylinder
nu_m = 0.24;                    % Poisson's ratio for middle cylinder
nu_o = 0.36 ;                   % Poisson's ratio for outer cylinder
E_i = 215000000000 ;           % Young's modulus for inner cylinder (Pa)
E_m = 160000000000 ;           % Young's modulus for middle cylinder (Pa)
E_o = 114000000000 ;           % Young's modulus for outer cylinder (Pa)
rho_i = 7700;                   % Density for inner cylinder (kg/m^3)
rho_m = 7500 ;                  % Density for middle cylinder (kg/m^3)
rho_o = 4400 ;                  % Density for outer cylinder (kg/m^3)
sigma_i_allow = 450000000;      % Allowable stress for inner cylinder (Pa)
sigma_m_allow = 850000000;      % Allowable stress for middle cylinder (Pa)
sigma_o_allow = 880000000;      % Allowable stress for outer cylinder (Pa)
```

FIGURE 8.5: Multi-criteria selection.

For this optimisation problem, the materials chosen were those shown in Table 5.1 from Chapter 5, to represent a working electromagnetic rotor and are repeated

in Table 8.3. The allowable stress properties were taken from Burnand et al. [11] and MatWeb [172]. As the middle cylinder must be held in compression, the compressive strength value was used, whereas the tensile yield strength was used for the inner and outer cylinders.

Material Property	Inner Cylinder	Middle Cylinder	Outer Cylinder
Young's Modulus (GPa)	215	160	114
Poisson's ratio	0.29	0.24	0.36
Density (kgm^{-3})	7700	7500	4400
Coefficient of thermal expansion (K^{-1})	1×10^{-5}	5×10^{-6}	9×10^{-6}
Allowable Stress (MPa)	450	850	880

TABLE 8.3: Selected material properties.

8.3.7 Stress Equation Input

Once the rotor properties in Table 8.3 have been output to the criteria function file, the GPS analysis can take place. As shown in Figure 8.1, the analysis takes place in the file Robust_constraint_function, however three further function files are called within this file to conduct the GPS analysis and apply the constraints while. The function GPS_matrix_equations_function is applied first.

In Chapter 4, equations 4.52, 4.53, and 4.86 were derived as the radial, circumferential, and axial GPS stress equations, respectively. Following the theory, equations 4.92, 4.93, 4.100, and 4.101 were derived after incorporating the GPS conditions. These four equations were then simplified into equations 4.102 - 4.122 to identify the four unknown variables S_1, S_2, F_{zi}, and F_{zo}. The function GPS_matrix_equations_function contains equations 4.102 - 4.122 to identify the unknown variables. Design variables and the rotor parameters from Table 8.3 are input into the function, which returns the unknown variables as outputs into Robust_constraint_function.

Figure 8.6 has been taken from Appendix B and shows the MatLab code for equations 4.102 - 4.122, where array B contains the four unknown values.

Following Figure 8.1, from within Robust_constraint_function, GPS_stress_equations_function is then called which contains the stress equations 4.52, 4.53, and 4.86.

```
F = -1/(E_m*pi*(R_mc^2 - R_md^2));
G = 1/(E_i*pi*(R_ic^2 - R_ii^2)) - 1/(E_m*pi*(R_mc^2 - R_md^2));
H = (2*R_md^2*nu_m)/(E_m*(R_mc^2 - R_md^2));
I = (2*R_ic^2*nu_i)/(E_i*(R_ic^2 - R_ii^2)) - (2*R_mc^2*nu_m)/(E_m*(R_mc^2 - R_md^2));
J = (-(omega^2*(nu_m*pi*R_mc^4 - nu_m*pi*R_md^4))/(2*E_m*pi*(R_mc^2 - R_md^2)))*rho_m +...
    (2*Delta_T*E_m*alpha_m*pi*R_mc^2 - 2*Delta_T*E_m*alpha_m*pi*R_md^2)/(2*E_m*pi*(R_mc^2 - R_md^2))...
    + (rho_i*nu_i*pi*R_ic^4*omega^2 - 2*Delta_T*E_i*alpha_i*pi*R_ic^2 - rho_i*nu_i*pi*R_ii^4*omega^2 +...
    2*Delta_T*E_i*alpha_i*pi*R_ii^2)/(2*E_i*pi*(R_ic^2 - R_ii^2));

K = 1/(E_m*pi*(R_mc^2 - R_md^2)) + 1/(E_o*pi*(R_od^2 - R_oo^2));
L = 1/(E_m*pi*(R_mc^2 - R_md^2));
M = - (2*R_md^2*nu_m)/(E_m*(R_mc^2 - R_md^2)) - (2*R_od^2*nu_o)/(E_o*(R_od^2 - R_oo^2));
N = (2*R_mc^2*nu_m)/(E_m*(R_mc^2 - R_md^2));
O = - (-(omega^2*(nu_m*pi*R_mc^4 - nu_m*pi*R_md^4))/(2*E_m*pi*(R_mc^2 - R_md^2)))*rho_m -...
    (2*Delta_T*E_m*alpha_m*pi*R_mc^2 - 2*Delta_T*E_m*alpha_m*pi*R_md^2)/(2*E_m*pi*(R_mc^2 - R_md^2))...
    - (rho_o*nu_o*pi*R_od^4*omega^2 - 2*Delta_T*E_o*alpha_o*pi*R_od^2 - rho_o*nu_o*pi*R_oo^4*omega^2 +...
    2*Delta_T*E_o*alpha_o*pi*R_oo^2)/(2*E_o*pi*(R_od^2 - R_oo^2));

P = (R_mc*nu_m)/(E_m*pi*(R_mc^2 - R_md^2));
Q = (R_mc*nu_m)/(E_m*pi*(R_mc^2 - R_md^2)) - (R_ic*nu_i)/(E_i*pi*(R_ic^2 - R_ii^2));
R = -(2*R_mc*R_md^2)/(E_m*(R_mc^2 - R_md^2));
T = (R_mc*(pi*R_mc^2 + pi*R_md^2 - pi*R_mc^2*nu_m + pi*R_md^2*nu_m))/(E_m*pi*(R_mc^2 - R_md^2)) -...
    (R_ic*(pi*R_ic^2 + pi*R_ii^2 - pi*R_ic^2*nu_i + pi*R_ii^2*nu_i))/(E_i*pi*(R_ic^2 - R_ii^2));
U = R_mc*((rho_m*(R_md^2*nu_m - R_mc^2*nu_m + R_mc^2 + 3*R_md^2)*omega^2)/(4*E_m) + Delta_T*alpha_m + 1)...
    - R_ic*((rho_i*(R_ii^2*nu_i - R_ic^2*nu_i + R_ic^2 + 3*R_ii^2)*omega^2)/(4*E_i) + (Delta_T*E_i*R_ic^2*alpha_i*pi...
    - Delta_T*E_i*R_ii^2*alpha_i*pi)/(E_i*pi*(R_ic^2 - R_ii^2)) + 1);

V = (R_md*nu_m)/(E_m*pi*(R_mc^2 - R_md^2)) + (R_od*nu_o)/(E_o*pi*(R_od^2 - R_oo^2));
W = (R_md*nu_m)/(E_m*pi*(R_mc^2 - R_md^2));
X = - (R_md*(pi*R_mc^2 + pi*R_md^2 + pi*R_mc^2*nu_m - pi*R_md^2*nu_m))/(E_m*pi*(R_mc^2 - R_md^2))...
    - (R_od*(pi*R_od^2 + pi*R_oo^2 - pi*R_od^2*nu_o + pi*R_oo^2*nu_o))/(E_o*pi*(R_od^2 - R_oo^2));
Y = (2*R_mc^2*R_md)/(E_m*(R_mc^2 - R_md^2));
Z = R_md*((rho_m*(R_mc^2*nu_m - R_md^2*nu_m + 3*R_mc^2 + R_md^2)*omega^2)/(4*E_m) + Delta_T*alpha_m + 1)...
    - R_od*((rho_o*(R_oo^2*nu_o - R_od^2*nu_o + R_od^2 + 3*R_oo^2)*omega^2)/(4*E_o) + (Delta_T*E_o*R_od^2*alpha_o*pi...
    - Delta_T*E_o*R_oo^2*alpha_o*pi)/(E_o*pi*(R_od^2 - R_oo^2)) + 1);

A = [F,G,H,I;K,L,M,N;P,Q,R,T;V,W,X,Y] ;
C = [J; O; U; Z] ;
B = inv(A) * C ;
F_zo = B(1) ;
F_zi = B(2) ;
S_2 = B(3) ;
S_1 = B(4) ;
F_zm = -(F_zo + F_zi) ;
```

FIGURE 8.6: MatLab code used to calculate GPS unknown variables.

To calculate rotor stresses S_1, S_2, F_{zi}, and F_{zo} are fed into GPS_stress_equations_function. However, equations 4.52, 4.53, and 4.86, represent the middle cylinder stress equations, therefore the corresponding equations for the inner and outer cylinders were also required. Figure 8.7 shows the MatLab code used to determine the radial, circumferential, and axial stress equations for all three cylinders.

```
%%% Inner cylinder %%%
sigma_theta_ii  = (rho_i*(2*R_ic^2*nu_i + 2*R_ii^2*nu_i - 3*R_ic^2 - R_ii^2)*omega^2)/(4*nu_i - 4)...
                  - (2*R_ic^2*S_1)/(R_ic^2 - R_ii^2);
sigma_theta_ic  = (rho_i*(2*R_ic^2*nu_i + 2*R_ii^2*nu_i - R_ic^2 - 3*R_ii^2)*omega^2)/(4*nu_i - 4)...
                  - (R_ic^2*S_1)/(R_ic^2 - R_ii^2) - (R_ii^2*S_1)/(R_ic^2 - R_ii^2);
sigma_rii       = 0 ;
sigma_ric       = -S_1 ;
sigma_zic       = (rho_i*nu_i*(R_ic^2 - R_ii^2)*omega^2)/(4*nu_i - 4) + F_zi/(pi*(R_ic^2 - R_ii^2));
sigma_zii       = F_zi/(pi*(R_ic^2 - R_ii^2)) - (omega^2*rho_i*nu_i*(R_ic^2 - R_ii^2))/(4*(nu_i - 1));

%%% Middle cylinder %%%
sigma_theta_mc  = (rho_m*(2*R_mc^2*nu_m + 2*R_md^2*nu_m - R_mc^2 - 3*R_md^2)*omega^2)/(4*nu_m - 4)...
                  - (R_mc^2*S_1 - R_md^2*S_2)/(R_mc^2 - R_md^2) - (R_md^2*(S_1 - S_2))/(R_mc^2 - R_md^2);
sigma_theta_md  = (rho_m*(2*R_mc^2*nu_m + 2*R_md^2*nu_m - 3*R_mc^2 - R_md^2)*omega^2)/(4*nu_m - 4)...
                  - (R_mc^2*S_1 - R_md^2*S_2)/(R_mc^2 - R_md^2) - (R_mc^2*(S_1 - S_2))/(R_mc^2 - R_md^2);
sigma_rmc       = -S_1 ;
sigma_rmd       = -S_2 ;
sigma_zmc       = (rho_m*nu_m*(R_mc^2 - R_md^2)*omega^2)/(4*nu_m - 4) - F_zm/(pi*(R_mc^2 - R_md^2));
sigma_zmd       = - F_zm/(pi*(R_mc^2 - R_md^2)) - (omega^2*rho_m*nu_m*(R_mc^2 - R_md^2))/(4*(nu_m - 1));

%%% Outer cylinder %%%
sigma_theta_oo  = (rho_o*(2*R_od^2*nu_o + 2*R_oo^2*nu_o - 3*R_od^2 - R_oo^2)*omega^2)/(4*nu_o - 4)...
                  - (2*R_od^2*S_2)/(R_od^2 - R_oo^2);
sigma_theta_od  = (rho_o*(2*R_od^2*nu_o + 2*R_oo^2*nu_o - R_od^2 - 3*R_oo^2)*omega^2)/(4*nu_o - 4)...
                  - (R_od^2*S_2)/(R_od^2 - R_oo^2) - (R_oo^2*S_2)/(R_od^2 - R_oo^2);
sigma_roo       = 0 ;
sigma_rod       = -S_2 ;
sigma_zod       = (rho_o*nu_o*(R_od^2 - R_oo^2)*omega^2)/(4*nu_o - 4) - F_zo/(pi*(R_od^2 - R_oo^2));
sigma_zoo       = - F_zo/(pi*(R_od^2 - R_oo^2)) - (omega^2*rho_o*nu_o*(R_od^2 - R_oo^2))/(4*(nu_o - 1));
```

FIGURE 8.7: MatLab code for circumferential, radial, and axial stress equations.

Using the results from the calculations made using the analysis in Figure 8.7, the Von Mises stresses were also calculated within the GPS_stress_equations_function file. The Von Mises yield criterion was selected as it is less conservative than the Tresca yield criterion, as demonstrated by Ayob and Elbasheer [173], and the main function was to demonstrate the functionality of the optimisation tool. Figure 8.8 shows the MatLab code used to determine the Von Mises stresses for all three cylinders. Following the analysis shown in Figures 8.7 and 8.8, the circumferential and Von Mises stress calculations are output into Robust_constraint_function.

```
%%%%%% Von Mises %%%%%%
VM_ic = sqrt(0.5*((sigma_ric - sigma_theta_ic)^2 + (sigma_theta_ic - sigma_zic)^2 + (sigma_zic - sigma_ric)^2));
VM_ii = sqrt(0.5*((sigma_rii - sigma_theta_ii)^2 + (sigma_theta_ii - sigma_zii)^2 + (sigma_zii - sigma_rii)^2));
VM_mc = sqrt(0.5*((sigma_rmc - sigma_theta_mc)^2 + (sigma_theta_mc - sigma_zmc)^2 + (sigma_zmc - sigma_rmc)^2));
VM_md = sqrt(0.5*((sigma_rmd - sigma_theta_md)^2 + (sigma_theta_md - sigma_zmd)^2 + (sigma_zmd - sigma_rmd)^2));
VM_od = sqrt(0.5*((sigma_rod - sigma_theta_od)^2 + (sigma_theta_od - sigma_zod)^2 + (sigma_zod - sigma_rod)^2));
VM_oo = sqrt(0.5*((sigma_roo - sigma_theta_oo)^2 + (sigma_theta_oo - sigma_zoo)^2 + (sigma_zoo - sigma_roo)^2));
```

FIGURE 8.8: MatLab code for Von Mises stress equations.

8.3.8 Constraints

As shown in Figure 8.1, once the GPS analysis has taken place and the stress results have been output into the file Robust_constraint_function, the function Constraints_function is called. This file defines the constraints set by the user and populates the empty constraint vector. MatLab uses the notation *cons(n)* for constraints where n is used to distinguish the different constraints using numbers. This enables the code to populate the empty constraint vector, which is also defined in terms of cons, as shown in Figure 8.9. The number of zeros is determined by the number of constraints thus enabling all constraint violations to be logged.

As discussed in Section 2.4.1.1, criteria and design variable constraints are user defined limits imposed on said aspects. Functional constraints place limits on other parameters that are not criteria. Most of the papers focussing on mechanical optimisation incorporated functional and design variable constraints into their model, whereas few placed constraints on the chosen criteria. Most papers only identified a single optimised design and little work was conducted on robust optimisation where manufacturing factors are considered. The optimisation model in this section produces a set of optimal results, enabling the user to decide which rotor configuration

```
cons = [0,0,0,0,0,0,0,0,0,0,0];   % Constraint vector

if S_1<0
    cons(1) = abs(S_1);             % Constraint 1 & 2
end                                 % Do not allow separation between cylinders
if S_2<0
    cons(2) = abs(S_2);
end
if sigma_theta_mc>0
    cons(3) = abs(sigma_theta_mc);  % Constraint 3 & 4
end                                 % Do not allow magnets to go into tension
if sigma_theta_md>0
    cons(4) = abs(sigma_theta_md);
end
if abs(VM_ic)>sigma_i_allow
    cons(5) = abs(VM_ic);           % Constraint 5 & 6
end                                 % Inner cylinder must not exceed allowable stress
if abs(VM_ii)>sigma_i_allow
    cons(6) = abs(VM_ii);
end
if abs(VM_mc)>sigma_m_allow
    cons(7) = abs(VM_mc);           % Constraint 7 & 8
end                                 % Middle cylinder must not exceed allowable stress
if abs(VM_md)>sigma_m_allow
    cons(8) = abs(VM_md);
end
if abs(VM_od)>sigma_o_allow
    cons(9) = abs(VM_od);           % Constraint 9 & 10
end                                 % Outer cylinder must not exceed allowable stress
if abs(VM_oo)>sigma_o_allow
    cons(10) = abs(VM_oo);
end
if R_oo>0.028
    cons(11) = abs(R_oo);           % Constraint 11
end                                 % Diameter limit
end
```

FIGURE 8.9: Functional Constraints.

is most suited to their needs. Manufacturing considerations were also included to ensure that any feasible design is robust and will remain successful despite manufacturing tolerances.

To ensure the optimised rotor designs were feasible, the following functional constraints were imposed.

- Contact pressure must be maintained between cylinders.
- The middle cylinder (magnets) must remain in compression.
- Material allowable stress limits must not be exceeded.
- Maximum rotor diameter must be less than 56 mm.

As identified in Chapter 5, some rotor designs are predicted to lose contact pressure due to large centrifugal forces, leading to rotor failure. Chapter 1 discusses the low tensile strength of sintered permanent magnets which must be held in compression to avoid failure. These potential failures must be avoided whilst not exceeding the allowable stress limit of the materials used. As outlined earlier, the rotor must fit within the bearing housing designed in Chapter 6 and therefore has a maximum diameter limit of 56 mm. Figure 8.9 shows how these constraints were input into a function for the optimisation tool.

Constraints 1 and 2 ensure that the contact pressure between cylinders remains positive. If the contact pressure value becomes negative, then the rotor cylinders have been predicted to separate which would result in rotor failure. Constraints 3 and 4 ensure that the circumferential stress at the inner and outer surface of the middle cylinder remains negative and therefore compressive. Constraints 5 to 10 ensure that the Von Mises stress at the inner and outer surfaces of each cylinder remains under the material allowable stress limit so no part of the rotor will yield or fail. Constraint 11 ensures that all successful rotor designs have a maximum outer radius of less than 28 mm, enabling it to fit within the 56 mm window in the bearing housing.

During the optimisation, the stress results and shrinkage pressures identified earlier are fed into the constraints in Figure 8.9, as shown in Figure 8.1. If any constraints are violated, the constraint value populates the constraint vector. After analysing all constraints, the constraint vector is output back into the file, Robust_constraint_ function.

8.3.9   Robustness Constraint

From Figure 8.1, the bulk of the analysis takes place using the three function files called within Robust_constraint_function. However, when the constraint vector is output into Robust_constraint_function, only eleven constraints have been analysed, as shown in Figure 8.9. As shown in Figure 8.2, twelve constraints are applied in the optimisation process. The final constraint is applied within Robust_constraint_ function and determines whether the rotor design being analysed is a robust design.

A rotor design is considered feasible if it operates successfully within all the constraints outlined in Section 8.3.8. However, this does not ensure the rotor is robust. The following constraints were imposed to ensure the optimised rotor design could be considered robust.

- Rotor design must remain successful when dimensions change ±0.001 mm.
- Rotor design must remain successful under the following operating conditions.
    - Stationary at ambient temperature.

– Maximum speed at ambient temperature.

– Stationary at maximum temperature.

– Maximum speed and temperature.

As discussed in Section 8.3.6 the rotor properties were assumed to be constant. However, it would be possible to include variations of these values for robustness, but it was excluded at this stage to reduce complexity.

To ensure that the rotor design is robust, the rotor must still pass all constraints when dimension changes due to manufacturing tolerances are considered. The rotor must also remain successful when operating at all operating conditions, covered by the four operating states outlined in Section 5.3.1. To demonstrate the capability of the robust constraint whilst retaining a high volume of results, a small tolerance value of 0.001 mm was selected. The user has the capability to adjust this value depending on their manufacturing process. Figure 8.10 shows how the tolerances were defined.

```
tol = 0.000001;            % Tolerance value applied to dimensions (m)

l_R_ii = R_ii - tol;       % Upper and lower boundaries on the rotor...
u_R_ii = R_ii + tol;       % dimensions created using the value 'tol'.
l_R_ic = R_ic - tol;
u_R_ic = R_ic + tol;
l_R_mc = R_mc - tol;
u_R_mc = R_mc + tol;
l_R_md = R_md - tol;
u_R_md = R_md + tol;
l_R_od = R_od - tol;
u_R_od = R_od + tol;
l_R_oo = R_oo - tol;
u_R_oo = R_oo + tol;
```

FIGURE 8.10: Tolerance definition.

A single tolerance value was specified making it easy for the user to adjust to their requirements. This value was then used to created upper and lower limits on the radial dimensions of the rotor parts, simulating potential fluctuations occurring during the manufacturing process.

To be able to conduct analysis on all possible combinations of tolerance variation and operating conditions, a loop command was defined within Robust_constraint_ function. Figure 8.11 shows how the loop command was specified within the function.

Vectors for the potential radial dimensions and the operating conditions were defined and then called via for statements to enable the code to loop through all

```
R_ii_range = [l_R_ii,u_R_ii,R_ii]; % Vectors created to loop through lower, upper, and...
R_ic_range = [l_R_ic,u_R_ic,R_ic]; % original rotor dimensions and operating conditions
R_mc_range = [l_R_mc,u_R_mc,R_mc];
R_md_range = [l_R_md,u_R_md,R_md];
R_od_range = [l_R_od,u_R_od,R_od];
R_oo_range = [l_R_oo,u_R_oo,R_oo];
omega_range = [0,omega];
Delta_T_range = [0,Delta_T];
                              % Empty constraint array created to hold one value per loop cycle.
Constr_array = zeros(length(R_ii_range),length(R_ic_range),length(R_mc_range),length(R_md_range),...
                     length(R_od_range),length(R_oo_range),length(omega_range),length(Delta_T_range));

for R_ii_vector = 1:length(R_ii_range)  % Loop command to simulate all possible combinations...
    R_ii = R_ii_range(R_ii_vector) ;    % of potential tolerance or operating condition changes.

    for R_ic_vector = 1:length(R_ic_range)
        R_ic = R_ic_range(R_ic_vector) ;

        for R_mc_vector = 1:length(R_mc_range)
            R_mc = R_mc_range(R_mc_vector) ;

            for R_md_vector = 1:length(R_md_range)
                R_md = R_md_range(R_md_vector) ;

                for R_od_vector = 1:length(R_od_range)
                    R_od = R_od_range(R_od_vector) ;

                    for R_oo_vector = 1:length(R_oo_range)
                        R_oo = R_oo_range(R_oo_vector) ;

                        for speed_vector = 1:length(omega_range)
                            omega = omega_range(speed_vector) ;

                            for temp_vector = 1:length(Delta_T_range)
                                Delta_T = Delta_T_range(temp_vector) ;
```

FIGURE 8.11: Loop command definition.

possible combinations. Each potential rotor design was therefore subject to over 2900 variation simulations to ensure it remained robust. A constraint array was created, at a size of one value per loop, to be able to log if a rotor design variation violated any constraints.

Within the loop, the process outlined in Sections 8.3.7 and section 8.3.8 was conducted. This is also shown in Figure 8.1 as the GPS analysis and constraint functions are called within Robust_constraint_function. Figure 8.12 shows how this was specified within the optimisation code.

```
% Call GPS Matrix Equations
[F_zo,F_zi,F_zm,S_1,S_2]...
    = GPS_matrix_equations_function(R_ii,R_ic,R_mc,R_md,R_od,R_oo,Delta_T,alpha_i,...
            alpha_o,alpha_m,nu_i,nu_m,nu_o,E_o,E_i,E_m,rho_i,rho_o,rho_m,omega);

% Call GPS Stress Equations
[VM_ic,VM_ii,VM_mc,VM_md,VM_od,VM_oo,sigma_theta_mc,sigma_theta_md]...
    = GPS_stress_equations_function(F_zo,F_zi,F_zm,S_1,S_2,R_ii,R_ic,...
            R_mc,R_md,R_od,R_oo,nu_i,nu_m,nu_o,rho_i,rho_o,rho_m,omega);

% Apply the constraints
[cons] = Constraints_function(VM_ic,VM_ii,VM_mc,VM_md,VM_od,VM_oo,...
                sigma_theta_mc,sigma_theta_md,S_1,S_2,sigma_i_allow,...
                    sigma_m_allow,sigma_o_allow);

% Convert any constraint violations into binary value '1'.
constr_fail = any(cons);

% Store each binary '1' produced during any loop.
Constr_array(R_ii_vector,R_ic_vector,R_mc_vector,R_md_vector,R_od_vector,...
    R_oo_vector,speed_vector,temp_vector)= constr_fail;
```

FIGURE 8.12: GPS and constraint analysis.

As discussed in Section 8.3.8, the constraint array is output into Robust_constraint_function after the eleven initial constraints are analysed. The code then produces a failure outcome (constr_fail), if any constraints have been violated, using the value *1*. With each loop the process is repeated, and any fail outcomes are stored within a constraints array (Constr_array). The constraint array is then analysed by the final part of the code to determine if the robust constraint has been violated. Figure 8.13 shows this was specified within the optimisation code.

```
% Analyse the constraints array
Robust_constr_fail = any(Constr_array, 'all');

% Trigger the final constraint violation in...
% the constraint vector
if Robust_constr_fail == 1
    cons(12) = abs(Robust_constr_fail);
end
```

FIGURE 8.13: Robust constraint analysis.

The constraint array is analysed for any values of *1* which would indicate that a failure has occurred in one or more of the rotor variations analysed during the loop. Any failures render the robustness constraint violated and therefore the twelfth and final constraint within the constraint vector would be triggered.

As shown in Figure 8.1, the constraint vector is the output into the criteria function, where the criteria vector is stored. This enables the optimisation to take place as the criteria and constraint vectors will be analysed during the optimisation process when the criteria function file is called. Designs with any constraint failures are removed from the optimisation process and the results converge with each iteration as the criteria are minimised. By simultaneously using the criteria, design variables, constraints, and GPS theory outlined in this section, the user can perform robust optimisation for a three-cylinder compound rotor design.

8.4 Results

8.4.1 Feasible and Pareto Sets

As mentioned in Section 8.2.2, genetic algorithms can require many iterations to converge, and the total value is at the discretion of the user. To ensure the optimisation

tool successfully converged to a Pareto set, one thousand iterations were specified. However, this may be excessive for users to regularly use as there is an optimal stopping point where continued iterations bring minimal benefit. The Pareto set is a set of optimal points that have been converged to form a surface in the 3D design space. This enables the user to decide which criteria to prioritise as the effects of changing criteria values can be visualised.

After running one thousand iterations, with a population of five hundred potential designs per iteration, all successful designs were extracted and plotted on the 3D graph shown in Figure 8.14. This represents the feasible set and shows the range of potential designs that meet the requirements specified in the optimisation process using the criteria, design variables and constraints outlined in Section 8.3.
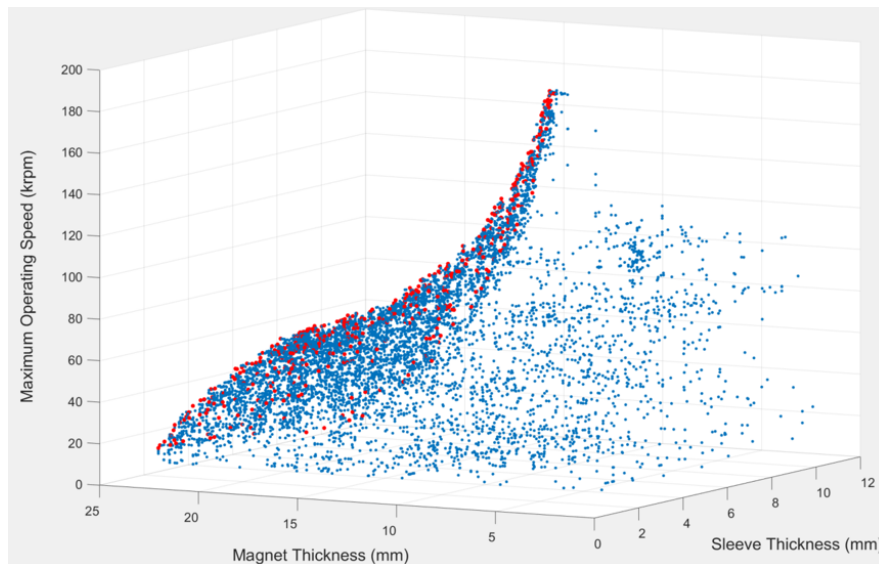
FIGURE 8.14: Feasible set from the optimisation run.

Whilst all points shown in Figure 8.14 represent the feasible set, within it the Pareto set is visibly shown by the red markers while the rest of the feasible set is represented by blue markers. As the optimisation process completes, more points are generated progressively closer towards the Pareto front based on the criteria set, shown by the increasing density of the blue markers. Figure 8.14 shows that the Pareto front is a surface that is convex with respect to the magnet thickness and sleeve thickness in ascending direction. With respect to the operating speed, the Pareto front is convex with changing magnet thickness, but concave with changing sleeve thickness.

Figure 8.15 shows that successful designs were generated across almost the full range of sleeve and magnet thicknesses possible within the design constraints. However, as the magnet thickness increases, the range of successful sleeve thicknesses decreases and tends towards a lower sleeve thickness. Eventually the magnet thickness is increased to circa 23 mm and then no successful designs are produced within the constraints. This is due to the limiting radial value constraint of 28 mm placed on the rotor. As the minimum inner and outer cylinder thicknesses are 1 mm, along with an initial 3 mm radius to carry the shaft, the maximum possible value for the magnet thickness is 23 mm. This is verified by observing that as the sleeve thickness increases by 1 mm, the maximum magnet thickness decreases by 1 mm.
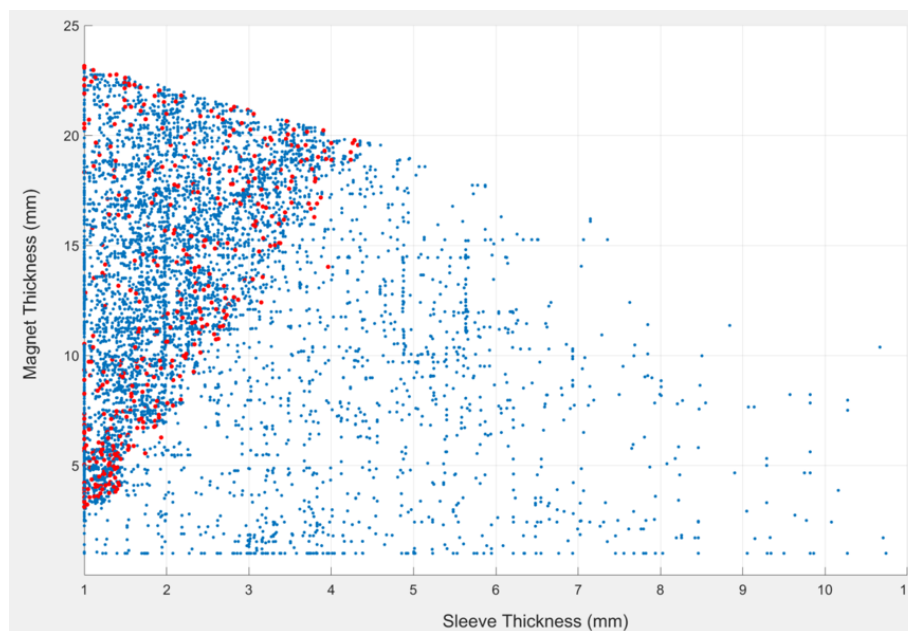
FIGURE 8.15: Sleeve thickness versus magnet thickness in the feasible set from the optimisation run.

Shown in Figure 8.15, for lower sleeve thicknesses the Pareto front forms the boundary of the feasible set. As the sleeve thickness increases, fewer optimal designs are produced, and the range of magnet thicknesses narrows significantly, towards a single point at circa 20 mm. At this point, the Pareto set ends while the feasible set continues to extend across the full sleeve thickness range. This boundary for the Pareto set is limited by an inability to achieve higher operating speeds without losing dominance. Higher speeds increase the stresses and centrifugal forces, contributing to the violation of constraints. Conversely, as the sleeve thickness is minimised, as

per the criteria, a wider range of magnet thicknesses from circa 3 - 23 mm are found to produce optimal results. The optimisation aims to reduce the sleeve thickness and increase the magnet thickness which should identify designs that would tend towards the top left-hand corner of Figure 8.15. However, lower magnet thicknesses enable higher operating speeds and extends the Pareto front.

Figure 8.16 shows the relationship between the sleeve thickness and maximum operating speed for the feasible and Pareto sets. The feasible set contains designs across the full operating speed range. When the sleeve thickness increases up to 2 mm the maximum speed range drops quickly to circa 150 krpm. This is due to the increased centrifugal forces, generated by a heavier sleeve, limiting the top speed of the rotor. However, this trend reduces, and successful designs are produced across most of the sleeve thickness range that can successfully operate at over 100 krpm. More successful designs are generated at a lower operating speed.
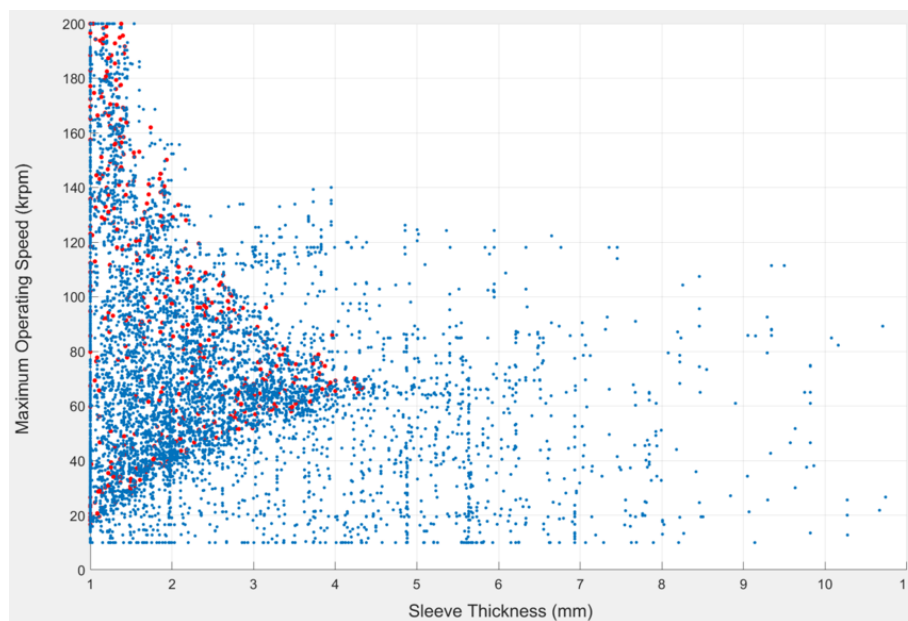
FIGURE 8.16: Sleeve thickness versus operating speed in the feasible set from the optimisation run.

Figure 8.16 shows that at the minimum sleeve thickness the Pareto set spans a wide range of speeds from under 20 krpm up to 200 krpm. As discussed, increasing the sleeve thickness requires a lower speed is to ensure various constraints are not broken due to the increased centrifugal forces. Therefore, the maximum operating speed reduces from 200 krpm to circa 70 krpm as the sleeve thickness increase.

However, the minimum operating speed on the Pareto front increases and converges towards 70 krpm despite the increase in sleeve thickness. As shown in Figure 8.15, this is due to a corresponding reduction in magnet thickness. Maintaining the same overall diameter ensures the increase in sleeve thickness does not significantly affect the centrifugal forces, while the added sleeve thickness provides additional capability to withstand stresses and achieve a higher operating speed. Fewer optimal designs are produced as the sleeve thickness increases and no further optimal designs are produced after the Pareto front converges to circa 70 krpm operating speed.

As shown in Figures 8.15 and 8.16, the limiting factor on the sleeve thickness is the minimum of 1 mm design variable constraint placed on it, rather than the magnitude of the sleeve stress. This is unexpected as to generate compression on the magnets, a radial force from the sleeve is required. Therefore, decreasing the sleeve thickness will increase the stress within the sleeve for the same force. The stress in the sleeve should therefore become a limiting factor. To show this, the optimisation was repeated, however the lower design variable constraint placed on the sleeve thickness was reduced to 0.001 mm. Figure 8.17 shows the results.
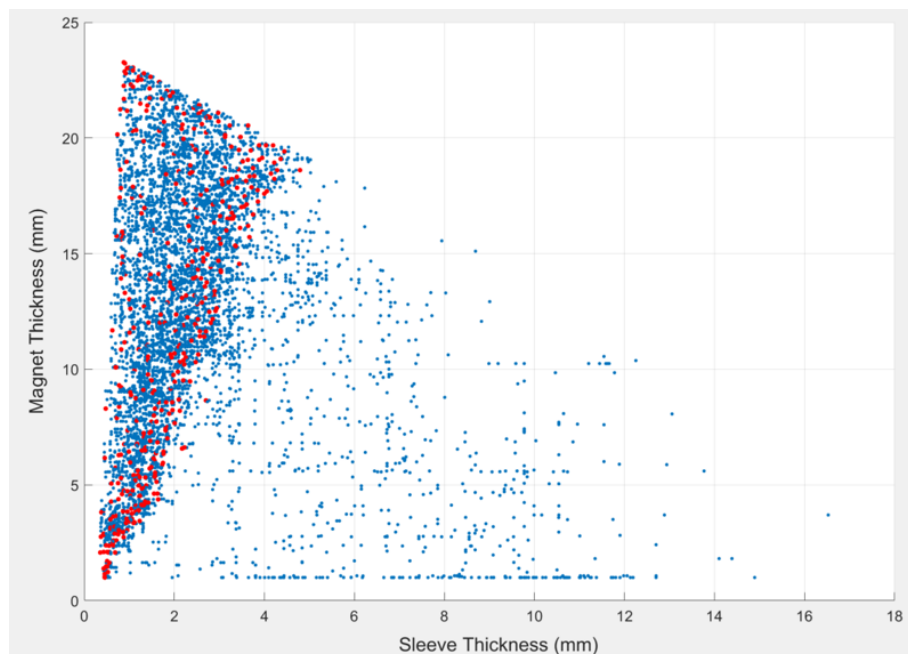
FIGURE 8.17: Sleeve thickness versus magnet thickness in the feasible set with a reduced sleeve thickness constraint.

Figure 8.17 shows that the sleeve is no longer limited by the design variable constraint and is therefore limited by the sleeve stress as discussed above. The sleeve thickness is limited to circa 0.5 mm at low magnet thicknesses and circa 1 mm at larger magnet thicknesses. However, a wall thickness of less than 1 mm was deemed to be infeasible to manufacture accurately . Therefore, these low sleeve thickness designs were not included in the original optimisation.

Figure 8.18 shows that the maximum operating speed has a more defined limit against magnet thickness than sleeve thickness. The defined limit is also shown to form part of the Pareto set. The feasible set shows potential designs can be found away from the Pareto set across most of the magnet thickness range. This is to be expected as reducing the operating speed will help the designs remain successful.

On the limits of constraints, increasing the magnet thickness requires the sleeve thickness to be increased keep the magnets in compression. This is shown by the Pareto front boundary in Figure 8.15. As both cylinder thicknesses increase, the maximum rotor speed decreases, shown in Figures 8.16 and 8.18. Figure 8.18 also shows that as the middle cylinder thickness is decreased beyond 5 mm, the maximum operating speed begins to increase exponentially but the number of successful designs decrease. Much higher speeds are limited due to the increased centrifugal
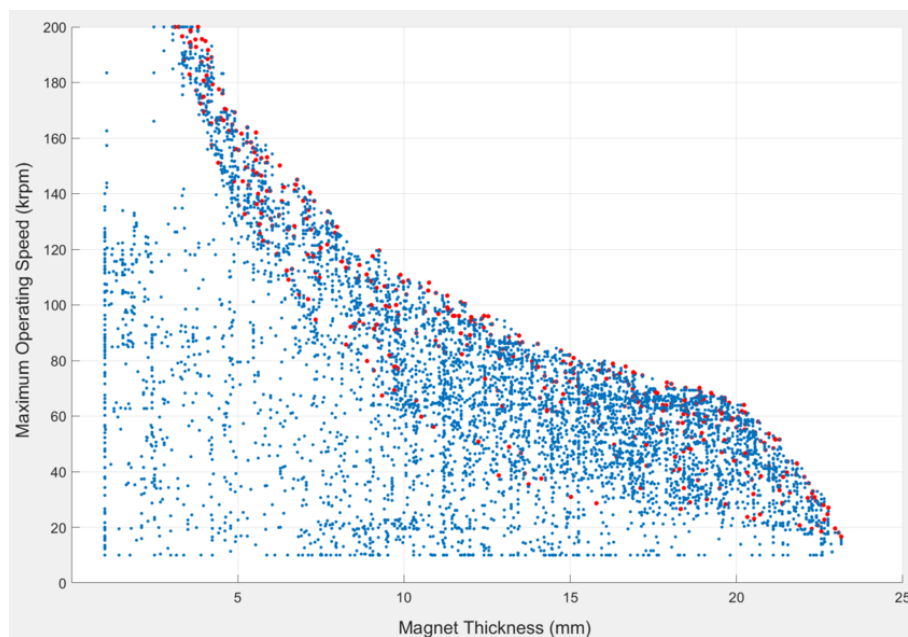
FIGURE 8.18: Magnet thickness versus operating speed in the feasible set from the optimisation run.

forces causing constraints to be broken. Increased centrifugal forces increase the risk of breaking a range of constraints imposed on the rotor. The stresses generated within the rotor will be higher, increasing the risk of exceeding the Von Mises yield stress limits. Excessive centrifugal forces will also attempt to pull the rotor apart, reducing the contact pressure between cylinders. This reduces the retaining pressure from the sleeve and therefore increases the risk that the magnets will go into tensions. To alleviate the risk of breaking these constraints, a slower operating speed is required to reduce the centrifugal forces.

As the magnet thickness becomes thinner than circa 3 mm, very few designs are produced over 140 krpm, but some designs show possible topologies can be found in that region. This is due to the highest speeds being attainable only when the sleeve and the magnet thicknesses are minimal because the centrifugal forces will be lower. Therefore, the range to identify potential designs is much narrower. The design variable constraint for the maximum operating speed limited the analysis and the Pareto set may have extended to higher speeds with magnets thinner than 3 mm. However, as discussed, the number of potential designs found in this region was rapidly decreasing.

8.4.2 Optimised Designs Comparison

Table 8.4 shows the design parameters of the two optimised designs selected for comparison, while Figure 8.19 shows the Pareto set with the two designs labelled *1* and *2*.

Design Variable	Optimised Design 1	Optimised Design 2
Inner radius of inner cylinder (mm)	3	3
Inner cylinder thickness (mm)	1	1
Middle cylinder thickness (mm)	4.65	18.44
Outer cylinder thickness (mm)	1.32	3.39
Inner/middle cylinder interference (mm)	0.001	0.001
Middle/outer cylinder interference (mm)	0.063	0.16
Maximum operating speed (rpm)	170299	65658
Maximum temperature elevation (^{o}C)	2.17	0

TABLE 8.4: Optimised designs parameters.
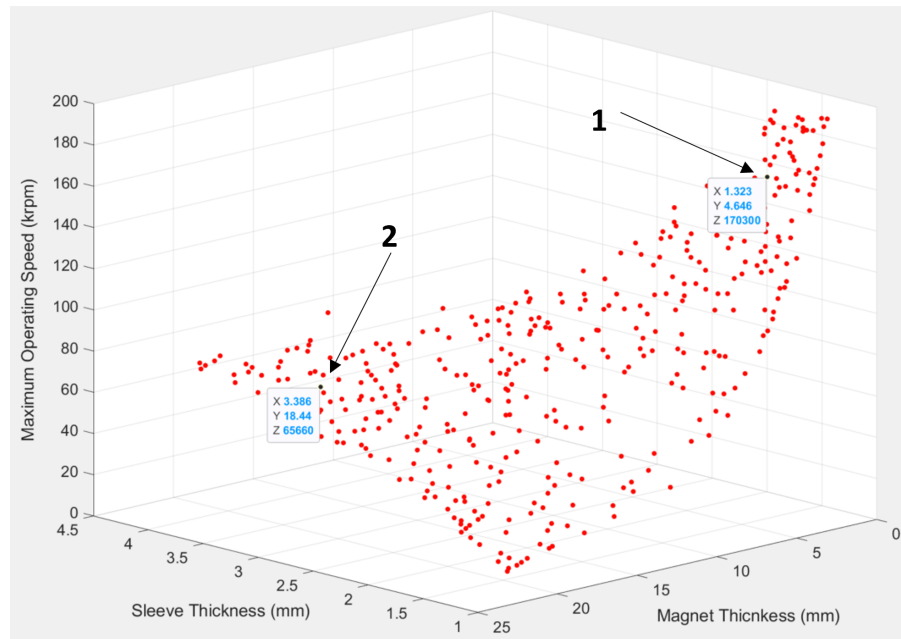
FIGURE 8.19: Optimised designs selected for comparison.

Design 2 has a thick magnet at the expense of sleeve thickness and rotor speed, whereas Design 1 has a much higher maximum operating speed at the expense of magnet thickness. The sleeve thickness of Design 1 is lower than Design 2 but is relatively thick when compared to the middle cylinder. Design 2 requires a much larger interference at the sleeve to maintain contact pressure and compression of the magnets due to the higher centrifugal forces caused by the thicker rotor dimensions.

Despite the rotor designs being at opposite sides of the Pareto set, there are similarities between the designs. Both designs require the minimum inner cylinder thickness, and the minimum interference with the inner cylinder. Figure 8.20 shows the feasible and Pareto set plotted against the interference at the inner cylinder on the *z*-axis rather than operating speed. Almost all feasible designs have the lowest possible interference at the inner cylinder even though there are many different rotor topologies that can achieve a wide range of operating speeds.

When the rotor operates, the interference at the sleeve will be the first to lose contact pressure due to centrifugal forces. Therefore, if the interference at the inner cylinder only affects the material yield stress constraints, then minimising this value will be optimum to keep stresses as low as possible so a higher speed can be achieved.
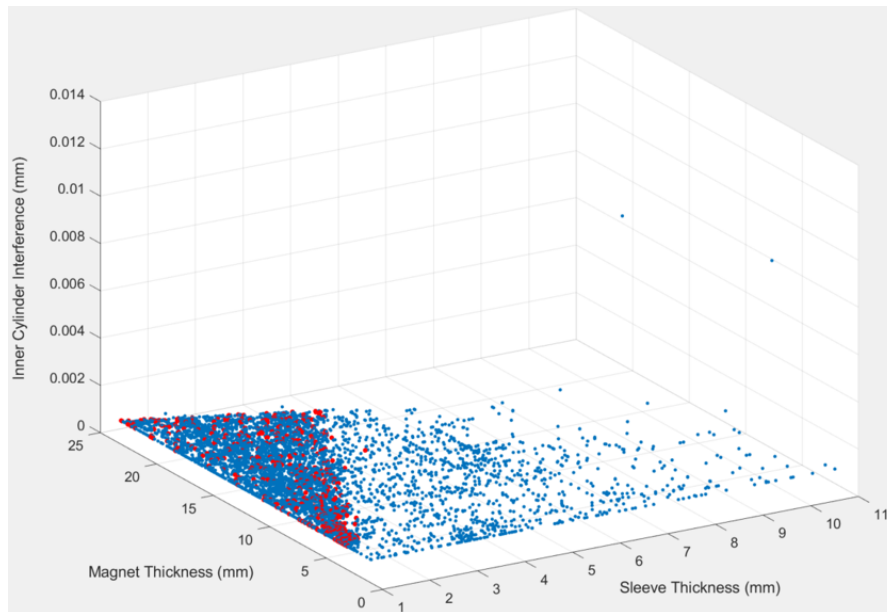
FIGURE 8.20: Feasible set inner cylinder interference.

Figure 8.21 shows the feasible and Pareto set plotted against the inner cylinder thickness on the *z*-axis. This shows that almost all optimal designs have a near minimal thickness for the inner cylinder, approaching a value of 1 mm when the design variable range was specified as 1 mm to 40 mm, as shown in Table 8.2. Feasible designs are achieved with thicker inner cylinders; however they are less frequent and not optimal.
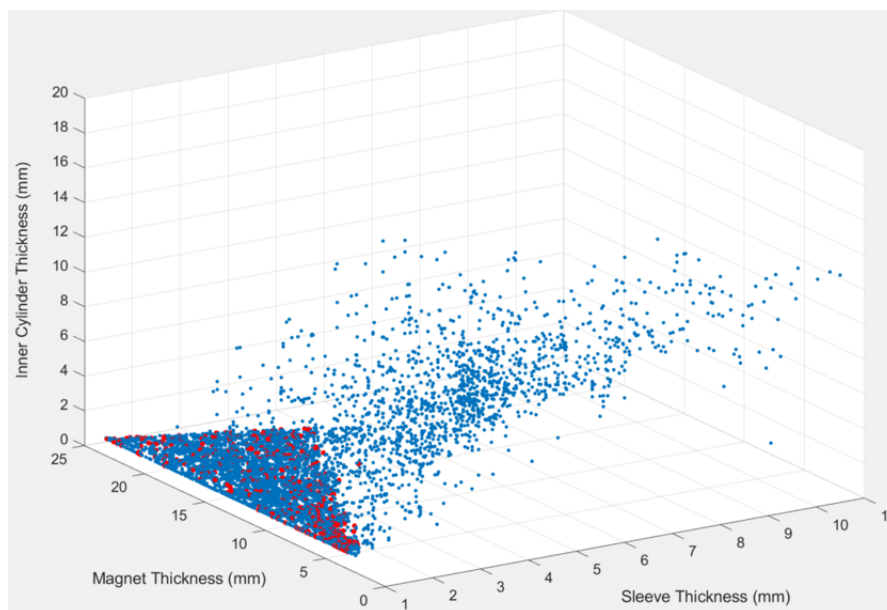
FIGURE 8.21: Feasible set inner cylinder thickness.

Due to the optimisation criteria, minimising the inner cylinder thickness enables the magnet thickness to be maximised. It also enables a higher speed to be achieved before constraints are broken as the centrifugal forces from the inner cylinder rotation are minimised. Both the interference and thickness of the inner cylinder have been limited by the design variable limits outlined in Table 8.2. However, it is important to remember that without the minimum limits, the optimised designs may minimise these features until they are unrealistic to manufacture. Therefore, sensible limits must be imposed to ensure feasible designs are produced by the optimisation tool.

8.4.3   Case Scenario for an Optimised Design

To confirm that the optimisation model produces successful rotor designs, FEA simulations can be carried out to verify the results. However, as discussed in Chapter 5, the generalised plane strain theory is relevant for the axial mid-point of the rotor. The theory does not account for the behaviour at the ends of the rotor, which were found to separate prior to the theory predicting separation at the centre of the rotor. As the rotor designs from the Pareto front are optimal, and a criterion was set to maximise the operating speed, the rotors produced will separate at the ends when simulated by the FEA, affecting the results throughout the rotor. Therefore, the rotor will be simulated at the maximum speed where the ends of the rotor do not separate. For Design 1 of the optimised rotors identified in Table 8.4 this was found to be 145 krpm , while Design 2 required a reduction to 50 krpm. The rotors were modelled as long rotors to minimise the impact from the unaccounted end-effect. The same FEA process used in Chapter 5 was used to complete the optimised rotor validations. Tables 8.5 and 8.6 show the GPS results predicted using the theoretical equations for the Design 1 and Design 2 rotor topologies.

The GPS predicted results show that the optimised design meets the constraints from Sections 8.3.8 and 8.3.9, specified during the optimisation process. Across all operating conditions the rotors maintain contact pressure between all cylinders, whilst ensuring the magnets remain in compression and the allowable stress limit was not exceeded for each cylinder. This shows that the optimisation process has

Stress	$\omega(0krpm)$ $\Delta T(0^oC)$	$\omega(0krpm)$ $\Delta T(2.17^oC)$	$\omega(145krpm)$ $\Delta T(0^oC)$	$\omega(145krpm)$ $\Delta T(2.17^oC)$
S_1	80.72	81.19	51.59	52.07
S_2	115.2	115	106.1	106
$\sigma_{\theta mc}$	-166	-164.8	-76.55	-75.44
$\sigma_{\theta md}$	-132.8	-132.3	-89.53	-89.04
σ_{VMii}	316.8	318.4	178.2	180.2
σ_{VMic}	188.3	189	101.8	103
σ_{VMmc}	84.45	83.45	23.7	22.32
σ_{VMmd}	44.76	44.98	15.23	15.66
σ_{VMod}	807.3	806.3	831.9	830.9
σ_{VMoo}	619.5	618.8	643.2	642.5

TABLE 8.5: Design 1 - Optimised rotor GPS results.

Stress (MPa)	$\omega(0krpm)$ $\Delta T(0^oC)$	$\omega(50krpm)$ $\Delta T(0^oC)$
S_1	76.16	48.87
S_2	114.2	106.4
$\sigma_{\theta mc}$	-154.7	-81.32
$\sigma_{\theta md}$	-116.7	-89.74
σ_{VMii}	304.8	190.8
σ_{VMic}	175.3	107
σ_{VMmc}	78.27	28.26
σ_{VMmd}	38.73	20.23
σ_{VMod}	809.7	824.1
σ_{VMoo}	614.5	629.2

TABLE 8.6: Design 2 - Optimised rotor GPS results.

been successfully applied. As Design 2 was not subject to any temperature eleva-
tion, only two operating conditions were required, shown in Table 8.6. To further
validate that the rotor optimisation had been successful, FEA was carried out on
the chosen optimised rotor design. For Design 1, Table 8.7 shows the GPS results
from Table 8.5, compared to the corresponding FEA simulation results. For Design
2, Table 8.8 shows the results from Table 8.6 compared to the FEA results.

Observing the results which are relevant to the optimisation constraints, the dif-
ference between the FEA results and the GPS results does not exceed 5% for either
design. 60% of the measured results remain within a 2% difference for Design 1,
while Design 2 achieves 90% within 2% of the FEA. These results align with the cor-
responding percentage difference results shown in Chapter 5 for thin, long cylinders

using the GPS theory. Therefore, the optimisation process successfully produces optimised rotor designs that meet the specified criteria and have been verified via FEA simulations.

Stress	$\omega(0krpm)$ $\Delta T(0^oC)$	$\omega(0krpm)$ $\Delta T(2.17^oC)$	$\omega(145krpm)$ $\Delta T(0^oC)$	$\omega(145krpm)$ $\Delta T(2.17^oC)$
S_1	1.00	0.99	1.71	1.69
S_2	0.51	0.51	0.69	0.69
$\sigma_{\theta mc}$	1.65	1.65	3.22	3.26
$\sigma_{\theta md}$	1.25	1.25	2.14	2.15
σ_{VMii}	3.06	3.05	3.89	3.85
σ_{VMic}	0.10	0.11	0.19	0.15
σ_{VMmc}	3.08	3.11	3.68	3.76
σ_{VMmd}	3.40	3.38	4.59	4.55
σ_{VMod}	0.61	0.61	0.62	0.62
σ_{VMoo}	0.85	0.84	0.80	0.80

TABLE 8.7: Design 1 - Optimised rotor GPS results compared to FEA.

Stress	$\omega(0krpm)$ $\Delta T(0^oC)$	$\omega(50krpm)$ $\Delta T(0^oC)$
S_1	0.84	1.07
S_2	0.48	0.61
$\sigma_{\theta mc}$	1.08	1.79
$\sigma_{\theta md}$	0.38	0.61
σ_{VMii}	0.64	0.85
σ_{VMic}	0.93	1.03
σ_{VMmc}	1.58	2.38
σ_{VMmd}	1.03	4.47
σ_{VMod}	0.38	0.38
σ_{VMoo}	0.21	0.22

TABLE 8.8: Design 2 - Optimised rotor GPS results compared to FEA.

8.5 Summary

Based on the work completed in this chapter, the development of the optimisation tool was considered a success. The rotor designs produced were shown to operate with the constraints and were aligned with the FEA results. The key outcomes of this chapter are listed below, enabling conclusions to be drawn regarding the overall success of the project and any potential further work required beyond the end of the project.

- The requirement for an optimisation tool was identified as the rotor design process used in Chapter 6 was inefficient and did not discover the optimal rotor design.

- Current literature centred around optimising the electromagnetic performance of permanent magnet rotors, while little consideration was given to the mechanical performance.

- Most of the literature exploring mechanical optimisation of rotors focussed on a single criterion, produced one optimal design .

- Specifying multiple criteria enables the user to have more customisation of the optimisation process to be able to suit their needs.

- Robust optimisation was under investigated in the current literature, meaning some papers produced optimised design that may not have been feasible to manufacture.

- NSGA-II was identified as a simple optimisation evolutionary algorithm that had the capability to specify multiple criteria and produce a Pareto optimal set.

- A NSGA-II code, composed in MatLab, was utilised with the GPS theory derived in Chapter 4, to produce a robust, multi-criteria optimisation tool for three-cylinder compound rotors.

- The feasible set was extracted to show the range of possible rotor topologies that would meet the specified constraints.

- From the feasible set, a Pareto set was identified providing users with many optimised rotor designs that could be selected from, to best fit their specific requirements.

- The criteria specified for the example rotor caused the inner cylinder thickness and interference to be minimised, highlighting the importance of realistic design variable constraints to ensure optimised designs remain feasible.

- Optimised design dimensions were input into the GPS theory to validate the rotor was operating within the optimisation constraints.

- FEA validated the success of the optimised rotor designs as all GPS results were within 5% of the FEA and aligned with the corresponding results in Chapter 5 for long, thin rotors.

9 Conclusion

9.1 Introduction

After the development and testing of the optimisation tool in Chapter 8, conclusions can be drawn regarding the overall success of the project and any significant achievements. This chapter will explore the results of the project and the contributions to knowledge, before outlining the further work that has arisen from this project.

9.2 Results Summary

Three-layered surface-mounted permanent magnet (SPM) rotors were identified in Chapter 1 as the most suitable configuration for high-speed electric machines (HSEMs). However, the permanent magnets (PMs) are sintered rare earth magnets and are therefore weak in tension. Accurate stress analysis of high-speed rotors was identified as critical due to the fragile nature of the permanent magnets. To achieve this, the project aim was outlined as to develop an efficient methodology of accurately predicting high-speed SPM rotor stresses to enable the selection of an optimal rotor design based on a variety of design parameters. Following the project methodology and structure outlined in Chapter 1, the project conclusions were:

After reviewing the current state of literature regarding closed form analysis techniques for calculating SPM rotor stresses, gaps in the knowledge were identified. Thin cylinder theory, plane stress, plane strain, and generalised plane strain (GPS) were the theoretical models used. GPS was identified as the most realistic model regarding rotor behaviour while the other models made incorrect assumptions. Almost all existing research focussed on two-cylinder rotors, leaving a major knowledge gap in exploring three-cylinder rotor stresses. However, plane strain and GPS theory were also vastly under-explored for two-cylinder rotors. Therefore, deeper investigation was required between all theories for SPM rotors.

When exploring the finite element analysis (FEA) methodologies used in the literature, the approaches applied were 2D, axisymmetric, and 3D models. 2D axial section models were most used, however axisymmetric models were identified as suitable for compound rotor analysis. When the magnets are held in compression, the rotor does not experience stress changes in the circumferential direction. Therefore, for functional rotors, axisymmetric models should provide the same results as a 2D axial section whilst also enabling the exploration of axial stress changes and being much more efficient than 3D models. However, axisymmetric FEA models were considerably under-explored with only three sources using them, and only one justifying their use. There were no papers that used axisymmetric FEA models for three-cylinder rotors, thus leaving a substantial gap in the existing knowledge, to be investigated.

It was identified in the literature that the mechanical aspect of rotor design was of little focus during experimental testing and the current extent of rotor testing was limited to using a pass or fail criteria based on test success. There was no investigation into identifying rotor stresses through testing which could then be used to verify FEA and theoretical models. Therefore, there was a large knowledge gap to fill by identifying a testing technique to extract mechanical results, enabling much deeper analysis.

Regarding experimental rotor testing, most papers focussed on the electromagnetic performance of a rotor, however test simplification was possible when focussing on mechanical design. Simpler air handling devices could be used to power the test rig instead of HSEMs and it was identified that alternative materials could be used to replace fragile sintered PMs. Shrink-fitting cylinders was deemed the most suitable rotor assembly method to avoid stressing components during a press-fit procedure. Digital image correlation (DIC) was also identified as the ideal measuring technique due to it providing a whole surface analysis and requiring no parts in contact with a high-speed rotor, reducing testing complexities.

The literature showed that an optimisation process could be applied to engineering design and allow the user to define design variables, constraints, and criteria to identify a set of optimal designs. However, the optimisation of the mechanical performance of an SPM rotor had limited exploration. Furthermore, only one criterion

was typically used with only one optimal design produced. It was identified that using multiple criteria and producing multiple optimal designs would ensure the results could be more tailored to the user's requirements. Therefore, there was a gap in the knowledge to explore multi-criteria optimisation for the mechanical design of an SPM rotor.

Non-dominated Superiority Genetic Algorithm-II (NSGA-II) is a multi-criteria evolutionary algorithm (MCEA) that was recognised as a popular optimisation method due to its simplicity and superiority over other methods. Robust optimisation was also identified as an important concept to produce optimal designs that could still operate successfully despite minor variations caused by factors such as the manufacturing procedure. Therefore, the development of an efficient NSGA-II optimisation tool for three-cylinder SPM rotor design required investigating.

Following on from the closed form analysis findings discussed earlier, Chapter 3 explored the differences between the theories. The theoretical fundamentals were explored and found that thick cylinder theory was more accurate than thin cylinder approximation by correctly including stress changes through the cylinder wall. For plane stress, plane strain and GPS, preliminary results showed major differences between the theories at speed despite similar results when the rotor was stationary. Due to the significant differences, all theories were investigated for three-cylinder SPM rotors.

Chapter 4 explored plane stress, plane strain, and GPS theories for three-cylinder SPM rotors. The derivation of the theory was detailed for each methodology, leading to novel equations for plane strain and GPS approaches. Comparisons were made with the established two-cylinder equations of each theory, by simulating a two-cylinder rotor within the three-cylinder equations. The results differences were negligible proving that the three-cylinder equations for each methodology were derived correctly. Any differences found between the two- and three-cylinder equations were shown to be caused by the two-cylinder equations using a common radius at interfering locations.

After identifying the knowledge gap regarding axisymmetric FEA simulations for SPM rotors, Chapter 5 showed that SPM rotor behaviour was axisymmetric while the magnets were held in compression. It was demonstrated that once the magnets

are no longer held in compression, the rotor will fail, therefore SPM rotors behave axisymmetric when operating successfully. Axisymmetric FEA models were therefore used to assess and validate the accuracy of the three-cylinder theoretical models. Using axisymmetric FEA models, the assumptions made by the plane strain and plane stress models were shown to be incorrect while the GPS assumptions were justified.

Chapter 5 compared the three-cylinder theories against verified FEA models. For long rotors, plane stress and plain strain theory results were compromised with significant differences, but the GPS theory remained accurate across all operating conditions with over 93% of results within 3% of the FEA results. However, this was relevant for most of the rotor length away from the rotor ends. It was found that at the rotor ends, there is a loss of axial load transfer between the cylinders due to slip, eliminating the state of GPS and distorting the results in that region. For short rotors, this effect consumed the length of the rotor causing significant differences between the FEA and all three theoretical models. Therefore, the GPS theory was verified as accurate and reliable across all operating conditions for long rotors, where the rotor operates in a state of GPS away from the rotor ends. Verifying the accuracy of the GPS theory enabled the possibility of efficient optimised rotor design using the theory.

As discussed earlier, the literature exposed a knowledge gap for experimental testing to be used to verify theoretical stress predictions. After exploring the existing testing methodologies, Chapter 6 detailed a test rig design that could be used to extract strain results from a test SPM rotor using DIC. This enabled the calculation of stresses that could be compared to FEA and theoretical calculations. The design process of a three-cylinder SPM rotor to use within the test rig, was also shown. It was shown that rotor design constraints are conflicting, and the process of producing a suitable test rotor was slow with no guarantee of identifying an optimal design. This highlighted the need for an efficient optimisation tool to identify optimal rotor designs.

Chapter 7 showed the testing process for the test rotor and test rig designed in Chapter 6. Despite procedural changes, the testing showed that the test rig design

was a successful concept and could be used with DIC to extract strain results at high-speed with improvements of the bearing system. Strain results due to interference were extracted using DIC from the designed test SPM rotor. However, there were large fluctuations across the strain maps produced during the interference testing caused by the build-up of condensation and a potentially sub-optimal speckle pattern. Therefore, it was difficult to extract reliable results. However, results based on median values across the strain maps were shown to prospectively align with the corresponding rotor FEA simulation, adding potential validity to the accuracy of the GPS theory. This indicated that the theory was suitable to use in the development of an efficient optimisation tool for three-cylinder SPM rotor design.

Following the knowledge gap exposed in the literature, Chapter 8 detailed the development of a multi-criteria optimisation tool for SPM rotor design that was based on the GPS theory developed in Chapter 4. The verified GPS theory and optimisation parameters were developed in MatLab and were designed to interact with an externally sourced NSGA-II code to produce an optimisation tool for three-cylinder SPM rotor design. The optimisation tool provided an unrestricted number of criteria, design variables, and constraints to use, making it highly adaptable to the user's needs. The optimisation tool successfully produced a Pareto set of rotor designs, providing the user with further freedom to select from a large range of optimal designs to best fit their specific requirements. Sampled designs from the Pareto set were then verified against theoretical and FEA simulations to show the optimisation tool produce reliable and accurate results. Therefore, an efficient optimisation too for three-cylinder SPM rotor design had been successfully produced.

9.3 Achievement of Project Objectives & Contributions to Knowledge

The project objectives were outlined in in Section 1.3. Based on the conclusions drawn in Section 9.2, the achievement of project objectives and the contribution to knowledge from the project can be assessed.

As discussed in Section 9.2, theoretical stress calculations for three-cylinder SPM rotor were derived using plane stress, plane strain, and GPS assumptions, achieving

the first objective. For the plane strain and GPS theories, this provided a significant contribution to existing knowledge as three-cylinder calculations had not been derived before.

Chapters 3 and 5 explored the differences between the plane stress, plane strain, and GPS theories. Chapter 3 explored the differences between the theories when applied to a two-cylinder SPM rotor, which was an expansion of the work published by Barrans and Mallin [153]. Chapter 5 compared how each theory for three-cylinder SPM rotors performed against FEA simulations. Both chapters completed comparisons across a range of rotor topologies, achieving the second objective. As the plane strain and GPS stress equations were novel, the comparisons between the theories in Chapter 5 were also novel. The results provide a significant contribution to the existing knowledge of rotor stress analysis methods and highlight substantial benefits to using the GPS methodology.

In Chapter 5 it was proven that three-cylinder SPM rotors behave axisymmetric when operating successfully. Axisymmetric FEA studies for multiple across topologies and operating conditions were then successfully produced and compared against theoretical models, achieving the third objective. Completing three-cylinder axisymmetric FEA studies was a significant contribution to knowledge as no papers had explored this before. It improved on the typical FEA models used in the literature by enabling the analysis of stress changes along the axis.

Chapter 6 showed the development of a test rig design for high-speed, three-cylinder rotor testing. The rig utilised the turbine housing and the shaft and rotor wheel assembly from a sourced turbocharger. However, it was adapted via a new bearing housing design which was designed with a pocket to accommodate a three-cylinder SPM rotor and enable DIC measurements by ensuring the rotor was visible. Therefore, the fourth objective was achieved, and the novelty of the design contributed to the existing knowledge. The test rig design provides a method of identify rotor stresses, something which was not attempted in the literature.

The outer diameter of the three-cylinder rotor designed in Chapter 6 was shown to fit within the bearing housing pocket of the test rig. The rotor was successfully designed to produce enough outer surface strain and remain together at high-speed,

while alternative rotor materials were identified to avoid using weak sintered permanent magnets (PMs), reducing testing complexities. Chapter 7 demonstrated that the rotor design was also successfully shrink-fit and therefore met the requirements of the fifth project objective.

Due to the high-speed testing being removed from the project scope, that part of the sixth objective was not achieved. However, all other aspects of the project objective were achieved. Despite reliability challenges, Chapter 7 shows stationary testing results being extracted using DIC. The thermal effects were eliminated from the strain readings, revealing the prospective outer surface strain due to interference. When compared against an FEA simulation good accuracy was shown, indicating that the GPS theory can be applied to physical three-cylinder SPM rotors. This was a significant contribution to knowledge as it demonstrated the potential for rotor stresses to be identified and used to verify the success of a rotor test, FEA simulation, or theoretical analysis, which had not been completed before.

Chapter 8 outlines the development of a multi-criteria optimisation tool in MatLab, based on the NSGA-II evolutionary algorithm. Multiple criteria, design variables, and constraints can be set within the optimisation tool based on the user's specific requirements, achieving the seventh project objective. The optimisation produces a Pareto set of rotor designs for the user select from. Chapter 8 also compares GPS results for optimal rotor designs against corresponding axisymmetric FEA studies. The results were accurate and aligned with those found in Chapter 5, therefore verifying the success of the optimisation tool, and achieving the final project objective.

The optimisation tool provides a novel, proven, and efficient methodology of accurately predicting high-speed rotor stresses and enables the selection of optimal rotor designs based on a range of design parameters. Chapter 6 identified the difficulties of designing a successful three-cylinder SPM rotor, whilst not achieving an optimal result. The optimisation solves that problem and combines novel GPS theory to produce accurate results much more efficiently than FEA simulations. Therefore, the optimisation tool is a substantial contribution to the field of rotor stress predictions and demonstrates that the overall aim of this project from Section 1.2, has been achieved.

Overall, the project methodology and objectives outlined in Chapter 1 formed a successful plan for the project. It enabled multiple both theoretical and experimental validation for the novel stress analysis theory developed in Chapter 4. The optimisation tool then demonstrated the value of the novel theory and how it would be applied by engineers to a range of rotor design problems. The development of the novel theory was verified with respect to the assumptions used and any aspects outside of these assumptions were significant bodies of work and suitably designated as further work outside of this project. Similarly with the FEA, the simulation results were produced for a significant range of rotor topologies and used to validate the results produced by the novel theory. Possible work arising from identification of the end-effect was regarded as further work due to the significant amount of work required to investigate the phenomenon.

The experimental testing aspect of the project resulted in the only unachieved objective and therefore improvements could have been made. During the project it was decided that the high-speed DIC testing would fall outside of the scope of the project due to the added workload that would be required. However, the expectation of this test still drove the design of the test rig presented in Chapter 6. Had the decision to eliminate this aspect of experimental testing been decided earlier in the project then the design requirements for the test rig would have been less restrictive. Therefore, the final test rig design may have been much simpler and allowed more time for experimental testing. This would have improved the depth of the experimental results as due to facility closures and complications arising from the 2020 coronavirus pandemic, the experimental testing could not be completed to the planned depth.

The development of the optimisation tool in Chapter 8 was successful and demonstrated the advantage it provides engineers to complex SPM rotor design problems. The potential for expansion of this tools is significant to achieve complete robustness and was correctly designated as further work. However, aspects of robust optimisation were successfully developed and demonstrated, providing strong results for this project.

9.4   Future Work

Proceeding this project, further work avenues should be explored to expand on the project findings and produce further contributions to knowledge.

The GPS theory is currently only suitable for isotropic materials; therefore, the theory should be further developed to incorporate anisotropic materials. As discussed in Section 2.5.3, carbon fibre wire wrapped sleeves can be used instead of shrink-fit metallic sleeves. The existing GPS theory developed in this project would not be applicable for a carbon fibre wire-wrapped sleeve as the material is anisotropic.

As identified in Chapter 5, an end-effect occurs at the rotor ends during operation which renders the GPS theory inapplicable at that region. Therefore, further investigation is required into the stress changes at the rotor ends to enable accurate prediction of rotor stresses across the whole rotor length.

As discussed in Chapter 7, it was decided that high-speed DIC testing would fall outside the scope of this project due to the increase in workload required. Therefore, DIC testing was only performed at stationary. Further DIC testing is required at high-speed which will use the DIC strobe light addition to identify rotor stresses during operation and add further verification to the accuracy of the GPS theory. While the ability to use DIC to extract rotor strain results was proven, further investigation and optimisation of the DIC process is required to increase the reliability and accuracy of the results produced.

The test rig designed in Chapter 6 was demonstrated to operate, validating the design concept. However, further design iterations are required to improve the bearing system, allowing higher speeds to be achieved. This will then enable high-speed DIC testing of the SPM rotor.

The optimisation tool developed in Chapter 8 explored robust optimisation and incorporated machining tolerances into the process to ensure optimal rotor designs would remain successful despite variation in dimensions due to the machining process. However, as discussed in Section 2.4.3, there are more sources of error than machining tolerances and further exploration into robust optimisation is required to enable the expansion of the optimisation tool. This could include incorporating

rotor parameter uncertainty to allow for a Monte Carlo approach, with a view to achieving a completely robust optimisation process for three-cylinder SPM rotors.

9.5 Summary

Overall, based on the conclusions drawn in this chapter, the project aim from Section 1.2 was achieved. The methodology outlined in Section 1.2 was followed and was proved to be successful. Only one of the objectives from Section 1.3 was not achieved, however this did not impact upon the success of the project and the contents of the objective was listed as further work arising from the project. Therefore, the core plan and outcomes of the project can be considered a success.

References

[1] A. Tenconi, S. Vaschetto, and A. Vigliani, "Electrical machines for high-speed applications: Design considerations and tradeoffs," *IEEE Transactions on Industrial Electronics*, vol. 61, no. 6, pp. 3022–3029, 2014.

[2] M. Rahman, A. Chiba, and T. Fukao, "Super high speed electrical machines - summary," in *IEEE Power Engineering Society General Meeting*, vol. 2. IEEE, 2004, Conference Proceedings, pp. 1272–1275.

[3] H. Fang, R. Qu, J. Li, P. Zhang, and X. Fan, "Rotor design for high-speed high-power permanent-magnet synchronous machines," *IEEE Transactions on Industry Applications*, vol. 53, no. 4, pp. 3411–3419, 2017.

[4] S. Li and B. Sarlioglu, "Assessment of high-speed multi-megawatt electric machines," in *Electric Machines and Drives Conference*. IEEE, 2015, Conference Proceedings, pp. 1573–1579.

[5] Z. Kolondzovski, A. Arkkio, J. Larjola, and P. Sallinen, "Power limits of high-speed permanent-magnet electrical machines for compressor applications," *IEEE Transactions on Energy Conversion*, vol. 26, no. 1, pp. 73–82, 2011.

[6] K. Laskaris and A. Kladas, "High torque internal permanent magnet wheel motor for electric traction applications," in *2008 18th International Conference on Electrical Machines*. IEEE, 2008, Conference Proceedings, pp. 1–4.

[7] R. Keller, E. Mese, and J. Maguire, "Integrated system for electrical generation and boosting (isgb)," in *International Conference on Electrical Machines and Systems (ICEMS)*. IEEE, 2014, Conference Proceedings, pp. 2567–2572.

[8] C. Gerada, A. Boglietti, and A. Cavagnino, "High-speed electrical machines and drives," *IEEE Transactions on Industrial Electronics*, vol. 61, no. 6, pp. 2943–2945, 2014.

[9] D. Gerada, A. Mebarki, N. Brown, C. Gerada, A. Cavagnino, and A. Boglietti, "High-speed electrical machines: Technologies, trends and developments." *IEEE Transactions on Industrial Electronics*, vol. 61, no. 6, pp. 2946–2959, 2014.

[10] S. Barrans, M. Al-Ani, and J. Carter, "Mechanical design of rotors for permanent magnet high-speed electric motors for turbocharger applications," *IET Electrical Systems in Transportation*, vol. 7, no. 4, pp. 278–286, 2017.

[11] G. Burnand, D. Araujo, and Y. Perriard, "Very-high-speed permanent magnet motors: Mechanical rotor stresses analytical model," in *Electric Machines and Drives Conference*. IEEE, 2017, Conference Proceedings, pp. 1–7.

[12] C. Zwyssig, J. Kolar, and S. Round, "Megaspeed drive systems: Pushing beyond 1 million r/min," *IEEE/ASME Transactions on Mechatronics*, vol. 14, no. 5, pp. 564–574, 2009.

[13] P. Tsao, M. Senesky, and S. Sanders, "An integrated flywheel energy storage system with homopolar inductor motor/generator and high-frequency drive," *IEEE Transactions on Industry Applications*, vol. 39, no. 6, pp. 1710–1725, 2003.

[14] P. Tsao, "An integrated flywheel energy storage system with homopolar inductor motor/generator and high-frequency drive," PhD Thesis, University of California, Berkeley, CA, 2003.

[15] W. Lee, E. Schubert, Y. Li, S. Li, D. Bobba, and B. Sarlioglu, "Overview of electric turbocharger and supercharger for downsized internal combustion engines," *IEEE Transactions on Transportation Electrification*, vol. 3, no. 1, p. 12, 2016.

[16] N. Terdich and R. Martinez-Botas, "Experimental efficiency characterization of an electrically assisted turbocharger," in *11th International Conference on Engines & Vehicles*, no. 2013-24-0122. SAE International, 2013, Conference Proceedings.

[17] Continental, "Worldwide emission standards and related regulations," pp. 1–4, 2019. [Online]. Available: https://www.continental-automotive.com/getattachment/8f2dedad-b510-4672-a005-3156f77d1f85/EMISSIONBOOKLET_2019.pdf (accessed Apr. 04, 2022)

[18] I. Arsie, A. Cricchio, C. Pianese, M. De Cesare, and W. Nesci, "A comprehensive powertrain model to evaluate the benefits of electric turbo compound (etc) in reducing co2 emissions from small diesel passenger cars," *SAE Technical Paper*, no. 2014-01-1650, 2014.

[19] W. Gis and J. Merkisz, "The development status of electric (bev) and hydrogen (fcev) passenger cars park in the world and new research possibilities of these cars in real traffic conditions," *Combustion Engines*, vol. 58, no. 3, pp. 144–149, 2019.

[20] European Commision, "Reducing co2 emissions from heavy-duty vehicles," 2019. [Online]. Available: https://ec.europa.eu/clima/eu-action/transport-emissions/road-transport-reducing-co2-emissions-vehicles/reducing-co2-emissions-heavy-duty-vehicles_en (accessed Apr. 04, 2022)

[21] E. Çabukoglu, G. Georges, L. Küng, G. Pareschi, and K. Boulouchos, "Battery electric propulsion: An option for heavy-duty vehicles? results from a swiss case-study," *Transportation Research Part C: Emerging Technologies*, vol. 88, pp. 107–123, 2018.

[22] J. Merkisz, P. Lijewski, P. Fuc, M. Siedlecki, and A. Ziolkowski, "Development of the methodology of exhaust emissions measurement under rde (real driving emissions) conditions for non-road mobile machinery (nrmm) vehicles," in *IOP Conference Series: Materials Science and Engineering*, vol. 148, no. 012077. IOP, 2016, Conference Proceedings.

[23] UK Government, "Non-road mobile machinery (nrmm) practical guide," pp. 4–6, 2017. [Online]. Available: https://www.lambeth.gov.uk/sites/default/files/cs-nrmm-practical-guide.pdf (accessed Apr. 06, 2022)

[24] A. Borisavljevic, H. Polinder, and J. Ferreira, "Enclosure design for a high-speed permanent magnet rotor," in *Power Electronics, Machines and Drives*. IET, 2010, Conference Proceedings, pp. 1–6.

[25] A. Binder, T. Schneider, and M. Klohr, "Fixation of buried and surface-mounted magnets in high-speed permanent-magnet synchronous machines," *IEEE Transactions on Industry Applications*, vol. 42, no. 4, pp. 1031–1037, 2006.

[26] J. Gieras, "Design of permanent magnet brushless motors for high speed applications," in *International Conference on Electrical Machines and Systems*. IEEE, 2014, Conference Proceedings, pp. 1–16.

[27] D. Smith, B. Mecrow, G. Atkinson, A. Jack, and A. Mehna, "Shear stress concentrations in permanent magnet rotor sleeves," in *International Conference on Electrical Machines*. IEEE, 2010, Conference Proceedings, pp. 1–6.

[28] L. Mallin and S. Barrans, "A review of the high-speed permanent magnet rotor stress analysis used for automotive air-handling machines," *European Journal of Engineering Research and Science*, vol. 5, no. 4, pp. 448–456, 2020.

[29] Wolfram Research Inc, "Closed-form solution," 2022. [Online]. Available: https://mathworld.wolfram.com/Closed-FormSolution.html (accessed Apr. 13, 2022)

[30] E. Hearn, "Mechanics of materials 2," ser. Mechanics of Materials. Oxford, UK: Butterworth-Heinemann, 1997, pp. 254–256.

[31] E. Hearn, "Mechanics of materials 2," ser. Mechanics of Materials. Oxford, UK: Butterworth-Heinemann, 1997, pp. 124–125.

[32] A. Kotousov and C. Wang, "Fundamental solutions for the generalised plane strain theory," *International Journal of Engineering Science*, vol. 40, no. 15, pp. 1775–1790, 2002.

[33] F. Zhang, G. Du, T. Wang, G. Liu, and W. Cao, "Rotor retaining sleeve design for a 1.12-mw high-speed pm machine," *IEEE Transactions on Industry Applications*, vol. 51, no. 5, pp. 3675–3685, 2015.

[34] D. Xu, X. Wang, and G. Li, "Optimization design of the sleeve for high speed permanent magnet machine," in *Industrial Electronics and Applications (ICIEA)*. IEEE, 2016, Conference Proceedings, pp. 2531–2535.

[35] K. Chen and C. Zhu, "Rotor strength analysis for high speed permanent magnet machines," in *International Conference on Electrical Machines and Systems (ICEMS)*. IEEE, 2014, Conference Proceedings, pp. 65–69.

[36] C. Zhu and L. Chen, "Rotor strength analysis for stator-permanent magnet machines," in *International Conference on Electrical Machines and Systems (ICEMS)*. IEEE, 2017, Conference Proceedings, pp. 1–6.

[37] L. Chen and C. Zhu, "Strength analysis for surface-mounted permanent magnet rotor in high-speed motor," *TELKOMNIKA Indonesian Journal of Electrical Engineering*, vol. 12, no. 10, pp. 7131–7142, 2014.

[38] W. Cheng, G. Xu, Y. Sun, H. Geng, and L. Yu, "Optimum design of ultra high speed hybrid rotor of pm machines," in *International Conference on Mechatronics and Automation*. IEEE, 2014, Conference Proceedings, pp. 1388–1393.

[39] T. Wang, F. Wang, H. Bai, and J. Xung, "Optimization design of rotor structure for high speed permanent magnet machines," in *International Conference on Electrical Machines and Systems (ICEMS)*. IEEE, 2007, Conference Proceedings, pp. 1438–1442.

[40] A. Borisavljevic, H. Polinder, and B. Ferreira, "Overcoming limits of high-speed pm machines," in *International Conference on Electrical Machines (ICEM)*. IEEE, 2008, Conference Proceedings, pp. 1–6.

[41] P. Pfister and Y. Perriard, "A 200 000 rpm, 2 kw slotless permanent magnet motor," in *International Conference on Electrical Machines and Systems*. IEEE, 2008, Conference Proceedings, pp. 3054–3059.

[42] A. Borisavljevic, H. Polinder, and J. Ferreira, "On the speed limits of permanent-magnet machines," *IEEE Transactions on Industrial Electronics*, vol. 57, no. 1, pp. 220–227, 2010.

[43] P. Pfister and Y. Perriard, "Very-high-speed slotless permanent-magnet motors: Analytical modeling, optimization, design, and torque measurement methods," *IEEE Transactions on Industrial Electronics*, vol. 57, no. 1, pp. 296–303, 2010.

[44] A. Gilson, F. Dubas, D. Depernet, and C. Espanet, "Comparison of high-speed pm machine topologies for electrically-assisted turbocharger applications," in *Electrical Machines and Systems (ICEMS)*. IEEE, 2016, Conference Proceedings, pp. 1–5.

[45] N. Uzhegov, E. Kurvinen, J. Nerg, J. Pyrhönen, J. Sopanen, and S. Shirinskii, "Multidisciplinary design process of a 6-slot 2-pole high-speed permanent-magnet synchronous machine," *IEEE Transactions on Industrial Electronics*, vol. 63, no. 2, pp. 784–795, 2016.

[46] D. Xu, X. Wang, and G. Li, "Design and test for high speed permanent magnet wind generator and research on rotor protection measures," in *Industrial Electronics and Applications (ICIEA)*. IEEE, 2016, Conference Proceedings, pp. 2026–2031.

[47] Y. Wan, S. Cui, S. Wu, L. Song, I. Milyaev, and S. Yuryevich, "Shock-resistance rotor design of a high-speed pmsm for integrated pulsed power system," *IEEE Transactions on Plasma Science*, vol. 45, no. 7, pp. 1399–1405, 2017.

[48] A. Damiano, A. Floris, G. Fois, M. Porru, and A. Serpi, "Modelling and design of pm retention sleeves for high-speed pm synchronous machines," in *Electric Drives Production Conference (EDPC)*. IEEE, 2016, Conference Proceedings, pp. 118–125.

[49] D. Gerada, A. Mebarki, R. Mokhadkar, and C. Gerada, "Design issues of high-speed permanent magnet machines for high-temperature applications," in *IEEE International Electric Machines and Drives Conference*. IEEE, 2009, Conference Proceedings, pp. 1036–1042.

[50] L. Papini, C. Gerada, D. Gerada, and A. Mebarki, "High speed solid rotor induction machine: Analysis and performances," in *International Conference on*

Electrical Machines and Systems (ICEMS).   IEEE, 2014, Conference Proceedings, pp. 2759–2765.

[51] J. Yon, P. Mellor, R. Wrobel, J. Booker, and S. Burrow, "Analysis of semipermeable containment sleeve technology for high-speed permanent magnet machines," *IEEE Transactions on Energy Conversion*, vol. 27, no. 3, pp. 646–653, 2012.

[52] Y. Zhou and J. Fang, "Strength analysis of enclosure for a high-speed permanent magnet rotor," *AASRI Procedia*, vol. 3, pp. 652–660, 2012.

[53] B. Riemer, M. Leßmann, and K. Hameyer, "Rotor design of a high-speed permanent magnet synchronous machine rating 100,000 rpm at 10kw," in *IEEE Energy Conversion Congress and Exposition*.   IEEE, 2010, Conference Proceedings, pp. 3978–3985.

[54] H. Czichos, *Grundlagen der Ingenieurwissenschaften*, ser. Hutte.   Berlin, Heidelberg: Springer Verlag, 1989.

[55] B. Varaticeanu, P. Minciunescu, and D. Fodorean, "Mechanical design and analysis of a permanent magnet rotors used in high-speed synchronous motor," *Electrotehnica, Electronica, Automatica*, vol. 62, no. 1, pp. 9–17, 2014.

[56] Z. Tao, Y. Xiaoting, Z. Huiping, and J. Hongyun, "Strength design on permanent magnet rotor in high speed motor using finite element method," *TELKOMNIKA Indonesian Journal of Electrical Engineering*, vol. 12, no. 2, pp. 1758–1763, 2014.

[57] Z. Huang and J. Fang, "Multiphysics design and optimization of high-speed permanent-magnet electrical machines for air blower applications," *IEEE Transactions on Industrial Electronics*, vol. 63, no. 5, pp. 2766–2774, 2016.

[58] G. Berardi, N. Bianchi, and D. Gasperini, "A high speed pm generator for an organic rankine cycle system," in *Electric Machines and Drives Conference (IEMDC)*.   IEEE, 2017, Conference Proceedings, pp. 1–8.

[59] J. Ahn, J. Choi, C. Park, C. Han, C. Kim, and T. Yoon, "Correlation between rotor vibration and mechanical stress in ultra-high-speed permanent magnet

synchronous motors," *IEEE Transactions on Magnetics*, vol. 53, no. 11, pp. 1–6, 2017.

[60] A. Thomas, Z. Zhu, and G. Jewll, "Comparison of flux switching and surface mounted permanent magnet generators for high-speed applications," in *Power Electronics, Machines and Drives (PEMD)*.   IET, 2011, Conference Proceedings, pp. 111–116.

[61] W. Fernando and C. Gerada, "High speed permanent magnet machine design with minimized stack-length under electromagnetic and mechanical constraints," *International Journal of Applied Electromagnetics and Mechanics*, vol. 46, no. 1, pp. 95–109, 2013.

[62] J. Luomi, C. Zwyssig, A. Looser, and J. Kolar, "Efficiency optimization of a 100-w, 500 000-rpm permanent-magnet machine including air friction losses," in *IEEE Industry Applications Conference*.   IEEE, 2007, Conference Proceedings, pp. 861–868.

[63] J. Luomi, C. Zwyssig, A. Looser, and J. Kolar, "Efficiency optimization of a 100-w 500 000-r/min permanent-magnet machine including air-friction losses," *IEEE Transactions on Industry Applications*, vol. 45, no. 4, pp. 1368–1377, 2009.

[64] C. Zwyssig and J. Kolar, "Design of a 100 w, 500000 rpm permanent-magnet generator for mesoscale gas turbines," in *Industry Applications Conference*, vol. 1.   IEEE, 2005, Conference Proceedings, pp. 253–260.

[65] S. Zhu, M. Cheng, and X. Sun, "Mechanical design of outer-rotor structure for dual mechanical port machine," in *Electrical Machines and Systems (ICEMS)*.   IEEE, 2011, Conference Proceedings, pp. 1–6.

[66] E. Schubert and B. Sarlioglu, "Mechanical design method for a high-speed surface permanent magnet rotor," in *IEEE Energy Conversion Congress and Exposition (ECCE)*, 2016, Conference Proceedings, pp. 1–6.

[67] H. Mitterhofer and W. Amrhein, "Design aspects and test results of a high speed bearingless drive," in *Power Electronics and Drive Systems (PEDS)*.   IEEE, 2011, Conference Proceedings, pp. 705–710.

[68] R. Benlamine, T. Hamiti, F. Vangraefschèpe, and D. Lhotellier, "Electromagnetic, mechanical and thermal analysis of a high-speed surface-mounted pm machine for automotive application," in *International Conference on Electrical Machines (ICEM)*. IEEE, 2016, Conference Proceedings, pp. 1662–1667.

[69] T. Wang, G. Du, Z. Yu, F. Zhang, and Z. Bai, "Design and develop of a mw direct drive highspeed permanent-magnet machine for compression," in *International Conference on Electrical Machines and Systems (ICEMS)*. IEEE, 2013, Conference Proceedings, pp. 892–895.

[70] H. Lahne, D. Gerling, S. D, and C. Y, "Design of a 50000 rpm high-speed high-power six-phase pmsm for use in aircraft applications," in *International Conference on Ecological Vehicles and Renewable Energies (EVER)*. IEEE, 2016, Conference Proceedings, pp. 1–11.

[71] J. Dong, Y. Huang, L. Jin, and H. Lin, "Comparative study of surface-mounted and interior permanent-magnet motors for high-speed applications," *IEEE Transactions on Applied Superconductivity*, vol. 26, no. 4, pp. 1–4, 2016.

[72] B. Su, F. Hossainzadeh, C. Truman, and D. Smith, "Residual stresses in machined and shrink-fitted assemblies," *International Centre for Diffraction Data*, pp. 675–682, 2009.

[73] M. Eifler, I. C. Garretson, B. S. Linke, J. Das, F. Torner, and J. Seewig, "Effects of vibratory finishing of 304 stainless steel samples on areal roughness parameters: A correlational analysis for anisotropy parameters," *Journal of Materials Processing Technology*, vol. 273, p. 116256, 2019.

[74] J.-M. Kim, M.-H. Yoon, J.-P. Hong, and S.-I. Kim, "Analysis of cogging torque caused by manufacturing tolerances of surface-mounted permanent magnet synchronous motor for electric power steering," *IET Electric Power Applications*, vol. 10, no. 8, pp. 691–696, 2016.

[75] M. A. Khan, I. Husain, M. R. Islam, and J. T. Klass, "Design of experiments to address manufacturing tolerances and process variations influencing cogging

torque and back emf in the mass production of the permanent-magnet synchronous motors," *IEEE Transactions on Industry Applications*, vol. 50, no. 1, pp. 346–355, 2013.

[76] R. Lewis, M. Marshall, and R. Dwyer-Joyce, "Measurement of interface pressure in interference fits," *Proceedings of the Institution of Mechanical Engineers, Part C: Journal of Mechanical Engineering Science*, vol. 219, no. 2, pp. 127–139, 2005.

[77] N. Uzhegov, J. Barta, J. Kurfurst, C. Ondrusek, and J. Pyrhonen, "Comparison of high-speed electrical motors for a turbo circulator application," *IEEE Transactions on Industry Applications*, vol. 53, no. 5, pp. 4308–4317, 2017.

[78] N. Bianchi, S. Bolognani, and F. Luise, "Analysis and design of a pm brushless motor for high-speed operations," *IEEE Transactions on Energy Conversion*, vol. 20, no. 3, pp. 629–637, 2005.

[79] M. Beshrati, K. Pullen, J. Widmer, G. Atkinson, and V. Pickert, "Investigation of the mechanical constraints on the design of a super-high-speed switched reluctance motor for automotive traction," in *IET International Conference on Power Electronics, Machines and Drives (PEMD).* IET, 2014, Conference Proceedings, pp. 1–6.

[80] B. Suthar and A. Patel, "Design optimization of axial flux surface mounted permanent magnet brushless dc motor for electrical vehicle based on genetic algorithm," *International Journal of Engineering*, vol. 31, no. 7, pp. 1050–1056, 2018.

[81] Y. Li, C. Zhu, L. Wu, and Y. Zheng, "Multi-objective optimal design of high-speed surface-mounted permanent magnet synchronous motor for magnetically levitated flywheel energy storage system," *IEEE Transactions on Magnetics*, vol. 55, no. 7, pp. 1–8, 2019.

[82] J. Wang, X. Yuan, and K. Atallah, "Design optimization of a surface-mounted permanent-magnet motor with concentrated windings for electric vehicle applications," *IEEE Transactions on Vehicular Technology*, vol. 62, no. 3, pp. 1053–1064, 2012.

[83] Z. Belli and M. Mekideche, "Optimization of magnets segmentation for eddy current losses reduction in permanent magnets electrical machines," in *2013 Eighth International Conference and Exhibition on Ecological Vehicles and Renewable Energies (EVER)*. IEEE, 2013, Conference Proceedings, pp. 1–7.

[84] K. Abbaszadeh, F. Alam, and S. Saied, "Cogging torque optimization in surface-mounted permanent-magnet motors by using design of experiment," *Energy Conversion and Management*, vol. 52, no. 10, pp. 3075–3082, 2011.

[85] I. Das and J. Dennis, "Normal-boundary intersection: A new method for generating the pareto surface in nonlinear multicriteria optimization problems," *SIAM journal on optimization*, vol. 8, no. 3, pp. 631–657, 1998.

[86] T. Marler and J. Arora, "Survey of multi-objective optimization methods for engineering," *Structural and multidisciplinary optimization*, vol. 26, no. 6, pp. 369–395, 2004.

[87] K. Mela, T. Tiainen, and M. Heinisuo, "Comparative study of multiple criteria decision making methods for building design," *Advanced Engineering Informatics*, vol. 26, no. 4, pp. 716–726, 2012. [Online]. Available: http://www.sciencedirect.com/science/article/pii/S1474034612000201 (accessed Aug. 11, 2020)

[88] G. Odu and O. Charles-Owaba, "Review of multi-criteria optimization methods–theory and applications," *IOSR Journal of Engineering (IOSRJEN)*, vol. 3, no. 10, pp. 1–14, 2013.

[89] N. Gunantara, "A review of multi-objective optimization: Methods and its applications," *Cogent Engineering*, vol. 5, no. 1, p. 1502242, 2018.

[90] M. Akram, A. Al-Kenani, and J. Alcantud, "Group decision-making based on the vikor method with trapezoidal bipolar fuzzy information," *Symmetry*, vol. 11, no. 10, p. 1313, 2019.

[91] K. Deb, "Multi-objective optimisation using evolutionary algorithms: an introduction," in *Multi-objective evolutionary optimisation for product design and manufacturing*, L. Wang, A. Ng, and K. Deb, Eds. London: Springer, 2011, pp. 3–34.

[92] J. Vrugt and B. Robinson, "Improved evolutionary optimization from genetically adaptive multimethod search," *Proceedings of the National Academy of Sciences*, vol. 104, no. 3, pp. 708–711, 2007.

[93] K. Deb, A. Pratap, S. Agarwal, and T. Meyarivan, "A fast and elitist multiobjective genetic algorithm: Nsga-ii," *IEEE transactions on evolutionary computation*, vol. 6, no. 2, pp. 182–197, 2002.

[94] E. Asadi, M. da Silva, C. Antunes, and L. Dias, "A multi-objective optimization model for building retrofit strategies using trnsys simulations, genopt and matlab," *Building and Environment*, vol. 56, pp. 370–378, 2012.

[95] Y. Tian, R. Cheng, X. Zhang, and Y. Jin, "Platemo: A matlab platform for evolutionary multi-objective optimization [educational forum]," *IEEE Computational Intelligence Magazine*, vol. 12, no. 4, pp. 73–87, 2017.

[96] S. Lin, "Ngpm - a nsga-ii program in matlab v1.4," 2020. [Online]. Available: https://www.mathworks.com/matlabcentral/fileexchange/31166-ngpm-a-nsga-ii-program-in-matlab-v1-4

[97] R. Kierkels, R. Visser, H. Bijl, J. Langendijk, A. van't Veld, R. Steenbakkers, and E. Korevaar, "Multicriteria optimization enables less experienced planners to efficiently produce high quality treatment plans in head and neck cancer radiotherapy," *Radiation oncology*, vol. 10, no. 1, p. 87, 2015.

[98] Y. Yu, J. Zhang, G. Cheng, M. Schell, and P. Okunieff, "Multi-objective optimization in radiotherapy: applications to stereotactic radiosurgery and prostate brachytherapy," *Artificial Intelligence in*

Medicine, vol. 19, no. 1, pp. 39–51, 2000. [Online]. Available: http://www.sciencedirect.com/science/article/pii/S0933365799000494 (accessed Aug. 14, 2020)

[99] B. Vitoriano, T. Ortuňo, G. Tirado, and J. Montero, "A multi-criteria optimization model for humanitarian aid distribution," *Journal of Global optimization*, vol. 51, no. 2, pp. 189–208, 2011.

[100] J. Ferrer, J. Martín-Campo, T. Ortuňo, A. Pedraza-Martínez, G. Tirado, and B. Vitoriano, "Multi-criteria optimization for last mile distribution of disaster relief aid: Test cases and applications," *European Journal of Operational Research*, vol. 269, no. 2, pp. 501–515, 2018.

[101] W. Gutjahr and P. Nolz, "Multicriteria optimization in humanitarian aid," *European Journal of Operational Research*, vol. 252, no. 2, pp. 351–366, 2016.

[102] J. Wang, Y. Jing, C. Zhang, G. Shi, and X. Zhang, "A fuzzy multi-criteria decision-making model for trigeneration system," *Energy Policy*, vol. 36, no. 10, pp. 3823–3832, 2008.

[103] P. Pilavachi, S. Stephanidis, V. Pappas, and N. Afgan, "Multi-criteria evaluation of hydrogen and natural gas fuelled power plant technologies," *Applied Thermal Engineering*, vol. 29, no. 11-12, pp. 2228–2234, 2009.

[104] M. Jureczko, M. Pawlak, and A. Mężyk, "Optimisation of wind turbine blades," *Journal of materials processing technology*, vol. 167, no. 2-3, pp. 463–471, 2005.

[105] C. Hopfe, M. Emmerich, R. Marijt, and J. Hensen, "Robust multi-criteria design optimisation in building design," *Proceedings of building simulation and optimization, Loughborough, UK*, pp. 118–125, 2012.

[106] W. Chen, J. Unkelbach, A. Trofimov, T. Madden, H. Kooy, T. Bortfeld, and D. Craft, "Including robustness in multi-criteria optimization for intensity-modulated proton therapy," *Physics in Medicine & Biology*, vol. 57, no. 3, p. 591, 2012.

[107] Y. M. Goh, J. Booker, and C. McMahon, "Uncertainty modelling of a suspension unit," *Proceedings of the Institution of Mechanical Engineers, Part D: Journal of Automobile Engineering*, vol. 219, no. 6, pp. 755–771, 2005.

[108] Y. M. Goh, C. McMahon, and J. Booker, "Improved utility and application of probabilistic methods for reliable mechanical design," *Proceedings of the Institution of Mechanical Engineers, Part O: Journal of Risk and Reliability*, vol. 223, no. 3, pp. 199–214, 2009.

[109] D. Hong, B. Woo, and D. Koo, "Rotordynamics of 120000 r/min 15 kw ultra high speed motor," *IEEE transactions on magnetics*, vol. 45, no. 6, pp. 2831–2834, 2009.

[110] J. Wang, F. Wang, W. Bao, and E. Guan, "Rotor design and strength analysis of high speed permanent magnet machine," *Proceedings-Chinese Society of Electrical Engineering*, vol. 25, no. 15, p. 140, 2005.

[111] J. Ahn, C. Han, C. Kim, and J. Choi, "Rotor design of high-speed permanent magnet synchronous motors considering rotor magnet and sleeve materials," *IEEE Transactions on Applied Superconductivity*, vol. 28, no. 3, pp. 1–4, 2017.

[112] G. Jang, J. Ahn, B. Kim, D. Lee, J. Bang, and J. Choi, "Design and characteristic analysis of a high-speed permanent magnet synchronous motor considering the mechanical structure for high-speed and high-head centrifugal pumps," *IEEE Transactions on Magnetics*, vol. 54, no. 11, pp. 1–6, 2018.

[113] T. Juuma, "Torsional fretting fatigue strength of a shrink-fitted shaft with a grooved hub," *Tribology International*, vol. 33, no. 8, pp. 537–543, 2000.

[114] Z. Yang, P. Yang, T. Zhao, L. Chen, S. Li, and J. Zhang, "Carbon-fiber-wrapped rotor strength analysis for high-speed permanent magnet synchronous machine," in *2019 22nd International Conference on Electrical Machines and Systems (ICEMS)*.   IEEE, 2019, Conference Proceedings, pp. 1–8.

[115] L. Chen, C. Zhu, Z. Zhong, B. Liu, and A. Wan, "Rotor strength analysis for high-speed segmented surface-mounted permanent magnet synchronous machines," *IET Electric Power Applications*, vol. 12, no. 7, pp. 979–990, 2018.

[116] R. Sanchez, A. Yoon, X. Yi, L. Zheng, Y. Chen, K. Haran, A. Provenza, and J. Veres, "Mechanical validation of a high power density external cantilevered rotor," *IEEE Transactions on Industry Applications*, vol. 54, no. 4, pp. 3208–3216, 2018.

[117] G. Du, W. Xu, J. Zhu, and N. Huang, "Rotor stress analysis for high-speed permanent magnet machines considering assembly gap and temperature gradient," *IEEE Transactions on Energy Conversion*, vol. 34, no. 4, pp. 2276–2285, 2019.

[118] G. Atkinson, B. Mecrow, A. Jack, D. Atkinson, P. Sangha, and M. Benarous, "The analysis of losses in high-power fault-tolerant machines for aerospace applications," *IEEE Transactions on Industry Applications*, vol. 42, no. 5, pp. 1162–1170, 2006.

[119] D. Hong, T. Lee, and Y. Jeong, "Design and experimental validation of a high-speed electric turbocharger motor considering variation of the l/d ratio," *IEEE Transactions on Magnetics*, vol. 54, no. 11, pp. 1–4, 2018.

[120] Y. Wang, Q. Feng, X. Li, and W. Ma, "Design, analysis, and experimental test of a segmented-rotor high-temperature superconducting flux-switching generator with stationary seal," *IEEE Transactions on Industrial Electronics*, vol. 65, no. 11, pp. 9047–9055, 2018.

[121] F. Ismagilov, V. Vavilov, A. Miniyarov, and R. Urazbakhtin, "Super high-speed electric motor with amorphous magnetic circuit for the hydrogen fuel cell air supply system," *International Journal of Hydrogen Energy*, vol. 43, no. 24, pp. 11 180–11 189, 2018.

[122] C. Gong, S. Li, and T. Habetler, "Rotor dynamic analysis of ultra-high speed switched reluctance machines over 1 million rpm," in *2018 IEEE Energy Conversion Congress and Exposition (ECCE)*. IEEE, 2018, Conference Proceedings, pp. 1704–1709.

[123] G. Burnand and Y. Perriard, "Very-high-speed miniaturized permanent magnet motors: Modeling and experimental validation," in *2019 IEEE Energy Conversion Congress and Exposition (ECCE)*. IEEE, 2019, Conference Proceedings, pp. 5251–5257.

[124] C. Gong, S. Li, and T. Habetler, "High-strength rotor design for ultra-high speed switched reluctance machines," *IEEE Transactions on Industry Applications*, vol. 56, no. 2, pp. 1432–1442, 2020.

[125] P. Bonello and M. Bin Hassan, "An experimental and theoretical analysis of a foil-air bearing rotor system," *Journal of Sound and Vibration*, vol. 413, pp. 395–420, 2018.

[126] G. Argrawal, "Foil air/gas bearing technology—an overview," in *ASME 1997 international gas turbine and aeroengine congress and exhibition*, vol. 1: Aircraft Engine; Marine; Turbomachinery; Microturbines and Small Turbomachinery. ASME, 1997, Conference Proceedings, pp. 1–11.

[127] S. Ha, M. Kim, S. Han, and T. Sung, "Design and spin test of a hybrid composite flywheel rotor with a split type hub," *Journal of composite materials*, vol. 40, no. 23, pp. 2113–2130, 2006.

[128] C. Warren, C. Niezrecki, and P. Avitabile, "Applications of digital image correlation and dynamic photogrammetry for rotating and non-rotating structures," in *Proceedings of the 7th International Workshop on Structural Health Monitoring, Stanford, CA*, vol. 2, 2009, Conference Proceedings, pp. 1603–1612.

[129] J. Baqersad, P. Poozesh, C. Niezrecki, and P. Avitabile, "Photogrammetry and optical methods in structural dynamics–a review," *Mechanical Systems and Signal Processing*, vol. 86 Part B, pp. 17–34, 2017.

[130] J. Baqersad, C. Niezrecki, and P. Avitabile, "Extracting full-field dynamic strain on a wind turbine rotor subjected to arbitrary excitations using 3d point tracking and a modal expansion technique," *Journal of Sound and Vibration*, vol. 352, pp. 16–29, 2015.

[131] J. Sirohi and M. Lawson, "Measurement of helicopter rotor blade deformation using digital image correlation," *Optical Engineering*, vol. 51, no. 4, p. 043603, 2012.

[132] M. Marshall, R. Lewis, B. Drinkwater, and R. Dwyer-Joyce, "An ultrasonic approach for contact stress mapping in machine joints and concentrated contacts," *The Journal of Strain Analysis for Engineering Design*, vol. 39, no. 4, pp. 339–350, 2004.

[133] H. Brunskill, A. Hunter, L. Zhou, R. D. Joyce, and R. Lewis, "An evaluation of ultrasonic arrays for the static and dynamic measurement of wheel–rail contact pressure and area," *Proceedings of the Institution of Mechanical Engineers, Part J: Journal of Engineering Tribology*, vol. 234, no. 10, pp. 1580–1593, 2020.

[134] S. Yoneyama and G. Murasawa, "Digital image correlation," *Experimental mechanics*, vol. 207, pp. 1–10, 2009.

[135] M. Tekieli, S. De Santis, G. de Felice, A. Kwiecień, and F. Roscini, "Application of digital image correlation to composite reinforcements testing," *Composite Structures*, vol. 160, pp. 670–688, 2017.

[136] B. Bahrami, M. Ayatollahi, and A. Torabi, "Application of digital image correlation method for determination of mixed mode stress intensity factors in sharp notches," *Optics and Lasers in Engineering*, vol. 124, p. 105830, 2020.

[137] X. Shao, X. Dai, Z. Chen, and X. He, "Real-time 3d digital image correlation method and its application in human pulse monitoring," *Applied optics*, vol. 55, no. 4, pp. 696–704, 2016.

[138] M. Hokka, N. Mirow, H. Nagel, M. Irqsusi, S. Vogt, and V. Kuokkala, "In-vivo deformation measurements of the human heart by 3d digital image correlation," *Journal of biomechanics*, vol. 48, no. 10, pp. 2217–2220, 2015.

[139] F. Shadmehri and S. Hoa, "Digital image correlation applications in composite automated manufacturing, inspection, and testing," *Applied Sciences*, vol. 9, no. 13, p. 2719, 2019.

[140] P. Corigliano, V. Crupi, E. Guglielmino, and A. Sili, "Full-field analysis of al/fe explosive welded joints for shipbuilding applications," *Marine Structures*, vol. 57, pp. 207–218, 2018.

[141] P. Mazzoleni and E. Zappa, "Vision-based estimation of vertical dynamic loading induced by jumping and bobbing crowds on civil structures," *Mechanical systems and signal processing*, vol. 33, pp. 1–12, 2012.

[142] M. Helfrick, C. Niezrecki, P. Avitabile, and T. Schmidt, "3d digital image correlation methods for full-field vibration measurement," *Mechanical systems and signal processing*, vol. 25, no. 3, pp. 917–927, 2011.

[143] W. Wang, J. Mottershead, A. Ihle, T. Siebert, and H. Schubach, "Finite element model updating from full-field vibration measurement using digital image correlation," *Journal of Sound and Vibration*, vol. 330, no. 8, pp. 1599–1620, 2011.

[144] C. Warren, C. Niezrecki, P. Avitabile, and P. Pingle, "Comparison of frf measurements and mode shapes determined using optically image based, laser, and accelerometer measurements," *Mechanical Systems and Signal Processing*, vol. 25, no. 6, pp. 2191–2202, 2011.

[145] M. Genç, "Unsteady aerodynamics and flow-induced vibrations of a low aspect ratio rectangular membrane wing with excess length," *Experimental thermal and fluid science*, vol. 44, pp. 749–759, 2013.

[146] T. Schmidt, J. Tyson, and K. Galanulis, "Full-field dynamic displacement and strain measurement—specific examples using advanced 3d image correlation photogrammetry: Part ii," *Experimental Techniques*, vol. 27, no. 4, pp. 22–26, 2003. [Online]. Available: https://doi.org/10.1111/j.1747-1567.2003.tb00118.x (accessed Sept. 02, 2020)

[147] P. Sousa, F. Barros, P. Tavares, and P. Moreira, "Displacement measurement and shape acquisition of an rc helicopter blade using digital image correlation," *Procedia Structural Integrity*, vol. 5, pp. 1253–1259, 2017.

[148] J. Sicard and J. Sirohi, "Measurement of the deformation of an extremely flexible rotor blade using digital image correlation," *Measurement Science and Technology*, vol. 24, no. 6, p. 065203, 2013.

[149] S. Rizo-Patron and J. Sirohi, "Operational modal analysis of a helicopter rotor blade using digital image correlation," *Experimental Mechanics*, vol. 57, no. 3, pp. 367–375, 2017.

[150] P. Reu, "High/ultra-high speed imaging as a diagnostic tool," *Applied Mechanics and Materials*, vol. 70, pp. 69–74, 2011. [Online]. Available: https://www.scientific.net/AMM.70.69 (accessed Sept. 05, 2020)

[151] P. Sousa, F. Carneiro, V. Ramos, P. Tavares, and P. Moreira, "Development of led-based illumination system for high-speed digital image correlation," *Procedia Structural Integrity*, vol. 17, pp. 828–834, 2019.

[152] R. Bigger, A. Carpenter, N. Scott, K. Dannemann, S. Chocron, and C. Williams, "Dynamic response of aluminum 5083 during taylor impact using digital image correlation," *Experimental Mechanics*, vol. 58, no. 6, pp. 951–961, 2018.

[153] S. Barrans and L. Mallin, "Mechanical design of rotors with surface mounted permanent magnets," in *Electric Machines for Smart Grids Applications-Design, Simulation and Control*, A. El-Shahat, Ed. London: IntechOpen, 2018, pp. 87–106.

[154] L. Mallin and S. Barrans, "Comparison of theoretical approaches to determine the stresses in surface mounted permanent magnet rotors for high speed electric machines," *The Journal of Strain Analysis for Engineering Design*, vol. 57, no. 3, pp. 177–192, 2022.

[155] E. Hearn, "Mechanics of materials 2," ser. Mechanics of Materials. Oxford, UK: Butterworth-Heinemann, 1997, pp. 119–120.

[156] R. Fenner and J. Reddy, "Mechanics of solids." Florida, USA: CRC Press, 1991, p. 534.

[157] L. Mallin, "Design of a rig to assess the structural performance of rotors for high speed electric machines," in *Advances in Manufacturing Engineering and*

Materials II. ICMEM 2021. Lecture Notes in Mechanical Engineering. Springer International Publishing, 2021, Conference Proceedings, pp. 301–323.

[158] Rotrex, "Rotrex e-charger. technical datasheet. ec-8/15/30/38," pp. 1–7, 2015. [Online]. Available: https://www.rotrex.com/wp-content/uploads/2020/09/Rotrex-E-charger-Datasheet-V1.60-Gen-1.pdf (accessed Feb. 27, 2020)

[159] Garrett Advancing Motion, "Gt2871r turbocharger. exhaust flow chart," 2020. [Online]. Available: https://www.garrettmotion.com/wp-content/uploads/2018/05/Turbine-Flow-GT28.jpg (accessed Feb. 27, 2020)

[160] A. Acciaioli, G. Lionello, and M. Baleani, "Experimentally achievable accuracy using a digital image correlation technique in measuring small-magnitude homogeneous strain fields," *Materials*, vol. 11, no. 5, p. 751, 2018. [Online]. Available: https://www.mdpi.com/1996-1944/11/5/751 (accessed Sept. 25, 2021)

[161] MatWeb, "Aluminum 6061-t6; 6061-t651," 2022. [Online]. Available: https://matweb.com/search/DataSheet.aspx?MatGUID=b8d536e0b9b54bd7b69e4124d8f1d20a&ckck=1 (accessed Mar. 31, 2022)

[162] MatWeb, "Uninhibited naval brass, uns c46400, h01 (8%) temper 25 mm rod/bar," 2022. [Online]. Available: https://matweb.com/search/DataSheet.aspx?MatGUID=c3bea3ce78e34dea82cd2fd16b0e5abf (accessed Apr. 01, 2022)

[163] MatWeb, "304 stainless steel," 2022. [Online]. Available: https://www.matweb.com/search/DataSheet.aspx?MatGUID=abc4415b0f8b490387e3c922237098da&ckck=1 (accessed Apr. 01, 2022)

[164] Metal Supermarkets, "Brass round bar cz121," 2022. [Online]. Available: https://www.metalsupermarkets.co.uk/product/brass-round-bar-cz121/ (accessed Apr. 07, 2022)

[165] HME Brass Germany GmbH, "Test report 2.2 acc. to din en 10204: En12164 brass," Berlin, Germany, p. 1, 2019.

[166] Metal Supermarkets, "Engineering steel round bar en16," 2022. [Online]. Available: https://www.metalsupermarkets.co.uk/product/engineering-steel-round-bar-en16/#:˜:text=Engineering%20Steel%20Round%20Bar%20EN16%20is%20a%20round%20shaped%20EN16,low%20alloy%20high%20tensile%20steel. (accessed Apr. 07, 2022)

[167] MatWeb, "Architectural bronze, uns c38500," 2022. [Online]. Available: https://matweb.com/search/DataSheet.aspx?MatGUID=4661cca129844a0d 801a4696d5fb0195 (accessed Apr. 07, 2022)

[168] MatWeb, "Ovako 38mnmo6-3 605m36, 5905 (m) steel, +ar," 2022. [Online]. Available: https://matweb.com/search/DataSheet. aspx?MatGUID=4e4b10e3e0d84a008ef2658b8cf95889 (accessed Apr. 07, 2022)

[169] A. Davoudinejad, G. Tosello, P. Parenti, and M. Annoni, "3d finite element simulation of micro end-milling by considering the effect of tool run-out," *Micromachines*, vol. 8, no. 6, p. 187, 2017.

[170] Aalco Metals Ltd, "Aluminium alloy 6082 - t6 extrusions," Sandwell, UK, pp. 1–2, 2019.

[171] L. Mallin and S. Barrans, "Development of an optimisation tool for the mechanical design of permanent magnet rotors in high-speed electric machines," in *2021 12th International Conference on Mechanical and Aerospace Engineering (ICMAE)*, 2021, pp. 208–214.

[172] MatWeb, "Alliance n-33 neodymium iron boron magnetic material," 2022. [Online]. Available: https://matweb.com/ search/DataSheet.aspx?MatGUID=7f8b78c89b054b16accee80f9a363626 (accessed Apr. 20, 2022)

[173] A. Ayob and M. K. Elbasheer, "Optimum autofrettage pressure in thick cylinders," *Jurnal Mekanikal*, vol. 24, pp. 1–14, 2007.

A Three Cylinder Closed Form Analysis MatLab Codes

A.1   Generalised Plane Strain

```matlab
%%%%%%%%%%%%%%%%%%%%%%%%%---Inputs---%%%%%%%%%%%%%%%%%%%%%%%%%
R_ii = 0.003 ;                % Inner surface of inner cylinder
R_ic = 0.004;                 % Outer surface of inner cylinder
R_mc = 0.003999;              % Inner surface of middle cylinder
R_md = 0.022439;              % Outer surface of middle cylinder
R_od = 0.022279;              % Inner surface of outer cylinder
R_oo = 0.025669;              % Outer surface of outer cylinder
Delta_T = 0;                  % Change in temperature (C)
alpha_i = 0.000010 ;          % coefficient of thermal expansion for inner cylinder
alpha_m = 0.000005 ;          % coefficient of thermal expansion for middle cylinder
alpha_o = 0.000009 ;          % coefficient of thermal expansion for outer cylinder
nu_i = 0.29 ;                 % Poisson's ratio for inner cylinder
nu_m = 0.24;                  % Poisson's ratio for middle cylinder
nu_o = 0.36 ;                 % Poisson's ratio for outer cylinder
E_i = 215000000000 ;          % Young's modulus for inner cylinder (Pa)
E_m = 160000000000 ;          % Young's modulus for middle cylinder (Pa)
E_o = 114000000000 ;          % Young's modulus for outer cylinder (Pa)
rho_i = 7700;                 % Density for inner cylinder (kg/m^3)
rho_m = 7500 ;                % Density for middle cylinder (kg/m^3)
rho_o = 4400 ;                % Density for outer cylinder (kg/m^3)
omega = 50000 * (2*pi / 60) ; % Operating speed (rad/s)

%%%%%%%%%%%%%%%%%%%%%%%%%%%% GPS Equations %%%%%%%%%%%%%%%%%%%%%%
GPS_F = -1/(E_m*pi*(R_mc^2 - R_md^2));
GPS_G = 1/(E_i*pi*(R_ic^2 - R_ii^2)) - 1/(E_m*pi*(R_mc^2 - R_md^2));
GPS_H = (2*R_md^2*nu_m)/(E_m*(R_mc^2 - R_md^2));
GPS_I = (2*R_ic^2*nu_i)/(E_i*(R_ic^2 - R_ii^2)) - (2*R_mc^2*nu_m)/(E_m*(R_mc^2 - R_md^2));
GPS_J = (-(omega^2*(nu_m*pi*R_mc^4 - nu_m*pi*R_md^4))/(2*E_m*pi*(R_mc^2 - R_md^2)))*rho_m ...
      + (2*Delta_T*E_m*alpha_m*pi*R_mc^2 - 2*Delta_T*E_m*alpha_m*pi*R_md^2)/(2*E_m*pi*(R_mc^2 - R_md^2))...
      + (rho_i*nu_i*pi*R_ic^4*omega^2 - 2*Delta_T*E_i*alpha_i*pi*R_ic^2 - rho_i*nu_i*pi*R_ii^4*omega^2 ...
      + 2*Delta_T*E_i*alpha_i*pi*R_ii^2)/(2*E_i*pi*(R_ic^2 - R_ii^2));

GPS_K = 1/(E_m*pi*(R_mc^2 - R_md^2)) + 1/(E_o*pi*(R_od^2 - R_oo^2));
GPS_L = 1/(E_m*pi*(R_mc^2 - R_md^2));
GPS_M = - (2*R_md^2*nu_m)/(E_m*(R_mc^2 - R_md^2)) - (2*R_od^2*nu_o)/(E_o*(R_od^2 - R_oo^2));
GPS_N = (2*R_mc^2*nu_m)/(E_m*(R_mc^2 - R_md^2));
GPS_O = - (-(omega^2*(nu_m*pi*R_mc^4 - nu_m*pi*R_md^4))/(2*E_m*pi*(R_mc^2 - R_md^2)))*rho_m ...
      - (2*Delta_T*E_m*alpha_m*pi*R_mc^2 - 2*Delta_T*E_m*alpha_m*pi*R_md^2)/(2*E_m*pi*(R_mc^2 - R_md^2))...
      - (rho_o*nu_o*pi*R_od^4*omega^2 - 2*Delta_T*E_o*alpha_o*pi*R_od^2 - rho_o*nu_o*pi*R_oo^4*omega^2 ...
      + 2*Delta_T*E_o*alpha_o*pi*R_oo^2)/(2*E_o*pi*(R_od^2 - R_oo^2));

GPS_P = (R_mc*nu_m)/(E_m*pi*(R_mc^2 - R_md^2));
GPS_Q = (R_mc*nu_m)/(E_m*pi*(R_mc^2 - R_md^2)) - (R_ic*nu_i)/(E_i*pi*(R_ic^2 - R_ii^2));
GPS_R = -(2*R_mc*R_md^2)/(E_m*(R_mc^2 - R_md^2));
GPS_T = (R_mc*(pi*R_mc^2 + pi*R_md^2 - pi*R_mc^2*nu_m + pi*R_md^2*nu_m))/(E_m*pi*(R_mc^2 - R_md^2))...
      - (R_ic*(pi*R_ic^2 + pi*R_ii^2 - pi*R_ic^2*nu_i + pi*R_ii^2*nu_i))/(E_i*pi*(R_ic^2 - R_ii^2));
GPS_U = R_mc*((rho_m*(R_md^2*nu_m - R_mc^2*nu_m + R_mc^2 + 3*R_md^2)*omega^2)/(4*E_m) + Delta_T*alpha_m + 1)...
      - R_ic*((rho_i*(R_ii^2*nu_i - R_ic^2*nu_i + R_ic^2 + 3*R_ii^2)*omega^2)/(4*E_i)...
      + (Delta_T*E_i*R_ic^2*alpha_i*pi - Delta_T*E_i*R_ii^2*alpha_i*pi)/(E_i*pi*(R_ic^2 - R_ii^2)) + 1);

GPS_V = (R_md*nu_m)/(E_m*pi*(R_mc^2 - R_md^2)) + (R_od*nu_o)/(E_o*pi*(R_od^2 - R_oo^2));
GPS_W = (R_md*nu_m)/(E_m*pi*(R_mc^2 - R_md^2));
GPS_X = - (R_md*(pi*R_mc^2 + pi*R_md^2 + pi*R_mc^2*nu_m - pi*R_md^2*nu_m))/(E_m*pi*(R_mc^2 - R_md^2))...
      - (R_od*(pi*R_od^2 + pi*R_oo^2 - pi*R_od^2*nu_o + pi*R_oo^2*nu_o))/(E_o*pi*(R_od^2 - R_oo^2));
GPS_Y = (2*R_mc^2*R_md)/(E_m*(R_mc^2 - R_md^2));
GPS_Z = R_md*((rho_m*(R_mc^2*nu_m - R_md^2*nu_m + 3*R_mc^2 + R_md^2)*omega^2)/(4*E_m) + Delta_T*alpha_m + 1)...
      - R_od*((rho_o*(R_oo^2*nu_o - R_od^2*nu_o + R_od^2 + 3*R_oo^2)*omega^2)/(4*E_o)...
      + (Delta_T*E_o*R_od^2*alpha_o*pi - Delta_T*E_o*R_oo^2*alpha_o*pi)/(E_o*pi*(R_od^2 - R_oo^2)) + 1);

GPS_A = [GPS_F,GPS_G,GPS_H,GPS_I;GPS_K,GPS_L,GPS_M,GPS_N;GPS_P,GPS_Q,GPS_R,GPS_T;GPS_V,GPS_W,GPS_X,GPS_Y] ;
GPS_C = [GPS_J; GPS_O; GPS_U; GPS_Z] ;
GPS_B = inv(GPS_A) * GPS_C ;
GPS_F_zo = GPS_B(1) ;
GPS_F_zi = GPS_B(2) ;
GPS_S_2 = GPS_B(3) ;
GPS_S_1 = GPS_B(4) ;
GPS_F_zm = -(GPS_F_zo + GPS_F_zi) ;
```

```matlab
%%% Use variables to calculate stresses %%%
%%% Inner cylinder %%%
GPS_sigma_theta_ii = (rho_i*(2*R_ic^2*nu_i + 2*R_ii^2*nu_i - 3*R_ic^2 - R_ii^2)*omega^2)/(4*nu_i - 4)...
                - (2*R_ic^2*GPS_S_1)/(R_ic^2 - R_ii^2);
GPS_sigma_theta_ic = (rho_i*(2*R_ic^2*nu_i + 2*R_ii^2*nu_i - R_ic^2 - 3*R_ii^2)*omega^2)/(4*nu_i - 4)...
                - (R_ic^2*GPS_S_1)/(R_ic^2 - R_ii^2) - (R_ii^2*GPS_S_1)/(R_ic^2 - R_ii^2);
GPS_sigma_rii = 0 ;
GPS_sigma_ric = -GPS_S_1 ;
GPS_sigma_zic = (rho_i*nu_i*(R_ic^2 - R_ii^2)*omega^2)/(4*nu_i - 4) + GPS_F_zi/(pi*(R_ic^2 - R_ii^2));
GPS_sigma_zii = GPS_F_zi/(pi*(R_ic^2 - R_ii^2)) - (omega^2*rho_i*nu_i*(R_ic^2 - R_ii^2))/(4*(nu_i - 1));

%%% Middle cylinder %%%
GPS_sigma_theta_mc = (rho_m*(2*R_mc^2*nu_m + 2*R_md^2*nu_m - R_mc^2 - 3*R_md^2)*omega^2)/(4*nu_m - 4)...
                - (R_mc^2*GPS_S_1 - R_md^2*GPS_S_2)/(R_mc^2 - R_md^2) - (R_md^2*(GPS_S_1 - GPS_S_2))/(R_mc^2 - R_md^2);
GPS_sigma_theta_md = (rho_m*(2*R_mc^2*nu_m + 2*R_md^2*nu_m - 3*R_mc^2 - R_md^2)*omega^2)/(4*nu_m - 4)...
                - (R_mc^2*GPS_S_1 - R_md^2*GPS_S_2)/(R_mc^2 - R_md^2) - (R_mc^2*(GPS_S_1 - GPS_S_2))/(R_mc^2 - R_md^2);
GPS_sigma_rmc = -GPS_S_1 ;
GPS_sigma_rmd = -GPS_S_2 ;
GPS_sigma_zmc = (rho_m*nu_m*(R_mc^2 - R_md^2)*omega^2)/(4*nu_m - 4) - GPS_F_zm/(pi*(R_mc^2 - R_md^2));
GPS_sigma_zmd = - GPS_F_zm/(pi*(R_mc^2 - R_md^2)) - (omega^2*rho_m*nu_m*(R_mc^2 - R_md^2))/(4*(nu_m - 1));

%%% Outer cylinder %%%
GPS_sigma_theta_oo = (rho_o*(2*R_od^2*nu_o + 2*R_oo^2*nu_o - 3*R_od^2 - R_oo^2)*omega^2)/(4*nu_o - 4)...
                - (2*R_od^2*GPS_S_2)/(R_od^2 - R_oo^2);
GPS_sigma_theta_od = (rho_o*(2*R_od^2*nu_o + 2*R_oo^2*nu_o - R_od^2 - 3*R_oo^2)*omega^2)/(4*nu_o - 4)...
                - (R_od^2*GPS_S_2)/(R_od^2 - R_oo^2) - (R_oo^2*GPS_S_2)/(R_od^2 - R_oo^2);
GPS_sigma_roo = 0 ;
GPS_sigma_rod = -GPS_S_2 ;
GPS_sigma_zod = (rho_o*nu_o*(R_od^2 - R_oo^2)*omega^2)/(4*nu_o - 4) - GPS_F_zo/(pi*(R_od^2 - R_oo^2));
GPS_sigma_zoo = - GPS_F_zo/(pi*(R_od^2 - R_oo^2)) - (omega^2*rho_o*nu_o*(R_od^2 - R_oo^2))/(4*(nu_o - 1));

%%%%%% Von Mises %%%%%%
GPS_VM_ic = sqrt(0.5*((GPS_sigma_ric - GPS_sigma_theta_ic)^2 ...
            + (GPS_sigma_theta_ic - GPS_sigma_zic)^2 + (GPS_sigma_zic - GPS_sigma_ric)^2));
GPS_VM_ii = sqrt(0.5*((GPS_sigma_rii - GPS_sigma_theta_ii)^2 ...
            + (GPS_sigma_theta_ii - GPS_sigma_zii)^2 + (GPS_sigma_zii - GPS_sigma_rii)^2));
GPS_VM_mc = sqrt(0.5*((GPS_sigma_rmc - GPS_sigma_theta_mc)^2 ...
            + (GPS_sigma_theta_mc - GPS_sigma_zmc)^2 + (GPS_sigma_zmc - GPS_sigma_rmc)^2));
GPS_VM_md = sqrt(0.5*((GPS_sigma_rmd - GPS_sigma_theta_md)^2 ...
            + (GPS_sigma_theta_md - GPS_sigma_zmd)^2 + (GPS_sigma_zmd - GPS_sigma_rmd)^2));
GPS_VM_od = sqrt(0.5*((GPS_sigma_rod - GPS_sigma_theta_od)^2 ...
            + (GPS_sigma_theta_od - GPS_sigma_zod)^2 + (GPS_sigma_zod - GPS_sigma_rod)^2));
GPS_VM_oo = sqrt(0.5*((GPS_sigma_roo - GPS_sigma_theta_oo)^2 ...
            + (GPS_sigma_theta_oo - GPS_sigma_zoo)^2 + (GPS_sigma_zoo - GPS_sigma_roo)^2));

%%%%%%%% Circumferential strains %%%%%%%%
GPS_epsilon_theta_ic = (1/E_i)*(GPS_sigma_theta_ic - nu_i*GPS_sigma_ric - nu_i*GPS_sigma_zic);
GPS_epsilon_theta_ii = (1/E_i)*(GPS_sigma_theta_ii - nu_i*GPS_sigma_rii - nu_i*GPS_sigma_zii);
GPS_epsilon_theta_mc = (1/E_m)*(GPS_sigma_theta_mc - nu_m*GPS_sigma_rmc - nu_m*GPS_sigma_zmc);
GPS_epsilon_theta_md = (1/E_m)*(GPS_sigma_theta_md - nu_m*GPS_sigma_rmd - nu_m*GPS_sigma_zmd);
GPS_epsilon_theta_od = (1/E_o)*(GPS_sigma_theta_od - nu_o*GPS_sigma_rod - nu_o*GPS_sigma_zod);
GPS_epsilon_theta_oo = (1/E_o)*(GPS_sigma_theta_oo - nu_o*GPS_sigma_roo - nu_o*GPS_sigma_zoo);

%%%%%%%% Radial strains %%%%%%%%
GPS_epsilon_ric = (1/E_i)*(GPS_sigma_ric - nu_i*GPS_sigma_theta_ic - nu_i*GPS_sigma_zic);
GPS_epsilon_rii = (1/E_i)*(GPS_sigma_rii - nu_i*GPS_sigma_theta_ii - nu_i*GPS_sigma_zii);
GPS_epsilon_rmc = (1/E_m)*(GPS_sigma_rmc - nu_m*GPS_sigma_theta_mc - nu_m*GPS_sigma_zmc);
GPS_epsilon_rmd = (1/E_m)*(GPS_sigma_rmd - nu_m*GPS_sigma_theta_md - nu_m*GPS_sigma_zmd);
GPS_epsilon_rod = (1/E_o)*(GPS_sigma_rod - nu_o*GPS_sigma_theta_od - nu_o*GPS_sigma_zod);
GPS_epsilon_roo = (1/E_o)*(GPS_sigma_roo - nu_o*GPS_sigma_theta_oo - nu_o*GPS_sigma_zoo);

%%%%%%%% Axial strains %%%%%%%%
GPS_epsilon_zic = (1/E_i)*(GPS_sigma_zic - nu_i*GPS_sigma_ric - nu_i*GPS_sigma_theta_ic);
GPS_epsilon_zii = (1/E_i)*(GPS_sigma_zii - nu_i*GPS_sigma_rii - nu_i*GPS_sigma_theta_ii);
GPS_epsilon_zmc = (1/E_m)*(GPS_sigma_zmc - nu_m*GPS_sigma_rmc - nu_m*GPS_sigma_theta_mc);
GPS_epsilon_zmd = (1/E_m)*(GPS_sigma_zmd - nu_m*GPS_sigma_rmd - nu_m*GPS_sigma_theta_md);
GPS_epsilon_zod = (1/E_o)*(GPS_sigma_zod - nu_o*GPS_sigma_rod - nu_o*GPS_sigma_theta_od);
GPS_epsilon_zoo = (1/E_o)*(GPS_sigma_zoo - nu_o*GPS_sigma_roo - nu_o*GPS_sigma_theta_oo);
```

A.2 Plane Strain

```matlab
%%%%%%%%%%%%%%%%%%%%%%%%%%%---Inputs---%%%%%%%%%%%%%%%%%%%%%%%%%%%%
R_ii = 0.003 ;              % Inner surface of inner cylinder
R_ic = 0.004;               % Outer surface of inner cylinder
R_mc = 0.003999;            % Inner surface of middle cylinder
R_md = 0.022439;            % Outer surface of middle cylinder
R_od = 0.022279;            % Inner surface of outer cylinder
R_oo = 0.025669;            % Outer surface of outer cylinder
Delta_T = 0;                % Change in temperature (C)
alpha_i = 0.000010 ;        % coefficient of thermal expansion for inner cylinder
alpha_m = 0.000005 ;        % coefficient of thermal expansion for middle cylinder
alpha_o = 0.000009 ;        % coefficient of thermal expansion for outer cylinder
nu_i = 0.29 ;               % Poisson's ratio for inner cylinder
nu_m = 0.24;                % Poisson's ratio for middle cylinder
nu_o = 0.36 ;               % Poisson's ratio for outer cylinder
E_i = 215000000000 ;        % Young's modulus for inner cylinder (Pa)
E_m = 160000000000 ;        % Young's modulus for middle cylinder (Pa)
E_o = 114000000000 ;        % Young's modulus for outer cylinder (Pa)
rho_i = 7700;               % Density for inner cylinder (kg/m^3)
rho_m = 7500 ;              % Density for middle cylinder (kg/m^3)
rho_o = 4400 ;              % Density for outer cylinder (kg/m^3)
omega = 50000 * (2*pi / 60) ;   % Operating speed (rad/s)

%%%%%%%%%%%%%%%%%%%%%%%%%%%%%%% Plane strain Equations %%%%%%%%%%%%%%%%%%%%%%%%%%
p_strain_U = (R_ic*(v_i + 1)*(4*R_ic^2 - 8*R_ic^2*v_i + 4*R_ii^2))/(4*E_i*(R_ic^2 - R_ii^2))...
            - (R_mc*(v_m + 1)*(4*R_mc^2 - 8*R_mc^2*v_m + 4*R_md^2))/(4*E_m*(R_mc^2 - R_md^2));
p_strain_V = -(R_mc*(v_m + 1)*(8*R_md^2*v_m - 8*R_md^2))/(4*E_m*(R_mc^2 - R_md^2));
p_strain_W = R_ic*(((4*Delta_T*E_i*alpha_i*R_ic^2 - 4*Delta_T*E_i*alpha_i*R_ii^2)*(v_i + 1))...
            /(4*E_i*(R_ic^2 - R_ii^2)) - (omega^2*rho_i*(v_i + 1)*(2*R_ic^2*v_i + 2*R_ii^2*v_i ...
            - R_ic^2 - 3*R_ii^2))/(4*E_i) + 1) - R_mc*(((4*Delta_T*E_m*alpha_m*R_mc^2 ...
            - 4*Delta_T*E_m*alpha_m*R_md^2)*(v_m + 1))/(4*E_m*(R_mc^2 - R_md^2)) ...
            - (omega^2*rho_m*(v_m + 1)*(2*R_mc^2*v_m + 2*R_md^2*v_m - R_mc^2 - 3*R_md^2))/(4*E_m) + 1);

p_strain_X = (R_md*(v_m + 1)*(8*R_mc^2*v_m - 8*R_mc^2))/(4*E_m*(R_mc^2 - R_md^2));
p_strain_Y = (R_md*(v_m + 1)*(4*R_mc^2 - 8*R_md^2*v_m + 4*R_md^2))/(4*E_m*(R_mc^2 - R_md^2))...
            + (R_od*(v_o + 1)*(4*R_od^2 - 8*R_od^2*v_o + 4*R_oo^2))/(4*E_o*(R_od^2 - R_oo^2));
p_strain_Z = R_od*(((4*Delta_T*E_o*alpha_o*R_od^2 - 4*Delta_T*E_o*alpha_o*R_oo^2)*(v_o + 1))...
            /(4*E_o*(R_od^2 - R_oo^2)) - (omega^2*rho_o*(v_o + 1)*(2*R_od^2*v_o + 2*R_oo^2*v_o ...
            - R_od^2 - 3*R_oo^2))/(4*E_o) + 1) - R_md*(((4*Delta_T*E_m*alpha_m*R_mc^2 ...
            - 4*Delta_T*E_m*alpha_m*R_md^2)*(v_m + 1))/(4*E_m*(R_mc^2 - R_md^2)) ...
            - (omega^2*rho_m*(v_m + 1)*(2*R_mc^2*v_m + 2*R_md^2*v_m - 3*R_mc^2 - R_md^2))/(4*E_m) + 1);

p_strain_A = [p_strain_U,p_strain_V;p_strain_X,p_strain_Y] ;
p_strain_C = [p_strain_W;p_strain_Z] ;
p_strain_B = inv(p_strain_A) * p_strain_C ;
p_strain_S_1 = p_strain_B(1) ;
p_strain_S_2 = p_strain_B(2) ;

%%% Use variables to calculate stresses %%%
%%% Inner cylinder %%%
p_strain_sigma_theta_ii = (rho_i*(2*R_ic^2*v_i + 2*R_ii^2*v_i - 3*R_ic^2 - R_ii^2)*omega^2)/(4*v_i - 4)...
                        - (2*R_ic^2*p_strain_S_1)/(R_ic^2 - R_ii^2);
p_strain_sigma_theta_ic = (rho_i*(2*R_ic^2*v_i + 2*R_ii^2*v_i - R_ic^2 - 3*R_ii^2)*omega^2)/(4*v_i - 4) ...
                        - (R_ic^2*p_strain_S_1)/(R_ic^2 - R_ii^2) - (R_ii^2*p_strain_S_1)/(R_ic^2 - R_ii^2);
p_strain_sigma_rii = 0 ;
p_strain_sigma_ric = -p_strain_S_1 ;
p_strain_sigma_zic = (rho_i*v_i*(2*R_ic^2*v_i + 2*R_ii^2*v_i - R_ic^2 - 3*R_ii^2)*omega^2)/(4*v_i - 4) ...
                   - (2*R_ic^2*p_strain_S_1*v_i + Delta_T*E_i*R_ic^2*alpha_i - Delta_T*E_i*R_ii^2*alpha_i)/(R_ic^2 - R_ii^2);
p_strain_sigma_zii = (rho_i*v_i*(2*R_ic^2*v_i + 2*R_ii^2*v_i - 3*R_ic^2 - R_ii^2)*omega^2)/(4*v_i - 4) ...
                   - (2*R_ic^2*p_strain_S_1*v_i + Delta_T*E_i*R_ic^2*alpha_i - Delta_T*E_i*R_ii^2*alpha_i)/(R_ic^2 - R_ii^2);

%%% Middle cylinder %%%
p_strain_sigma_theta_mc = (rho_m*(2*R_mc^2*v_m + 2*R_md^2*v_m - R_mc^2 - 3*R_md^2)*omega^2)/(4*v_m - 4) ...
                        - (R_mc^2*p_strain_S_1 - R_md^2*p_strain_S_2)/(R_mc^2 - R_md^2) ...
                        - (R_md^2*(p_strain_S_1 - p_strain_S_2))/(R_mc^2 - R_md^2);
p_strain_sigma_theta_md = (rho_m*(2*R_mc^2*v_m + 2*R_md^2*v_m - 3*R_mc^2 - R_md^2)*omega^2)/(4*v_m - 4) ...
                        - (R_mc^2*p_strain_S_1 - R_md^2*p_strain_S_2)/(R_mc^2 - R_md^2) ...
                        - (R_mc^2*(p_strain_S_1 - p_strain_S_2))/(R_mc^2 - R_md^2);
p_strain_sigma_rmc = -p_strain_S_1 ;
p_strain_sigma_rmd = -p_strain_S_2 ;
p_strain_sigma_zmc = (rho_m*v_m*(2*R_mc^2*v_m + 2*R_md^2*v_m - R_mc^2 - 3*R_md^2)*omega^2)/(4*v_m - 4) ...
                   - (2*R_mc^2*p_strain_S_1*v_m - 2*R_md^2*p_strain_S_2*v_m + Delta_T*E_m*R_mc^2*alpha_m ...
                   - Delta_T*E_m*R_md^2*alpha_m)/(R_mc^2 - R_md^2);
p_strain_sigma_zmd = (rho_m*v_m*(2*R_mc^2*v_m + 2*R_md^2*v_m - 3*R_mc^2 - R_md^2)*omega^2)/(4*v_m - 4) ...
                   - (2*R_mc^2*p_strain_S_1*v_m - 2*R_md^2*p_strain_S_2*v_m + Delta_T*E_m*R_mc^2*alpha_m ...
                   - Delta_T*E_m*R_md^2*alpha_m)/(R_mc^2 - R_md^2);
```

```matlab
%%% Outer cylinder %%%
p_strain_sigma_theta_oo = (rho_o*(2*R_od^2*v_o + 2*R_oo^2*v_o - 3*R_od^2 - R_oo^2)*omega^2)/(4*v_o - 4) ...
                - (2*R_od^2*p_strain_S_2)/(R_od^2 - R_oo^2);
p_strain_sigma_theta_od = (rho_o*(2*R_od^2*v_o + 2*R_oo^2*v_o - R_od^2 - 3*R_oo^2)*omega^2)/(4*v_o - 4) ...
                - (R_od^2*p_strain_S_2)/(R_od^2 - R_oo^2) - (R_oo^2*p_strain_S_2)/(R_od^2 - R_oo^2);
p_strain_sigma_roo = 0 ;
p_strain_sigma_rod = -p_strain_S_2 ;
p_strain_sigma_zod = (rho_o*v_o*(2*R_od^2*v_o + 2*R_oo^2*v_o - R_od^2 - 3*R_oo^2)*omega^2)/(4*v_o - 4) ...
        - (2*R_od^2*p_strain_S_2*v_o + Delta_T*E_o*R_od^2*alpha_o - Delta_T*E_o*R_oo^2*alpha_o)/(R_od^2 - R_oo^2);
p_strain_sigma_zoo = (rho_o*v_o*(2*R_od^2*v_o + 2*R_oo^2*v_o - 3*R_od^2 - R_oo^2)*omega^2)/(4*v_o - 4) ...
        - (2*R_od^2*p_strain_S_2*v_o + Delta_T*E_o*R_od^2*alpha_o - Delta_T*E_o*R_oo^2*alpha_o)/(R_od^2 - R_oo^2);

%%%%%% Von Mises %%%%%%
p_strain_VM_ic = sqrt(0.5*((p_strain_sigma_ric - p_strain_sigma_theta_ic)^2 ...
                + (p_strain_sigma_theta_ic - p_strain_sigma_zic)^2 + (p_strain_sigma_zic - p_strain_sigma_ric)^2));
p_strain_VM_ii = sqrt(0.5*((p_strain_sigma_rii - p_strain_sigma_theta_ii)^2 ...
                + (p_strain_sigma_theta_ii - p_strain_sigma_zii)^2 + (p_strain_sigma_zii - p_strain_sigma_rii)^2));
p_strain_VM_mc = sqrt(0.5*((p_strain_sigma_rmc - p_strain_sigma_theta_mc)^2 ...
                + (p_strain_sigma_theta_mc - p_strain_sigma_zmc)^2 + (p_strain_sigma_zmc - p_strain_sigma_rmc)^2));
p_strain_VM_md = sqrt(0.5*((p_strain_sigma_rmd - p_strain_sigma_theta_md)^2 ...
                + (p_strain_sigma_theta_md - p_strain_sigma_zmd)^2 + (p_strain_sigma_zmd - p_strain_sigma_rmd)^2));
p_strain_VM_od = sqrt(0.5*((p_strain_sigma_rod - p_strain_sigma_theta_od)^2 ...
                + (p_strain_sigma_theta_od - p_strain_sigma_zod)^2 + (p_strain_sigma_zod - p_strain_sigma_rod)^2));
p_strain_VM_oo = sqrt(0.5*((p_strain_sigma_roo - p_strain_sigma_theta_oo)^2 ...
                + (p_strain_sigma_theta_oo - p_strain_sigma_zoo)^2 + (p_strain_sigma_zoo - p_strain_sigma_roo)^2));

%%%%%%%%% Circumferential strains %%%%%%%
p_strain_epsilon_theta_ic = (1/E_i)*(p_strain_sigma_theta_ic - v_i*p_strain_sigma_ric - v_i*p_strain_sigma_zic)+Delta_T*alpha_i;
p_strain_epsilon_theta_ii = (1/E_i)*(p_strain_sigma_theta_ii - v_i*p_strain_sigma_rii - v_i*p_strain_sigma_zii)+Delta_T*alpha_i;
p_strain_epsilon_theta_mc = (1/E_m)*(p_strain_sigma_theta_mc - v_m*p_strain_sigma_rmc - v_m*p_strain_sigma_zmc)+Delta_T*alpha_m;
p_strain_epsilon_theta_md = (1/E_m)*(p_strain_sigma_theta_md - v_m*p_strain_sigma_rmd - v_m*p_strain_sigma_zmd)+Delta_T*alpha_m;
p_strain_epsilon_theta_od = (1/E_o)*(p_strain_sigma_theta_od - v_o*p_strain_sigma_rod - v_o*p_strain_sigma_zod)+Delta_T*alpha_o;
p_strain_epsilon_theta_oo = (1/E_o)*(p_strain_sigma_theta_oo - v_o*p_strain_sigma_roo - v_o*p_strain_sigma_zoo)+Delta_T*alpha_o;

%%%%%%%%% Radial strains %%%%%%%
p_strain_epsilon_ric = (1/E_i)*(p_strain_sigma_ric - v_i*p_strain_sigma_theta_ic - v_i*p_strain_sigma_zic);
p_strain_epsilon_rii = (1/E_i)*(p_strain_sigma_rii - v_i*p_strain_sigma_theta_ii - v_i*p_strain_sigma_zii);
p_strain_epsilon_rmc = (1/E_m)*(p_strain_sigma_rmc - v_m*p_strain_sigma_theta_mc - v_m*p_strain_sigma_zmc);
p_strain_epsilon_rmd = (1/E_m)*(p_strain_sigma_rmd - v_m*p_strain_sigma_theta_md - v_m*p_strain_sigma_zmd);
p_strain_epsilon_rod = (1/E_o)*(p_strain_sigma_rod - v_o*p_strain_sigma_theta_od - v_o*p_strain_sigma_zod);
p_strain_epsilon_roo = (1/E_o)*(p_strain_sigma_roo - v_o*p_strain_sigma_theta_oo - v_o*p_strain_sigma_zoo);

%%%%%%%%% Axial strains %%%%%%%
p_strain_epsilon_zic = 0;
p_strain_epsilon_zii = 0;
p_strain_epsilon_zmc = 0;
p_strain_epsilon_zmd = 0;
p_strain_epsilon_zod = 0;
p_strain_epsilon_zoo = 0;
```

A.3 Plane Stress

```
%%%%%%%%%%%%%%%%%%%%%%%%---Inputs---%%%%%%%%%%%%%%%%%%%%%%%%
R_ii = 0.003 ;                    % Inner surface of inner cylinder
R_ic = 0.004;                     % Outer surface of inner cylinder
R_mc = 0.003999;                  % Inner surface of middle cylinder
R_md = 0.022439;                  % Outer surface of middle cylinder
R_od = 0.022279;                  % Inner surface of outer cylinder
R_oo = 0.025669;                  % Outer surface of outer cylinder
Delta_T = 0;                      % Change in temperature (C)
alpha_i = 0.000010 ;              % coefficient of thermal expansion for inner cylinder
alpha_m = 0.000005 ;              % coefficient of thermal expansion for middle cylinder
alpha_o = 0.000009 ;              % coefficient of thermal expansion for outer cylinder
nu_i = 0.29 ;                     % Poisson's ratio for inner cylinder
nu_m = 0.24;                      % Poisson's ratio for middle cylinder
nu_o = 0.36 ;                     % Poisson's ratio for outer cylinder
E_i = 215000000000 ;              % Young's modulus for inner cylinder (Pa)
E_m = 160000000000 ;              % Young's modulus for middle cylinder (Pa)
E_o = 114000000000 ;              % Young's modulus for outer cylinder (Pa)
rho_i = 7700;                     % Density for inner cylinder (kg/m^3)
rho_m = 7500 ;                    % Density for middle cylinder (kg/m^3)
rho_o = 4400 ;                    % Density for outer cylinder (kg/m^3)
omega = 50000 * (2*pi / 60) ;     % Operating speed (rad/s)

%%%%%%%%%%%%%%%%%%%%%%%%%%%% Plane stress equations %%%%%%%%%%%%%%%%%%%%%%%%
p_stress_U = (R_ic*(R_ii^2*v_i - R_ic^2*v_i + R_ic^2 + R_ii^2))/(E_i*(R_ic^2 - R_ii^2)) ...
           - (R_mc*(R_md^2*v_m - R_mc^2*v_m + R_mc^2 + R_md^2))/(E_m*(R_mc^2 - R_md^2));
p_stress_V = (2*R_mc*R_md^2)/(E_m*(R_mc^2 - R_md^2));
p_stress_W = R_ic*((rho_i*(R_ii^2*v_i - R_ic^2*v_i + R_ic^2 + 3*R_ii^2)*omega^2)/(4*E_i) ...
           + Delta_T*alpha_i + 1) - R_mc*((rho_m*(R_md^2*v_m - R_mc^2*v_m + R_mc^2 ...
           + 3*R_md^2)*omega^2)/(4*E_m) + Delta_T*alpha_m + 1);

p_stress_X = -(2*R_mc^2*R_md)/(E_m*(R_mc^2 - R_md^2));
p_stress_Y = (R_md*(R_mc^2*v_m - R_md^2*v_m + R_mc^2 + R_md^2))/(E_m*(R_mc^2 - R_md^2)) ...
           + (R_od*(R_oo^2*v_o - R_od^2*v_o + R_od^2 + R_oo^2))/(E_o*(R_od^2 - R_oo^2));
p_stress_Z = R_od*((rho_o*(R_oo^2*v_o - R_od^2*v_o + R_od^2 + 3*R_oo^2)*omega^2)/(4*E_o) ...
           + Delta_T*alpha_o + 1) - R_md*((rho_m*(R_mc^2*v_m - R_md^2*v_m + 3*R_mc^2 ...
           + R_md^2)*omega^2)/(4*E_m) + Delta_T*alpha_m + 1);

p_stress_A = [p_stress_U,p_stress_V;p_stress_X,p_stress_Y] ;
p_stress_C = [p_stress_W;p_stress_Z] ;
p_stress_B = inv(p_stress_A) * p_stress_C ;
p_stress_S_1 = p_stress_B(1);
p_stress_S_2 = p_stress_B(2) ;

%%% Use variables to calculate stresses %%%
%%% Inner cylinder %%%
p_stress_sigma_theta_ii = (rho_i*(R_ic^2*v_i - R_ii^2*v_i + 3*R_ic^2 + R_ii^2)*omega^2)/4 ...
                        - (2*R_ic^2*p_stress_S_1)/(R_ic^2 - R_ii^2);
p_stress_sigma_theta_ic = (rho_i*(R_ii^2*v_i - R_ic^2*v_i + R_ic^2 + 3*R_ii^2)*omega^2)/4 ...
                        - (R_ic^2*p_stress_S_1)/(R_ic^2 - R_ii^2) - (R_ii^2*p_stress_S_1)/(R_ic^2 - R_ii^2);
p_stress_sigma_rii = 0 ;
p_stress_sigma_ric = -p_stress_S_1 ;
p_stress_sigma_zic = 0;
p_stress_sigma_zii = 0;

%%% Middle cylinder %%%
p_stress_sigma_theta_mc = (rho_m*(R_md^2*v_m - R_mc^2*v_m + R_mc^2 + 3*R_md^2)*omega^2)/4 ...
                        - (R_mc^2*p_stress_S_1 - R_md^2*p_stress_S_2)/(R_mc^2 - R_md^2) ...
                        - (R_md^2*(p_stress_S_1 - p_stress_S_2))/(R_mc^2 - R_md^2);
p_stress_sigma_theta_md = (omega^2*rho_m*(2*R_md^4 - 2*R_md^4*v_m + 6*R_mc^2*R_md^2 + 2*R_mc^2*R_md^2*v_m))/(8*R_md^2) ...
                        - (R_mc^2*(8*p_stress_S_1 - 8*p_stress_S_2))/(8*(R_mc^2 - R_md^2)) - (p_stress_S_1*R_mc^2 ...
                        - p_stress_S_2*R_md^2)/(R_mc^2 - R_md^2);
p_stress_sigma_rmc = -p_stress_S_1 ;
p_stress_sigma_rmd = -p_stress_S_2 ;
p_stress_sigma_zmc = 0;
p_stress_sigma_zmd = 0;

%%% Outer cylinder %%%
p_stress_sigma_theta_oo = (rho_o*(R_od^2*v_o - R_oo^2*v_o + 3*R_od^2 + R_oo^2)*omega^2)/4 ...
                        - (2*R_od^2*p_stress_S_2)/(R_od^2 - R_oo^2);
p_stress_sigma_theta_od = (rho_o*(R_oo^2*v_o - R_od^2*v_o + R_od^2 + 3*R_oo^2)*omega^2)/4 ...
                        - (R_od^2*p_stress_S_2)/(R_od^2 - R_oo^2) - (R_oo^2*p_stress_S_2)/(R_od^2 - R_oo^2);
p_stress_sigma_roo = 0 ;
p_stress_sigma_rod = -p_stress_S_2 ;
p_stress_sigma_zod = 0;
p_stress_sigma_zoo = 0;
```

```
%%%%%% Von Mises %%%%%%
p_stress_VM_ic = sqrt(0.5*((p_stress_sigma_ric - p_stress_sigma_theta_ic)^2 ...
                + (p_stress_sigma_theta_ic - p_stress_sigma_zic)^2 + (p_stress_sigma_zic - p_stress_sigma_ric)^2));
p_stress_VM_ii = sqrt(0.5*((p_stress_sigma_rii - p_stress_sigma_theta_ii)^2 ...
                + (p_stress_sigma_theta_ii - p_stress_sigma_zii)^2 + (p_stress_sigma_zii - p_stress_sigma_rii)^2));
p_stress_VM_mc = sqrt(0.5*((p_stress_sigma_rmc - p_stress_sigma_theta_mc)^2 ...
                + (p_stress_sigma_theta_mc - p_stress_sigma_zmc)^2 + (p_stress_sigma_zmc - p_stress_sigma_rmc)^2));
p_stress_VM_md = sqrt(0.5*((p_stress_sigma_rmd - p_stress_sigma_theta_md)^2 ...
                + (p_stress_sigma_theta_md - p_stress_sigma_zmd)^2 + (p_stress_sigma_zmd - p_stress_sigma_rmd)^2));
p_stress_VM_od = sqrt(0.5*((p_stress_sigma_rod - p_stress_sigma_theta_od)^2 ...
                + (p_stress_sigma_theta_od - p_stress_sigma_zod)^2 + (p_stress_sigma_zod - p_stress_sigma_rod)^2));
p_stress_VM_oo = sqrt(0.5*((p_stress_sigma_roo - p_stress_sigma_theta_oo)^2 ...
                + (p_stress_sigma_theta_oo - p_stress_sigma_zoo)^2 + (p_stress_sigma_zoo - p_stress_sigma_roo)^2));

%%%%%%%%% Circumferential strains %%%%%%%%
p_stress_epsilon_theta_ic = (1/E_i)*(p_stress_sigma_theta_ic - v_i*p_stress_sigma_ric - v_i*p_stress_sigma_zic);
p_stress_epsilon_theta_ii = (1/E_i)*(p_stress_sigma_theta_ii - v_i*p_stress_sigma_rii - v_i*p_stress_sigma_zii);
p_stress_epsilon_theta_mc = (1/E_m)*(p_stress_sigma_theta_mc - v_m*p_stress_sigma_rmc - v_m*p_stress_sigma_zmc);
p_stress_epsilon_theta_md = (1/E_m)*(p_stress_sigma_theta_md - v_m*p_stress_sigma_rmd - v_m*p_stress_sigma_zmd);
p_stress_epsilon_theta_od = (1/E_o)*(p_stress_sigma_theta_od - v_o*p_stress_sigma_rod - v_o*p_stress_sigma_zod);
p_stress_epsilon_theta_oo = (1/E_o)*(p_stress_sigma_theta_oo - v_o*p_stress_sigma_roo - v_o*p_stress_sigma_zoo);

%%%%%%%%% Radial strains %%%%%%%%
p_stress_epsilon_ric = (1/E_i)*(p_stress_sigma_ric - v_i*p_stress_sigma_theta_ic - v_i*p_stress_sigma_zic);
p_stress_epsilon_rii = (1/E_i)*(p_stress_sigma_rii - v_i*p_stress_sigma_theta_ii - v_i*p_stress_sigma_zii);
p_stress_epsilon_rmc = (1/E_m)*(p_stress_sigma_rmc - v_m*p_stress_sigma_theta_mc - v_m*p_stress_sigma_zmc);
p_stress_epsilon_rmd = (1/E_m)*(p_stress_sigma_rmd - v_m*p_stress_sigma_theta_md - v_m*p_stress_sigma_zmd);
p_stress_epsilon_rod = (1/E_o)*(p_stress_sigma_rod - v_o*p_stress_sigma_theta_od - v_o*p_stress_sigma_zod);
p_stress_epsilon_roo = (1/E_o)*(p_stress_sigma_roo - v_o*p_stress_sigma_theta_oo - v_o*p_stress_sigma_zoo);

%%%%%%%%% Axial strains %%%%%%%%
p_stress_epsilon_zic = (1/E_i)*(p_stress_sigma_zic - v_i*p_stress_sigma_ric - v_i*p_stress_sigma_theta_ic);
p_stress_epsilon_zii = (1/E_i)*(p_stress_sigma_zii - v_i*p_stress_sigma_rii - v_i*p_stress_sigma_theta_ii);
p_stress_epsilon_zmc = (1/E_m)*(p_stress_sigma_zmc - v_m*p_stress_sigma_rmc - v_m*p_stress_sigma_theta_mc);
p_stress_epsilon_zmd = (1/E_m)*(p_stress_sigma_zmd - v_m*p_stress_sigma_rmd - v_m*p_stress_sigma_theta_md);
p_stress_epsilon_zod = (1/E_o)*(p_stress_sigma_zod - v_o*p_stress_sigma_rod - v_o*p_stress_sigma_theta_od);
p_stress_epsilon_zoo = (1/E_o)*(p_stress_sigma_zoo - v_o*p_stress_sigma_roo - v_o*p_stress_sigma_theta_oo);
```

B Multi-Criteria Optimisation Tool MatLab Code

```
%*************************************************************************
% Test Problem : 'CONSTR'
% Description:
%    (1)constrained
%
% Reference : [1] Deb K, Pratap A, Agarwal S, et al. A fast and elitist
%    multiobjective genetic algorithm NSGA-II[J]. Evolutionary Computation.
%    2002, 6(2): 182-197.
%*************************************************************************

options = nsgaopt();                                % create default options structure
options.popsize = 500;                              % populaion size
options.maxGen  = 1000;                             % max iterations

options.numObj = 3;                                 % number of criterion
options.numVar = 8;                                 % number of design variables
options.numCons = 12;                               % number of constraints
options.lb = [0.003  0.001  0.000001  0.001  0.000001  0.00001  10000  0];   % lower bound of variable x
options.ub = [0.003  0.04  0.001  0.04  0.001  0.03  200000  200];    % upper bound of variable x
options.objfun = @GPSOpt_Constr_Objfun;             % criteria function handle
options.plotInterval = 100;                         % interval between two calls of "plotnsga".

result = nsga2(options);                            % begin the optimization!

function [y, cons] = GPSOpt_Constr_Objfun(x)

 y = [0,0,0];         % Criteria vector

 % Design Variables
 R_ii = x(1);                    % x(1) = Inner cylinder inner radius (m)
 R_ic = R_ii + x(2);             % x(2) = Inner cylinder thickness (m)
 R_mc = R_ic - x(3);             % x(3) = Inner cylinder / middle cylinder interference (m)
 R_md = R_mc + x(4);             % x(4) = Middle cylinder thickness (m)
 R_od = R_md - x(5);             % x(5) = Middle cylinder / outer clyinder interfernce (m)
 R_oo = R_od + x(6);             % x(6) = Outer cylinder thickness (m)
 omega = x(7) * (2*pi / 60);     % x(7) = Rotor Speed (RPM)
 Delta_T = x(8);                 % x(8) = Temperature change (C)

 %%%% Input Function %%%%%
 [alpha_i,alpha_m,alpha_o,nu_i,nu_m,nu_o,E_i,E_m,E_o,rho_i,rho_m,rho_o,sigma_VM_i_yield,...
     sigma_VM_m_yield,sigma_VM_o_yield]= Inputs_function;


 % Criteria
 y(1) = x(6);          % Outer cylinder thickness
 y(2) = x(4)*-1;       % Middle cylinder thickness
 y(3) = x(7)*-1;       % Rotor Speed

 %Robust Constraint Function
 [cons] = robust_constraint_function(R_ii,R_ic,R_mc,R_md,R_od,R_oo,alpha_i,alpha_m,alpha_o,nu_i,nu_m,...
                nu_o,E_i,E_m,E_o,rho_i,rho_m,rho_o,sigma_VM_i_yield,sigma_VM_m_yield,sigma_VM_o_yield,Delta_T,omega);

 function [alpha_i,alpha_m,alpha_o,nu_i,nu_m,nu_o,E_i,E_m,E_o,rho_i,rho_m,rho_o,sigma_VM_i_yield,...
     sigma_VM_m_yield,sigma_VM_o_yield]= Inputs_function

 %%%%%%%%%%%%%%%%%%%%%%%%%---Inputs---%%%%%%%%%%%%%%%%%%%%%%%%%

 alpha_i = 0.000010 ;              % coefficient of thermal expansion for inner cylinder
 alpha_m = 0.000005 ;              % coefficient of thermal expansion for middle cylinder
 alpha_o = 0.000009 ;              % coefficient of thermal expansion for outer cylinder
 nu_i = 0.29 ;                     % Poisson's ratio for inner cylinder
 nu_m = 0.24;                      % Poisson's ratio for middle cylinder
 nu_o = 0.36 ;                     % Poisson's ratio for outer cylinder
 E_i = 215000000000 ;             % Young's modulus for inner cylinder (Pa)
 E_m = 160000000000 ;             % Young's modulus for middle cylinder (Pa)
 E_o = 114000000000 ;             % Young's modulus for outer cylinder (Pa)
 rho_i = 7700;                     % Density for inner cylinder (kg/m^3)
 rho_m = 7500 ;                    % Density for middle cylinder (kg/m^3)
 rho_o = 4400 ;                    % Density for outer cylinder (kg/m^3)
 sigma_VM_i_yield = 450000000;    % Yield strength for inner cylinder (Pa)
 sigma_VM_m_yield = 850000000;    % Yield strength for middle cylinder (Pa)
 sigma_VM_o_yield = 880000000;    % Yield strength for outer cylinder (Pa)
```

```matlab
function [cons] = robust_constraint_function(R_ii,R_ic,R_mc,R_md,R_od,R_oo,alpha_i,alpha_m,alpha_o,nu_i,nu_m,...
                nu_o,E_i,E_m,E_o,rho_i,rho_m,rho_o,sigma_VM_i_yield,sigma_VM_m_yield,sigma_VM_o_yield,Delta_T,omega)

%Robustness

tol = 0.000001;              % Tolerance value applied to dimensions (m)

l_R_ii = R_ii - tol;         % Upper and lower boundaries on the rotor...
u_R_ii = R_ii + tol;         % dimensions created using the value 'tol'.
l_R_ic = R_ic - tol;
u_R_ic = R_ic + tol;
l_R_mc = R_mc - tol;
u_R_mc = R_mc + tol;
l_R_md = R_md - tol;
u_R_md = R_md + tol;
l_R_od = R_od - tol;
u_R_od = R_od + tol;
l_R_oo = R_oo - tol;
u_R_oo = R_oo + tol;

R_ii_range = [l_R_ii,u_R_ii,R_ii]; % Vectors created to loop through lower, upper, and...
R_ic_range = [l_R_ic,u_R_ic,R_ic]; % original rotor dimensions and operating conditions
R_mc_range = [l_R_mc,u_R_mc,R_mc];
R_md_range = [l_R_md,u_R_md,R_md];
R_od_range = [l_R_od,u_R_od,R_od];
R_oo_range = [l_R_oo,u_R_oo,R_oo];
omega_range = [0,omega];
Delta_T_range = [0,Delta_T];
                            % Empty constraint array created to hold one value per loop cycle.
Constr_array = zeros(length(R_ii_range),length(R_ic_range),length(R_mc_range),length(R_md_range),...
                length(R_od_range),length(R_oo_range),length(omega_range),length(Delta_T_range));

for R_ii_vector = 1:length(R_ii_range)  % Loop command to simulate all possible combinations...
    R_ii = R_ii_range(R_ii_vector) ;    % of potential tolerance or operating condition changes.

    for R_ic_vector = 1:length(R_ic_range)
        R_ic = R_ic_range(R_ic_vector) ;

        for R_mc_vector = 1:length(R_mc_range)
            R_mc = R_mc_range(R_mc_vector) ;

            for R_md_vector = 1:length(R_md_range)
                R_md = R_md_range(R_md_vector) ;

                for R_od_vector = 1:length(R_od_range)
                    R_od = R_od_range(R_od_vector) ;

                    for R_oo_vector = 1:length(R_oo_range)
                        R_oo = R_oo_range(R_oo_vector) ;

                        for speed_vector = 1:length(omega_range)
                            omega = omega_range(speed_vector) ;

                            for temp_vector = 1:length(Delta_T_range)
                                Delta_T = Delta_T_range(temp_vector) ;
%%%%%%%%%%%%%%%%%%%%%%%%%%%%%%% Test Equations %%%%%%%%%%%%%%%%%%%%%%%%%%
% Call GPS Matrix Equations
[F_zo,F_zi,F_zm,S_1,S_2]...
    = GPS_matrix_equations_function(R_ii,R_ic,R_mc,R_md,R_od,R_oo,Delta_T,alpha_i,...
            alpha_o,alpha_m,nu_i,nu_m,nu_o,E_o,E_i,E_m,rho_i,rho_o,rho_m,omega);

% Call GPS Stress Equations
[VM_ic,VM_ii,VM_mc,VM_md,VM_od,VM_oo,sigma_theta_mc,sigma_theta_md]...
    = GPS_stress_equations_function(F_zo,F_zi,F_zm,S_1,S_2,R_ii,R_ic,...
            R_mc,R_md,R_od,R_oo,nu_i,nu_m,nu_o,rho_i,rho_o,rho_m,omega);

% Apply the constraints
[cons] = Constraints_function(VM_ic,VM_ii,VM_mc,VM_md,VM_od,VM_oo,R_oo,...
                sigma_theta_mc,sigma_theta_md,S_1,S_2,sigma_VM_i_yield,...
                    sigma_VM_m_yield,sigma_VM_o_yield);

constr_fail = any(cons); % Convert any constraint violations into binary value '1'.

Constr_array(R_ii_vector,R_ic_vector,R_mc_vector,R_md_vector,R_od_vector,...   % Store each binary '1'
    R_oo_vector,speed_vector,temp_vector)= constr_fail;                       % produced during any loop.

                            end
                        end
                    end
                end
            end
        end
    end
end

Robust_constr_fail = any(Constr_array, 'all'); % Analyse the constraints array

if Robust_constr_fail == 1                      % Trigger the final constraint violation in...
    cons(12) = abs(Robust_constr_fail);         % the constraint vector
end
end
```

```matlab
function [F_zo,F_zi,F_zm,S_1,S_2]...
    = GPS_matrix_equations_function(R_ii,R_ic,R_mc,R_md,R_od,R_oo,Delta_T,alpha_i,alpha_o,alpha_m,nu_i,nu_m,nu_o,...
    E_o,E_i,E_m,rho_i,rho_o,rho_m,omega)

F = -1/(E_m*pi*(R_mc^2 - R_md^2));
G = 1/(E_i*pi*(R_ic^2 - R_ii^2)) - 1/(E_m*pi*(R_mc^2 - R_md^2));
H = (2*R_md^2*nu_m)/(E_m*(R_mc^2 - R_md^2));
I = (2*R_ic^2*nu_i)/(E_i*(R_ic^2 - R_ii^2)) - (2*R_mc^2*nu_m)/(E_m*(R_mc^2 - R_md^2));
J = (-(omega^2*(nu_m*pi*R_mc^4 - nu_m*pi*R_md^4))/(2*E_m*pi*(R_mc^2 - R_md^2)))*rho_m +...
        (2*Delta_T*E_m*alpha_m*pi*R_mc^2 - 2*Delta_T*E_m*alpha_m*pi*R_md^2)/(2*E_m*pi*(R_mc^2 - R_md^2))...
        + (rho_i*nu_i*pi*R_ic^4*omega^2 - 2*Delta_T*E_i*alpha_i*pi*R_ic^2 - rho_i*nu_i*pi*R_ii^4*omega^2 +...
        2*Delta_T*E_i*alpha_i*pi*R_ii^2)/(2*E_i*pi*(R_ic^2 - R_ii^2));

K = 1/(E_m*pi*(R_mc^2 - R_md^2)) + 1/(E_o*pi*(R_od^2 - R_oo^2));
L = 1/(E_m*pi*(R_mc^2 - R_md^2));
M = - (2*R_md^2*nu_m)/(E_m*(R_mc^2 - R_md^2)) - (2*R_od^2*nu_o)/(E_o*(R_od^2 - R_oo^2));
N = (2*R_mc^2*nu_m)/(E_m*(R_mc^2 - R_md^2));
O = - (-(omega^2*(nu_m*pi*R_mc^4 - nu_m*pi*R_md^4))/(2*E_m*pi*(R_mc^2 - R_md^2)))*rho_m -...
        (2*Delta_T*E_m*alpha_m*pi*R_mc^2 - 2*Delta_T*E_m*alpha_m*pi*R_md^2)/(2*E_m*pi*(R_mc^2 - R_md^2))...
        - (rho_o*nu_o*pi*R_od^4*omega^2 - 2*Delta_T*E_o*alpha_o*pi*R_od^2 - rho_o*nu_o*pi*R_oo^4*omega^2 +...
        2*Delta_T*E_o*alpha_o*pi*R_oo^2)/(2*E_o*pi*(R_od^2 - R_oo^2));

P = (R_mc*nu_m)/(E_m*pi*(R_mc^2 - R_md^2));
Q = (R_mc*nu_m)/(E_m*pi*(R_mc^2 - R_md^2)) - (R_ic*nu_i)/(E_i*pi*(R_ic^2 - R_ii^2));
R = -(2*R_mc*R_md)/(E_m*(R_mc^2 - R_md^2));
T = (R_mc*(pi*R_mc^2 + pi*R_md^2 - pi*R_mc^2*nu_m + pi*R_md^2*nu_m))/(E_m*pi*(R_mc^2 - R_md^2)) -...
        (R_ic*(pi*R_ic^2 + pi*R_ii^2 - pi*R_ic^2*nu_i + pi*R_ii^2*nu_i))/(E_i*pi*(R_ic^2 - R_ii^2));
U = R_mc*((rho_m*(R_md^2*nu_m - R_mc^2*nu_m + R_mc^2 + 3*R_md^2)*omega^2)/(4*E_m) + Delta_T*alpha_m + 1)...
        - R_ic*((rho_i*(R_ii^2*nu_i - R_ic^2*nu_i + R_ic^2 + 3*R_ii^2)*omega^2)/(4*E_i) + (Delta_T*E_i*R_ic^2*alpha_i*pi...
        - Delta_T*E_i*R_ii^2*alpha_i*pi)/(E_i*pi*(R_ic^2 - R_ii^2)) + 1);

V = (R_md*nu_m)/(E_m*pi*(R_mc^2 - R_md^2)) + (R_od*nu_o)/(E_o*pi*(R_od^2 - R_oo^2));
W = (R_md*nu_m)/(E_m*pi*(R_mc^2 - R_md^2));
X = - (R_md*(pi*R_mc^2 + pi*R_md^2 + pi*R_mc^2*nu_m - pi*R_md^2*nu_m))/(E_m*pi*(R_mc^2 - R_md^2))...
        - (R_od*(pi*R_od^2 + pi*R_oo^2 - pi*R_od^2*nu_o + pi*R_oo^2*nu_o))/(E_o*pi*(R_od^2 - R_oo^2));
Y = (2*R_mc^2*R_md)/(E_m*(R_mc^2 - R_md^2));
Z = R_md*((rho_m*(R_mc^2*nu_m - R_md^2*nu_m + 3*R_mc^2 + R_md^2)*omega^2)/(4*E_m) + Delta_T*alpha_m + 1)...
        - R_od*((rho_o*(R_oo^2*nu_o - R_od^2*nu_o + R_od^2 + 3*R_oo^2)*omega^2)/(4*E_o) + (Delta_T*E_o*R_od^2*alpha_o*pi...
        - Delta_T*E_o*R_oo^2*alpha_o*pi)/(E_o*pi*(R_od^2 - R_oo^2)) + 1);

A = [F,G,H,I;K,L,M,N;P,Q,R,T;V,W,X,Y] ; % Define matrix equation using above the equations
C = [J; O; U; Z] ;
B = inv(A) * C ;
F_zo = B(1) ;                           % Identify the unknown variables
F_zi = B(2) ;
S_2 = B(3) ;
S_1 = B(4) ;
F_zm = -(F_zo + F_zi) ;

end
function [VM_ic,VM_ii,VM_mc,VM_md,VM_od,VM_oo,sigma_theta_mc,sigma_theta_md]...
    = GPS_stress_equations_function(F_zo,F_zi,F_zm,S_1,S_2,R_ii,R_ic,R_mc,R_md,R_od,R_oo,...
    nu_i,nu_m,nu_o,rho_i,rho_o,rho_m,omega)

%%% Using the unknown variables to calculate stresses %%%
%%% Inner cylinder %%%
sigma_theta_ii = (rho_i*(2*R_ic^2*nu_i + 2*R_ii^2*nu_i - 3*R_ic^2 - R_ii^2)*omega^2)/(4*nu_i - 4)...
        - (2*R_ic^2*S_1)/(R_ic^2 - R_ii^2);
sigma_theta_ic = (rho_i*(2*R_ic^2*nu_i + 2*R_ii^2*nu_i - R_ic^2 - 3*R_ii^2)*omega^2)/(4*nu_i - 4)...
        -(R_ic^2*S_1)/(R_ic^2 - R_ii^2) - (R_ii^2*S_1)/(R_ic^2 - R_ii^2);
sigma_rii = 0 ;
sigma_ric = -S_1 ;
sigma_zic = (rho_i*nu_i*(R_ic^2 - R_ii^2)*omega^2)/(4*nu_i - 4) + F_zi/(pi*(R_ic^2 - R_ii^2));
sigma_zii = F_zi/(pi*(R_ic^2 - R_ii^2)) - (omega^2*rho_i*nu_i*(R_ic^2 - R_ii^2))/(4*(nu_i - 1));

%%% Middle cylinder %%%
sigma_theta_mc = (rho_m*(2*R_mc^2*nu_m + 2*R_md^2*nu_m - R_mc^2 - 3*R_md^2)*omega^2)/(4*nu_m - 4)...
        - (R_mc^2*S_1 - R_md^2*S_2)/(R_mc^2 - R_md^2) - (R_md^2*(S_1 - S_2))/(R_mc^2 - R_md^2);
sigma_theta_md = (rho_m*(2*R_mc^2*nu_m + 2*R_md^2*nu_m - 3*R_mc^2 - R_md^2)*omega^2)/(4*nu_m - 4)...
        - (R_mc^2*S_1 - R_md^2*S_2)/(R_mc^2 - R_md^2) - (R_mc^2*(S_1 - S_2))/(R_mc^2 - R_md^2);
sigma_rmc = -S_1 ;
sigma_rmd = -S_2 ;
sigma_zmc = (rho_m*nu_m*(R_mc^2 - R_md^2)*omega^2)/(4*nu_m - 4) - F_zm/(pi*(R_mc^2 - R_md^2));
sigma_zmd = - F_zm/(pi*(R_mc^2 - R_md^2)) - (omega^2*rho_m*nu_m*(R_mc^2 - R_md^2))/(4*(nu_m - 1));
```

```matlab
%%% Outer cylinder %%%
sigma_theta_oo = (rho_o*(2*R_od^2*nu_o + 2*R_oo^2*nu_o - 3*R_od^2 - R_oo^2)*omega^2)/(4*nu_o - 4)...
                - (2*R_od^2*S_2)/(R_od^2 - R_oo^2);
sigma_theta_od = (rho_o*(2*R_od^2*nu_o + 2*R_oo^2*nu_o - R_od^2 - 3*R_oo^2)*omega^2)/(4*nu_o - 4)...
                - (R_od^2*S_2)/(R_od^2 - R_oo^2) - (R_oo^2*S_2)/(R_od^2 - R_oo^2);
sigma_roo = 0 ;
sigma_rod = -S_2 ;
sigma_zod = (rho_o*nu_o*(R_od^2 - R_oo^2)*omega^2)/(4*nu_o - 4) - F_zo/(pi*(R_od^2 - R_oo^2));
sigma_zoo = - F_zo/(pi*(R_od^2 - R_oo^2)) - (omega^2*rho_o*nu_o*(R_od^2 - R_oo^2))/(4*(nu_o - 1));


%%%%%% Von Mises %%%%%%
VM_ic = sqrt(0.5*((sigma_ric - sigma_theta_ic)^2 + (sigma_theta_ic - sigma_zic)^2 + (sigma_zic - sigma_ric)^2));
VM_ii = sqrt(0.5*((sigma_rii - sigma_theta_ii)^2 + (sigma_theta_ii - sigma_zii)^2 + (sigma_zii - sigma_rii)^2));
VM_mc = sqrt(0.5*((sigma_rmc - sigma_theta_mc)^2 + (sigma_theta_mc - sigma_zmc)^2 + (sigma_zmc - sigma_rmc)^2));
VM_md = sqrt(0.5*((sigma_rmd - sigma_theta_md)^2 + (sigma_theta_md - sigma_zmd)^2 + (sigma_zmd - sigma_rmd)^2));
VM_od = sqrt(0.5*((sigma_rod - sigma_theta_od)^2 + (sigma_theta_od - sigma_zod)^2 + (sigma_zod - sigma_rod)^2));
VM_oo = sqrt(0.5*((sigma_roo - sigma_theta_oo)^2 + (sigma_theta_oo - sigma_zoo)^2 + (sigma_zoo - sigma_roo)^2));

function [cons] = Constraints_function(VM_ic,VM_ii,VM_mc,VM_md,VM_od,VM_oo,R_oo,...
                   sigma_theta_mc,sigma_theta_md,S_1,S_2,sigma_VM_i_yield,sigma_VM_m_yield,sigma_VM_o_yield)

cons = [0,0,0,0,0,0,0,0,0,0,0];   % Constraint vector

if S_1<0
    cons(1) = abs(S_1);              % Constraint 1 & 2
end                                  % Do not allow separation between cylinders
if S_2<0
    cons(2) = abs(S_2);
end
if sigma_theta_mc>0
    cons(3) = abs(sigma_theta_mc);  % Constraint 3 & 4
end                                  % Do not allow magnets to go into tension
if sigma_theta_md>0
    cons(4) = abs(sigma_theta_md);
end
if abs(VM_ic)>sigma_VM_i_yield
    cons(5) = abs(VM_ic);            % Constraint 5 & 6
end                                  % Inner cylinder must not yield
if abs(VM_ii)>sigma_VM_i_yield
    cons(6) = abs(VM_ii);
end
if abs(VM_mc)>sigma_VM_m_yield
    cons(7) = abs(VM_mc);            % Constraint 7 & 8
end                                  % Middle cylinder must not yield
if abs(VM_md)>sigma_VM_m_yield
    cons(8) = abs(VM_md);
end
if abs(VM_od)>sigma_VM_o_yield
    cons(9) = abs(VM_od);            % Constraint 9 & 10
end                                  % Outer cylinder must not yield
if abs(VM_oo)>sigma_VM_o_yield
    cons(10) = abs(VM_oo);
end
if R_oo>0.028                        % Constraint 11
    cons(11) = abs(R_oo);            % Diameter limit
end
end
```